

KAUNAS UNIVERSITY OF TECHNOLOGY

FARIZA KALYK

NANOSTRUCTURED METAL OXIDES
DOPED CERIA CERAMICS FOR LOW-
TEMPERATURE SOLID OXIDE FUEL CELLS
APPLICATION

Doctoral dissertation
Technological Sciences, Materials Engineering (T 008)

Kaunas, 2022

This doctoral dissertation was prepared at Kaunas University of Technology, Faculty of Mathematics and Natural Sciences, Department of Physics during the period of 2017–2021. The studies were supported by the Research Council of Lithuania.

Scientific Supervisor:

Assoc. Prof. Dr. Brigita ABAKEVIČIENĖ (Kaunas University of Technology, Physical Sciences, Physics, N 002).

Edited by: Dr. Armandas Rumšas (Publishing House *Technologija*), Rozita Znamenskaitė (Publishing House *Technologija*)

Dissertation Defence Board of Materials Engineering Science Field:

Prof. Dr. Habil. Arvidas GALDIKAS (Kaunas University of Technology, Technological Sciences, Materials Engineering, T 008) – **chairperson**;
Dr. Mindaugas ANDRULEVIČIUS (Kaunas University of Technology of Institute of Materials Sciences, Technological Sciences, Materials Engineering, T 008);
Dr. Viktoras GRIGALIŪNAS (Kaunas University of Technology of Institute of Materials Sciences, Technological Sciences, Materials Engineering, T 008);
Dr. Sebastian MOLIN (Gdansk University of Technology, Poland, Technological Sciences, Materials Engineering, T 008);
Assoc. Prof. Dr. Tomas ŠALKUS (Vilnius University, Technological Sciences, Materials Engineering, T 008).

The official defence of the dissertation will be held at 11 a.m. on 1st September, 2022 at the public meeting of Dissertation Defence Board of Materials Engineering Science Field in the Santaka Valley at Kaunas University of Technology.

Address: K. Baršausko St. 59–A228, Kaunas LT-51423, Lithuania
Phone: +370 37 300 042; fax: +370 37 324 144; e-mail doktorantura@ktu.lt

The doctoral dissertation was sent out on 1st August, 2022

The doctoral dissertation is available on the internet at <http://ktu.edu> and at the library of Kaunas University of Technology (Donelaičio 20, Kaunas LT-44239, Lithuania).

KAUNO TECHNOLOGIJOS UNIVERSITETAS

FARIZA KALYK

NANOSTRUKTŪRINĖS METALŲ OKSIDŲ
PRIEMAIŠOMIS LEGIRUOTOS CERIO OKSIDO
KERAMIKOS ŽEMATEMPERATŪRIAMS
KIETOJO OKSIDO KURO ELEMENTAMS

Daktaro disertacija
Technologijos mokslai, medžiagų inžinerija (T 008)

Kaunas, 2022

Disertacija rengta 2017–2021 metais Kauno technologijos universiteto Matematikos ir gamtos mokslų fakultete, Fizikos katedroje. Mokslinius tyrimus rėmė Lietuvos mokslo taryba.

Mokslinis vadovas:

Doc. dr. Brigita ABAKEVIČIENĖ (Kauno technologijos universitetas, fiziniai mokslai, fizika, N 002)

Redagavo: Dr. Armandas Rumšas (leidykla „Technologija“), Rozita Znamenskaitė (leidykla „Technologija“).

Medžiagų inžinerijos mokslo krypties disertacijos gynimo taryba:

Prof. habil. dr. Arvidas GALDIKAS (Kauno technologijos universitetas, technologiniai mokslai, medžiagų inžinerija, T 008) – **pirmininkas**;

Dr. Mindaugas ANDRULIČIUS (Kauno technologijos universiteto Medžiagų mokslo institutas, technologiniai mokslai, medžiagų inžinerija, T 008);

Dr. Viktoras GRIGALIŪNAS (Kauno technologijos universiteto Medžiagų mokslo institutas, technologiniai mokslai, medžiagų inžinerija, T 008);

Dr. Sebastian MOLIN (Gdanskio technologijos universitetas, Lenkija, technologiniai mokslai, medžiagų inžinerija, T 008);

Doc. dr. Tomas ŠALKUS (Vilniaus universitetas, technologiniai mokslai, medžiagų inžinerija, T 008).

Disertacija bus ginama viešame Medžiagų inžinerijos mokslo krypties disertacijos gynimo tarybos posėdyje 2022 m. rugsėjo 1 d. 11 val. Kauno technologijos universiteto „Santakos“ slėnyje, Posėdžių kambaryje.

Adresas:

K. Baršausko g. 59–A228, Kaunas LT-51423, Lietuva.

Tel: +370 37 300 042; faks: +370 37 324 144; el. paštas doktorantura@ktu.lt

Disertacija išsiųsta 2022 m. rugpjūčio 1 d.

Su disertacija galima susipažinti interneto svetainėje <http://ktu.edu> ir Kauno technologijos universiteto bibliotekoje (K. Donelaičio g. 20, Kaunas, LT-44239).

ABSTRACT

This dissertation is a systematic study on the formation of nanostructured ceria-based ceramics for low-temperature solid oxide fuel cells (LT-SOFC) application. The dissertation is devoted to the improvement of the preparation route of the SOFC cell components considering the influence of the method of chemical synthesis and the initial metal oxide materials, the dopant, and its concentration, as well as the methods of forming thin films and their parameters.

Combustion, co-precipitation, and sol-gel chemical synthesis methods were used to synthesise $\text{Ce}_{1-x}\text{M}_x\text{O}_{2-\delta}$ nanostructured ceramics with different dopants while varying their concentrations (where $M=\text{Sm}$ and Gd ; $x=0.1, 0.15, 0.2, 0.25, 0.3$). The properties of the formed ceramics have been comprehensively studied, which has made it possible to identify the synthesis method as well as the dopant with the required concentration in our pursuit to obtain the materials with the desired properties.

The obtained ceria-based ceramics were further used as a target material to form GDC and SDC electrolytes by using the electron-beam evaporation technique. A deviation of the composition of the formed films from the composition of the target material, as well as a deviation of the final thickness, was found. According to the obtained results, the optimal parameters of deposition by the electron beam technology were proposed and implemented. By changing the sintering conditions, the most favourable temperature for GDC thin films was determined.

Reactive magnetron sputtering in the DC mode was used to prepare GDC thin film depositing Gd_2O_3 and CeO_2 layer-by-layer. By varying the number of oxide layers (4, 6, and 12), we found that at least 12 layers are required to obtain a completely dense GDC structure without layer separation. Additional sintering after the formation of the films improved their quality.

Due to their chemical stability and high ionic conductivity, ceria-based ceramics can be used not only as an electrolyte, but also as a diffusion barrier layer between the cathode and electrolyte in SOFCs. An anode-supported cell (Ni/YSZ) with GDC as the diffusion barrier-layer was suggested for the low temperature μ -SOFC application. The ~ 700 nm thick GDC was deposited on top of the electrolyte of Ni/YSZ by using the electron beam evaporation technique. To employ the electron beam method and GDC as a barrier layer, it is necessary to apply a cathode material, and further investigations are required.

TABLE OF CONTENTS

ABSTRACT.....	5
TABLE OF CONTENTS	6
LIST OF FIGURES.....	9
LIST OF TABLES	11
LIST OF ABBREVIATIONS AND SYMBOLS	12
1. INTRODUCTION	15
Research goal.....	16
Research tasks	16
Scientific novelty.....	16
The key statements of the doctoral dissertation.....	17
Dissertation structure.....	17
Contribution of the author	17
2. LITERATURE REVIEW	19
2.1 Solid oxide fuel cells	19
2.2 Materials for SOFC structural elements.....	23
2.2.1 Anode	24
2.2.2 Cathode.....	26
2.2.3 Electrolyte	28
2.2.3.1 Methods of chemical synthesis.....	34
2.2.3.2 Thin films fabrication methods	35
3. EXPERIMENTAL TECHNIQUES AND METHODS.....	39
3.1 Chemical synthesis methods.....	39
3.1.1 Combustion synthesis method.....	40
3.1.1.1 Thermodynamics of combustion synthesis	42
3.1.1.2 Kinetics of combustion synthesis	44
3.1.1.3 Mechanism of combustion synthesis	45
3.1.2 Co-precipitation synthesis method.....	46
3.1.2.1 Mechanism of co-precipitation synthesis.....	48
3.1.3 Sol-gel synthesis method.....	49
3.1.3.1 Mechanism of sol-gel synthesis.....	50
3.1.4 Formation of ceramic pellets	51
3.2 Thin film formation methods	51
3.2.1 Electron beam evaporation	51
3.2.2 Magnetron sputtering.....	53
3.3 Analytical techniques.....	54
3.3.1 Thermogravimetric analysis.....	55
3.3.2 X-ray diffraction analysis.....	56
3.3.3 Brunauer-Emmett-Teller method	57
3.3.4 Scanning electron microscopy energy dispersive X-ray spectroscopy	58
3.3.5 Transmission electron microscopy	58
3.3.6 Inductively coupled plasma optical emission spectrometry	59
3.3.7 Fourier transform infrared spectroscopy	59
3.3.8 Electrochemical impedance spectroscopy	60
3.3.9 X-ray photoelectron spectroscopy	63
3.3.10 Atomic force microscopy.....	64
3.3.11 Raman spectroscopy	65
4. RESULTS AND DISCUSSION	66

4.1	Samarium-doped ceria	66
4.1.1	Characterisation of SDC nanopowders	66
4.1.2	Characterisation of SDC ceramic pellets	73
4.1.3	Characteristics of SDC thin films	77
4.1.4	Summary of the experimental results of SDC	81
4.2	Gadolinium-doped ceria.....	82
4.2.1	Characterisation of GDC nanopowders	82
4.2.2	Characterisation of GDC ceramic pellets.....	86
4.2.3	Characterisation of GDC thin films	90
4.2.3.1	GDC thin films obtained by the electron beam evaporation technique	90
4.2.3.2	GDC thin films obtained by magnetron sputtering techniques	94
4.2.4	Summary of the experimental results of GDC	96
4.3	Samarium-gadolinium-doped ceria.....	98
4.3.1	Characterisation of SGDC nanopowders	98
4.3.2	Characterisation of SGDC ceramic pellets	101
4.3.3	Summary of the experimental results of SGDC	103
4.4	Application of ceria-based ceramics as a diffusion barrier layer	104
5.	CONCLUSIONS	106
	SANTRAUKA	108
	IVADAS.....	108
	Tyrimo tikslas.....	109
	Tyrimo uždaviniai	109
	Mokslinis naujumas	109
	Ginamieji teiginiai.....	110
	Disertacijos struktūra	110
	Autorės asmeninis indėlis	110
	Darbo aprobavimas.....	111
	LITERATŪROS APŽVALGA	111
	MEDŽIAGOS, EKSPERIMENTINĖ ĮRANGA IR TYRIMŲ METODIKA	112
	Cheminių sintezių metodai	112
	Plonų dangų formavimo metodai.....	114
	Vakuuminis garinimas elektronų spinduliu.....	114
	Nuolatinės srovės reaktyvūs magnetroninis dulkimas	114
	Analitiniai tyrimo metodai	115
	REZULTATAI IR JŲ APTARIMAS	115
	Samario oksidu legiruotas cerio oksidas	116
	Samario oksidu legiruoto cerio oksido (SDC) nanomiltelių sintezė ir tyrimai.....	116
	Samario oksidu legiruoto cerio oksido (SDC) keramikų tyrimai.....	119
	Samario oksidu legiruoto cerio oksido (SDC) plonų dangų formavimas ir tyrimai	122
	Gadolinio oksidu legiruotas cerio oksidas.....	124
	Gadolinio oksidu legiruoto cerio oksido (GDC) nanomiltelių sintezė ir tyrimai.....	124
	Gadolinio oksidu legiruoto cerio oksido (GDC) keramikų tyrimai.....	125
	Gadolinio oksidu legiruoto cerio oksido (GDC) plonų dangų formavimas ir tyrimai	127
	GDC plonų dangų formavimas vakuuminio garinimu elektronų spindulių metodu .	127
	GDC plonų dangų formavimas nuolatinės srovės reaktyviojo magnetroninio dulkimo metodu	128
	Cerio oksido stabilizavimas	130
	SGDC keramikų tyrimai.....	132
	Legiruotų cerio oksidu keramikų kaip difuzinio (barjerinio) sluoksnio taikymas.	133

IŠVADOS.....	135
6. ACKNOWLEDGEMENTS	137
7. REFERENCES	138
8. CURRICULUM VITAE	162
9. LIST OF PUBLICATIONS AND CONFERENCES RELATED TO THE DISSERTATION	163
List of publications related to the dissertation.....	163
Publications in conference proceedings.....	163
List of conference contributions related to the dissertation	163

LIST OF FIGURES

Fig. 2.1. Types of solid oxide fuel cells: (a) tubular, (b) planar. Reproduced from [14]	21
Fig. 2.2. Path of oxygen migration in cathode where (a) is the surface path for LSM and LSCF cathodes and (b) is the bulk path for LSCF cathode.....	27
Fig. 2.3. (a) Crystal structure and (b) oxygen migration in fluorite ceria (the turquoise circle is oxygen, the red circle is cerium, and the empty square is a vacant oxygen site. Oxygen migration towards oxygen vacant sites is indicated with the arrow)	31
Fig. 2.4. The plot of the ionic conductivity vs ionic radius of various dopants in ceria. Reproduced from [5].....	32
Fig. 3.1. Scheme of the thermal structure of the wave during combustion synthesis [215] ..	45
Fig.3.2. Scheme of combustion synthesis of ceria-based ceramic nanopowders.....	46
Fig.3.3. Scheme of co-precipitation synthesis of ceria-based ceramic nanopowders	49
Fig.3.4. Scheme of sol-gel synthesis of ceria-based ceramic nanopowders	50
Fig. 3.5. Schematic principle of electron beam evaporation.....	52
Fig. 3.6. Schematic principle of magnetron sputtering deposition	54
Fig. 3.7. Scheme of X-Ray diffraction	56
Fig. 3.8. Example of the ICP–OES setup	59
Fig. 3.9. Schematic diagram of a <i>Michelson</i> interferometer for FT–IR.....	60
Fig. 3.10. (a) Schematic diagram of the complex impedance plot of ionic conductivity of bulk and grain boundary with an equivalent circuit, (b) the pellet configuration used for measurements	62
Fig. 4.1. Combined TG–DTG–DSC curves of 20 SDC synthesised by (a) combustion (CB), (b) co-precipitation (CP), and (c) sol-gel (SG) syntheses. Published in [A1, 204].....	67
Fig. 4.2. XRD patterns of SDC nanopowders uncalcined, calcined at 800 °C and 1200 °C synthesised by (a) combustion, (b) co-precipitation, (c) sol-gel	69
Fig. 4.3. Plot of the crystallite size (<i>D</i>) and lattice parameter (<i>a</i>) vs. calcination temperatures for 20 SDC nanopowders synthesised by various synthesis techniques	70
Fig. 4.4. SEM and TEM images of 20 SDC nanopowders calcined at 800 °C, where (a and b) combustion, (c and d) co-precipitation, (e and f) sol-gel syntheses were performed, respectively. The TEM results were published in [A1, 204]	71
Fig. 4.5. FT–IR spectra of (a) CeO ₂ and (b) Sm ₂ O ₃ powders synthesised by the combustion method and calcined at 800°C	72
Fig. 4.6. FT–IR spectra of 20 SDC synthesised by (a) combustion, (b) co-precipitation, and (c) sol-gel.....	73
Fig. 4.7. SEM images of the surface (a, c, e) and cross-section (b, d, f) of 20 SDC pellets pressed from (a and b) combustion (CB), (c and d) co-precipitation (CP), (e and f) sol-gel (SG) synthesised nanopowders. Published in [A1, 204]	74
Fig. 4.8. Complex impedance plots at (a) 280 °C, (b) 400 °C, (c) 600 °C, and (d) 800 °C of 20 SDC ceramic pellets synthesised by combustion, co-precipitation, and sol-gel syntheses. Insert in (a) is an equivalent circuit, where <i>CPE</i> is the constant phase element, <i>R</i> is the resistance for the grain (<i>G</i>), grain boundary (<i>GB</i>), and electrode (<i>E</i>), respectively. Published in [A1, 204].....	75
Fig. 4.9. Arrhenius plot of the total conductivity of SDC synthesised by combustion, co-precipitation, and sol-gel syntheses	77
Fig. 4.10. XRD patterns (a, c, e) and Raman spectra (b, d, f) of 26-SDC thin films on the Si substrate with different thicknesses synthesised by (a, b) combustion, (c, d) co-precipitation, and (e, f) sol-gel methods	78

Fig. 4.11. SEM and 3D AFM images of 26-SDC-CB thin films on Si substrate with different thicknesses, where (a, b) 100 nm, (c, d) 200 nm, (e, f) 400 nm, (g, h) 600 nm, (i, j) 800 nm	80
Fig. 4.12. Combined TGA–DTG–DTA curves of 10 GDC synthesised by (a) combustion (CB) and (b) co-precipitation (CP) syntheses. Figure (b) was published in [A3, 315]	83
Fig. 4.13. XRD patterns of 10 GDC nanopowders synthesised by (a) combustion and (b) co-precipitation calcined at various temperatures	84
Fig. 4.14. Plot of the crystallite size (D) and lattice parameter (a) vs. calcination temperatures for 10 GDC nanopowders	85
Fig. 4.15. SEM and TEM images of 10 GDC nanopowders synthesised by (a and b) combustion and (c and d) co-precipitation synthesis methods and calcined at 800 °C	86
Fig. 4.16. FT–IR spectra of 10 GDC synthesised by (a) combustion and (b) co-precipitation	86
Fig. 4.17. Surface view of 10 GDC synthesised by (a) CP and (b) CB annealed at 1200 °C. Figure (a) was published in [A3, 315]	87
Fig. 4.18. Complex impedance plots of (a), (b) GDC-CP; (c), (d) GDC-CB; and (e), (f) 10 GDC synthesised by combustion and co-precipitation at 400 °C and 600 °C	88
Fig. 4.19. Arrhenius plot of total conductivity for GDC synthesised by combustion and co-precipitation	89
Fig. 4.20. Photo, SEM, and 3D AFM images of (a) 10-GDC and (b) 15-GDC thin films as-evaporated (left) and annealed at 800 °C (right). Published in [A3, 315]	91
Fig. 4.21. Surface roughness parameters calculated from the AFM images of GDC-CP thin films as-evaporated and after additional thermal treatment at 600 °C, 700 °C, 800 °C, 900 °C for 1 h where R_q (the empty figures) is the root mean square and R_z (the filled figures) is the average height	92
Fig. 4.22. Raman spectra of (a) 10-GDC-CP, (b) 15-GDC-CP, and (c) 20-GDC-CP thin films unheated and annealed at several temperatures. Published in [A3, 315]	93
Fig. 4.23. Results of (a) XRD patterns (b) and Raman spectra of gadolinia-ceria multilayered films. Published in [A2, 302]	94
Fig. 4.24. SEM images of the cross-section of (a) GDC-4, (b) GDC-6, and (c) GDC-12. Published in [A2, 302]	95
Fig. 4.25. Experimental and simulated RBS spectra of (a) GDC-4, (b) GDC-6, and (c) GDC-12. Published in [A2, 302]	95
Fig. 4.26. Combined TGA–DTG–DTA curves of SGDC synthesised by (a) combustion (CB) and (b) co-precipitation (CP) syntheses.	98
Fig. 4.27. XRD patterns of SGDC nanopowders synthesised by (a) combustion and (b) co-precipitation calcined at various temperatures	99
Fig. 4.28. Plot of the crystallite size (D) and lattice parameter (a) vs. calcination temperatures for SGDC nanopowders	100
Fig. 4.29. FT–IR spectra of SGDC nanopowders synthesised by (a) combustion and (b) co-precipitation calcined at various temperatures	100
Fig. 4.30. SEM images of SGDC nanopowders synthesised by (a, c, e) combustion and (b, d, f) co-precipitation as-synthesised (a, b) and calcined at 900 °C (c, f) and 1100 °C (e, f)	101
Fig. 4.31. SEM images of SGDC pellets synthesised by (a) combustion and (b) co-precipitation methods and annealed at 1200 °C	102
Fig. 4.32. Complex impedance plots of SGDC ceramics at (a) 400, (b) 500, and (c) 600 °C. Arrhenius plots (d) of total conductivity of ceria-based ceramics	103
Fig. 4.33. Schematic model of the interaction between the cathode-barrier-electrolyte interfaces (a) without and with (b) 400 nm, (c) 800 nm thick GDC barrier layer. Reproduced from [196]	104

Fig. 4.34. Image of the (a) front side, (b) back side, and (c) SEM cross-sectional view of the YSZ–GDC on a porous metal substrate. The GDC barrier-layer is deposited on the smooth side (a) 105

LIST OF TABLES

Table 2.1. Types of fuel cells. Reproduced from [14].....	19
Table 2.2. Basic requirements for SOFC components. Reproduced from [16].....	23
Table 2.3. Total ionic conductivity, operating temperature, and preparation methods for various electrolyte materials for SOFC.....	29
Table 2.4. Comparison of the methods for producing thin and dense electrolytes for SOFC applications. Reproduced from [185]	36
Table 3.1. Summary of the synthesised ceria-based nanopowders	39
Table 3.2. Materials used for the synthesis and formation of thin films	39
Table 3.3. Most commonly used constituents for combustion synthesis	41
Table 3.4. Parameters of electron beam evaporation process.....	52
Table 3.5. Parameters of magnetron sputtering process.....	53
Table 3.6. Summary of analysis, characterisation tools, and their applications to study particular properties or applications.....	54
Table 4.1. Total conductivity and activation energy results of SDC ceramic pellets synthesised by combustion, co-precipitation, and sol-gel.....	76
Table 4.2. SEM estimated SDC thin film thicknesses.....	79
Table 4.3. Values of the activation energy at low (LT) and high (HT) temperature ranges and the total conductivity of GDC ceramic pellets. Results of the GDC-CP were published in [A3, 315].....	89
Table 4.4. Chemical composition of evaporated GDC thin films obtained from XPS and ICP–OES measurements. Results of the GDC-CP were published in [A3, 315].....	90
Table 4.5. Calculated values of the crystallite size (nm) for synthesised ceria-based nanopowders at various temperatures.....	99
Table 4.6. The activation energy at low (LT) and high (HT) temperature ranges and the total ionic conductivity of SGDC ceramics	102

LIST OF ABBREVIATIONS AND SYMBOLS

A	– lattice parameter
AC	– alternating current
AFM	– atomic force microscopy
ASR _{el}	– acceptable area specific resistance
BET	– Brunauer Emmett Teller
C	– concentration
CB	– combustion synthesis
CP	– co-precipitation synthesis
CTE	– coefficient of thermal expansion
CVD	– chemical vapour deposition
C_A^S	– concentration of element A in the vapour phase
C_B^S	– concentration of element B in the vapour phase
C_A^0	– initial concentrations of element A in the target material
C_B^0	– initial concentrations of element B in the target material
D	– thickness; the spacing between diffracting planes, or an interplanar distance
d_{th}	– theoretical density of the solid solution oxide
D_{BET}	– average particle size
DC	– direct current
DSC	– differential scanning calorimetry
DTA	– differential thermal analysis
E	– Young's modulus; voltage
E_a	– activation energy
E_0	– amplitude of the signal
$\Delta E_{b,gb}$	– bulk and grain boundary energies
ER	– electrical resistivity
EB-PVD, e-beam	– electron beam physical vapour deposition
EDX, EDS	– energy dispersive X-ray analysis
Φ	– phase shift
F	– Faraday's constant ($96485 \text{ C}\times\text{mol}^{-1}$)
F_i	– evaporation rate of a separate component
F_{max}	– evaporation rate
FT-IR	– Fourier transform infrared spectroscopy
FWHM	– full width at half maximum
GDC, CGO	– gadolinium doped ceria
GI-XRD	– grazing incidence X-ray diffraction
H	– distance between electrodes
HT	– high temperature
I	– current
I_0	– amplitude of the current
ICP	– inductively coupled plasma
ICP-OES	– inductively coupled plasma optical emission spectrometry
IR	– infrared
IS	– impedance spectroscopy
IT	– intermediate temperature
ICDD	– International Centre for Diffraction Data
$J(O_2)$	– oxygen flux

K	– Boltzmann’s constant (0.86×10^{-4} eV K ⁻¹)
Λ	– wavelength
L	– thickness of the electrolyte
LSGM	– magnesium-doped lanthanum gallate
LSC	– lanthanum strontium cobalt oxide
LSCF	– lanthanum strontium cobalt iron oxide
LSF	– lanthanum strontium ferrite
LT	– low temperature
μ_i	– mobility of the species
μ -SOFC	– micro solid oxide fuel cell
M	– mass of molecule
M	– atomic weight
N	– number of oxygen moles
N_A	– Avogadro constant
n_i	– number density
NIR	– near infrared
NMP	– N-methylpyrrolidon
Ω	– radial frequency
OT	– operating temperature
P	– resistivity
p_v	– vapour pressure
PVD	– physical vapour deposition
PLD	– pulsed laser deposition
q_i	– charge
R	– electrical resistance; universal gas constant
r_d	– ionic radius of dopant
r_O	– ionic radius of oxygen
R_{ku}	– kurtosis, measure of the height randomness and sharpness of a surface
r_{VO}	– oxygen vacancy
RE	– rare earth elements
RF	– radio frequency
r_{Ce}	– radius of the cerium ion
R_q	– root mean square roughness, rms
R_{sk}	– skewness,
Σ	– amplitude of the residual stresses
σ_e	– electronic conductivity
σ_i	– ionic conductivity
σ_0	– pre-exponential factor
S	– area of the electrodes
S	– seconds
S_1, S_2	– elasticity constants that can be expressed as a function of the Young’s modulus
S_{BET}	– specific surface area
SDC	– samarium doped ceria
SG	– sol-gel
SGDC	– ceria co-doped with samarium and gadolinium
ScSZ	– scandia stabilised zirconia
SE	– secondary electrons
SEM	– scanning electron microscopy
SOFC	– solid oxide fuel cell

T	– temperature
t	– the film/wafer thickness; time
TEM	– transmission electron microscopy
TGA	– thermogravimetric analysis
TG–DSC	– thermogravimetric and differential scanning calorimetry
TG–DTA	– thermogravimetry–differential thermal analysis
θ	– incident angle
UV	– ultraviolet
ν	– Poisson’s ratio
$V_{\text{O}}^{\cdot\cdot}$	– oxygen vacancy
X	– dopant concentration
x_d	– fraction of dopant
XPS	– X-ray photoelectron spectroscopy
XRD	– X-ray diffraction
Y_0	– capacitance
YSZ	– yttria stabilised zirconia

1. INTRODUCTION

For decades, the innovation and investigation of renewable and mobile energy sources have been a major focus of research. The rapid development of various mobile electronic devices, modern cars, smart technologies, various sensors, and even space satellites requires the increase of the energy production, as well as the development of batteries and fuel cells.

Due to the insufficient capacity of rechargeable batteries, the use of various types of fuel cells, which would minimise environmental pollution, have very low emissions yet high efficiency, could operate across a wide temperature range, and could withstand chemical and mechanical stress, has significantly increased [1–5].

One of the most frequently studied and used electrochemical energy conversion devices are solid oxide fuel cells (SOFCs). The attention to SOFCs has been drawn due to their advantages over other types of fuel cells such as high efficiency (60–85%), low activation loss, and a large amount of chemical energy conversion to electric power. SOFCs can operate within a wide temperature range from 400 °C to 1000 °C, depending on the type of the electrolyte. High temperature SOFCs (800–1000 °C) help to achieve higher efficiency, they are mostly used in stationary applications. However, high operating temperature (T_o) results in longer start-up times, a shorter cell component lifespan, expensive materials, as well as manufacturing difficulties for external components [5–7]. Therefore, it is important to reduce the operating temperature. The main issue is to stabilise the nanostructure of the components over an extended period of time at high T_o . Reducing the operating temperatures of SOFCs (< 600 °C) or stabilising the nanostructure are the main approaches towards obtaining sufficient long-term stability. Low-temperature SOFCs (LT-SOFCs), operating at 400–650 °C, are denoted by a shorter start-up time, do not require expensive materials, and can be used in portable devices [8]. One of the important factors for the successful commercialisation of LT-SOFCs is an electrolyte with high ionic conductivity [9,10]. To develop reliable LT-SOFCs, it is essential to reduce the cell area resistivity by developing new electrolytes and improving the electrode performance which is compatible with electrolytes.

Ceria-based ceramics are the most popular candidates for LT-SOFCs applications because of their high ionic conductivity. Many factors affect the value of ionic conductivity, such as the crystallite size, morphology, density, grain size, structure, and thermal expansion of ceria-based ceramics. These parameters can be controlled by the employed method of chemical synthesis, the type of the dopant and its concentration, as well as the sintering and annealing conditions. A detailed study presented in this dissertation suggests the most suitable conditions for the fabrication of nanostructured ceria-based ceramics with the desired properties.

The thin film formation method and its technological parameters influence the structural properties and determine the further application of films. Therefore, it is crucial to investigate the most advantageous ways to improve the qualities of thin films. The influence of additional heat treatment, which is another approach towards improving the quality of films, has been investigated, and the optimal conditions for annealing ceria-based thin films have been determined.

It is fundamentally difficult to find a material that will have all the desired properties, including good electrode compatibility, high ionic conductivity, and stability during operation or in a reducing atmosphere. However, by investigating the properties of widely used electrolytes such as gadolinium-doped ceria and samarium-doped ceria from the initial powders and sintering conditions to the manufacturing methods and the effect of the microstructure on ionic conductivity, one can find the most suitable approach for their manufacturing.

Research goal

To systematically and comprehensively study the formation of nanostructured metal oxide ceria-based ceramics for the application of low-temperature solid oxide fuel cells, while considering the influence of the chemical synthesis method, the initial metal oxide materials, the type of the dopant and its concentration, various calcination and annealing temperatures, and the deposition techniques of thin film formation.

Research tasks

1. To synthesise ceria-based nanostructured ceramics with various dopants and concentrations by using combustion, co-precipitation (with the same initial metal nitrates hexahydrates materials), and sol-gel chemical syntheses.
2. To investigate the dependences of the microstructure, surface morphology, and the electrical properties of the formed nanostructured ceria-based ceramics on the method of chemical synthesis, the starting metal oxide materials, and various annealing temperatures.
3. To apply the electron beam evaporation and direct current reactive magnetron sputtering techniques for the formation of thin films on Si (111) substrate and multilayer (with 4, 6, and 12 oxide layers) sandwich systems by varying the technological parameters and applying additional thermal treatment of thin films.
4. To investigate the elemental composition and morphology of thin films and the influence of the additional thermal treatment on the formed films.

Scientific novelty

1. Detailed investigation of the influence of a wide range of parameters, such as methods for the synthesis of nanopowders, the variation of the dopant and its concentration, thin film formation methods, as well as various sintering and annealing conditions, on the properties of nanostructured samarium-doped ceria, gadolinium-doped ceria and samarium-gadolinium-doped ceria has been performed.
2. The optimal methods and conditions for the formation of ceria-based ceramics with the desired properties for the application in LT-SOFCs have been determined.

The key statements of the doctoral dissertation

1. Combustion and co-precipitation synthesis methods produce ceramic nanopowders (samarium-doped ceria, gadolinium-doped ceria, and samarium and gadolinium-doped ceria) which further show the highest total ionic conductivity values.
2. It is crucial to determine the proper dopant concentration since its influence on ionic conductivity is significant: for SDC structures, the best concentration is up to 20 mol% of samarium, whereas for GDC structures, it is up to 10 mol% of gadolinium.
3. Co-doping of ceria helps to obtain thermally stable nanopowders of higher purity, and also substantially increases the ionic conductivity.
4. To obtain the desired concentration of the final films, the concentration of the target material used for the evaporation when using the electron beam evaporation technique should be ~28% higher. Layer-by-layer deposition when using reactive magnetron sputtering requires a higher number of layers (at least 12 layers of gadolinium and cerium oxides) for their better mixing and obtaining a homogeneous material.
5. The most suitable annealing temperature for ceria-based thin films is up to 800 °C.

Dissertation structure

The structure of the dissertation is composed to follow the set research tasks. The main body consists of 5 chapters: introduction, literature review, experimental technique and methods, results and discussion, and conclusions. The first chapter is a review of literature discussing LT-SOFC, covering its structure, materials, methods of formation and the emerging issues. Chapter 3 presents the experimental techniques and methods employed in this thesis. Chapter 4 presents the obtained results with the following discussion. The results are divided into 4 parts devoted to different materials, their characteristics, and applications (SDC, GDC, SGDC, and the application). Conclusions are presented in the final chapter, which emphasises the completion of the research objectives. Acknowledgments, a list of references, the curriculum vitae of the author, and a list of publications and international and national conferences are presented at the end of the dissertation. The volume of the dissertation is 166 pages, including 48 figures, 16 tables, 56 numbered equations, and 315 references.

Contribution of the author

The results and the research presented in the dissertation were carried out at the Institute of Materials Science of Kaunas University of Technology and during Erasmus+ internship at the Institute of Solid-State Ionics of Warsaw University of Technology.

The author independently planned all the experiments (calculation and requirements for the synthesis methods), performed combustion and co-precipitation

syntheses and thin film formation by the electron beam technique, measured electrical (impedance spectroscopy), structural and elemental (X-ray diffraction, Fourier transmission infrared spectroscopy, and Raman spectroscopy), the morphological (scanning electron microscopy and atomic force microscopy) properties of the samples, and analysed the obtained data.

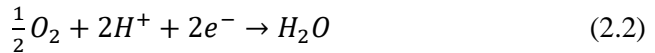
Sol-gel synthesis as well as the thermal analysis of the samples were performed by Dr. Artūras Žalga and PhD student Giedrė Gaidamavičienė from the Department of Applied Chemistry, Institute of Chemistry of Vilnius University. Dr. Mindaugas Andrulevičius performed X-ray photoelectron spectroscopy measurements. The co-precipitation method and impedance spectroscopy were taught by Dr. Marzena Leszczyńska from the Faculty of Physics, Warsaw University of Technology. Magnetron sputtering and RBS measurements were done by Dr. Brigita Abakevičienė and Jurgita Čyvienė. PhD student Lukas Bastakys prepared the simulation of RBS results by using the 'SIMNRA' programme. SEM measurements were supervised and done by Dr. Tomas Tamulevičius. PhD student Algita Stankevičiūtė from the Astronomical Observatory of the University of Warsaw helped with the analysis of the electrical properties and writing of the second manuscript. Brunauer-Emmett-Teller and ICP measurements were performed by Dr. Artūras Žalga from the Department of Applied Chemistry, Institute of Chemistry of Vilnius University. Thin films were prepared with the help and supervision of Dr. Andrius Vasiliauskas.

The analysis and interpretation of the results were done by the author in consultation with the scientific supervisor assoc. prof. Dr. Brigita Abakevičienė from Kaunas University of Technology. The scientific results presented in the dissertation have been published in 3 research papers in journals indexed in Clarivate Analytics Web of Science with the impact factor and delivered in 14 conference presentations, 9 of which have been presented in person by the dissertation author herself. The full list of publications and conference abstracts is given at the end of the dissertation. If the data presented in chapter 4 has been published in a paper, it is indicated with the letter [A] followed by the number which coincides with the number in The List of Publications and Conferences Related to the Dissertation.

2. LITERATURE REVIEW

2.1 Solid oxide fuel cells

The fast development of technologies used in daily life, the constant evolution of vehicles and aircraft, overall requiring the increase of the energy production, have caused various types of environmental problems, such as air and water pollution, deforestation, global warming, etc. [11, 12]. For the last decades, researchers have been concentrating on finding sustainable energy production that uses renewable sources [13]. Compared to fossil fuel combustion and conventional electric energy generators, fuel cells offer clean and efficient energy, low-pollution technology, fuel adaptability, and very low emissions. They can sustain chemical and mechanical stresses, ensure long-term stability and high efficiency, and can operate across a wide range of temperatures [1–5]. Fuel cells are electrochemical devices converting chemical potential energy from a fuel and oxidant directly into electrical energy [9]. Another electrochemical device is the battery, which has its chemicals stored inside, which results in a short lifetime. Meanwhile in the case of fuel cells, there is a constant flow of chemicals into the cell that produces the electricity [14, 15]. The chemicals which are most commonly used for oxidation-reduction processes occurring in fuel cells are hydrogen (reductants) and the ambient air (oxidants) [15]. The electrochemical reactions are as follows:



There are several types of fuel cells depending on the employed electrolyte material, which defines the electrochemical reactions in the cell along with the required catalysts and fuel, and the operation temperature [16]. Depending on the type of fuel cells they can be used in stationary power generation plants (i.e. solid oxide fuel cells (SOFCs)), or for small portable applications, for powering vehicles, mobile applications, and portable electronics (i.e. polymer electrolyte fuel cells (PEFCs)) [11]. Various types of fuel cells with their requirements, applications, advantages, and disadvantages are presented in Table 2.1.

Table 2.1. Types of fuel cells. Reproduced from [14]

	PEFC	AFC	PAFC	MCFC	SOFC
Operating T (°C)	40–80 °C	65–220 °C	150–210 °C	600–700 °C	400–1000 °C
Charge carrier	H^+	OH^-	H^+	CO_3^{2-}	O^{2-}
Cathode reaction	$\frac{1}{2}O_2 + 2H^+ + 2e^- \rightarrow H_2O$	$O_2 + 2H_2O + 4e^- \rightarrow 4OH^-$	$O_2 + 4H^+ + 4e^- \rightarrow H_2O$	$\frac{1}{2}O_2 + CO_2 + 2e^- \rightarrow CO_3^{2-}$	$\frac{1}{2}O_2 + 2e^- \rightarrow O^{2-}$

Anode reaction	$H_2 \rightarrow 2H^+ + 2e^-$	$2H_2 + 4OH^- \rightarrow 4H_2O + 4e^-$	$2H_2 \rightarrow 4H^+ + 4e^-$	$H_2O + CO_3^{2-} \rightarrow H_2O + CO_2 + 2e^-$	$O^2 + H_2 \rightarrow H_2O + 2e^-$
Electrolyte	Hydrated polymeric ion exchange membrane	Potassium hydroxide in asbestos matrix	Liquid phosphoric acid in silicon carbide	Liquid molten carbonate in $LiAlO_2$	Ion conducting ceramics (yttria-stabilised zirconia, gadolinia-doped ceria (GDC), lanthanum gallate)
Electrodes	Carbon	Transition metals	Carbon	Nickel and nickel oxide	Perovskite, cermet (perovskite/fluorite and metal cermet)
Fuel	Hydrogen or methanol	Hydrogen or hydrazine	Hydrogen and alcohol	Hydrogen, hydrocarbons	Hydrogen, hydrocarbons
Oxidant	O_2 /air	O_2 /air	O_2 /air	CO_2/O_2 /air	O_2 /air
Heat quality	-	Very low	Low	High	High
Advantages	<ul style="list-style-type: none"> • Solid electrolyte reduces corrosion and electrolyte management problems • Low operation temperature • Quick start-up 	<ul style="list-style-type: none"> • Fast cathodic reaction • Wide range of electro-catalysts 	<ul style="list-style-type: none"> • Tolerance to impurities in hydrogen 	<ul style="list-style-type: none"> • Fuel flexibility • Low-cost catalyst 	<ul style="list-style-type: none"> • All solid-state components • Fuel flexibility • Low-cost catalysts • No electrolyte flooding • Highest efficiency
Disadvantages	<ul style="list-style-type: none"> • Poisoning by trace contaminants in fuel • High-cost platinum catalyst • Difficulties in thermal and water management 	<ul style="list-style-type: none"> • High purity hydrogen 	<ul style="list-style-type: none"> • Slow cathodic reaction • Corrosive nature of phosphoric acid • High-cost platinum catalyst 	<ul style="list-style-type: none"> • Corrosive electrolyte • High operating temperature • Long-term reliability of materials due to high temperature 	<ul style="list-style-type: none"> • High operating temperature • High manufacturing cost • Long-term reliability of materials due to high temperature
Manufacturers	<i>Ballard Power Systems,</i>	<i>AFC Energy, UK</i>	<i>Clear Edge Power, USA; Toshiba Fuel</i>	<i>Fuel Cell Energy, USA; Ishikawajima-</i>	<i>Bloom Energy Corporation, USA;</i>

	Canada; <i>BaxiInnotech</i> , Germany; <i>SerEnergy</i> , Denmark; <i>M-Field Energy Ltd.</i> , China		<i>Cell Power Systems</i> , Japan	<i>Harima Heavy Industries (IHI)</i> , Japan	<i>Acumentrics Corporation</i> , USA; <i>Ceres Power</i> , UK; <i>Topose Fuel Cell</i> , Denmark; <i>Hexis AG</i> , Germany; <i>LG Fuel Cell</i> , South Korea; <i>Osaka Gas Ltd.</i> Japan; <i>Toto Ltd.</i> , Japan
--	---	--	--------------------------------------	--	--

Solid oxide fuel cells (SOFCs) are electrochemical devices converting chemical energy into electrical energy through a redox reaction with zero or low carbon emissions [12,17–19]. The main advantages of SOFCs are: exceptionally high efficiency (from 60% to 85%), low/zero CO₂ emissions (from 90% to 35%), fuel flexibility, reduction in the use of fossil fuels, kinetics of fast electrodes in the high-temperature range, low activation loss, high electrical efficiency, and lack of corrosion in the structural parts [17,19–25]. Since energy conversion is electrochemical and does not involve any other intermediate energy conversion steps, the electrical efficiency of SOFCs is relatively higher than that of similar mature technologies such as internal combustion engines or generators.

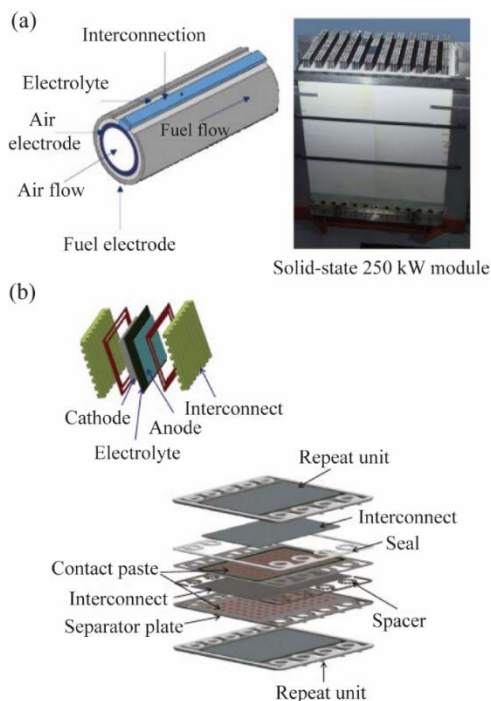
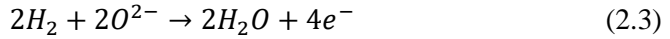


Fig. 2.1. Types of solid oxide fuel cells: (a) tubular, (b) planar. Reproduced from [14]

A typical SOFC power system consists of a fuel cell power module, a hydrocarbon fuel processor, energy conditioning equipment, and a process gas heat exchanger for temperature control [14,26,27]. The power module of a fuel cell consists of several cells connected in series and/or physically separated, but electrically connected with interconnects. Single cell geometries are divided into tubular and planar (Fig. 2.1) [28]. The power density of a planar cell is comparatively higher than that of a tubular cell, but a hermetic seal is necessary to prevent mixing and leakage of a gas [14,26].

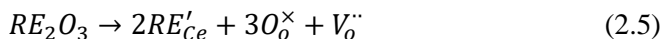
The layer-structured cells consist of two porous electrodes (anode/fuel electrode and cathode/air electrode) with a ceramic electrolyte between them. Oxygen is reduced to O^{2-} ions which are transferred from the cathode through the electrolyte conducting oxygen ions, and which oxidise the fuel at the anode, thus releasing electrons to generate electricity [14]. The electrochemical reactions happening in the anode (Eq. 2.3) and cathode (Eq. 2.4) are as follows [29]:



The interconnects provide the electrical connection between the cells as well as a path for the flow of fuel and air to the electrodes through the integrated gas channels. In addition, the interconnects help insulate the electrodes from incompatible gases (the cathode with fuel and the anode with air) [30].

Since the direct conversion of chemical energy to electrical energy does not suffer from the limitations of the thermodynamic efficiency of the traditional thermomechanical energy production methods, it is possible to substantially reduce the size of the entire device to micrometres without affecting the overall efficiency of the SOFC. Depending on the electrolyte materials, SOFC can operate in a wide temperature range (400–1000 °C) [14,15,17]. Subsequently, according to the operating temperature, low-temperature (LT), high-temperature (HT) and intermediate-temperature (IT) SOFCs are distinguished. HT-SOFCs (> 800 °C) have the advantage of achieving higher efficiency by converting waste heat into energy, however, their high operating temperature results in a lower durability of the cell components, longer start-up times, expensive metallic interconnects and sealants, and problems in constructing suitable external components [5–7]. Such disadvantages complicate the commercialisation of HT-SOFCs. Hence, numerous studies have been carried out with the objective to reduce the operating temperature [31], [32]. LT-SOFC (400–650 °C) has the potential to be commercialised by using low cost materials for the structural parts while reducing the size of the heat exchanger and insulation [8]. Moreover, LT-SOFC requires less start-up time and offers better thermal cycling resistance. Reducing the operating temperatures of SOFCs will make it possible to use them in portable devices. Achieving these low operating temperatures requires the development and revision of new materials, processing technologies and SOFCs architectures. For the successful implementation of LT-SOFCs, it is necessary to have a high ionic conductivity electrolyte, which, in turn, requires a partially occupied sublattice of oxygen ions

[9,10]. This can be achieved by creating oxygen vacancies V_o'' by doping the material with acceptor cations (Eq. 2.5) and weak defect-defect interaction [10,33–35]



where RE is the Rare Earth Element, V_o'' represents the oxygen vacancies, and O_o^{\times} indicates an oxygen ion sitting on an oxygen lattice site (o) with the neutral charge (\times). The ionic conductivity depends not only on the dopant but also on its concentration and the measuring temperature [33]. One of the approaches to optimise the ionic conductivity is to find the average ionic radius of the dopant that causes the least distortion of the host lattice [36–38]. Over the years, many studies have been carried out to find the best trivalent rare-earth (RE) dopant for ceria-based ceramics, providing the highest ionic conductivity. One of the methods to choose the RE dopant is according to the application temperature. The total and bulk conductivity indicates higher ionic conductivity of ceria doped with samarium and gadolinium compared to other dopants [9,10,35,39–44]. Co-doping of ceria with multiple RE dopants shows an increase in ionic conductivity as compared to single doped ceria. Therefore, it is important to conduct a detailed study of how the total concentration of the dopant and the ratio of individual co-dopants affect the ionic conductivity of ceria-based ceramics.

2.2 Materials for SOFC structural elements

The anode, cathode, electrolyte, and interconnect are the main components of SOFCs, and each has several functions. For the efficient operation of SOFC, its components must meet certain requirements (Table 2.2) [16].

Table 2.2. Basic requirements for SOFC components. Reproduced from [16]

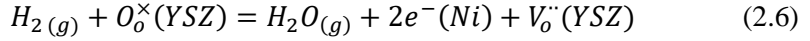
Components	Conductivity	Stability	Compatibility (chemical and thermal)	Electroactivity	Porosity
Electrolyte	High ionic conductivity, negligible electronic conductivity	Chemical, phase, electrical, morphological, and dimensional stability in fuel and oxidant environments (reducing and oxidising atmospheres)	No damaging chemical interactions, elemental migration or interdiffusion with adjoining components Close thermal expansion match with adjoining components	(Not required)	Fully dense
Anode	High electronic conductivity	Chemical, phase, electrical, morphological, and dimensional stability in fuel	No damaging chemical interactions, elemental migration or	Appropriate electroactivity for hydrogen oxidation reactions	Porous

		environment (reducing atmosphere)	interdiffusion with adjoining components Close thermal expansion match with adjoining components		
Cathode	High electric conductivity	Chemical, phase, electrical, morphological, and dimensional stability in oxidant environment (oxidising atmosphere)	No damaging chemical interactions, elemental migration or interdiffusion with adjoining components Close thermal expansion match with adjoining components	Appropriate electroactivity for oxygen reduction reactions	Porous
Interconnect	High electronic conductivity Negligible ionic conductivity	Chemical, phase, electrical, morphological, and dimensional stability in fuel and oxidant environments (reducing and oxidising atmospheres)	No damaging chemical interactions, elemental migration or interdiffusion with adjoining components Close thermal expansion match with adjoining components	(Not required)	Fully dense

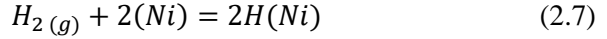
2.2.1 Anode

The most commonly used anodes for LT-SOFC are Ni-cermet anodes. Nickel is preferred as the anode for SOFC due to its high electrical conductivity, excellent catalytic activity in the hydrogen oxidation reaction, and stability in a reducing environment at high temperatures (~500–1000 °C) [15,24]. In order to minimise the coarsening of metal particles at the operating temperature and to provide a CTE (Coefficient of Thermal Expansion) for the anode that is reasonably close to the values of other cell components, a substrate material, such as yttria stabilised zirconia (YSZ) is used. Another function of YSZ is to improve the adhesion of the anode to the electrolyte and to increase the active areas of the anode by increasing the contact areas between Ni and YSZ. Due to the reforming and catalytic activity of Ni with respect to the oxidation of various fuel components, the high electronic conductivity of Ni and the ionic conductivity of YSZ to increase the triple-phase boundaries (TPBs are the intersect point of ionic phase, gas phase, and electronic phase) along the length, the Ni/YSZ cermet is considered a/the modern anode material for SOFC [14,45,46].

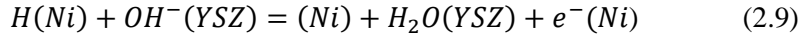
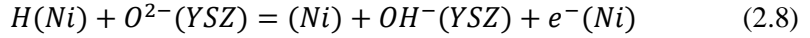
While nickel is an electrical conductor, YSZ is an ionic conductor, and fuel oxidation occurs in TPB. Ni/YSZ anodes for the fuels other than pure hydrogen can work directly with reformed products through external reforming, or on fuels such as alcohols or, hydrocarbons, through internal reforming or direct use. The functioning of Ni/YSZ anodes can be understood by the processes of reaction, adsorption, and transfer occurring near the TPB of Ni/YSZ, as well as considering the influence of the microstructure, in particular, the density of the TPB lines inside the anode. Let us first consider the hydrogen oxidation reaction, which can be divided into several steps that are believed to occur in/around TPB [47,48]:



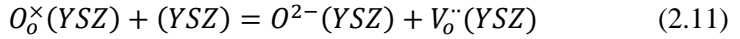
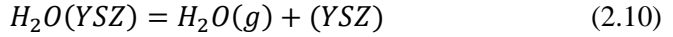
The first step is the dissociative adsorption/associative desorption of H_2 on the Ni surface:



where $H(Ni)$ is atomic hydrogen adsorbed on Ni, and (Ni) is the free area of the Ni surface. After the diffusion of the adsorbed hydrogen through TPB onto the YSZ surface, two successive charge transfer reactions occur:



The final steps include adsorption/desorption of H_2O on the oxide surface and the transfer of oxygen ions between the oxide bulk and the oxide surface:



where $e^-(Ni)$ is an electron inside Ni, $O_o^\times(YSZ)$ is lattice oxygen, and $V_o^{\cdot\cdot}(YSZ)$ is an oxygen vacancy, (YSZ) is an empty portion of the YSZ surface, $OH^-(YSZ)$, $O^{2-}(YSZ)$, and $H_2O(YSZ)$ are particles adsorbed on the surface of YSZ.

The second step of the charge-transfer (Eq. 2.9) is assumed to limit the rate so that the other stages are substantially balanced. An analysis based on Butler–Volmer charge transfer kinetics yields the following dependences:

$$j_A = j_A^0 \frac{(p_{H_2}/p_{H_2}^*)^{1/4} (p_{H_2O})^{3/4}}{(1+p_{H_2}/p_{H_2}^*)^{1/2}} \quad (2.12)$$

where j_A is the exchange current density, j_A^0 is the electrode current density, p_{H_2} and p_{H_2O} are partial pressures of H_2 and H_2O , respectively. This shows that the polarisation of the Ni/YSZ is highly dependent on the composition of the fuel gas [8,48].

The development of nano-sized Ni/YSZ anodes is a promising direction for the production of LT-SOFC. However, the Ni/YSZ anode suffers from some limitations, such as poor redox stability, carbon deposition, and poisoning with the subsequent

deactivation of catalytic properties due to the presence of impurities in the gas phase. Long term stability problems associated with Ni coarsening may arise even at lower operating temperatures. Among these limitations, poor redox stability is considered the main disadvantage of the Ni/YSZ anode [14,26,49–51]. The Ni/YSZ anode may become unstable due to Ni oxidation if the cell is operating in an extremely high fuel/high current environment, the fuel supply is interrupted, or a seal leak occurs. Ni oxidation increases the volume of the anode, while volumetric expansion creates compression in the anode and stretching in the electrolyte. This can cause cracks in the electrolyte (especially in thin electrolytes) [8]. Several ways have been suggested to solve the problem of the redox instability of the Ni/YSZ anode. First, to keep the oxygen partial pressure low enough to prevent anode oxidation [52]. Another approach is to modify the Ni/YSZ anode by changing its composition or microstructure [53]. Alternative materials that are resistant to oxidation-reduction can also be used [54].

The SOFC, consisting of a two-layer anode made of an outer Ni/YSZ support layer impregnated with Cu-CeO₂ and an electroactive inner Ni/YSZ layer, obtained a peak power density of $400 \text{ mW} \times \text{cm}^{-2}$ at 800 °C [55], which shows that modifying the anodes can increase the electrochemical performance of SOFC.

Oxides with mixed ionic-electronic conductivity (LaCrO₃, SrTiO₃, La_{1-x}Sr_xVO₃, Sr₂Fe_{1.5}Mo_{0.5}O₆₋₈, Sr₂MgMoO₆ -based perovskites) were studied as a potential anode material [49,56–64]. A suitable dopant for the above mentioned materials can improve the catalytic activity and conductivity, however, above the critical concentration, the structure can be destabilised. The performance of these materials is comparable to that of Ni/YSZ cermet and does not report inhibition of sulphur and carbon deposits. [58,65]. Alternative anodes also incur several disadvantages, such as the fact that their electronic conductivity may be insufficient for faster kinetics of fuel oxidation, and the long-term stability of these materials is questionable [66,67].

2.2.2 Cathode

Strontium-doped lanthanum manganite (LSM), lanthanum nickelate (La₂NiO₄), and strontium-doped lanthanum cobaltite ferrite (LSCF) perovskites are commonly used as potential cathode materials. The main factors when choosing the cathode material are high electrical conductivity and good electrocatalytic activity. For SOFC single cells with a minimal contribution to the ohmic resistance of the components, cathode polarisation is usually the main contribution to the loss of cell performance [7]. In order to improve cathode performance, infiltration for the formation of cathode nanostructures can be used [68,69]. By infiltrating yttria-doped ceria into the LSM/YSZ cathode, the peak power density at 700 °C was increased from 208 to 519 $\text{mW} \times \text{cm}^{-2}$ and power density was increased from 135 to 370 $\text{mW} \times \text{cm}^{-2}$ at 0.7 V [68].

LSM with a concentration of 20 mol% is considered to be the most advanced cathode material for HT-SOFCs [70]. Since oxygen is adsorbed and desorbed on the surface, in bulk LSM oxygen also migrates only through the surface, since the absence of an oxygen vacancy prevents oxygen migration through the bulk (Fig.

2.2). Thus, the electrochemical reaction happens at the cathode-electrolyte interfaces [71]. Cathodic displacement promotes the migration of oxygen through oxygen vacancies in the bulk, and oxygen vacancies, in turn, can be created by increasing the dopant level of strontium [70,72]. Despite the slow kinetics of oxygen reduction and low ionic conductivity, the LSM cathode remains appealing due to its thermochemical stability and a coefficient of thermal expansion (CTE) which matches YSZ electrolyte (CTE (LSM) is $\sim 11 \times 10^{-6} \text{ K}^{-1}$, CTE (YSZ) $10 \sim 11 \times 10^{-6} \text{ K}^{-1}$) [70]. The addition of an ionic phase such as YSZ will increase the length of the TPB, which can improve the kinetics of oxygen reduction and cathode performance [73,74]. However, LSM, upon contact with YSZ, reacts with the formation of an insulating phase of lanthanum zirconate ($\text{La}_2\text{Zr}_2\text{O}_7$) at high temperatures with changes in the overall microstructure. Thus, the performance of LSM/YSZ interfaces is fairly often limited to temperatures below 1150°C [16,69,75–80].

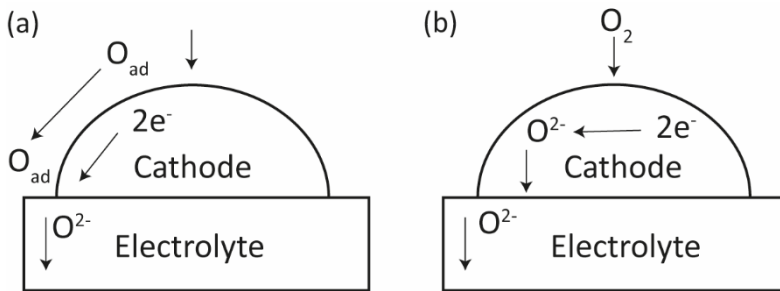


Fig. 2.2. Path of oxygen migration in cathode where (a) is the surface path for LSM and LSCF cathodes and (b) is the bulk path for LSCF cathode

In La_2NiO_4 cathodes, oxygen ions migrate through oxygen vacancies in the alternating perovskite LaNiO_3 and through interstices in La_2O_2 . The interstitial migration contributes to the ionic conductivity of excess oxygen $\text{La}_2\text{NiO}_{4+\delta}$ under normal operating conditions [81–86]. At 800°C La_2NiO_4 reacts with electrolytes (YSZ and GDC), thereby forming $\text{La}_4\text{NiO}_3\text{O}_{10-\delta}$ and $\text{La}_3\text{Ni}_2\text{O}_{7-\delta}$. $\text{La}_2\text{NiO}_{4+\delta}$ dissociates into La_2O_3 and Ni phases in reduced PO_2 [87,88]. Compared to LSCF, the surface oxygen exchange coefficient and diffusion coefficient, the specific surface resistance is higher for La_2NiO_4 . Limited understanding of the properties of La_2NiO_4 makes its investigation and implementation as a SOFC cathode material difficult [89,90].

LSCF is an oxygen-deficient perovskite with faster oxygen reduction kinetics and mixed ionic electron conductivity (MIEC), in which oxygen ions migrate through oxygen vacancies in the bulk of the material (Fig. 2.2) [81]. Oxygen is also adsorbed and ionised on the surface, and it migrates across the surface like an electronic conductor. Among the other LSCF compositions, $\text{La}_{0.6}\text{Sr}_{0.4}\text{Co}_{0.2}\text{Fe}_{0.8}\text{O}_{3-\delta}$ has the best bulk stability and corresponds to the thermal expansion of the electrolyte [51,91,92]. The CTE of LSCF is of a higher value ($\sim 15 \times 10^{-6} \text{ K}^{-1}$): nevertheless, due to its mixed conducting properties, LSCF shows good catalytic activity for oxygen reduction at low temperatures. Because of the solid-state reaction at $\sim 800^\circ\text{C}$ with the YSZ electrolyte, SrZrO_3 is formed, which limits the application

of LSCF for SOFCs [93–96]. To prevent the LSCF cathode from reacting with the electrolyte at operating temperatures, a barrier layer of CeO_2 can be used [97,98]. Although the interdiffusion of elements through the LSCF and GDC during the manufacturing of the device is high enough to segregate oxides at the grain boundaries and interfaces, which results in reduced cell performance, GDC is still the preferred electrolyte for LSCF cathodes [93,99–103].

The best characteristics among the above mentioned cathode materials are shown by LSCF, which features a higher surface exchange coefficient and oxygen diffusion coefficient, as well as lower polarisation resistance [104].

Along with the solid-state interaction with the electrolyte, the interaction of the cathode with impurities in air, silicon from the insulating materials and sealants, chromium vapour from the interconnects, and other impurities affect its performance [14]. In atmospheric air, the main impurities affecting the cathode are $\sim 400 \times 10^{-6}$ CO_2 , $\sim 3\%$ of H_2O , and sulphur at the 10^{-9} level in the form of $\text{SO}_2/\text{SO}_3/\text{H}_2\text{S}$ [14]. Moisture in the air precipitates SrO on the LSM and LSCF surfaces, thus increasing the ohmic and polarisation resistances, and consequently deteriorating the performance of the cathode. However, there is no general agreement on the mechanism of strontium segregation at the cathode. The transport of chromium in the form of $\text{CrO}_2(\text{OH})_2$ or CrO_3 vapour (chromium poisoning) from the metal interconnect in air also degrades the performance of the cathode [14,96]. $\text{CrO}_2(\text{OH})_2$ or CrO_3 are reduced to Cr_2O_3 and randomly deposit at the junction of the electronic, ionic conducting, and gas phases. The reaction products of Cr_2O_3 with the cathode are $(\text{Cr}, \text{Mn})_3\text{O}_4$ for LSM and SrCrO_4 for LSCF. However, the degradation is lower for the LSCF cathode compared to LSM because the distribution of chromium deposition across MIEC (e.g., LSCF) cathodes is random, and for LSM and LSM/YSZ cathodes, chromium deposition blocks the electrochemical reaction [14].

2.2.3 *Electrolyte*

Among the structural parts of SOFCs, electrolyte plays a decisive role in improving the overall characteristics and performance of SOFCs [5]. The operating temperature of SOFC is determined by the material of the solid electrolyte, and ionic conductivity is an important parameter for lowering the operating temperature [105–107]. The electrolyte material must have following properties (Table 2.2):

1. High ionic conductivity and negligible electronic conductivity
2. The CTE of the electrolyte should closely match the CTE of the electrode.
3. A very dense structure with a fine grain size. This will reduce the fuel leakage by avoiding direct reaction between fuel and air (oxygen).
4. Good chemical stability during oxidation and reduction, including reactions at the electrode/electrolyte interface as well as at the reagent/electrolyte interfaces.

The best known solid oxide ion conducting electrolytes for SOFCs are the fluorite-type oxide materials, ones that are zirconia-based or ceria-based, and perovskites such as lanthanum gallate. At high operating temperatures (800–1000 °C), yttria-stabilised zirconia (YSZ) is the most commonly used electrolyte due to its

high ionic conductivity and good chemical stability [108,109]. Prabhakaran K. *et al.* [110] reported the total ionic conductivity of $0.1 \text{ S}\times\text{cm}^{-1}$ at 1000°C for YSZ with 8 mol% yttria. However, due to the high activation energy of the oxide ion transfer, the ionic conductivity at low temperatures is low. In addition, high T_o reduces the lifetime of the cell and requires a longer start-up time. With the YSZ electrolyte, better conductivity values can be achieved when the size of the dopant is similar to the size of the host material since the dopant and host cations with different ionic radii will create defects with a higher charge and strong Coulomb interaction, leading to a decrease in the total conductivity [9].

Scandia-doped zirconia exhibits higher conductivity values compared to YSZ (Table 2.3), however, it is difficult to employ due to its high cost, a decrease in conductivity in the temperature range $700\text{--}1000^\circ\text{C}$, and the scandium-zirconia system is complex with a multicomponent assembly phase for most SOFC compositions [111,112].

Lattice deformation due to polymer transformation leads to elastic deformation during thermal cycling; therefore, the conductivity and the subsequent application of SCSZ and YSZ are good only for HT-SOFC ($\geq 800^\circ\text{C}$) [14].

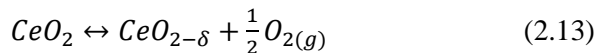
Lanthanum-based perovskites can be used to replace fluorite-type electrolytes, for instance, the optimised composition of $\text{La}_{1-x}\text{Sr}_x\text{Ga}_{1-y}\text{Mg}_y\text{O}_3$ offers a conductivity of $\sim 0.14 \text{ S}\times\text{cm}^{-1}$ [113]. The disadvantage of using perovskite materials is the phase purity; at higher sintering temperatures, loss of La is observed, which affects the interdiffusion properties [114]. In the reduced atmosphere (at $\sim 10^{-18} \text{ Pa PO}_2$ at 1000°C) there is a presence of the electronic conductivity, which makes it difficult to be used at higher temperatures. Moreover, at LT, the conductivity values are lower compared to ceria-based electrolytes [14]. Bismuth-based materials show good conductivity values ($\sim 10\text{--}100$ times higher than YSZ) but suffer from phase stabilisation problems; the bcc γ -phase is observed upon cooling from $\sim 700^\circ\text{C}$ to room temperature. Moreover, all bismuth-based oxides are easily reduced in a reducing atmosphere and become unsuitable for use as an electrolyte [115,116].

Table 2.3. Total ionic conductivity, operating temperature, and preparation methods for various electrolyte materials for SOFC

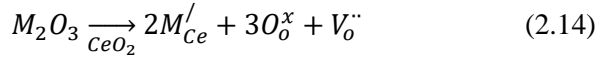
Material	σ_{total} ($\text{S}\times\text{cm}^{-1}$)	T ($^\circ\text{C}$)	Method	Reference
Single dopant				
8 YSZ	0.13	1000	Spray drying	[110]
5-10 YSZ	0.034	800	Thin film prepared by aerosol-assisted MOCVD	[117]
9-5 YSZ	0.057	900	Thick film prepared tape casts of nanopowders	[118]
10 YSZ	4.52×10^{-6}	400	Thick film prepared by ALD	[119]
15 GDC	4.07×10^{-2}	700	Solid state reaction	[120]

17 SDC	5.7×10^{-2}	600	Hydrothermal method	[121]
20 SDC	8.8×10^{-2}	800	Oxalate co-precipitation	[122]
20 YDC	$3-4 \times 10^{-2}$	700	Citric acid-nitrate combustion	[123]
$\text{Ce}_{0.925}\text{Mg}_{0.075}\text{O}_{1.925}$	3.11×10^{-4}	700	-	[124]
$\text{Sc}_2\text{O}_3\text{-ZrO}_2$ (6 mol%)	0.18	1000	The sintered film was treated by hot isostatic pressing	[125]
$\text{Sc}_2\text{O}_3\text{-ZrO}_2$ (9-11 mol%)	0.28–0.34	1000	Co-precipitation	[111]
$\text{Nd}_{0.2}\text{Ce}_{0.8}\text{O}_{2-\delta}$	-	600	Combustion	[126]
$(\text{Y}_2\text{O}_3)_{0.08}(\text{ZrO}_2)_{0.92}$	1.1×10^{-3}	500	-	[127]
$(\text{Sc}_2\text{O}_3)_{0.1}(\text{CeO}_2)_{0.01}(\text{ZrO}_2)_{0.89}$	2.5×10^{-3}	500	-	[127]
$\text{Gd}_{0.1}\text{Ce}_{0.9}\text{O}_{1.95}$	5.8×10^{-3}	500	-	[127]
$\text{Sm}_{0.2}\text{Ce}_{0.8}\text{O}_{1.9}$	1.54×10^{-3}	600	Combustion	[128]
Co-doped electrolyte system				
$\text{Ce}_{0.85}\text{Sm}_{0.15}\text{O}_{1.925}$	1.74×10^{-4}	500	-	[129]
$\text{Ce}_{0.85}\text{Gd}_{0.1}\text{Sm}_{0.05}\text{O}_{1.9}$	0.046	700	Citrate-nitrate combustion	[129]
$\text{Ce}_{0.85}\text{Gd}_{0.06}\text{Sm}_{0.09}\text{O}_{1.925}$	2.68×10^{-3}	500	Citrate-nitrate combustion	[129]
$\text{Ce}_{0.85}\text{Gd}_{0.09}\text{Sm}_{0.06}\text{O}_{1.925}$	2.49×10^{-3}	500	Citrate-nitrate combustion	[129]
$\text{Ce}_{0.925}\text{Mg}_{0.07}\text{La}_{0.01}\text{O}_{1.925}$	4.8×10^{-3}	700	Auto combustion	[124]
$\text{Ce}_{0.9}\text{Mg}_{0.05}\text{La}_{0.05}\text{O}_{1.92}$	2.54×10^{-2}	700	Auto combustion	[124]
$\text{Ce}_{0.95}\text{Al}_{0.025}\text{La}_{0.025}\text{O}_{1.975}$	3.04×10^{-4}	500	Auto combustion	[130]
$\text{Ce}_{0.84}\text{Gd}_{0.15}\text{Cu}_{0.01}\text{O}_{2-\delta}$	7.81×10^{-3}	600	Polymer precursor method	[131]
$\text{Ce}_{0.825}\text{Sm}_{0.0875}\text{Gd}_{0.0875}\text{O}_{1.9125}$	2.23	600	A citrate complexation	[9]
$\text{Ce}_{0.76}\text{La}_{0.08}\text{Pr}_{0.08}\text{Sm}_{0.08}\text{O}_{2-d}$	0.043	600	Sol-gel auto-combustion technique	[132]
$\text{Ce}_{0.76}\text{Pr}_{0.08}\text{Sm}_{0.08}\text{Gd}_{0.08}\text{O}_{2-\delta}$	1.86×10^{-2}	600	Sol-gel auto-combustion synthesis	[133]

Ceria-based materials ($\text{Ce}_{1-x}\text{M}_x\text{O}_{2-\delta}$, where M is usually Sm, Gd, Dy, Nb, Y, Ti, and Zn) are among the best materials for electrolytes in the operating temperature range of 400 °C to 800 °C [115,134,135]. CeO_2 features a cubic fluorite structure with the $[\text{Xe}] 4f^2 5d^0 6s^2$ electronic configuration, in which Me ions can exist in the 3+ and 4+ oxidation states [136]. The cubic structure of ceria is stable from room temperature to 2400 °C (its melting point) and can contain a high rate of point defects. In the presence of oxygen atmosphere, oxidative charges are unstable, and therefore stoichiometry depends on the partial pressure of oxygen and temperature [137,138]. When exposed to a reduced gas atmosphere, pure CeO_2 undergoes partial reduction and loses oxygen atoms, which leads to a high concentration of defects:



The reduction of ceria results in excessive metal defects and if the oxygen content is removed, then the composition will eventually acquire an overall positive charge due to the hole formation. Thus, in order to maintain charge neutrality, this must be compensated for by introducing (for each removed oxide ion), two electrons bonded to two cerium atoms, which become Ce^{3+} ($Ce^{4+} \rightarrow Ce^{3+}$) [5]. Oxide ion conductivity occurs when ceria is doped with trivalent or divalent cations, which results in the formation of oxygen vacancies (V_O) in the crystal system which increases with an increase in the optimal concentration of the dopant [139].



V_O is responsible for the conductivity of oxide ions in the crystal system due to the mechanism of vacancy migration (Fig. 2.3).

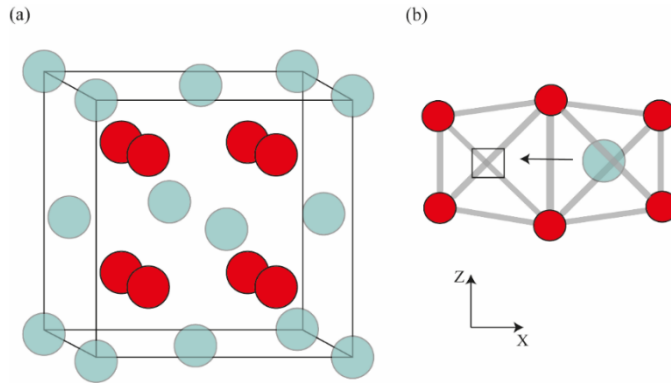


Fig. 2.3. (a) Crystal structure and (b) oxygen migration in fluorite ceria (the turquoise circle is oxygen, the red circle is cerium, and the empty square is a vacant oxygen site. Oxygen migration towards oxygen vacant sites is indicated with the arrow)

According to [140], the ionic radius of the dopant has an important role in achieving high ionic conductivity. With an increase in the ionic radius, the ionic conductivity also increases; however, at the critical ionic radius ($r > 1.09 \text{ \AA}$), the value of conductivity decreases.

Fig. 2.4 shows the influence of ionic radii of various dopants on the ionic conductivity of ceria [136]. As it can be seen, the conductivity values are higher for Sm^{3+} and Gd^{3+} since their ionic radii (1.08 \AA (Sm^{3+}) and 1.05 \AA (Gd^{3+})) are close to the radius of the Ce^{4+} ion (0.97 \AA), and the doped system has lower elastic energy. According to various studies, the maximum conductivity of ceria can be obtained by doping with 10~20 mol% Gd_2O_3 or Sm_2O_3 . At relatively higher values of oxygen partial pressure at higher temperatures ($\sim 10^{-14} \text{ Pa PO}_2$ at $700 \text{ }^\circ\text{C}$), the electronic conductivity dominates over ionic conductivity. Therefore, even with high conductivity values, ceria-based electrolytes are not suitable for HT-SOFC, but are ideal for LT-SOFC by virtue of reducing its $T_o \sim 650 \text{ }^\circ\text{C}$ [14].

Although doping creates oxygen vacancies in the CeO_2 lattice, fluorite structures admit a certain limit. Above this limit there is an association of defects at

the dopant level between the vacancy and the dopant cation, which leads to a decrease in ionic conductivity [141]. Therefore, minimising the association of defects with the preferred dopant at the optimum level can improve ionic conductivity. The dopant concentration and the preparation method are some other important parameters affecting the composition, morphology, and, subsequently, the conductivity of ceria-based electrolytes.

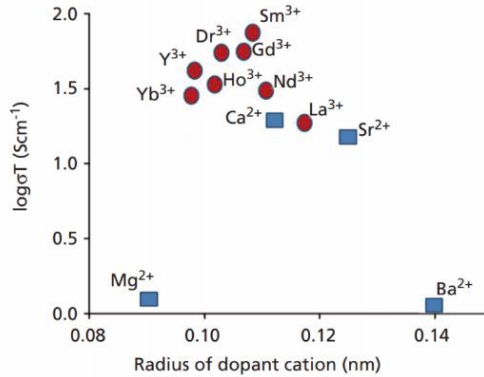


Fig. 2.4. The plot of the ionic conductivity vs ionic radius of various dopants in ceria. Reproduced from [5]

Steele [140] evaluated materials for IT-SOFC electrolytes at T_o 500 °C and reported that Gd^{3+} is the most suitable dopant compared to Sm^{3+} and Y^{3+} . $Gd_{0.1}Ce_{0.9}O_{2-\delta}$ had an ionic conductivity of $0.0253 S \times cm^{-1}$ at 600 °C, which was the highest among all the researched ceria-based samples. This result is comparatively low, which was explained by the harmful effects of SiO_2 impurities that are responsible for high grain boundary resistivities. According to [142–144] in the case of addition of a dopant, the minimum elastic deformation leads to the maximum ionic conductivity of fluorites based on the empirical relationship between the lattice parameter at room temperature and the radius and concentration of the dopant ion. Moreover, the authors showed that Gd^{3+} has the highest ionic conductivity since its ionic radius is close to the critical value. Yahiro *et al.* [145] investigated the total ionic conductivity of the $(CeO_2)_{0.8}(LnO_{1.5})_{0.2}$ series where $Ln = Sm, Gd, La, Nd, Eu, Ho, Y, Yb$, and Tm at 800 °C. The ionic conductivity of $(CeO_2)_{1-x}(SmO_{1.5})_x$ had the highest value among the samples ($0.0945 S \times cm^{-1}$), and La_2O_3 doped had the lowest value ($0.0416 S \times cm^{-1}$). The authors also reported that, when increasing the concentration of Sm_2O_3 ($x > 20$ mol%), the total conductivity decreases. Eguchi *et al.* [146] also reported the highest ionic conductivity for $(CeO_2)_{0.8}(SmO_{1.5})_{0.2}$ in comparison to that of the other RE elements. The authors stated that the change in the lattice constant depends linearly on the dopant concentration and increases to the solubility limit. Omar *et al.* [38] investigated the density functional theory (DFT) of the interaction energy between a dopant cation and an oxygen vacancy as another doping strategy. According to it, Sm^{3+} and Nd^{3+} offered 14% higher bulk

conductivity than Gd^{3+} at 550 °C. In their further work [147], the authors synthesised 10 mol% of $\text{D}_{0.1}\text{Ce}_{0.9}\text{O}_{2-\delta}$ (where $\text{D} = \text{Gd}^{3+}, \text{Sm}^{3+}, \text{Nd}^{3+}, \text{Lu}^{3+}, \text{Yb}^{3+}, \text{Er}^{3+}, \text{Y}^{3+}$, and Dy^{3+}) by using a conventional solid state reaction method and reported that $\text{Nd}_{0.1}\text{Ce}_{0.9}\text{O}_{2-\delta}$ had the highest total ionic conductivity and that the bulk conductivity at 500 °C is ~17% higher compared to $\text{Gd}_{0.1}\text{Ce}_{0.9}\text{O}_{2-\delta}$. Zhang *et al.* [127] made a systematic comparison of commercial YSZ, ScSZ, and GDC. The authors showed that GDC ceramic had more narrow grain size distribution and at low T_o (500 °C), had the highest conductivity of $5.8 \times 10^{-3} \text{ S} \times \text{cm}^{-1}$ and the lowest activation energy. It has been reported that with increasing the dopant concentration, the conductivity of aliovalent-doped ceria also increases, and, due to the defect association, reaches its maximum when the dopant concentration is ~10–20 mol% [126,148].

Over the years, various publications on ceria-based electrolytes reported a wide range of conductivity considering the dopant type and its concentration (M_2O_3 , $\text{M} = \text{Sm}, \text{Gd}, \text{Dy}, \text{Nb}, \text{Y}$, etc.; 10–20 mol%). The presented results differ from each other, and their disagreement is associated with different methods of preparation of materials, which influenced their properties, such as the microstructure. The properties of the starting material, the processing of powders, the sintering conditions, and the microstructure after sintering affect the ionic conductivity. However, not many publications provide detailed investigation on such properties. Mori *et al.* [149] examined the influence of the morphology and reported that the conductivity of $\text{Sm}_{0.2}\text{Ce}_{0.8}\text{O}_{1.9}$ was higher, and the activation energy was much lower for sintered powders consisting of round-shaped particle compared to elongated particles. Chen *et al.* [150] investigated the impact of the sintering/calcination conditions and showed that YSZ calcined at 1350 °C for 4 h had a conductivity of $0.105 \text{ S} \times \text{cm}^{-1}$, while YSZ calcined at 1250 °C for 8 h had a conductivity of $0.112 \text{ S} \times \text{cm}^{-1}$. These results are explained by the variation of the grain size and the relative density.

Although the doping of cerium oxide with low-valence REs helps to achieve high ionic conductivity, the single-doped ceria suffers from some disadvantages. The main problem is that the reduction of Ce^{4+} to Ce^{3+} decreases the oxide-ionic conductivity, thus increasing the electronic conductivity. This results in low power output, which affects the overall efficiency of the cell [41]. An approach that can improve the quality of electrolytes and enhance the conductivity is co-doping of ceria with more than one dopant.

Ruiz-Morales *et al.* [151] studied $\text{Ce}_{0.8}\text{Sm}_x\text{Gd}_y\text{Nd}_z\text{O}_{1.9}$ co-doped ceria electrolytes with various concentration of the dopants and reported that $\text{Ce}_{0.8}\text{Sm}_{0.1}\text{Gd}_{0.1}\text{O}_{1.9}$ showed the highest conductivity in the IT range (300–700 °C). In [152], the authors synthesised ceramics by using the citrate method and compared the properties of singly doped ceria ($\text{Ce}_{0.8}\text{Sm}_{0.2}\text{O}_{1.9}$ and $\text{Ce}_{1-x}\text{Gd}_x\text{O}_{2-0.5x}$ ($x = 0.1-0.2$)) with ceria co-doped with Gd and Sm ($\text{Ce}_{1-x}\text{Gd}_x\text{Sm}_y\text{O}_{2-0.5x}$ (where $x = 0.15$ or 0.2 and $0 \leq y \leq x$)). It was reported that at 700 °C the σ_{total} of $\text{Ce}_{0.85}\text{Gd}_{0.15-y}\text{Sm}_y\text{O}_{1.925}$ was $0.046 \text{ S} \times \text{cm}^{-1}$, which was higher than the highest values of singly doped ceria ($0.0316 \text{ S} \times \text{cm}^{-1}$ for $\text{Ce}_{0.85}\text{Gd}_{0.15}\text{O}_{1.925}$ and $0.041 \text{ S} \times \text{cm}^{-1}$ for $\text{Ce}_{0.8}\text{Sm}_{0.2}\text{O}_{1.9}$). In addition, for the co-doped system, the activation energy was lower, which was explained by the suppression of the ordering of oxygen vacancies [153]. Coles-

Aldridge and Baker [9] carried out a systematic study of ceria-based oxides co-doped with Gd and Sm for IT-SOFC. The authors synthesised two series of compositions of the co-doped system and found that in the IT range (550–900 °C) $\text{Ce}_{0.825}\text{Sm}_{0.0875}\text{Gd}_{0.0875}\text{O}_{1.9125}$ has the highest total conductivity among other concentrations of the co-doped system and its singly doped compound ($2.23 \text{ S}\times\text{cm}^{-1}$ at 600 °C) [9]. Similarly, Dikmen [154] reported higher values of conductivity for $\text{Ce}_{0.8}\text{Gd}_{0.1}\text{Sm}_{0.1}\text{O}_{2-\delta}$ compared to $\text{Ce}_{0.8}\text{Gd}_{0.2}\text{O}_{2-\delta}$ at 700 °C. Moreover, the author compared various metal co-dopants with Gd ($\text{Ce}_{0.8}\text{Gd}_{0.2-x}\text{M}_x\text{O}_{2-\delta}$, where M is Sm with $x = 0$ to 0.1 and M is La, Nd, and Bi with $x = 0.05$) and got the highest values when co-doping with Sm ($\sigma_{\text{total}} \sim 6.5 \times 10^{-2} \text{ S}\times\text{cm}^{-1}$ at 700 °C with $0.59 \text{ eV } E_a$).

2.2.3.1 Methods of chemical synthesis

Despite the variety of different methods of chemical synthesis for the fabrication of ceria-based materials, priority will be given to simple methods which allow to obtain finest and pure nanopowders [135,155–158]. Arabaci [159] synthesised $\text{Ce}_{0.8}\text{Gd}_{0.2-x}\text{Pr}_x\text{O}_{1.90}$ (where $x = 0$ to 0.10) by using citric acid-nitrate combustion and obtained σ_{total} of $5.1 \times 10^{-2} \text{ S}\times\text{cm}^{-1}$ at 750 °C for $\text{Ce}_{0.8}\text{Gd}_{0.1}\text{Pr}_{0.1}\text{O}_{1.9}$ and $3.4 \times 10^{-2} \text{ S}\times\text{cm}^{-1}$ at 750 °C for $\text{Ce}_{0.8}\text{Gd}_{0.2}\text{Pr}_{0.10}\text{O}_{1.9}$. In [160] $\text{Ce}_{0.9-x}\text{Gd}_{0.1}\text{Sm}_x\text{O}_{2-\delta}$ (where $x = 0, 0.05$, and 0.10) was synthesised by using the Pechini method; it had the highest conductivity of $4.23 \times 10^{-2} \text{ S}\times\text{cm}^{-1}$ at 750 °C for $\text{Ce}_{0.85}\text{Gd}_{0.1}\text{Sm}_{0.05}\text{O}_{1.925}$. Madhuri *et al.* [132] investigated the triple-doping of ceria ($\text{Ce}_{1-x}(\text{La}_{x/3}\text{Pr}_{x/3}\text{Sm}_{x/3})\text{O}_{2-\delta}$) synthesised by the sol-gel auto-combustion method and $\text{Ce}_{0.76}\text{La}_{0.08}\text{Pr}_{0.08}\text{Sm}_{0.08}\text{O}_{2-\delta}$ has the highest σ_{total} of $0.043 \text{ S}\times\text{cm}^{-1}$ with E_a of 0.76 eV .

Combustion (CB), co-precipitation (CP), and sol-gel (SG) are some of the simplest and most popular methods for the formation of complex ceria-based oxides; they are inexpensive and relatively fast, and help to synthesise nanopowders with a controlled homogeneous structure [161–164]. Kim *et al.* [126] synthesised aliovalent-doped ceria, such as Sm_2O_3 , Gd_2O_3 , and Nd_2O_3 , by using the combustion, solid-state, hydrothermal, and co-precipitation synthesis methods. It was shown that among other doped-ceria, $\text{Nd}_{0.2}\text{Ce}_{0.8}\text{O}_{2-\delta}$ (NDC) synthesised by combustion had the highest conductivity at 600 °C and below 550 °C. Moreover, it was shown that the ionic conductivity in the IT range increases with the increasing lattice parameter, the dopant ionic radius, and the concentration ($r_{\text{Gd}}^{3+} < r_{\text{Sm}}^{3+} < r_{\text{Nd}}^{3+}$ and $10 \text{ mol}\% < 20 \text{ mol}\%$), as well as at a lower annealing temperature. The grain boundary conductivity of the 20 NDC ceramics obtained by combustion and annealed at 1450 °C for 4 h was several magnitudes higher compared to the ceramics obtained by co-precipitation and solid-state reaction and annealed at 1650 °C for 10 h. The effect of the lower annealing temperature was explained by the space charge layers and the deleterious effect of SiO_2 impurities, which affect the resistivity of the grain boundaries. The authors concluded that the use of the combustion synthesis method and a lower annealing temperature can efficiently decrease the resistivity of the grain boundary [126]. Tian *et al.* [128] obtained the highest conductivity ($0.0154 \text{ S}\times\text{cm}^{-1}$ at 600 °C) for $\text{Sm}_{0.2}\text{Ce}_{0.8}\text{O}_{1.9}$ synthesised by combustion and annealed at 1300 °C; a further increase in the annealing temperature decreased the conductivity

value. Macedo *et al.* [165] studied the potential use of the sol-gel methods for the formation of $\text{Ce}_{0.8}\text{Sm}_{0.2}\text{O}_{1.9}$ and reported that the nanopowders possess good sintering ability with an average crystallite size of 12 nm; the obtained ceramics had a polygonal microstructure with the average grain size of $\sim 15\ \mu\text{m}$ and the total ionic conductivity of $0.0091\ \text{S}\times\text{cm}^{-1}$ at $600\ ^\circ\text{C}$ with the activation energy of 0.94 eV. Koettgen and Martin [41] synthesised $\text{Ce}_{1-x}\text{RE}_x\text{O}_{2-x/2}$ (where RE were Sm ($x = 0, 0.025, 0.05, 0.07, 0.075, 0.1, 0.125, 0.15, 0.2, 0.225, \text{ and } 0.25$) and Gd ($x = 0.07 \text{ and } 0.1$)) using sol-gel. The authors showed that, with an increasing temperature, the dopant fraction increased as well, thus leading to the maximum value of conductivity, and the highest total conductivity was found for Sm-doped ceria. Moreover, it was reported that the change of the annealing conditions leads to a scatter of conductivity by an order of magnitude. For instance, the bulk and grain boundary conductivity values of $\text{Ce}_{0.85}\text{Sm}_{0.15}\text{O}_{1.925}$ at $173\ ^\circ\text{C}$ that were annealed between 1111°C to 1514°C for 4 to 55 h were scattered by an order of magnitude.

2.2.3.2 Thin films fabrication methods

In order to improve the performance of the electrolyte and the overall development of LT-SOFC, it is necessary to lower the operating temperature. However, when decreasing the temperature, the resistivity of the electrolyte increases. This problem can be solved by reducing the electrolyte thickness. Yiming *et al.* [166] prepared a thin YSZ electrolyte by using novel dry pressing/heating/quenching/calcining, the obtained thicknesses were $78\ \mu\text{m}$. The authors stated that, at a lower thickness, the electrolyte offers low ohmic resistance and good electrochemical characteristics (the ohmic resistance is $0.19\ \Omega\times\text{cm}^2$ at $850\ ^\circ\text{C}$) [166].

The state-of-the-art electrolyte for the IT-SOFC, $\sim 10\ \mu\text{m}$ YSZ, at low temperatures does not show high ionic conductivity to achieve acceptable area specific resistance (ASR_{el}) from the electrolyte [127]:

$$ASR_{el} = L \times \sigma^{-1} \quad (2.15)$$

where σ is the ionic conductivity, and L is the thickness of the electrolyte. According to Equation 2.15, reduction of the thickness of the electrolyte will reduce the ASR_{el} .

It is necessary to choose a method for the formation of thin electrolyte films that will make it possible to produce films of the required thickness. Over the years, many methods have been introduced for making films of different thicknesses, and thin films can be obtained by chemical vapour deposition (CVD) [167,168], physical vapour deposition (PVD) ($1\text{--}5\ \mu\text{m}$ [169–173]), magnetron sputtering ($400\ \text{nm} - 5\ \mu\text{m}$, [174–176]), pulsed laser deposition (PLD) ($\sim 700\ \text{nm}$, [174,177,178]), screen printing ($7\ \mu\text{m}$, [174,176]), dip-coating (mesoporous layers, $100\text{--}700\ \text{nm}$ [179]), spin coating ($1\ \mu\text{m}$ [180]), spray pyrolysis ($700\ \text{nm}$ [174], [181]), electrostatic spray ($85\ \text{nm}$ [182]), and sol-gel infiltrated screen printing ($1.5\ \mu\text{m}$ [183,184]). A comparison of the methods is given in Table 2.4.

When applying the chemical deposition methods (chemical vapour deposition (CVD) and electrochemical vapour deposition (EVD)), a solid material is formed by

a gaseous precursor through an activation process [185]. The advantages of this method are the control of the chemical composition of the films, which are uniform, adherent, and pure. However, corrosive gases are present during CVD and EVD, the reaction temperature is high, and the deposition rate is low [185].

Various sputtering techniques, grouped as physical vapour deposition (PVD), are some of the most commonly used methods. Radio frequency sputtering (RF) was widely used to deposit YSZ films; however, the deposition rate is rather low ($0.25 \mu\text{m} \times \text{h}^{-1}$) [186,187]. Meanwhile, due to the higher sputtering yield, the deposition rate when using reactive magnetron sputtering shows a much higher value ($2.5 \mu\text{m} \times \text{h}^{-1}$) [188,189]. In addition, ion irradiation is involved during magnetron sputtering, which makes it possible to obtain high density films at low temperatures. When using magnetron sputtering, structures with specific properties and different compositions can be formed by changing the sputtering parameters and sputtering sources [190–192]. Thin electrolyte films can be deposited by vacuum deposition methods whose deposition rate is two orders of magnitude higher compared to the previously mentioned methods [193–195]. Although the use of electron beam evaporation (EB-PVD) on composite materials makes it challenging to control the composition of the films, the deposition area is large, the deposition rate is high, and it also gives better control of the thickness.

Table 2.4. Comparison of the methods for producing thin and dense electrolytes for SOFC applications. Reproduced from [185]

Technique	Film characteristics		Process features	
	Microstructure	Deposition rate or thickness	Cost	Characteristics and limitations
<i>Vapour phase</i>				
Thermal spray technologies		$100\text{--}500 \mu\text{m} \times \text{h}^{-1}$		High deposition rates, various compositions possible, thick, and porous coatings, high temperatures necessary
Electrochemical vapour deposition (EVD)	Columnar structures	$3\text{--}50 \mu\text{m} \times \text{h}^{-1}$	Expensive equipment and processing costs	High reaction temperatures necessary, corrosive gases
Chemical vapour deposition (CVD)	Columnar structures	$1\text{--}10 \mu\text{m} \times \text{h}^{-1}$	Expensive equipment	Various precursor materials possible, high reaction temperature necessary, corrosive gases
Physical vapour deposition (PVD) (Radio frequency and magnetron sputtering)	Columnar structures	$0.25\text{--}2.5 \mu\text{m} \times \text{h}^{-1}$	Expensive equipment	Tailor-made films, dense and crack-free films, low deposition temperatures, multipurpose technique, relatively small deposition rate

Laser ablation			Expensive equipment (laser)	Intermediate deposition temperatures, difficult upscaling, time-sharing of laser, relatively small deposition rate
Spray pyrolysis	Amorphous to polycrystalline	$5\text{--}60\ \mu\text{m} \times h^{-1}$	Economical	Robust technology, upscaling possible, easy control of parameters, corrosive salts, post-thermal treatment usually necessary
<i>Liquid phase</i>				
Sol-gel, Liquid precursor route	Polycrystalline	$0.5\text{--}1\ \mu\text{m} \times h^{-1}$ for each coating	Economical	Various precursors possible, very thin films, low temperature sintering, coating and drying/heating processes have to be repeated 5–10 times, crack formation during drying, many process parameters
<i>Solid phase</i>				
Tape casting	Polycrystalline slightly textured	$25\text{--}200\ \mu\text{m} \times h^{-1}$		Robust technology, upscaling possible, crack formation
Slip casting and slurry coating	Polycrystalline	$25\text{--}200\ \mu\text{m} \times h^{-1}$	Economical	Robust technology, crack formation, slow
Tape calendering	Polycrystalline	$5\text{--}200\ \mu\text{m} \times h^{-1}$		Upscaling possible, co-calendering possible
Electrophoretic deposition (EPD)	Polycrystalline	$1\text{--}200\ \mu\text{m} \times h^{-1}$		Short formation time, little restriction to shape of substrate, suitable for mass production, high deposition rates, inhomogeneous thickness
Transfer printing	Polycrystalline	$5\text{--}100\ \mu\text{m} \times h^{-1}$	Economical	Robust technology, rough substrate surfaces possible, adhesion on smooth substrates difficult
Screen printing	Polycrystalline	$10\text{--}100\ \mu\text{m} \times h^{-1}$	Economical	Robust technology, upscaling possible, crack formation

It is difficult to find a suitable method for the formation of thin films, since most of them form porous, rather thick, inhomogeneous films and may even require a high sintering temperature. The sintering temperature of ceria-based films should

not exceed 1100 °C, since above this point, a solid solution of GDC or SDC with low conductivity is formed [196–198].

From the relevant research and literature, it is evident that Gd and Sm, as single-doped or as a co-doped system in ceria-based electrolytes, increase conductivity to a greater extent compared to the other dopants of rare earth elements. Therefore, it is necessary to comprehensively and systematically study how dopants and their concentrations, as well as synthesis methods, affect the ionic conductivity of ceria-based electrolytes. The results of such study will allow us to understand how minor changes in the composition affect the parameters that determine the favourable characteristics of electrolytes for LT-SOFCs. Moreover, a comparison of two favourable PVD methods while varying their parameters will help to choose the best preparation route.

3. EXPERIMENTAL TECHNIQUES AND METHODS

3.1 Chemical synthesis methods

Ceria-based nanostructured ceramic powders were synthesised by using the combustion, co-precipitation, and sol-gel chemical synthesis methods. A summary of the synthesised nanopowders and their stoichiometric equations is presented in Table 3.1, and the materials used for the synthesis and formation of thin films are presented in Table 3.2.

Table 3.1. Summary of the synthesised ceria-based nanopowders

Notation	The molar concentration of dopants	Chemical formula	Notation of synthesis method
10 SDC	10 mol% of Sm_2O_3	$\text{Sm}_{0.1}\text{Ce}_{0.9}\text{O}_{2-\delta}$	CB, CP, SG
20 SDC	20 mol% of Sm_2O_3	$\text{Sm}_{0.2}\text{Ce}_{0.8}\text{O}_{2-\delta}$	CB, CP, SG
26 SDC	26 mol% of Sm_2O_3	$\text{Sm}_{0.26}\text{Ce}_{0.74}\text{O}_{2-\delta}$	CB, CP, SG
30 SDC	30 mol% of Sm_2O_3	$\text{Sm}_{0.3}\text{Ce}_{0.7}\text{O}_{2-\delta}$	CB, CP, SG
10 GDC	10 mol% of Gd_2O_3	$\text{Gd}_{0.1}\text{Ce}_{0.9}\text{O}_{2-\delta}$	CB, CP
15 GDC	15 mol% of Gd_2O_3	$\text{Gd}_{0.15}\text{Ce}_{0.85}\text{O}_{2-\delta}$	CB, CP
20 GDC	20 mol% of Gd_2O_3	$\text{Gd}_{0.2}\text{Ce}_{0.8}\text{O}_{2-\delta}$	CB, CP
25 GDC	25 mol% of Gd_2O_3	$\text{Gd}_{0.25}\text{Ce}_{0.75}\text{O}_{2-\delta}$	CB, CP
SGDC	0.0875 mol% of each Sm_2O_3 and Gd_2O_3	$\text{Ce}_{0.825}\text{Sm}_{0.0875}\text{Gd}_{0.0875}\text{O}_{2-\delta}$	CB, CP

Table 3.2. Materials used for the synthesis and formation of thin films

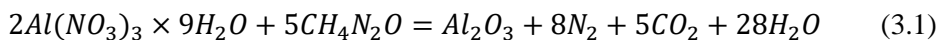
The initial synthesis materials were following:	
Reagents	Solutions
Cerium (III) nitrates hexahydrates ($\text{Ce}(\text{NO}_3)_3 \cdot 6\text{H}_2\text{O}$, 99.0%, <i>Fluka</i>)	Ammonium hydroxide 25% (NH_4OH , 25%, <i>Sigma Aldrich</i>)
Samarium (III) nitrates hexahydrates ($\text{Sm}(\text{NO}_3)_3 \cdot 6\text{H}_2\text{O}$, 99.9%, <i>Sigma Aldrich</i>)	Deionised water (H_2O)
Gadolinium (III) nitrates hexahydrates ($\text{Gd}(\text{NO}_3)_3 \cdot 6\text{H}_2\text{O}$, 99.9%, <i>Sigma Aldrich</i>)	
Glycine ($\text{NH}_2\text{CH}_2\text{COOH}$, $\geq 99.0\%$, <i>Sigma Aldrich</i>)	
Oxalic acid ($\text{C}_2\text{H}_2\text{O}_4$, $\geq 99.0\%$, <i>Sigma Aldrich</i>)	
(L-+)- Tartaric acid ($\text{C}_4\text{H}_6\text{O}_6$) (TA) $\geq 99.5\%$, <i>Sigma Aldrich</i>)	
Samarium (III) oxide (Sm_2O_3 , 99.99%, <i>AlfaAesar</i>)	
Ammonium cerium (IV) nitrate ($(\text{NH}_4)_2\text{Ce}(\text{NO}_3)_4$, 99.99%, <i>Sigma-Aldrich</i>)	
Nitric acid (HNO_3 , 66%, <i>Reachem</i>)	

The following substrates and materials for the cleaning of the substrates were used for the preparation of the thin films:	
Materials for the cleaning	Substrates
99.8% acetone (C ₃ H ₆ O) (<i>Reachem</i> Slovakia s.r.o.)	Silicon (Si) wafer with 500 µm thickness, orientations (100) and (111), p-type, single-side polished, (<i>Sigma-Aldrich</i>);
≥ 99% N,N-Dimethylformamide (<i>Sigma-Aldrich</i>)	Silicon oxide/silicon (SiO ₂ /Si) wafer with 1 µm thickness of SiO ₂ ((100), p-type, double-side polished, <i>Sigma-Aldrich</i>);
Nitrogen (N ₂) gas (<i>Aga Sia</i> , 96%)	α-Al ₂ O ₃ substrate (double-side polished, BK-100-1, <i>Kineshmo</i> , Russia)

3.1.1 Combustion synthesis method

Combustion synthesis (CB) is a complex, self-sustaining exothermic process that occurs in a homogeneous aqueous or a sol-gel precursor solution. CB is an inexpensive, relatively fast, and simple method for synthesising various nanoscale materials such as oxides, sulfides, alloys, and metals, which is why it has become one of the popular approaches to producing nanomaterials [199,200]. The process includes several thermally related exothermic reactions that lead to the formation of ultrafine solid oxides of the corresponding metal and a large amount of gas. CB begins at room temperature with the thermal decomposition and dehydration of a homogeneous solution of compounds in the solid state having a complex crystal structure. A unit crystal cell consists of atoms that function as fuel (H, C) and oxidising atoms (for example, O) which are separated by distances on the Angstrom scale [200]. The initial constituents are mixed at the molecular level, and the sizes of particles of a solid powder are approximately 10²–10⁵ nm.

A significant step for the detection of CB was the synthesis of aluminium nitrate hydrate (Al(NO₃)₃×9H₂O) (*oxidiser*) and urea (CH₄N₂O) (*fuel*). The combustion process of a dissolved in a distilled water oxidiser and fuel solution was observed at approximately 1350 °C and lasted ~3 min. The final product was α-Al₂O₃ and a large amount of gas, which leads to a substantial expansion of the solid product and a swift decrease in temperature. Consequently, the obtained powders are finely dispersed and porous. The reaction of the process is as follows [200]:



Combustion synthesis is classified by the chemical composition of different types of components (*oxidiser*, *fuel*, and *solvent*) used for the synthesis. Table 3.2 presents the most commonly used constituents for CB due to their advantages. The presented oxidisers have a relatively low decomposition temperature and offer good solubility in water which is one of the most commonly used solvents. For instance, aluminium nitrate hydrate (Al(NO₃)₃×9H₂O), which was present in the reaction (Eq. 3.1), decomposes at approximately 130 °C, and its solubility in water is ~64 wt% (at

room temperature). Meanwhile, aluminium sulfate ($\text{Al}_2(\text{SO}_4)_3$) decomposes at 600 °C with ~27 wt% of solubility in water (at room temperature).

The criteria for fuel are a low decomposition temperature (< 400 °C), high solubility, it should be compatible with the oxidiser, and should not lead to other residual mass. The presented fuels are a source of hydrogen and carbon, and they compose complexes with metal ions, which results in homogeneous mixing of cations. It should be noted that the fuel should not only provide the system with a sufficient amount of heat but also should ensure the formation of stable complexes with metal ions to increase their solubility and prevent the selective precipitation of metal ions during water removal [200].

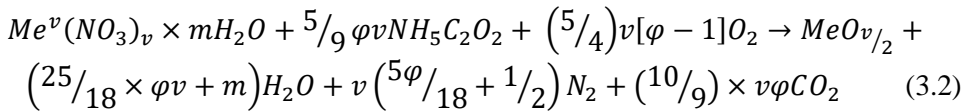
Table 3.3. Most commonly used constituents for combustion synthesis

Oxidizer	Fuel	Solvent
Metal nitrates or metal nitrate hydrates: $\text{Me}^v(\text{NO}_3)_v \times n\text{H}_2\text{O}$ v is metal valence	glycine ($\text{C}_2\text{H}_5\text{NO}_2$)	water (H_2O)
	sucrose ($\text{C}_{12}\text{H}_{22}\text{O}_{11}$)	hydrocarbons: kerosene benzene (C_6H_6)
	glucose ($\text{C}_6\text{H}_{12}\text{O}_6$)	
	citric acid ($\text{C}_6\text{H}_8\text{O}_7$)	
	urea ($\text{CH}_4\text{N}_2\text{O}$)	
Ammonium nitrate (NH_4NO_3)	hydrazine-based fuels: carbohydrazide ($\text{CH}_6\text{N}_4\text{O}$) oxalyldihydrazide ($\text{C}_2\text{H}_6\text{N}_4\text{O}_2$)	alcohols: ethanol ($\text{C}_2\text{H}_6\text{O}$) methanol (CH_4O) furfuryl alcohol ($\text{C}_5\text{H}_6\text{O}_2$) 2-methoxyethanol ($\text{C}_3\text{H}_8\text{O}_2$)
Nitric acid (HNO_3)	hexamethylenetetramine ($\text{C}_6\text{H}_{12}\text{N}_4$)	
	acetylacetone ($\text{C}_5\text{H}_8\text{O}_2$)	formaldehyde (CH_2O)

There are various types of combustion synthesis methods that are classified by the nature of the process and the state of the initial precursors [201]. According to the first classification, there are two types of the process, deflagration (subsonic reaction) and detonation (supersonic wave). In the course of the deflagration method, various mechanisms of mass transfer and heat conduction initiate the reaction from the burning part to the subsequent layers of the reactants. Meanwhile, the detonation process works like a supersonic wave, which heats the explosive, thus initiating the chemical reactions with the release of energy [201]. The synthesis of ceria-based materials is performed by using the deflagration mode; thus, we will continue to discuss this type of method [17,202–205]. There are two modes in the

deflagration combustion method: self-propagating high-temperature synthesis (SHS) and thermal explosion (or volume) [200,201]. In the SHS mode the combustion wave which self-propagates along the reactive mixture is initiated by the locally preheated volume ($\sim 1 \text{ mm}^3$) within the reactive solution or gel [200,201]. In the thermal explosion mode, the entire reactive mixture is heated uniformly to its boiling point, which results in the formation of the desired material [200,201]. The reaction and the cooling time of the process is one of the main parameters that influence the microstructure of the materials which, in both modes, are in the range of milliseconds. T_{max} of the synthesis is in the range of 1500 K to 4000 K and is limited by the thermodynamics of the system.

The second classification of CB is based on the initial state of the starting material which are the gas phase, gasless system, solution combustion, and solid-gas [201]. For the synthesis of a ceria-based ceramics solution, combustion synthesis is employed, which is a self-sustained chemical reaction occurring in an aqueous homogeneous solution of an oxidiser and fuel [17,200,201,205]. The chemical reaction of the solution CB where glycine is used as fuel and Me is any metal nitrates is as follows [200]:



where, if $\phi = 1$, external oxygen is not required for the initial solution to complete the fuel oxidation, if $\phi < 1$ (or > 1), it requires fuel-lean (or fuel-rich) conditions.

Among the variety of the heating methods of the reactive solution, the simplest and the most popular one is the use a hot plate. The initial solution is placed into a glass or ceramic beaker and heated on at hot plate where the temperature is usually around 300 to 400 °C. The mixture is constantly stirred during the processes that include heating, evaporation, gel formation and decomposition, self-ignition, combustion, and the formation of the final product.

The variety of CB methods for synthesising nanoscale materials is broad, and new directions in chemistry and technology are regularly created. Materials synthesised with CB offer a wide range of applications in different fields, such as fuel cells, batteries, supercapacitors, solar cells, heterogeneous catalysts, optical materials, semiconductors, nanoceramics, and thin films [41,161,206–210].

In order to understand the principle of combustion synthesis, it is important to know its fundamentals that include the thermodynamics and kinetics of the process as well as the mechanisms of the reactions.

3.1.1.1 Thermodynamics of combustion synthesis

Thermodynamics helps to calculate the maximum temperature of the reaction and the composition of the resulting equilibrium products. These calculations should be carried out under adiabatic conditions, where the heat transfer between the system and the environment should be neglected. Since the system is isolated, i.e., any exchange with the environment is excluded, the amount of the matter during the

synthesis and the total energy of the system remains constant. By using thermodynamic calculations of the initial temperature for the synthesis and gas pressure, it is possible to control the microstructure and phase composition of the desired material. In addition, such calculations make it possible to set the conditions for the synthesis of the material with the same phase composition but a larger or smaller amount of gas phase products and different maximum temperatures. The microstructure of the material depends on the amount of the gas phase products; generally, materials with a high specific surface area and a smaller particle size are obtained during the synthesis with a high amount of gas phase products and at a low temperature.

CB is a self-sustained exothermic redox reaction where the driving force is the intention of the system to reduce its Gibbs free energy (G) by converting the chemical potential into heat [200]. The heat of the reaction (Q) is the amount of the heat released during the synthesis, and it can be found by the following equation:

$$Q = \Delta H_j^0 = \sum_j n_j \Delta_f H_j^0 - \sum_i n_i \Delta_f H_i^0 \quad (3.3)$$

where ΔH_j^0 is the enthalpy of the formation of CB products; i and j indicate the reactants and products, respectively; n_i and n_j are the concentrations of each compound; and ΔH_f^0 is the standard enthalpy of the material.

Considering that the system is in adiabatic conditions, all the energy is used to increase the temperature of the reaction mixture to a/the maximum value defined as the adiabatic combustion temperature (T_{ad}) [200]. T_{ad} can be determined from the following equation if assuming no phase transitions:

$$Q = \int_{T_0}^{T_{ad}} \sum_j n_j C_{p,j} dT \quad (3.4)$$

where $C_{p,j}(T)$ is the specific heat of the product j as a function of temperature. Equation 3.4 assumes no phase transitions, such as decomposition or melting, where the transition enthalpies need to be accounted for [200]. The temperature dependence of the specific heats of compounds and substances can be found in handbooks [211] and usually are presented in the form of polynomials [200]:

$$C_p = A + B \times T + CT^2 \quad (3.5)$$

The equation for the calculation of T_{ad} which is frequently used in CB processes where the specific heat (B_i and $C_i = 0$ in Equation (3.5)) can be considered constant for each reaction product is as follows:

$$T_{ad} = T_0 + Q/\bar{c}_p \quad (3.6)$$

where $\bar{c}_p = \sum_j n_j A_j$ is the average specific heat capacity at room temperature. Such a rough estimation can be used only if the dependence of the heat capacities of the product on the temperature is not significant.

3.1.1.2 Kinetics of combustion synthesis

The formation of a material with the desired properties is controlled by the characteristic temperature and time of the synthesis which is highly dependent on the rate of the reaction moving towards equilibrium. This parameter can be described by the kinetics of the synthesis.

As the deflagration combustion method has two modes – thermal explosion (or volume) and self-propagating high-temperature synthesis (SHS) – there are two approaches to calculate the parameters of the reaction. Semenov developed the theory [212,213] for the thermal explosion mode where the heat release rate can be described by the Arrhenius law:

$$q_+ = k_0 \Phi(\eta_i) V \exp\left(-\frac{E_a}{RT}\right) = k_0 V Q e^{-E_a/RT} \quad (3.7)$$

where q_+ is the heat evolution rate (or the heat release rate), E_a is the activation energy, Q is the heat of the reaction, k_0 is the pre-exponential factor, η_i is the degree of the reaction conversion for the reagent i , $\Phi(\eta_i)$ is a function of the degree of conversion, R is the universal gas constant, V is the volume, and T is the temperature.

Thermal ignition is realised if the heat evolution resulting from the chemical reaction prevails over the heat removal, and heat evolution accelerates with the temperature higher than heat removal [214]:

$$q_+ \geq q_-; \quad dq_+/dT \geq dq_-/dT \quad (3.8)$$

where q_+ is the heat evolution rate (or the heat release rate), q_- is the rate of heat removal from the system (or the heat exchange), and T is the temperature.

By applying Eq. 3.7 and the conditions of Eq. 3.8, Semenov established the critical reaction conditions under which thermal explosion takes place:

$$T_{cr} = T_0 + \frac{RT_{cr}^2}{E_a} \approx T_0 + \frac{RT_0^2}{E_a} \quad (3.9)$$

where T_{cr} is the critical temperature, R is the universal gas constant, E_a is the activation energy, and T_0 is the ambient temperature. The self-propagating mode is not as widely used as the thermal explosion mode, although it is more controllable. During the self-propagating combustion reaction, the heating-reaction zone exchanges energy and matter with the environment, and internal chemical energy is released and converted into heat. A temperature profile of CB is shown in Fig. 3.1

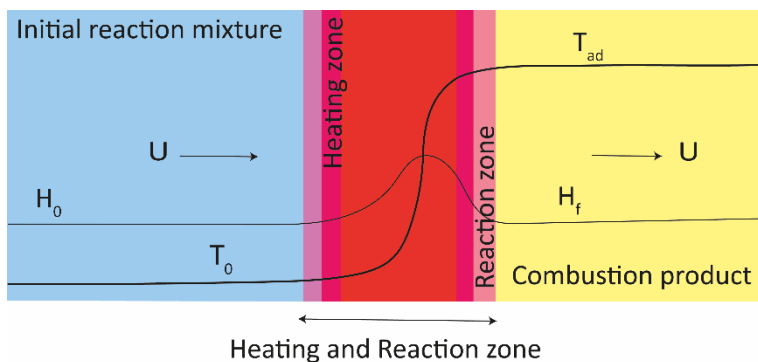


Fig. 3.1. Scheme of the thermal structure of the wave during combustion synthesis [215]

A stationary combustion wave along the reactive media can be determined using the quasi-homogeneous approximation:

$$\frac{d}{dx} \left(\lambda \frac{dT}{dx} \right) - cpU \frac{dT}{dx} + QW = 0 \quad (3.10)$$

with the boundary conditions set at infinity as:

$$x = -\infty, T = T_0; x = +\infty, T = T_{ad} \quad (3.11)$$

where U is the velocity of the combustion wave, λ is the heat conductivity, c is the heat capacity, ρ is the density of the reaction media, Q is the heat of the reaction, and the boundary conditions which were set [200]

In order to control the combustion wave propagation characteristics, it is important to know the activation energy and the pre-exponential function of the reaction. An analytical solution of the problem (Eq. 3.10 and Eq. 3.11) with the Arrhenius kinetics (Eq. 3.7) in an approximation of the narrow reaction zone can be represented as follows [200]:

$$U \approx \frac{1}{cp(T_c - T_0)} \sqrt{2Q\lambda k_0 \int_{T_0}^{T_c} e^{-E/RT} dT} \quad (3.12)$$

Optimisation of the temperature-time history of the reaction helps to obtain a material with the desired properties and to control its nanostructure; therefore, it is important to know the kinetics of the synthesis in both modes.

3.1.1.3 Mechanism of combustion synthesis

Combustion synthesis route using samarium (III) nitrate hexahydrate ($\text{Sm}(\text{NO}_3)_3 \times 6\text{H}_2\text{O}$, 99.9%, *Sigma-Aldrich*), gadolinium (III) nitrate hexahydrate ($\text{Gd}(\text{NO}_3)_3 \times 6\text{H}_2\text{O}$, 99.9%, *Sigma-Aldrich*), and cerium (III) nitrate hexahydrate ($\text{Ce}(\text{NO}_3)_3 \times 6\text{H}_2\text{O}$, 99.0%, *Fluka*) as the source of metal cations and glycine ($\text{NH}_2\text{CH}_2\text{COOH}$, $\geq 99.0\%$, *Sigma-Aldrich*) as fuel were applied to prepare ceria-based nanopowders. The scheme of the synthesis is shown in Fig.3.2.

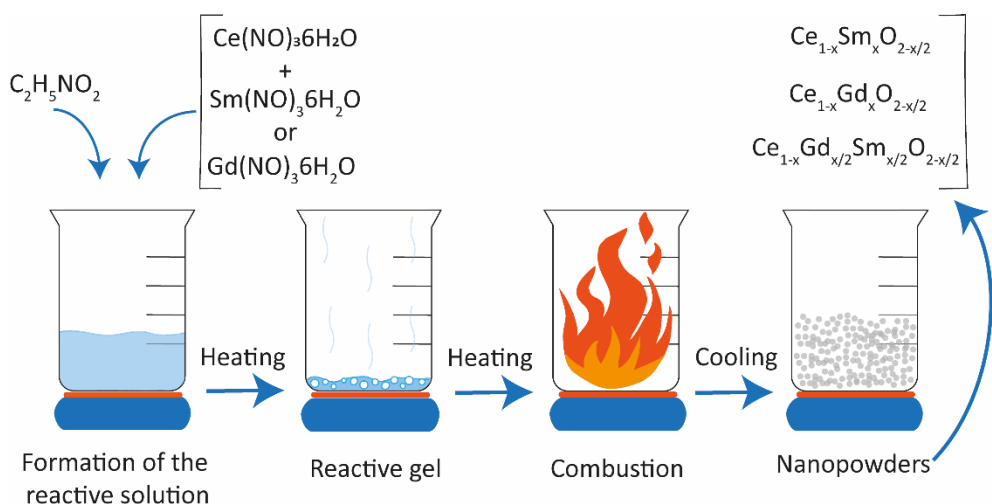
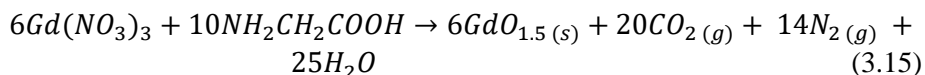
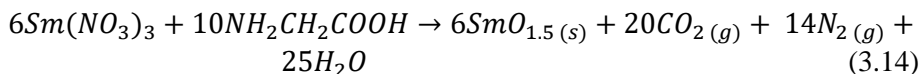
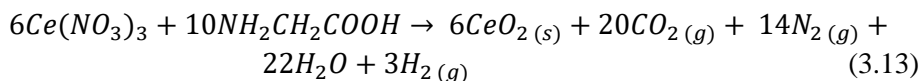


Fig.3.2. Scheme of combustion synthesis of ceria-based ceramic nanopowders

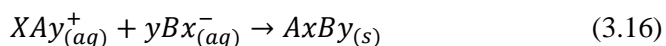
Metal nitrates and fuel were dissolved separately in ~15–20 ml of distilled water, according to their stoichiometric equations. An aqueous mixture of all the reagents was placed on a magnetic stirrer and heated from 90 °C to 150 °C for 1 hour, resulting in the formation of a gel. The resulting gel solution was heated from 200 °C to 350 °C for ~15 minutes until the combustion process began.

The chemical reactions of the obtained oxides from nitrates with glycine as a fuel under the condition of complete combustion of the redox mixture [216] are as follows:



3.1.2 Co-precipitation synthesis method

Co-precipitation (CP) is a simple and low-temperature synthesis method which produces a large number of fine, homogeneous particles. Subjected to a strong supersaturation, the products formed during the synthesis are insoluble. The supersaturation conditions cause precipitation, which can be described by the following reaction:

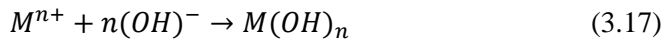


where $+/-$ is the valence for metal cations and oxidizer ions, s is a solid material, aq is the liquid component, A and B are the initial molecules, AB is the final product, and x and y are free atoms and radicals.

During the CP reaction, the processes of nucleation, growth, coarsening, and/or agglomeration are simultaneously involved [217]. Inclusion, adsorption, and occlusion are the three main mechanisms for the co-precipitation synthesis method. If the charge of the impurity and its ionic radius is similar to the carrier, we observe crystallographic defects. This mechanism is called inclusion and occurs when an impurity occupies a lattice site in the crystal structure of the carrier. After the impurity has been adsorbed to the surface of the precipitate (adsorption), it gets physically trapped inside the crystal (occlusion).

By using CP, it is possible to synthesise metals by the reduction from non-aqueous solutions, decomposition of organometallic precursors, and electrochemical reduction, oxides obtained from non-aqueous and aqueous solutions. In order to perform CP synthesis and to obtain the material with the desired properties, it is important to understand the precipitation behaviour of the precursor and the effect of the precipitation agent.

The precipitation of metal hydroxide $M(OH)_n$, where n is the valence of metal ions in the solution, can be described as follows:



Considering that the ionic product of water under ambient pressure at 25 °C is $10^{-14} M^2$ and is as follows, we get:

$$-\log[H^+] - \log[OH^-] = pH + pOH = 14 \quad (3.18)$$

The solubility constant (K_{SP}) of $M(OH)_n$ is:

$$K_{SP} = [M^{n+}][OH^-]^n \quad (3.19)$$

$$\log K_{SP} = \log[M^{n+}] - 14n - n\log[H^+] \quad (3.20)$$

$$\log[M^{n+}] = -\log K_{SP} + 14n - npH \quad (3.21)$$

where $[M^{n+}]$ and $[OH^-]$ are the molar concentrations of M^{n+} and OH^- , respectively. The solubility constant $\log K_{SP}$ can be found from the compilation of solubility data on oxides, hydroxides, and hydroxide salts [218].

In order to achieve better homogeneity, the pH of the solution, which is related to the target products, must be kept constant. Changes in pH during the synthesis can affect the uniformity of the particle size and the composition homogeneity. The choice of the pH value is determined by the precipitant used for the synthesis, and it is desirable to ensure that the solution is not alkaline (basic). In the case of using oxalic acid and NH_4OH as a complex precipitant, the optimal pH is ~6.5; however, in order to neutralise the solution of oxalic acid, a double molar amount of NH_4OH is required [219].

The precipitant exerts great influence on the physical and chemical properties of the final product. The most commonly used precipitants for the formation of nanocrystalline powders are diethylamine (DEA), formic acid, urea,

hexamethylenetetramine, ammonium carbonate, NH_4OH or hydrazine hydrate, and oxalic acid. By applying the alkoxide process where hydrated metal nitrates are used as precursors, and organic solvents are used as precipitants, nanocrystalline powders with weak agglomeration, high reactivity, and high sintering activity are usually synthesised [219–221]. For the synthesis of weakly agglomerated nanocrystalline powders, diethylamine shows the advantages of using it as a precipitant in comparison with ammonium hydroxide. Diethylamine shows a strong tendency to gain protons from hydroxide complexes and has an important role in the formation of hydrogen bonds with hydrated water of the metal salts [219,222]. The buffer-solution method (with the NH_4OH – NH_4HCO_3 system as the precipitant) can be used for the synthesis of various kinds of oxides [219,223]. Compared to the synthesis of single-phase materials, the synthesis of composite materials is a complex process in which the sequence of the addition of precipitants and their concentration must be carefully considered. The concentration of the precipitant affects the completeness of precipitation, the composition of the precursor, and the morphology [224]. Another parameter that influences the morphology is the reaction temperature. At room temperature, the obtained powders, together with fine and spherical particles, can contain many coarse rod-band structured particles [224]. Pellets pressed from such uncrushed powders are denoted by relatively low density. At higher temperatures (40–60 °C), the formation of such structures with hard aggregates is suppressed [224].

3.1.2.1 Mechanism of co-precipitation synthesis

The same metal cations as those for CB synthesis were used as the precursors for the co-precipitation synthesis to form ceria-based nanopowders. Oxalic acid ($\text{C}_2\text{H}_2\text{O}_4$, $\geq 99.0\%$, *Sigma-Aldrich*) and ammonium hydroxide (NH_4OH , 25%, *Sigma-Aldrich*) were used as precipitating agents, and the solvent was distilled water. The scheme of the synthesis is shown in Fig. 3.3.

The stoichiometric amount of the precursors and precipitants was dissolved in distilled water separately. The pH ratio of the solution was adjusted to ~8–9 by slowly adding ammonium hydroxide. The solution of the dissolved precursors was added dropwise to the oxalic acid solution under vigorous stirring by using a magnetic stirrer at 50 °C. The co-precipitates were filtered by vacuum filtration while using a Büchner funnel and dried overnight at room temperature.

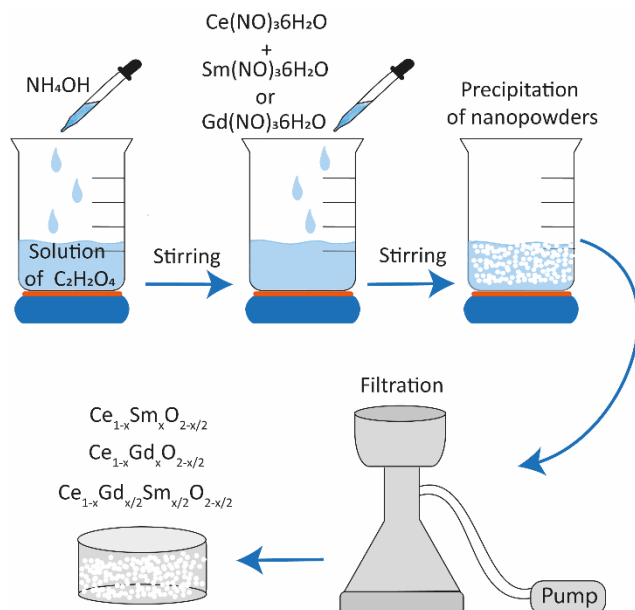


Fig.3.3. Scheme of co-precipitation synthesis of ceria-based ceramic nanopowders

3.1.3 Sol-gel synthesis method

Sol-gel (SG) synthesis is one of the widely used methods for producing nanoparticles, starting with molecular precursors that form an oxide network through inorganic polymerisation reactions [219,225,226]. The complex process includes the preparation of a sol (a colloidal solution of particles), gelation, and removal of the solvent (transition to a solid material) [225]. During the synthesis, the colloidal solution acts as a precursor for an integrated network of discrete particles (gel). By changing the ratio of the precursors (usually, metal alkoxides) in the solution, the composition of the product can be reproduced. The sol-gel method enables the synthesis of powders with high phase purity, high surface activity, good compositional homogeneity on the molecular level, and uniform nanostructures at low temperatures. Due to these advantages, it is applicable for the preparation of composite nanopowders, oxide nanoparticles, metal oxides, as well as ceramic materials that can be used as an electrolyte, an interlayer, or a cathode for SOFCs [204,225,227–229]. Despite its advantages, the process is very sensitive to such synthesis parameters as the chemical composition, the nature of the solvent, the reactant concentration, the temperature, and pH [219]. In turn, these parameters affect the properties of the final product. The morphology and crystallographic symmetry of the resulting powders are highly dependent on the chemical procedure.

Complexing agents (the complexant) can play a decisive role in homogeneous solution condensation in the SG process. The electronegativity of the ligands affects the complexation between the metal ions and the complexing agents [219]. If the electronegativity of the complexant is less than the electronegativity of the ligand, electrons are transferred from the complexant to the precursor. The negative charge

of the complexant decreases, and the covalent metal ion bond increases. If the complexant is more electronegative than the ligand, electrons are attracted to the complexant from the precursor. This, in turn, increases the negative charge of the complexing agents, thus making the bond more ionic and making it difficult to bond with the metal cations [219,230,231].

SG is an inorganic polymerisation reaction of metal alkoxides, and in the case of non-silicate tetravalent alkoxides, the condensation rate of the complexing agents must be reduced in order to prevent hydroxide precipitation [219,230]. These alkoxides must be kept in dry atmosphere as they are quite sensitive to moisture. Inorganic acids, carboxylic acids, β -diketones, or other complexing ligands can be used as modifiers to control the reactivity.

Since the sol-gel is based on hydrolysis and condensation processes, the gelation time decreases with an increase in the molar ratio of the water content in the synthesis. Thus, the gelation time can be controlled by the amount of water being used [230–232]. More water leads to faster gelation, but the gel under these conditions will become inhomogeneous. A lower ratio results in fewer impurities and better homogeneity in the final powders [229,233].

Catalysts can be used to control the rate of hydrolysis and condensation during SG synthesis; however, depending on the type of the catalyst, the rate of gel formation and its structure can be altered. In order to ensure gel homogeneity, the kinetics of hydrolysis and condensation reactions must be low [233,234].

3.1.3.1 Mechanism of sol-gel synthesis

The synthesis of ceria-based ceramics was prepared by aqueous sol-gel (SG) synthesis while using tartaric acid as a chelating agent, which reacts as a ligand at the molecular level with the reaction mixture both during dissolution in water and during the formation of the sol-gel.

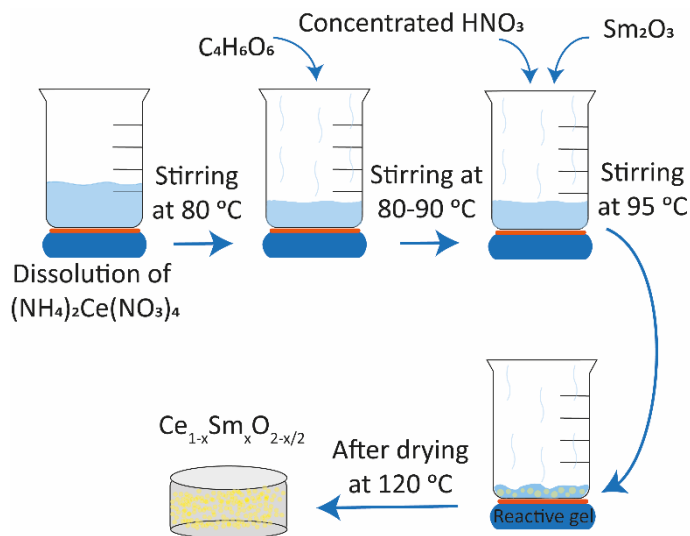
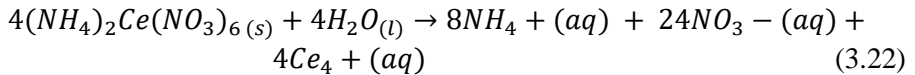


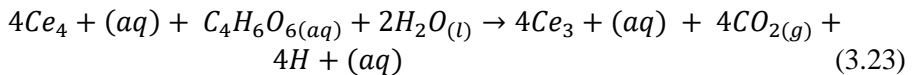
Fig.3.4. Scheme of sol-gel synthesis of ceria-based ceramic nanopowders

Samarium (III) oxide (Sm_2O_3 , 99.99%, *AlfaAesar*), ammonium cerium (VI) nitrate ($(\text{NH}_4)_2\text{Ce}(\text{NO}_3)_4$, 99.99%, *Sigma-Aldrich*) were used as the starting materials and weighed according to the desired stoichiometric ratio. Nitric acid (HNO_3 , 66%, *Reachem*) and distilled water were used as reagents to reduce the pH of the solutions and to improve the solubility of samarium (III) oxide. Tartaric acid (L-(+)- Tartaric acid ($\text{C}_4\text{H}_6\text{O}_6$) (TA) $\geq 99.5\%$, *Sigma-Aldrich*) was applied to increase the solubility due to the coordination of the starting compounds in the reaction mixture, especially during the changes in pH and evaporation before the formation of sol-gel.

First, ammonium cerium (VI) nitrate was dissolved in distilled water at 80 °C. The dissolution process can be written as follows:



After several minutes of stirring and evaporating in an open beaker, the reduction of Ce^{4+} ions to Ce^{3+} was completed by the addition of tartaric acid. The oxidation-reduction reaction between the cerium (IV) ion and tartaric acid is as follows:



This oxidation-reduction process (see Eq. 3.23) was confirmed both by observing the release of a large amount of CO_2 gas and by the colour change of the solution from orange to colourless. Then, after continuous stirring at approximately 80–90 °C, samarium (III) oxide and concentrated nitric acid were added to the beaker. A clear solution was obtained, which was then concentrated by rapidly evaporating the reaction mixture at 95 °C. In the following stage, a yellow transparent sol was formed after almost 95% of the water had evaporated under continuous stirring. After drying in an oven at 120 °C for several hours in air, fine-grained pale yellow gel powders were obtained.

3.1.4 Formation of ceramic pellets

Ceria-based nanostructured ceramic powders synthesised by CB, CP, and SG were calcined at various temperatures (200, 400, 600, 800, 900, 1000, 1100, 1200 °C) for 5h in air. Ceramic pellets of a diameter of 10 mm were formed from the ground and calcined at 800 °C synthesised powders by using a uniaxial press at 4 MPa and annealed at 1200 °C for 2 h in air. Subsequently, the pellets were used as the target material for the formation of thin films.

3.2 Thin film formation methods

3.2.1 Electron beam evaporation

SDC and GDC ceramics were used as a target material for the formation of thin films on various substrates (for details, see Subchapter 3.1.1) by using a UVN-71P3

electron beam evaporation system (e-beam). The basic principle of the e-beam technique is presented in Fig. 3.5.

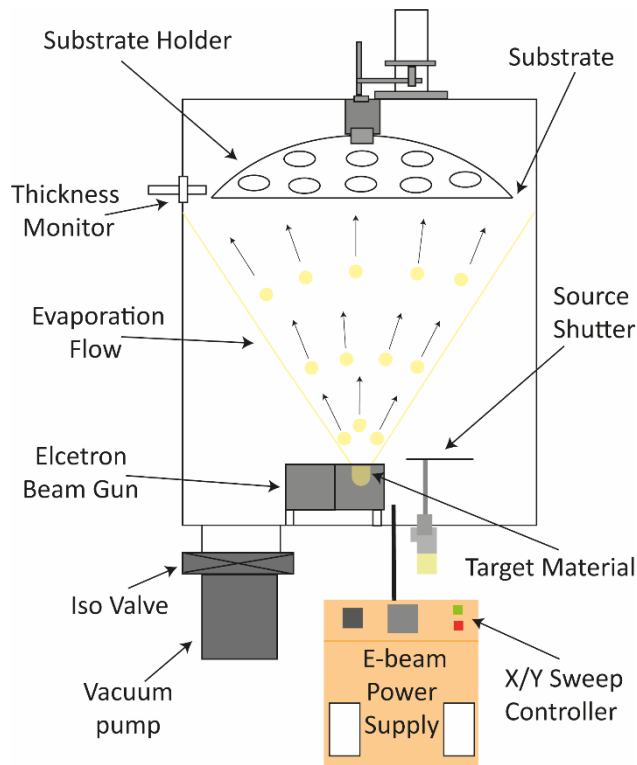


Fig. 3.5. Schematic principle of electron beam evaporation

The evaporation process was carried out at a pressure of 0.7 Pa with an evaporation rate of ~2 nm/s. The substrate was heated with infrared lamp heaters in a vacuum chamber and the temperature of the substrate was constant (200 °C). The distance between the substrate and the e-gun (power 10 kW) was 250 mm. All the main parameters of the process are presented in Table 3.4.

Table 3.4. Parameters of electron beam evaporation process

Pressure in the chamber	10 ⁻⁵ Pa
Deposition pressure	0.7 Pa
Electron gun power	10 kW
Maximum emission current	500 mA
Deflection of electrons	180°
Diameter of the electron beam	5 mm
Temperature of the substrate	200 °C
Growth rate	~2 nm/s
Distance between the e-gun and the substrate	250 mm
Thickness monitoring	quartz crystal deposition controller

The thickness of the formed thin films varied from ~100 nm to ~1 μm and was controlled with a quartz crystal deposition controller.

3.2.2 Magnetron sputtering

Reactive magnetron sputtering in the direct current mode (*Kurt J. Lesker* company) which was integrated with a *Leybold Heraeus-A-700-QE* vacuum system was used to deposit Gd_2O_3 and CeO_2 thin films multilayer systems with 4, 6, and 12 layers (denoted as GDC4, GDC6, GDC12) on Si (111) substrates. The deposition was layer-by-layer in the reactive O_2/Ar gas mixture environment by using CeO_2 and Gd_2O_3 targets. The base pressure was 2×10^{-4} Pa, and the sputtering gas pressure in the chamber during the deposition was 0.065 Pa. The distance between the target and the substrate was 16 cm. The substrate was heated to 150 $^\circ\text{C}$ with infrared lamp heaters in the vacuum. All the main parameters of the process are presented in Table 3.5.

Table 3.5. Parameters of magnetron sputtering process

Base pressure	2×10^{-4} Pa
Sputtering gas	O_2/Ar gas mixture
Sputtering gas pressure	0.065 Pa
Targets	CeO_2 and Gd_2O_3
Temperature of the substrate	150 $^\circ\text{C}$
Distance between the target and the substrate	16 cm
Voltage	510 V
Current	0.4 A
Growth rate monitoring	quartz crystal deposition controller

In order to study the effect of only the number of layers on the inter-mixing process, all the films were deposited with an expected thickness of ~600–700 nm. The deposition rate was determined considering the desired concentration of CeO_2 (90 mol%) and Gd_2O_3 (10 mol%). Subsequently, deposited thin film multilayer systems were annealed at 700 $^\circ\text{C}$ for 1 h in air.

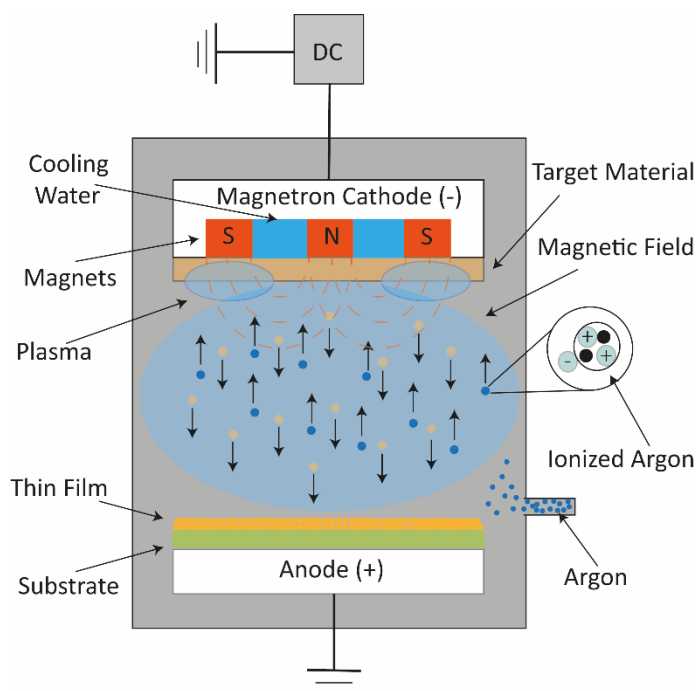


Fig. 3.6. Schematic principle of magnetron sputtering deposition

3.3 Analytical techniques

Table 3.6. Summary of analysis, characterisation tools, and their applications to study particular properties or applications

Methods	Characterisation Techniques	Obtained Information and parameters
Thermal analysis	Differential scanning calorimetry (DSC)	Amorphous content and polymorphism
	Thermal gravimetric analysis (TGA)	Kinetic, physical, and chemical properties
	Differential Thermal Analysis (DTA)	Phase transitions, crystallisation temperatures
Structural analysis	X-ray diffraction (XRD)	Crystallinity, structure type, and crystallite size
	X-ray photon spectroscopy (XPS)	Chemical surface analysis, binding energy, and uniformity of composition
	Raman spectroscopy	Bonding structure
Surface analysis	Brunauer-Emmett-Teller (BET)	Surface area and pore size distribution
Elemental analysis	Energy dispersive X-ray (EDX)	Chemical composition and purity
	Inductively coupled plasma optical emission spectrometry (ICP-OES)	Elemental-chemical composition
	Fourier transmission infrared	Identification of functional

	spectroscopy (FT–IR)	groups and chemical bonding
Size and morphology analysis	Scanning electron microscopy (SEM)	Topology, size, morphology, crystallographic structure, and composition
	Transmission electron microscopy (TEM)	Topology, size, morphology, and crystallographic structure
	Atomic force microscopy (AFM)	Size, morphology, surface roughness, and texture
Electrical properties analysis	Electrochemical impedance spectroscopy (IS)	Electrical properties

3.3.1 Thermogravimetric analysis

Thermal analysis is a group of methods studying the change of the properties of at material with the change in temperature and time under an atmosphere of air or another gas. There are several methods depending on the measured properties. Thermogravimetric analysis (TGA) is an analytical technique investigating the change in the weight of a substance as a function of time or temperature. TGA allows studying various thermal events such as absorption, adsorption, desorption, phase transition, vaporisation, sublimation, decomposition, chemisorption, oxidation, and reduction [235]. The TGA equipment consists of a very sensitive scale measuring the weight changes, which is positioned above at programmable furnace [235,236].

Differential Scanning Calorimetry (DSC) is a method measuring the energy (absorbed or released) in materials as a function of time and temperature which provides information about changes in the heat capacity and endothermic or exothermic processes. DSC operates isothermally in a given atmosphere, with a constant rate of the temperature change. The temperature of the material changes due to several events, such as the melting point, the degradation temperature, phase transitions, the loss of solvent, and the crystallisation temperature [236].

Differential Thermal Analysis (DTA) measures the temperature difference between a sample and a reference as the temperature increases. DTA, similarly to DSC, determines thermal events such as phase transitions, crystallisation temperatures, and melting points which result in temperature changes, but, unlike DSC, it does not quantify the amount of energy [236].

A simultaneous thermal analyser (STA) 6000 PerkinElmer, combining DSC/DTA and TGA, was used to examine thermal decomposition processes of ceria-based nanopowders. Uncalcined, dried powders of 5–10 mg were heated from 30 to 950 °C at a heating rate of 20 °C/min under an atmosphere of air with a gas flow of 20 ml/min. Measurements were performed in alumina ceramic crucibles. The analysis of an empty crucible was made before every measurement in order to eliminate the crucible background.

3.3.2 X-ray diffraction analysis

X-ray diffraction (XRD) is a powerful analytical technique used to characterise crystalline materials at the atomic scale which provides information on the preferred crystal orientations, phases, structure, average grain size, crystallinity, crystal defects, and deformation. A monochromatic beam of X-rays is scattered from each set of lattice planes at specific angles forming XRD peaks. The intensities of the peaks are determined by the position of the atoms in the lattice planes [237].

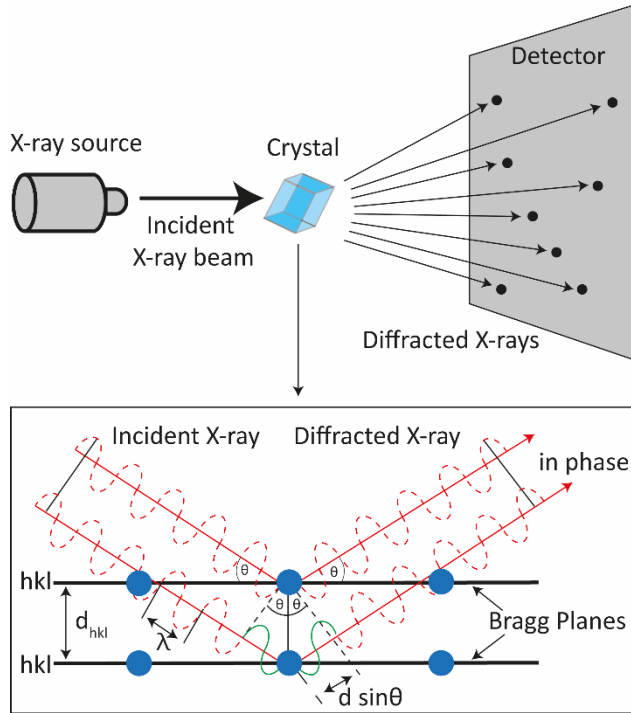


Fig. 3.7. Scheme of X-Ray diffraction

The principle of XRD is that it sends out X-rays passing through the sample, reflecting off the atoms in the structure and changing the direction of the beam at the diffraction angle. Some diffracted beams cancel each other out, while constructive interference occurs when the beams are of the same wavelength. The diffraction angle can be used to determine the difference between atomic planes by using Bragg's law

$$2d \sin \theta = n\lambda \quad (3.24)$$

where λ is the wavelength of the X-ray beam, θ is the diffraction angle, d is the distance between atomic planes (d -spacing), and n is an integer. Diffraction peaks are generated due to constructive wave interference, and their conversion to d -spacing helps to determine the composition or the crystalline structure of the material [238–240].

The crystal structure of synthesised ceria-based nanopowders was investigated by using a *D8 Discover (Bruker AXS GmbH)* diffractometer with a Cu K α_1 ($\lambda = 0.154$ nm) radiation source and parallel beam focusing geometry with a 60 mm Göbel mirror. The peak intensities were measured in the 20–90°, coupled 2θ – θ scans, over the range of 5–135° with a 0.02° step size, and a 0.2 s timespan per step. The measurements of thin films (the grazing incidence) were performed over the 0–5° scanning range with a 0.0025° step size, and 0.1 s timespan per step while using the grazing incident angle. The X-ray generator used the voltage and current of 40 kV and 40 mA, respectively. Phase identification was performed by comparing the obtained XRD patterns with the powder diffraction file database of the *International Centre for Diffraction Data (ICDD)*. *DIFFRAC.EVA* software was used to process the obtained diffractograms. Considering that in all cases single-phase compounds were obtained, the Rietveld refinement using *X'pert HighScore Plus* software was performed to calculate the crystallite sizes and the lattice parameters. The crystallite sizes can be calculated by using the Scherer equation:

$$d = \frac{K\lambda}{\beta \cos\theta} \quad (3.25)$$

where d is the crystallite size, λ is the X-ray wavelength, θ is the diffraction angle, β is the line broadening at half the maximum intensity (FWHM), K is a shape factor, and 1.00 constant value was employed [241,242]. The crystalline lattice parameters can be calculated with the following Equation 3.26:

$$a = \frac{\lambda\sqrt{h^2+k^2+l^2}}{2 \sin\theta} \quad (3.26)$$

where h , k , l are the indices of the crystallographic plane.

3.3.3 Brunauer-Emmett-Teller method

The Brunauer-Emmett-Teller (BET) surface analysis technique is used for the characterisation of the specific surface area of nanoscale materials. Its principle is based on the physical adsorption of a gas molecule on a solid surface. BET is a quick, relatively simple, and accurate method and its theory applies to systems of multilayer adsorption. Probing gases, which do not chemically react with the material's surfaces are used as adsorbates to quantify the specific surface area. Standard BET usually works at 77 K, the boiling temperature of N₂, as nitrogen is the most commonly used gaseous adsorbate. Further probing adsorbates including argon, carbon dioxide, and water, are also utilised, although less commonly; they allow the measurement of a surface area at different temperatures and measurement scales [243–245].

A Brunauer-Emmett-Teller (BET) surface area analyser (*Sorptometer KELVIN 1042*) was used to determine the bulk surface area of synthesised powders calcined at 900 °C. The quantities of the specific surface area determined through BET may depend on the adsorbate molecule and its adsorption cross-section, as the specific surface area is a scale-dependent property, with no single true value of the specific

surface area being definable [243,244]. The BET surface area and the equivalent particle size can be calculated by the following equation [246]:

$$D_{BET} = \frac{6 \times 10^3}{d_{th} S_{BET}}, \quad (3.27)$$

where D_{BET} (nm) is the average particle size, S_{BET} (m²/g) is the specific surface area, and d_{th} is the theoretical density of the solid solution oxide (g/cm³) calculated according to the following Equation 3.28:

$$d_{th} = \frac{4[(1-x)M_{Ce} + xM_{Gd} + (2-x/2)M_O]}{a^3 N_A} \quad (3.28)$$

where x is the dopant concentration, N_A is the Avogadro constant, M is the atomic weight, and a is the lattice constant of the solid solution.

3.3.4 Scanning electron microscopy energy dispersive X-ray spectroscopy

Scanning Electron Microscopy (SEM) provides information about the microstructure, morphology, and homogeneity of a sample by scanning the surface with a focused high-energy electron beam. Electrons penetrate the surface during elastic or inelastic interactions between the beam and the sample, which results in the emission of electrons and photons. The signals from the emitted particles are collected with an appropriate detector, and the intensity of the detected signals is combined with the position of the beam to produce a high resolution image [247,248]. Signals from a secondary electron provide information about the surface features of the sample down to nanometres [249]. Signals from backscattered electrons provide information about the topography, atomic composition, magnetism, and crystallinity of the sample [250,251].

Energy-dispersive X-ray spectroscopy (EDX) can be used to analyse the chemical composition or elemental analysis of a material; it allows detecting elements with the atomic number from 4 to 92. The X-ray spectrum gives information about the atomic structure of the elements and is formed during inelastic collisions of an electron beam and an electron in an inner shell of atoms [252,253].

The microstructure and the elemental composition of ceria-based ceramics annealed at 1200 °C and thin films were investigated with scanning electron microscope *Quanta 200 FEG (FEI)* equipped with energy dispersive X-ray spectrometer *Bruker XFlash 4030*. The measurements were carried out in a high vacuum (< 6e – 4 Pa) with an accelerating voltage of 30 kV, a resolution of 1.2 nm, an emission current of 160 µA. The images were analysed with the '*ImageJ2x*' program, and the chemical concentrations were calculated into atomic percentages.

3.3.5 Transmission electron microscopy

Transmission electron microscopy (TEM) is a microscope technique similar to SEM, except that an electron beam is transmitted through the sample to form an image. When electrons interact with the sample, they diffract from the lattice planes in the crystalline phase of the materials or undergo coherent scattering, thus

providing phase identification [236]. Transmission electron microscopy (TEM) images were taken with a *Tecnai G2 F20 X-TWIN* (FEI, Netherlands, 2011) with a 200 kV Schottky type field emission electron source.

3.3.6 Inductively coupled plasma optical emission spectrometry

Inductively coupled plasma optical emission spectrometry (ICP-OES) is an elemental analysis technique that helps to identify the atomic composition of a sample. ICP-OES consists of the sample introduction system, plasma (the excitation source), a spectrometer, and a detector. Data are collected from the emission spectra of atoms and ions excited in an inductively coupled plasma. The data give information about the concentrations of the compound. The spectrometer detaches the element-specific wavelengths of light and focuses the resolved light on the detector [245].

In order to determine the elemental compositions of ceramic nanopowders, at solution of 100 mg of the samples dissolved in concentrated sulphuric acid was analysed with an Inductively Coupled Plasma Optical Emission Spectrometer (ICP-OES, *Vista-Pro*, *Varian*).

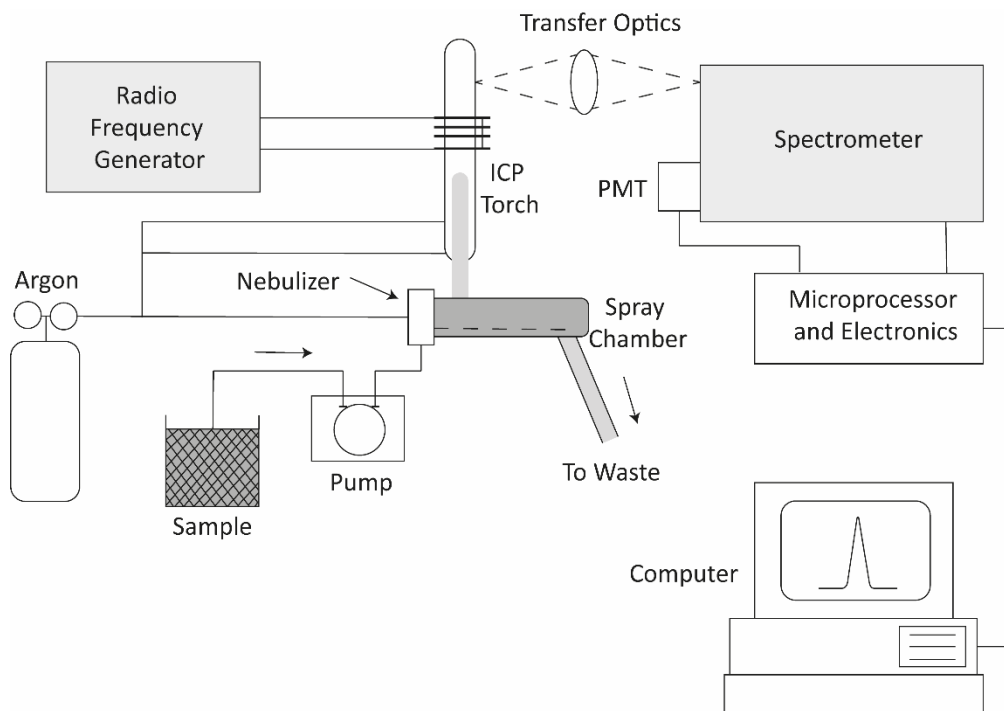


Fig. 3.8. Example of the ICP-OES setup

3.3.7 Fourier transform infrared spectroscopy

Fourier transform infrared (FT-IR) spectroscopy helps to determine various functional groups and the chemical bonding of nanoparticles by obtaining an

infrared spectrum of the emission or absorption of a gas, a liquid or a solid. An FT-IR spectrometer collects spectral data over a wide range which can bring the qualitative investigation of various types of organic and inorganic samples [243].

The principle of work is that various molecules in a sample, depending on their three-dimensional orientation and chemical structure, will absorb a different portion of the infrared light. In this manner, the chemical bond will vibrate in different ways, depending on its nature. The position of the bands from the recorded spectrum provides the information related to the strength and nature of the bonds, the functional groups, molecular structures, and interactions.

Infrared spectroscopy enables to detect the rotational and vibrational modes of the molecular bonds; therefore, it facilitates the identification of the functional groups in the sample. Since all the syntheses produced SDC powders, Diffusive Reflectance Infrared Fourier Transformed spectroscopy (FT-IRs) was used for the analysis of the pure sample. The chemical composition and functional groups were identified with Kubelka–Munk transformation in Fourier transform infrared (FT-IR) spectroscopy, where the spectral recording area was from 400 to 4000 cm^{-1} with a resolution of 1 cm^{-1} . A *Vertex 70 FT-IR* spectrometer (*Bruker Optik GmbH*), equipped with *EasiDiff* high quality diffuse reflectance equipment (*PIKE Technologies*) with the fixed 30° angle of incidence (3/16" sampling area mask), was used in this experiment.

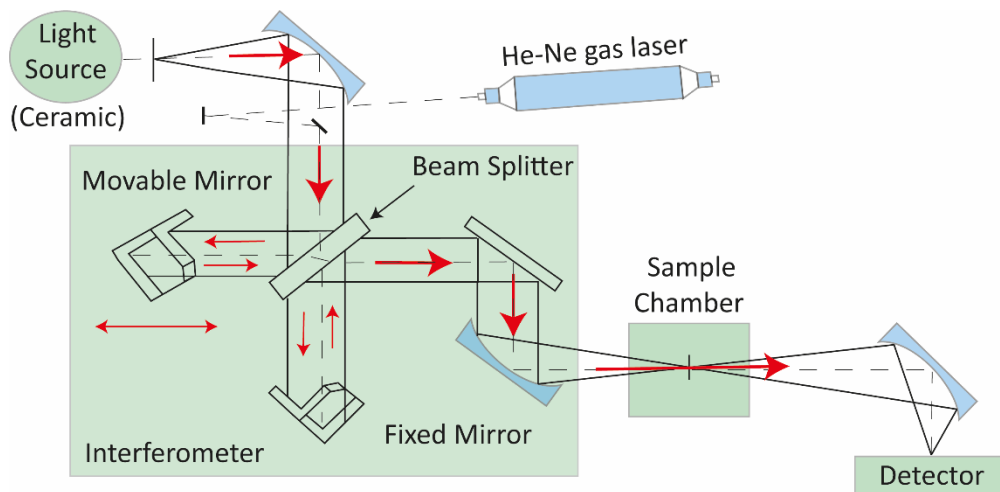


Fig. 3.9. Schematic diagram of a *Michelson* interferometer for FT-IR

3.3.8 *Electrochemical impedance spectroscopy*

The electrical properties of ceria-based ceramics were investigated by employing AC impedance spectroscopy (IS) while using a completely automated system, involving *Solartron 1255* and an in-house current-voltage amplifier based on an *LM7171* voltage feedback amplifier and an *OPA604* FET-input operation amplifier. A complex impedance plot, based on the simultaneous measurement of resistance (R) and capacitance (C) of a cell over a wide frequency range, helps to

determine the electrical properties (such as the bulk, grain boundary, and electrode response) and to investigate the nature of the mobile charge carriers. Electrochemical impedance is usually carried out by applying a small alternating signal (AC) potential to a system (an electrochemical cell) and measuring the AC current through the cell [254,255]. The response to the sinusoidal potential excitation, which is applied to the electrochemical device, is an alternating current signal. The current signal can be analysed as a sum of sinusoidal functions and can be expressed as the following equation:

$$I_t = I_0 \sin(\omega t + \phi) \quad (3.29)$$

where I_0 is the amplitude of the current, ω is the angular frequency ($\omega = 2\pi f$), ϕ is the initial phase, and t is time. The current response to the potential will be a sinusoid shifted in phase $\pi/2$, but within the same frequency range. This occurs in a pseudo-linear system, for which the AC excitation voltage should be less than the thermal E_a and is typically set to be less than 10 mV.

When applying Ohm's law, impedance can be expressed as follows:

$$Z = \frac{E_t}{I_t} = \frac{E_0 \sin(\omega t)}{I_0 \sin(\omega t + \phi)} = Z_0 \frac{\sin(\omega t)}{\sin(\omega t + \phi)} \quad (3.30)$$

where E_t and I_t are the potential and current values at the time, E_0 and I_0 are the amplitudes of the potential and the current. The complex impedance can be expressed by applying Euler's formula:

$$Z(i\theta) = Z_0 e^{i\theta} = Z_0 \cos\theta - iZ_0 \sin\theta = Z' + iZ'' \quad (3.31)$$

where Z' is the real impedance corresponding to R (resistance), iZ'' is the imaginary impedance corresponding to the resistance of the C (capacitor) $\frac{-i}{\omega C}$. Subsequently, with $|Z| = E_t/I_t$ and $\tan\phi = Z''/Z'$, impedance can be represented by the following Expression 3.32:

$$|Z| = Z' + j\omega Z'' \quad (3.32)$$

Plotting the values of Z' and $-Z''$ on the coordinate axes yields a Nyquist plot [256], which reveals the information about the processes occurring in the material (Fig. 3.10). A typical complex impedance plot of ionic conductivity of the bulk and grain boundary is represented in Fig.3.10.

The frequency increases from right to left. Together with plotting Z' and $-Z''$, IS results are usually investigated by applying the equivalent circuit. Generally, the equivalent circuit has two series of in-parallel connected R and C elements ($R \parallel C$), representing the bulk and grain boundary (an example is plotted in Fig. 3.10). However, in real cases, the semicircles from the impedance spectra deviate from the ideal model and cannot be fitted with such capacitance elements.

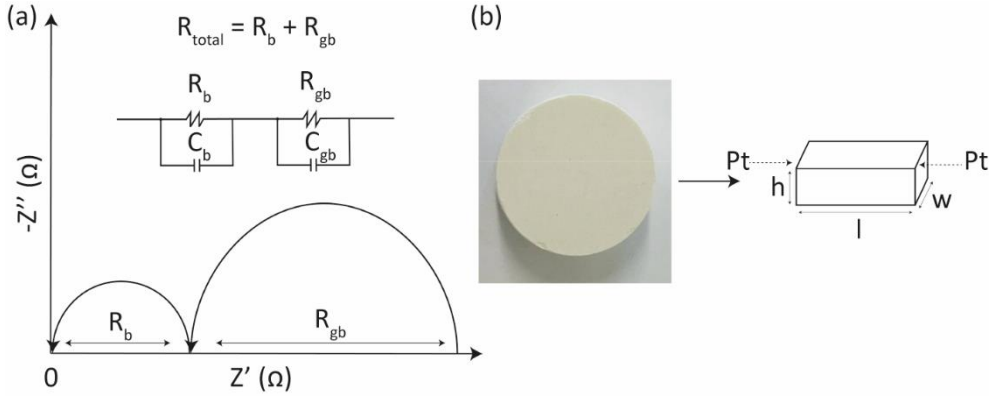


Fig. 3.10. (a) Schematic diagram of the complex impedance plot of ionic conductivity of bulk and grain boundary with an equivalent circuit, (b) the pellet configuration used for measurements

Therefore, constant phase element (*CPE*) can be used instead of at capacitor. The impedance of *CPE* is expressed as follows [254–256]:

$$Z_{CPE} = \frac{1}{(j\omega)^{\alpha} Y_0} \quad (3.33)$$

where Y_0 is the capacitance (C), α is the fitting parameter with values between 0 and 1 ($\alpha = 1$ for the ideal capacitor). For the $R \parallel Y_0$ circuit, the impedance is as follows [254–256]:

$$Z = \frac{R(1 + RY_0\omega^{\alpha}c_{\alpha})}{1 + R^2Y_0^2\omega^{2\alpha} + 2RY_0\omega^{\alpha}c_{\alpha}} - i \frac{R^2Y_0\omega^{\alpha}s_{\alpha}}{1 + R^2Y_0^2\omega^{2\alpha} + 2RY_0\omega^{\alpha}c_{\alpha}} \quad (3.34)$$

where $c_{\alpha} = \cos(\frac{\pi\alpha}{2})$, and $s_{\alpha} = \sin(\frac{\pi\alpha}{2})$.

The resistance values R_b (bulk), R_{gb} (grain boundary), and R_e (electrode) can be obtained from the intercept of the semicircles with Z_{real} (from the fitted IS spectra). When knowing these values, the ionic conductivity can be obtained as follows:

$$\sigma = \frac{h}{RS} \quad (3.35)$$

where h is the distance between the electrodes which should be parallel and congruent (so that to avoid uneven electrical potential distribution), and S is the area of the electrodes.

For ionic conduction in solid state materials, the activation energy can be obtained from the Arrhenius Equation 3.36:

$$\sigma_{total} = \sigma_0 \exp\left(-\frac{\Delta E_a}{kT}\right) \quad (3.36)$$

where σ_0 is the pre-exponential factor, ΔE_a is the activation energy, k is the Boltzmann's constant (0.86×10^{-4} eV K⁻¹). By measuring the conductivity value at different temperatures and plotting $\log \sigma$ against $1000/T$, we obtain the Arrhenius

plot. By using Eq. 3.36 and the Arrhenius plot, the conductivity and activation energy for the bulk and grain boundary can be calculated as well.

The ionic conductivity of SDC and GDC ceramics was measured within the 1 Hz to 1 MHz frequency range over at temperature range from 200 °C to 800 °C with 20 °C increments. Samples for the impedance spectroscopy measurements were cut from annealed ceramic pellets (1200 °C for 2 hours) as rectangular blocks ($5 \times 5 \times 2$ mm³) by using a diamond saw. Platinum electrodes were sputtered by cathodic discharge on polished surfaces for 30 minutes (for each side) in the range of electrical current (15–35 mA). For standard measurements, the impedance spectra were recorded over two cycles of the heating and cooling run at stabilised temperatures. The impedance at each frequency was measured repeatedly until reaching consistency (2% tolerance in FT–IR) was achieved or a maximum number of 25 repeats had been reached [257]. The obtained complex impedance plots were analysed by using the *Z-view* software, which is based on the equivalent circuit method.

3.3.9 X-ray photoelectron spectroscopy

X-ray photoelectron spectroscopy (XPS) is a quantitative technique based on the photoemission effect that can be used to determine the elemental composition of the surface of a material as well as the binding state of the elements. XPS is an ultra-high vacuum technique which typically probes down to 10 nm [258,259]. Surface analysis using elemental sensitivity factors can be performed with 5% relative accuracy and a detection limit of ~0.1% atomic concentration. When X-rays interact with the electrons of the atoms on the surface of the sample, the atoms are photoionized and photoelectrons are emitted. Along with photoionisation, two more processes occur, specifically, X-ray fluorescence and the Auger effect. The ejected electrons and the kinetic energy are measured with an energy analyser. The kinetic energy of the ejected electrons is related to the binding energy of electrons with the following Equation 3.37:

$$BE = hv - KE - \phi_s \quad (3.37)$$

where KE is the kinetic energy of electrons, BE is the binding energy between electrons and the nucleus, ϕ_s is the release function of the spectrometer, which is eliminated during the calibration of the spectrometer. By counting the ejected electrons within the kinetic energy range, a peak in the photoelectron spectrum is recorded, which gives information about the element and its chemical state, as well as the number of the detected elements.

The surface of ceria-based thin films was analysed without surface cleaning on a *Thermo Scientific ESCALAB 250Xi* spectrometer with monochromatised X-rays (AlK α radiation, $h\nu = 1486.6$ eV). For the spectra acquisitions, the x-ray spot size was 0.3 mm, the base pressure in the analytical chamber was 2×10^{-7} Pa, and the transmission energy was 40 eV. The atomic concentrations were calculated by using the *ESCALAB 250Xi Advantage* software and the energy scale was calibrated according to the position of the Cu 2p $_{3/2}$, Ag 3d $_{5/2}$, and Au 4f $_{7/2}$ peaks.

3.3.10 Atomic force microscopy

Atomic force microscopy (AFM) is a high resolution scanning probe microscopy for the quantitative and qualitative analysis of various properties such as the morphology, surface roughness, texture, and size at a sub-nanometer-scale resolution [243,260]. The principle of AFM operation is to scan the sample surface with a sharp tip at the end of a flexible cantilever. During the scanning process, the cantilever is deflected when the tip touches the surface. The deflection is caused by the attractive or repulsive forces between the tip and the sample and is usually measured by reflecting a laser beam off the back of the cantilever into a split photodiode detector [261]. There are three operating modes: contact, non-contact, and tapping. In the contact mode of operation, the constant force of the interactions for the tip and the sample is utilised by maintaining a constant tip deflection. The constant force is determined by Hooke 's law:

$$F = -kx \quad (3.38)$$

where F is the force, k is the elastic constant, x is the cantilever deflection, and the constant forces are usually in the range between 0.01 to 1.0 N/m. Although the contact mode has higher chances to deform the sample surface, it allows achieving atomic resolution and has the fastest scanning time.

In the non-contact mode, the cantilever fluctuates above its resonance frequency, which decreases as the tip approaches the surface. This mode applies less force on the sample, which increases the lifetime of the tip. However, compared to other modes of operation, it usually does not provide very good resolution [261].

During the scanning in the tapping mode, the cantilever oscillates on the surface at its resonance frequency (~300 kHz). When the tip reaches the sample surface the electrostatic force increases and the amplitude of the oscillation decreases. The amplitude of the oscillation is detected by using the laser deflection method, and it provides information about the surface and the type of the scanned material. Although scanning requires a longer time, the tapping mode avoids damage to the surface of the scanning material. Moreover, it eliminates the lateral shear forces which are present in the contact scanning mode [261].

AFM offers a wide range of applications and may be used in various areas as it can operate in many different environments and at ambient temperatures. It can be used to investigate various samples, such as nanoparticles, polymers, semiconductors, biotechnology, and cells. The most common application is morphological studies seeking to understand the topography of a sample [243,261–263].

The morphology, topography, and surface roughness of GDC and SDC thin films on various substrates were analysed by using an *NT-206 (Microtestmachines Co.)* atomic force microscope and the SPM-data processing software *SurfaceXplorer*. The measurement was performed at room temperature in air. A silicon cantilever with a tip curvature radius of 10 nm, a spring constant of 3N/m, and a cone angle of 20° was operating in the contact scanning mode with a 12 µm × 12 µm field of view. From the obtained AFM surface topography images, the

roughness parameters (R_q , R_{sk} , Z_{mean} , and R_{ku}) and surface morphologies of ceria-based electrolyte thin films were investigated.

3.3.11 Raman spectroscopy

Raman spectroscopy is based on the inelastic scattering of photons (the Raman scattering effect) with elemental vibrational excitations in the material. The position and the shape of the bands are determined by the chemical composition and the crystalline structure of the measured samples [264]. When light is scattered by a molecule, the photon's oscillating electromagnetic field induces polarisation of the molecular electron cloud, thus causing the molecule to enter a higher energy state, with the photon's energy being transferred to the [265,266]. This can be viewed as the formation of a very short-lived complex between the molecule and the photon, which is commonly called the virtual state of the molecule which is unstable and the photon is almost immediately re-emitted as scattered light [265,266]. In the vast majority of cases of scattering, the energy of the molecule does not change after the interaction with the photon; and the energy – and hence the wavelength – of the scattered photon is equal to the energy of the incident photon. This is called the elastic or Rayleigh scattering [264–266].

Raman shifts are usually in wavenumbers and inversely proportional to length, since this value is directly related to energy. [264–266]. The spectral wavelength and the shift wavenumbers in the Raman spectrum can be converted by the following formula [264–266]:

$$\Delta\bar{\nu}(cm^{-1}) = \left(\frac{1}{\lambda_0(nm)} - \frac{1}{\lambda_1(nm)} \right) \times \frac{(10^7 nm)}{(cm)} \quad (3.39)$$

where $\Delta\bar{\nu}$ is the Raman shift expressed in the wavenumber (cm^{-1}), λ_0 is the excitation wavelength, and λ_1 is the Raman spectrum wavelength.

For the characterisation of the bonding structure of SDC and GDC thin films on the Si (100) substrate, a *Renishaw inVia* Raman spectrometer equipped with a 532 nm wavelength and 45 mW power excitation laser was used. The measurements were performed within the 100–800 cm^{-1} spectral range with an exposure time of 10 s and 1% of the laser power. The background was subtracted from the obtained Raman spectra and was fitted with Lorentzian- shape lines in the spectral range of 440–490 cm^{-1} .

4. RESULTS AND DISCUSSION

In order to understand which chemical synthesis method is more beneficial for the preparation of ceria-based ceramics and which concentration of the doping component is better, samarium-doped ceria (SDC) nanopowders ($\text{Ce}_{1-x}\text{Sm}_x\text{O}_{2-\delta}$, where $x = 0.1, 0.2$, and 0.3) were synthesised by using the glycine-nitrate precursor combustion, oxalate precursor co-precipitation, and tartrate gel precursor sol-gel chemical synthesis methods. The synthesised materials were investigated by using various analytical techniques, and the results are presented in Subchapter 4.1.

To analyse the properties of gadolinium-doped ceria (GDC) ceramics and compare them with SDC, $\text{Ce}_{1-x}\text{Gd}_x\text{O}_{2-\delta}$, (where $x = 0.1, 0.15$, and 0.2) was synthesised by the glycine-nitrate precursor combustion and oxalate precursor co-precipitation chemical synthesis methods. Further, GDC thin films were formed by using the e-beam (for details, see Subchapter 3.2.1) and reactive magnetron sputtering (for details, see Subchapter 3.2.2) techniques. The influence of various parameters, such as the formation method, additional heat treatment of the films and the concentration of the target material, on the obtained GDC thin films were analysed, and the obtained results are presented in Subchapter 4.2.

In order to test the influence of co-doping on the total ionic conductivity values, ceria was co-doped with Sm and Gd ($\text{Ce}_{0.825}\text{Gd}_{0.0875}\text{Sm}_{0.0875}\text{O}_{2-\delta}$) by using the CB and CP synthesis methods. The obtained results are presented in Subchapter 4.3.

The calcination and annealing conditions were the same for all synthesised materials.

4.1 Samarium-doped ceria

4.1.1 Characterisation of SDC nanopowders

Thermal analysis was used for a detailed investigation of the thermal decomposition behaviour of Sm–Ce–O, Gd–Ce–O (Section 4.2.1), and Sm–Gd–Ce–O (Section 4.3.1) precursors and the crystallisation of the final ceramics. During the thermal treatment, similar processes of the decomposition of the organometallic precursors synthesised by various synthesis methods are observed. However, the results obtained for the crystallisation of the final double oxides differ significantly. This effect is more likely associated with the energy released in the form of heat during the combustion of the carbon-oxygen residue in the precursor powders, which significantly affects the initial crystallisation of the $\text{Ce}_{0.8}\text{Sm}_{0.2}\text{O}_{2-\delta}$ compound. Thermal analysis was performed for all the concentrations of SDC nanopowders; however, the obtained results differ in the synthesis method, regardless of its concentration. Thus, TGA–DTG–DTA of 20 SDC synthesised by CB, CP, and SG methods are presented.

The thermal decomposition of 20 SDC synthesised by the combustion method is relatively simple. It consists of at least three mass changes. A special characteristic for the combustion synthesis reveals the general mass change that consists of only 3.5% and which was estimated in the range of temperature from

26.85 °C to 896.85 °C (Fig. 4.1 (a)). Given the initial composition of the glycine gel precursor, such a small amount of organic matter found after the synthesis procedure is a good result. Nevertheless, judging by the TG curve, this volatile fraction is relatively stable, and further heat treatment only slightly affects its decomposition and combustion. The first significant mass change is directly related to the evaporation of water molecules from the burnt precursor, and it starts at room temperature. This process ends at 248.03 °C and gives a trend to the further decomposition of the gel-residue. The following exothermic event overlaps at about 312.84 °C with the crystallisation of the final compound and continues until the end of the heating of the sample. According to the DTG curve, the crystallisation of the double oxide begins at about 171.42 °C and reaches its peak at 622.05 °C. This temperature range is especially important because of the maximum influence on the crystallisation of the ceramic material and the growth of crystallites.

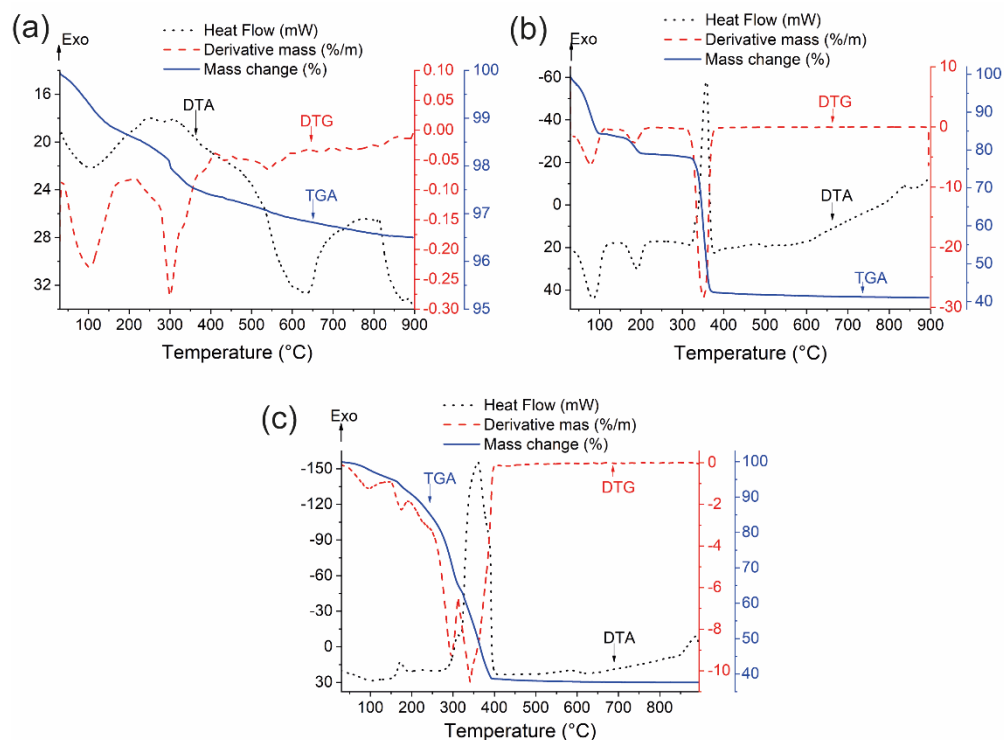


Fig. 4.1. Combined TG–DTG–DSC curves of 20 SDC synthesised by (a) combustion (CB), (b) co-precipitation (CP), and (c) sol-gel (SG) syntheses. Published in [A1, 204]

The decomposition behaviour of the corresponding initial compounds of 20 SDC synthesised by co-precipitation is typical for metal oxalate hydrates (Fig. 4.1 (b)) [267]. In the first step of the heat treatment, water molecules evaporate in the range of temperature from 51.43 °C to 108.10 °C. This endothermic effect can be seen in the DSC curve, with its enthalpy of 284.054 J/g and a peak position at 84.79 °C. Thereafter, the decomposition of the corresponding metal oxalates begins at

163.21 °C, which is confirmed by a well-defined endothermic peak on the DTA curve. The final step of the decomposition of the oxalate precursor occurs at a temperature between 337.42 °C to 368.05 °C. The exothermic effect on the DTA curve shows the decomposition of the formed metal carbonates into the more stable compounds such as CO and CO₂. A further mass change, starting at 377.29 °C, is only 1.34% without any additional clearly pronounced decomposition effects. Such a result predicts a smooth crystallisation process of the final double oxide when increasing the heating temperature [268].

Completely different results of thermal decomposition were observed for 20 SDC synthesised by the sol-gel method when using a tartrate gel precursor (Fig. 4.1 (c)). In this case, the mass change (34.79%) of the gel is characteristic of the decomposition of tartaric acid from 29.85 °C to 311.79 °C [257]. A further increase in the temperature leads to the decomposition of metal tartrates formed during the gelation process, and this process ends at about 391.94 °C. Right after that, the crystallisation of Ce_{0.8}Sm_{0.2}O_{2-δ} double oxide begins. As with CP, after the main decomposition of the gel precursor, a further increase in the heating temperature from 391.94 °C to 699.85 °C leads to only a small mass change equal to 0.87%.

Summarising the results of the thermal analysis, for all the synthesis methods, the decomposition of the corresponding precursors is different up to 896.85 °C. This assumes the possible uneven growth of crystallites and different crystallisation mechanisms in each case for Ce_{0.8}Sm_{0.2}O_{2-δ} ceramics at somewhat higher temperatures.

The elemental analysis of the synthesised powders, evaluated by ICP–OES and EDX, showed that the value of the Sm concentration in Ce_{1-x}Sm_xO_{2-δ}, , approximately coincides with the theoretical value. A summary of the elemental analysis results was published in [A1, 204].

Fig. 4.2. illustrates the XRD patterns of SDC powders without heating and calcined at 800 °C and 1200 °C for 5 h for each of the three routes of synthesis. From the obtained results, SDC, regardless of the synthesis path, is denoted by a phase-pure cubic fluorite structure with the Fm-3m space group (JCPDS No: 75-0158).

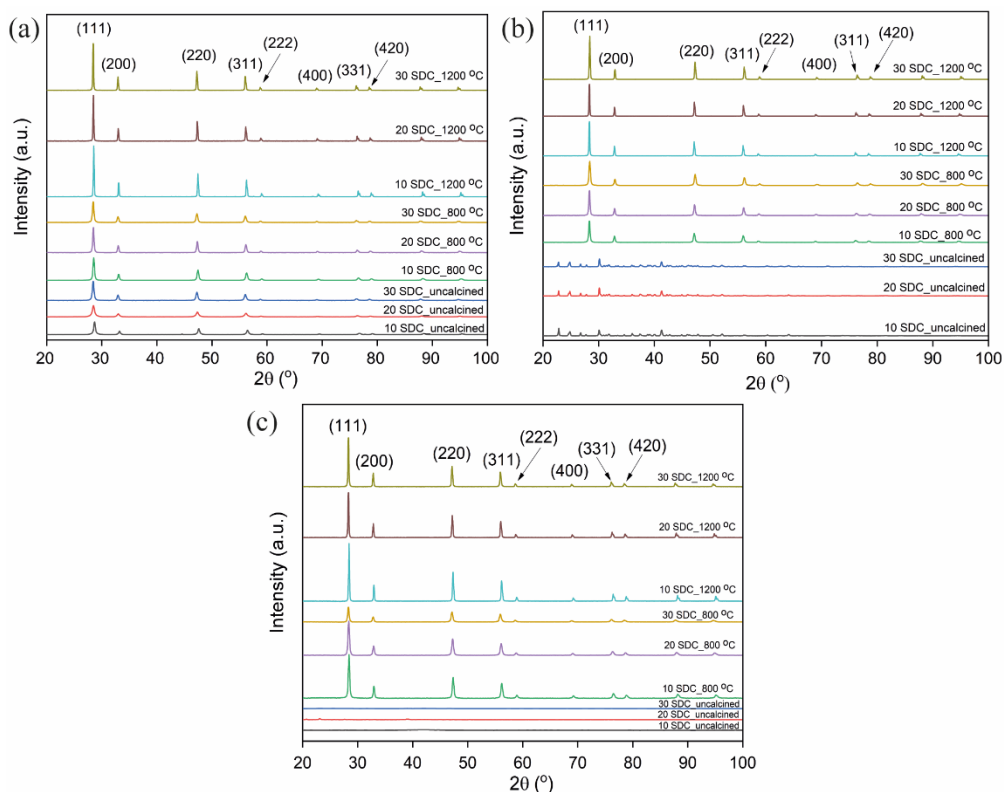


Fig. 4.2. XRD patterns of SDC nanopowders uncalcined, calcined at 800 °C and 1200 °C synthesised by (a) combustion, (b) co-precipitation, (c) sol-gel

In SDC synthesised by CB (111), (200), (220) and (311) diffraction peaks were mostly visible in all the temperature ranges. However, additional diffraction peaks were observed in uncalcined SDC-CP powders. These peaks can be associated with residues of oxalic acid [267] since the detected diffraction peaks are similar to pure oxalic acid [269]. An amorphous phase similar to GDC synthesised by the Pechini method [270] was observed in uncalcined SDC-SG powders. In all the synthesis methods, with an increase in the calcination temperature, the intensity of the diffraction peaks increases, becomes narrow and sharp, which leads to an increase in crystallinity. The calculated crystallite sizes and lattice parameters of the synthesised nanopowders are shown in Fig. 4.3.

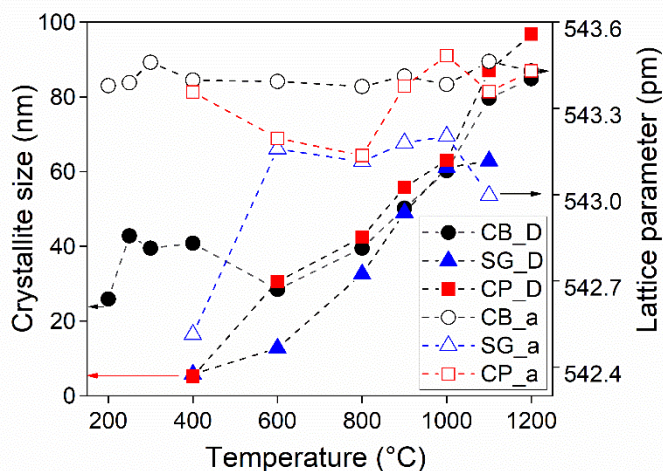


Fig. 4.3. Plot of the crystallite size (D) and lattice parameter (a) vs. calcination temperatures for 20 SDC nanopowders synthesised by various synthesis techniques

As it can be seen from the results obtained from combustion synthesis, the growth of crystallites is strongly accelerated by the temperature and their cooling rate, especially in the range from 126.85 °C to 426.85 °C. This tendency of crystallite growth is strongly influenced by the decomposition of volatile compounds, as shown in the DSC curve (Fig. 4.1 (a)). This exothermic effect slows down the crystallisation process and also destroys the formed crystallites, especially at temperatures above 526.85 °C. Lastly, after the primary exothermic decomposition of volatile compounds, a further increase in the heating temperature determines the usual growth of crystallites across the entire investigated range. Moreover, in the temperature range from 726.85 °C to 826.85 °C, almost the same increase in the crystallite growth is observed in all three cases of synthesis. At higher temperatures, the growth of crystallites occurred faster for CP synthesis; nevertheless, their size distribution varied over a wider range than in the other cases. According to Fig. 4.3, the crystallisation mechanism and the crystallite growth rate are highly dependent on the synthesis route (especially at lower temperatures). With an increase in temperature, the differences in the growth of crystallites tend to disappear; however, their size distribution remains uneven.

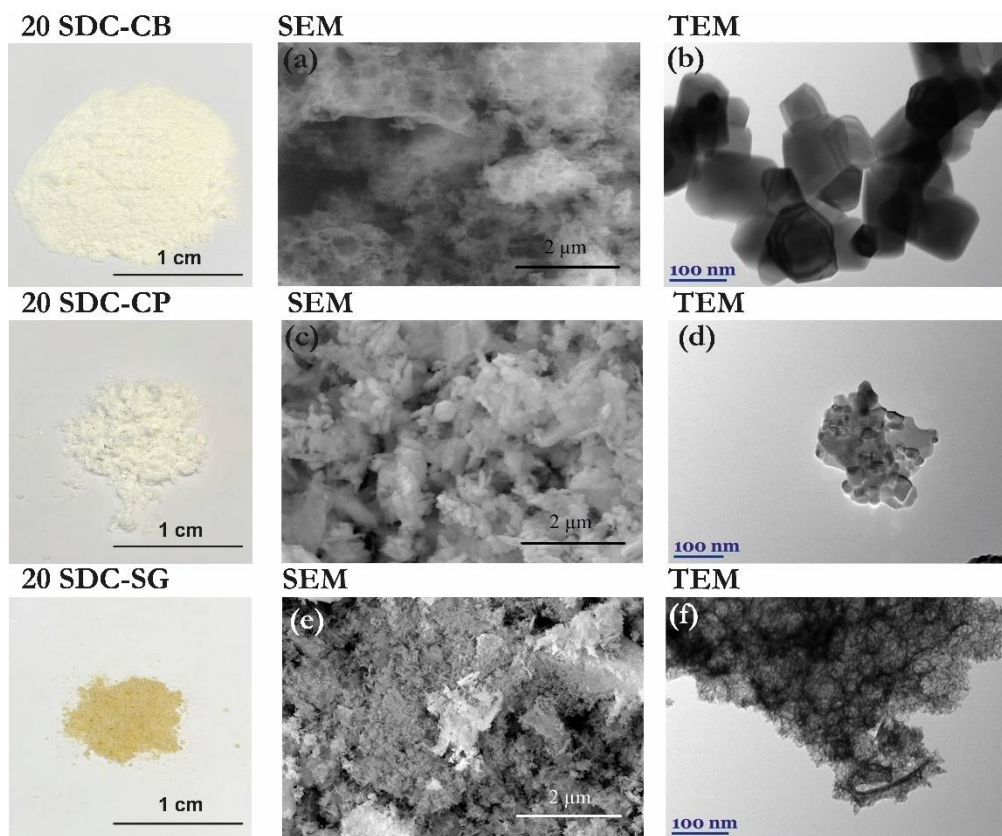


Fig. 4.4. SEM and TEM images of 20 SDC nanopowders calcined at 800 °C, where (a and b) combustion, (c and d) co-precipitation, (e and f) sol-gel syntheses were performed, respectively. The TEM results were published in [A1, 204]

The morphological and structural properties of $\text{Ce}_{0.8}\text{Sm}_{0.2}\text{O}_{2-\delta}$ nanopowders synthesised by different methods and calcined at 800 °C for 5 h were analysed by scanning and transmission electron microscopy (Fig. 4.4). The microstructure of SDC nanopowders consists of uniform particles of a small size. The TEM image of SDC-CB shows porous hermetically assembled nanocrystallites with the average grain size of 90 nm. This can be explained by the fact that radical ignition forms inhomogeneous particles during combustion synthesis [271]. Meanwhile, SDC-CP and SDC-SG are more homogeneous with an average grain size of 36 nm (SDC-CP), whereas it was difficult to determine the grain size for SDC-SG. The SEM image of SDC-CB shows a spongy structure of a low density, while the structure of CP and SG powders is denser with the presence of fragments and protrusions.

The FT-IR spectra of Sm_2O_3 and CeO_2 powders synthesised by the combustion method and calcined at 800 °C are shown in Fig. 4.5. Broad bands in the range of 2500-3800 cm^{-1} are related to the O-H stretching vibration mode and can be attributed either to the water adsorbed on the surface of compounds or to the (Ce or Sm)-OH groups [272,273]. The peaks appearing between 1200 and 1700 cm^{-1} can

be attributed to carbonate species formed on coordinatively unsaturated oxide surfaces, mainly to bicarbonate-like and monodentate carbonate species with O–C–O stretching frequencies [274,275]. Minor peaks around 1050 cm^{-1} (Fig. 4.5 (a)) and 1060 cm^{-1} (Fig. 4.5 (b)) also indicate the existence of the carbonate species, while intense peaks below 770 cm^{-1} appear due to the stretching modes of Ce–O and Sm–O [274].

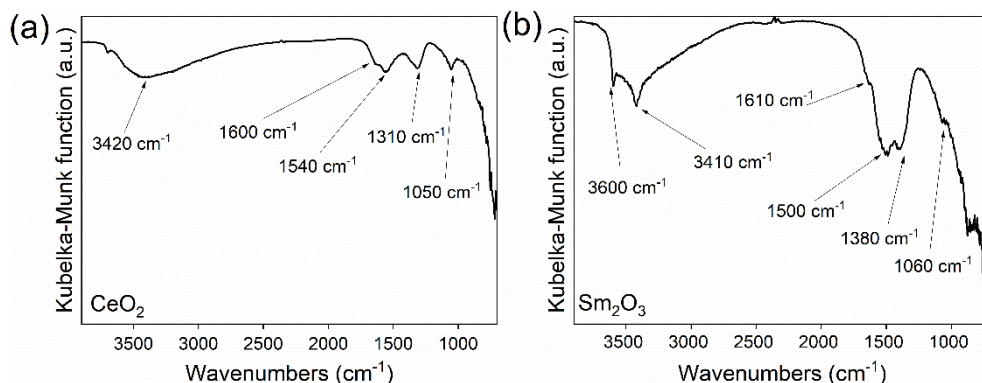


Fig. 4.5. FT-IR spectra of (a) CeO_2 and (b) Sm_2O_3 powders synthesised by the combustion method and calcined at 800°C

The FT-IR spectra of 10 SDC, 20 SDC and 30 SDC can be characterised by the same major features regardless of the synthesis method and concentration, thus only the spectra of 20 SDC synthesised by the CB, CP, and SG methods and calcined at various temperatures are presented (Fig. 4.6). In all the spectra, a broad band was observed in range between 2500–3800 cm^{-1} which can be assigned to the O–H stretching mode of physically adsorbed water [273]. Due to the adsorption of linearly coordinated CO_2 molecules on the surface, a minor band in the range of 2300–2400 cm^{-1} is visible in several spectral lines. Due to the use of organic compounds in all the synthesis methods, the traces of carbonate and bicarbonate are inevitable in the range between 1000–1600 cm^{-1} [274]. SDC-CP has the lowest amount of these residues. Nevertheless, at 200 °C, the nanopowders produced by CP and SG exhibit an intense peak at about 1700 cm^{-1} , which is associated with functional groups containing carbonyl [276].

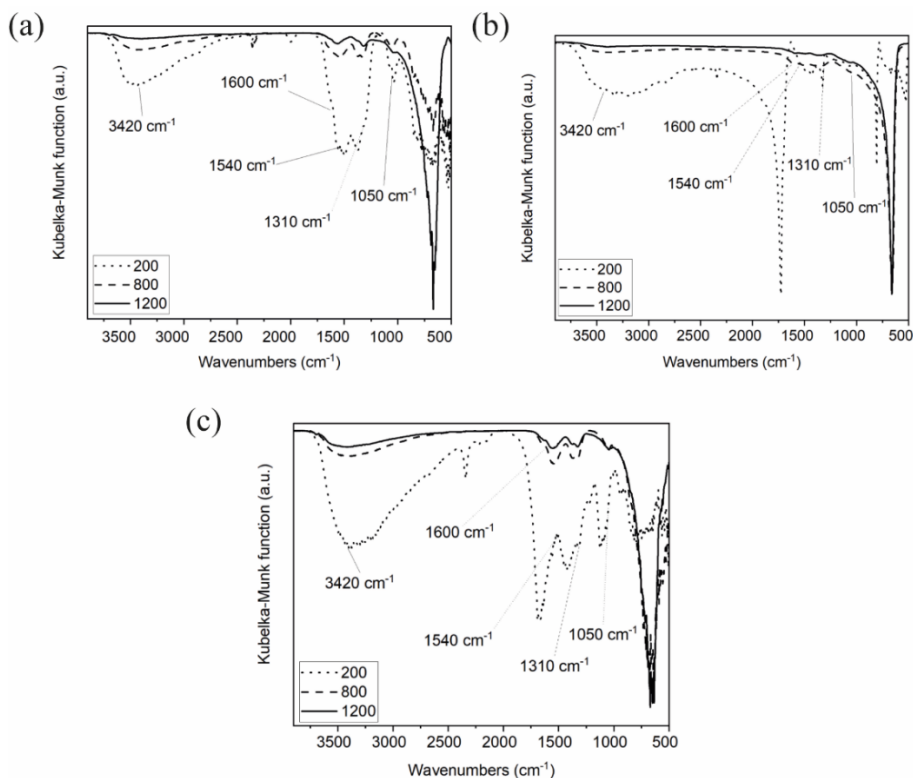


Fig. 4.6. FT-IR spectra of 20 SDC synthesised by (a) combustion, (b) co-precipitation, and (c) sol-gel

In addition, with an increase in the calcination temperature, the intensities of all the bands mentioned above decrease; therefore, the concentrations of the corresponding bonds and the functional groups containing these bonds decrease as well. In all the three spectra, after the final heating, the O–H bond band is virtually absent, which indicates the physical desorption of all water. However, traces of organic residues can still be found after the final calcination, especially in SDC-CB and SDC-SG. Similar results were provided by Mokkelbost *et al.* [272] who, after heating the samples at 1000 °C for 12 h, found traces of organic compounds.

The most important feature of these spectra is a broad intense band below 770 cm^{-1} which is associated with the metal-oxygen bond and corresponds to the phonon mode of CeO_2 [274,277]. This peak increases with an increase in the calcination temperature. This, together with a decrease in the intensities of the residual bond, indicates that the purity of the powders increases with an increase in the calcination temperature.

4.1.2 Characterisation of SDC ceramic pellets

The microstructure of the synthesised pellets, their grain size and distribution, as well as homogeneity affect the ionic conductivity of the material [271,278]. For

example, the grain boundary resistance can increase due to the increased porosity and the low sintering properties of the material [279]. SEM images of the surface and the cross-section of 20 SDC ceramic pellets annealed at 1200 °C for 2 h are shown in Fig. 4.7.

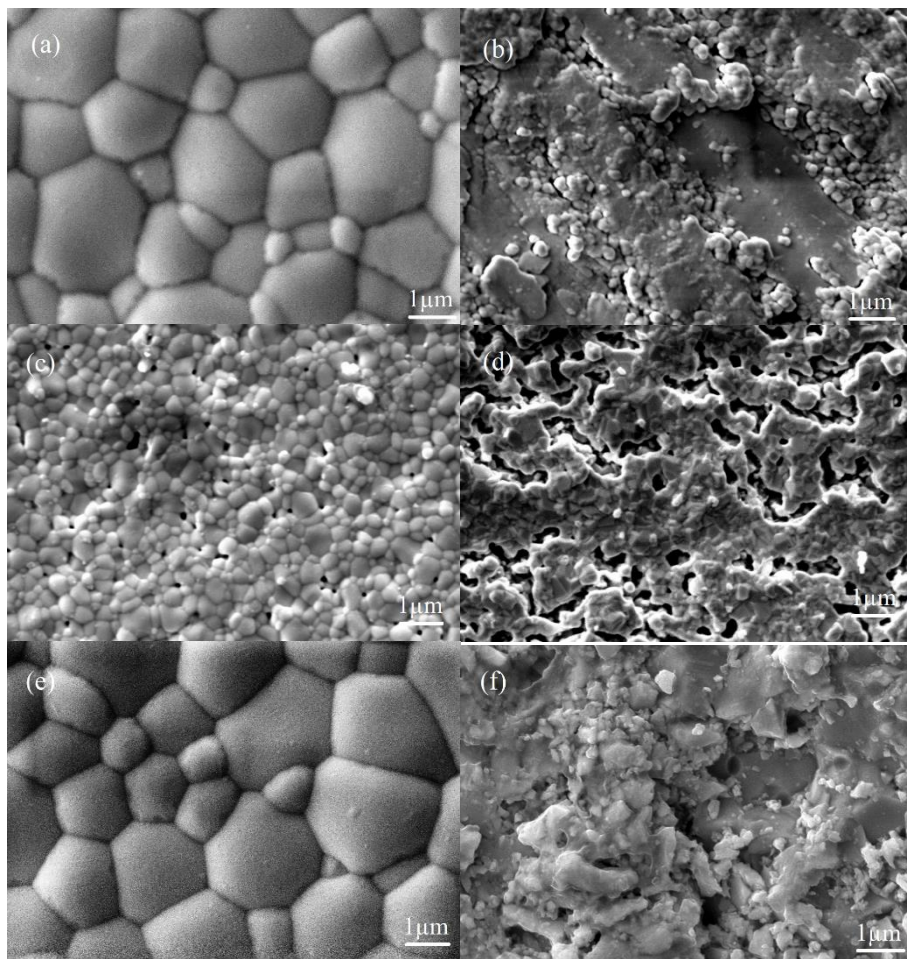


Fig. 4.7. SEM images of the surface (a, c, e) and cross-section (b, d, f) of 20 SDC pellets pressed from (a and b) combustion (CB), (c and d) co-precipitation (CP), (e and f) sol-gel (SG) synthesised nanopowders. Published in [A1, 204]

The surface of 20 SDC-CB and 20 SDC-SG consists of heterogeneous, and unequal in size, spherical grains with an average grain size of 2.1 μm (CB) and 2 μm (SG) and without any cracks and/or gaps (Fig. 4.7 (a, e)). Whereas the surface of 20 SDC-CP is denoted by several small gaps, and it consists of relatively smaller grains with an average grain size of 0.5 μm (Fig. 4.7 (c)). From the cross-section view, we can observe that the structure of 20 SDC-CB is dense and has low porosity (Fig. 4.7 (b)); meanwhile, 20 SDC-CP and 20 SDC-SG exhibit a more porous nature (Fig. 4.7 (d, f)), which might be the result of the insufficient sintering of the samples.

However, compared to 20 SDC-CP, 20 SDC-SG have a denser structure with fewer pores [152].

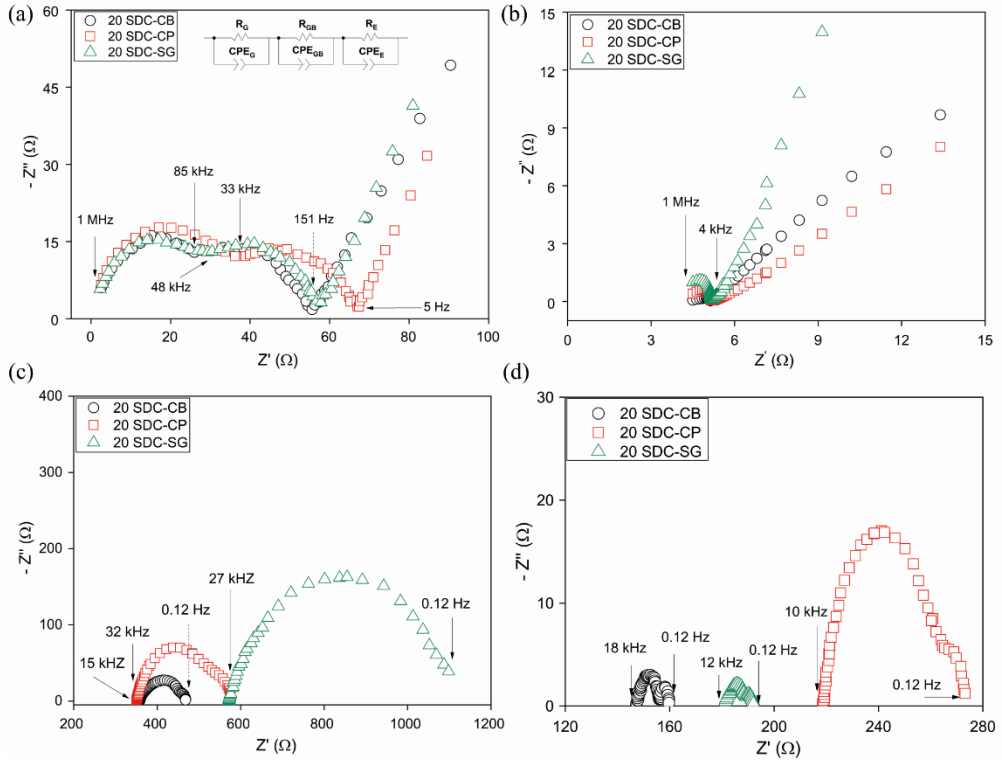


Fig. 4.8. Complex impedance plots at (a) 280 °C, (b) 400 °C, (c) 600 °C, and (d) 800 °C of 20 SDC ceramic pellets synthesised by combustion, co-precipitation, and sol-gel syntheses.

Insert in (a) is an equivalent circuit, where CPE is the constant phase element, R is the resistance for the grain (G), grain boundary (GB), and electrode (E), respectively. Published in [A1, 204]

The results of impedance spectroscopy (which helps to separate grain, grain boundary, and the total ionic conductivities [280,281]) show that all the SDC ceramic pellets, regardless of the synthesis method and concentration of samarium, have different Nyquist plots (complex impedance plots) at various temperature and frequency ranges typical of the SOFC electrolyte (Fig. 4.8.). The resulting arc (semicircle) at the high frequency range is the response from the oxygen ion relaxation in grain (G ; 1st arc), in the intermediate frequency range is the response from the ionic migration in the grain boundary (GB ; 2nd arc) and, in the low frequency range is the response of the electrode (E ; 3rd arc) [152,280,282,283]. The frequency increases from right to left, and every arc can be presented as an equivalent circuit of a parallel-connected resistor (R) and a constant phase element (CPE) corresponding to the grain (G), grain boundary (GB), or electrode (E) [281]. An example of a circuit is shown in (Fig. 4.8 (a)). All three well-defined arcs were observed at 280 °C (Fig. 4.8 (a)), but the grain resistance disappeared as the

temperature increased to 400 °C and 600 °C (Fig. 4.8 (b, c)). The disappearance of the grain and the grain boundary arcs is associated with a shorter polarisation time at a higher temperature than from the electrode [282,284].

At 800 °C (Fig. 4.8 (d)), we observe a splitting of the semicircle corresponding to the electrode response, which can be caused by two separate physical-electrochemical processes occurring in the electrode. This is due to the strong polarisation of the electrodes [280], as well as the formation of an additional diffusion barrier layer between the electrolyte and the Pt electrode during the movement of oxygen ions [283]. As it can be seen, when the temperature increases, the resistance decreases, which leads to an increase in conductivity. According to [280] and the results presented in Fig. 4.8., the grain boundary resistance is calculated with the following Equation 4.1:

$$R_{gb} = R_{23} - R_{12} , \quad (4.1)$$

where $R_{12} = R_g$ is the grain interior resistance, $R_{23} = R_t$ is the total electrolyte resistance. The oxygen ion conductivity in SDC can be calculated by using Eq. 3.34.

From the obtained results, the highest total conductivity value at all temperatures was calculated for 20 SDC synthesised by the combustion synthesis, and it has a maximum value of $3.04 \times 10^{-2} \text{ S} \times \text{cm}^{-1}$ at 800 °C, which is higher than the pellets synthesised by co-precipitation ($2.35 \times 10^{-2} \text{ S} \times \text{cm}^{-1}$) and sol-gel ($2.65 \times 10^{-2} \text{ S} \times \text{cm}^{-1}$). The values of the total ionic conductivity and activation energy of all SDC pellets at various temperatures are shown in Table 4.1. At lower temperatures (400 °C and 600 °C), the total conductivity of 20 SDC-CB is $0.82 \times 10^{-2} \text{ S} \times \text{cm}^{-1}$ and $1.1 \times 10^{-2} \text{ S} \times \text{cm}^{-1}$, respectively. Similarly, Kim *et al.* [271] reported the highest total ionic conductivity for combustion-synthesised samples, and Peng *et al.* [285] also obtained a maximum σ_{total} value of $0.082 \text{ S} \times \text{cm}^{-1}$ at 800 °C for the SDC pellet using the glycine-nitrate process. Wen *et al.* [286] reported a σ_{total} value of $2.24 \times 10^{-2} \text{ S} \times \text{cm}^{-1}$ at 800 °C for the 20 SDC synthesised by co-precipitation. Wattanathana *et al.* [284] obtained $1.86 \times 10^{-2} \text{ S} \times \text{cm}^{-1}$ at 600 °C for 20 SDC synthesised by the thermal decomposition of metal organic complexes; however, the maximum conductivity value was obtained for 15 SDC ($2.06 \times 10^{-2} \text{ S} \times \text{cm}^{-1}$ at 600 °C). The authors state that, due to the formation of the amorphous Sm_2O_3 phase, an increase in the doping concentration leads to a lower value of conductivity.

Table 4.1. Total conductivity and activation energy results of SDC ceramic pellets synthesised by combustion, co-precipitation, and sol-gel

Sample	ΔE_a (eV)		Total conductivity (10^{-2}) ($\text{S} \times \text{cm}^{-1}$)		
	LT	HT	400 °C	600 °C	800 °C
10 SDC-CB	0.81	0.61	0.67	0.71	2.06
20 SDC-CB	0.88	0.77	0.82	1.1	3.04
30 SDC-CB	1.11	0.97	0.031	0.59	1.47
10 SDC-CP	0.84	0.7	0.67	0.79	2.18
20 SDC-CP	0.95	0.8	0.78	0.92	2.35
30 SDC-CP	1.14	0.98	0.038	0.47	1.82
10 SDC-SG	0.92	0.71	0.34	0.7	2.16
20 SDC-SG	0.89	0.78	0.58	0.95	2.65
30 SDC-SG	1.1	0.99	0.078	0.54	1.67

The temperature dependence of ionic conductivity obeys the Arrhenius law (Eq. 3.34), and its plot is shown in Fig. 4.9. However, a break in the slope, resulting in two different temperature ranges (low (LT) and high (HT) temperature ranges), can be observed.

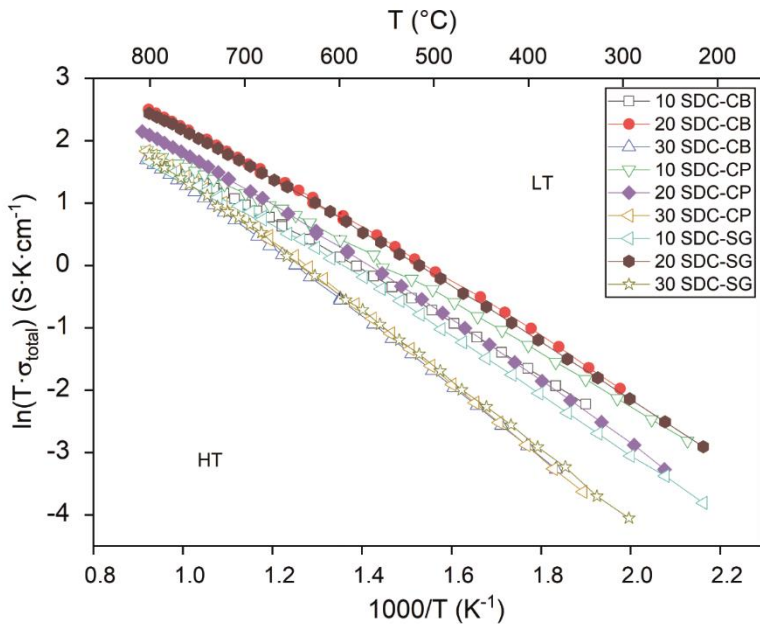


Fig. 4.9. Arrhenius plot of the total conductivity of SDC synthesised by combustion, co-precipitation, and sol-gel syntheses

The presence of the different temperature ranges can be explained by redox reactions occurring in the CeO_2 lattice, or by the thermodynamics of the defect species and their interactions [287,288]. In the low-temperature range, the concentration of the charge carrying defects is determined by its thermodynamic equilibrium and the Coulomb interaction [287]. As the temperature increases, different conduction mechanisms cause a change in the activation energy [147]. In the high-temperature range, the association enthalpy is absent and only migration enthalpy is present, which results in a lower activation energy. The lowest activation energies in both the low-temperature (LT) and high-temperature (HT) ranges were obtained for SDC ceramics synthesised by the combustion method (Table 4.1).

4.1.3 Characteristics of SDC thin films

To investigate the possibility of using the electron beam evaporation technique, 26 SDC ceramic pellets were used as a target material for the formation of thin ceria-based films. The aim was to obtain thin films of certain thicknesses, such as 100, 200, 400, 600, 800 nm, and to investigate the kinetics of the growth of thin films.

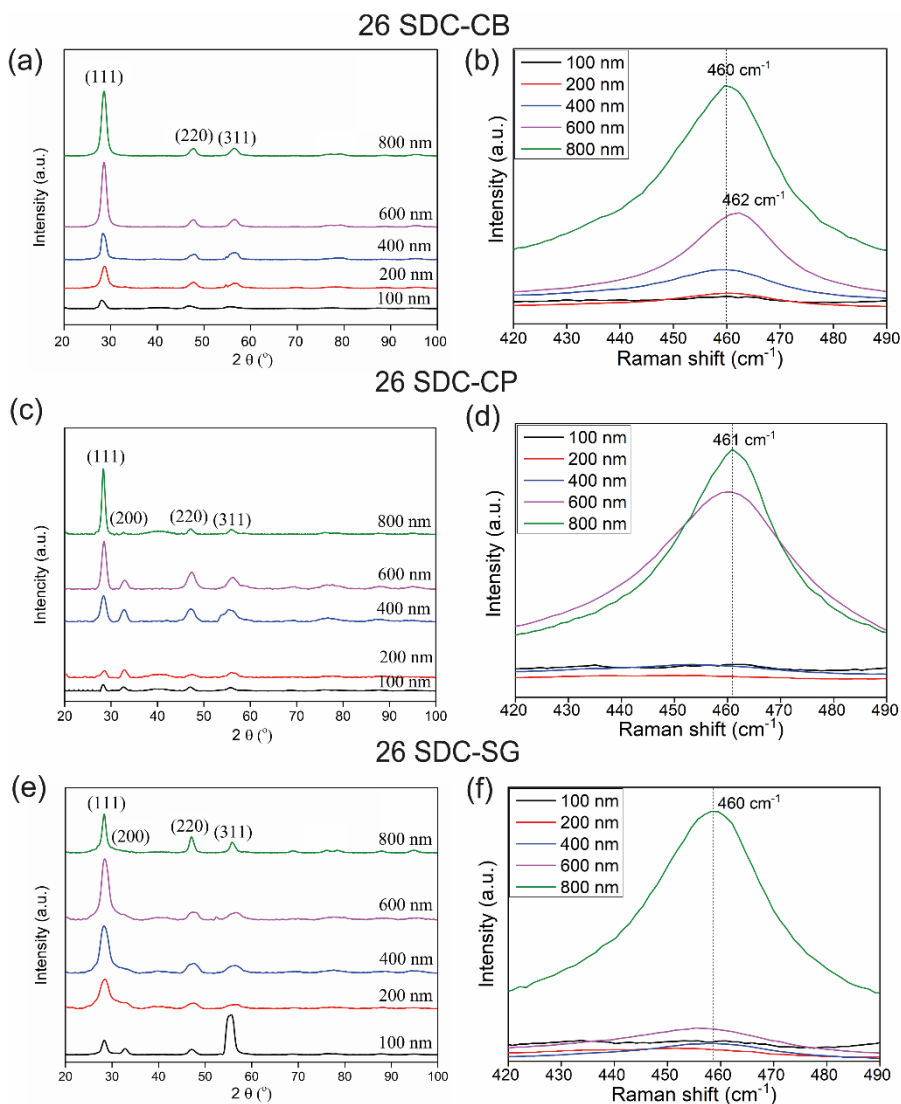


Fig. 4.10. XRD patterns (a, c, e) and Raman spectra (b, d, f) of 26-SDC thin films on the Si substrate with different thicknesses synthesised by (a, b) combustion, (c, d) co-precipitation, and (e, f) sol-gel methods

Fig. 4.10 (a, c, e) shows the XRD results of the films on the Si substrate. Despite the thickness of the films and the synthesis method, all the observed peaks correspond to the fluorite structure. The intensity of the peaks varies with the thickness and the maximum crystallite size was calculated at 800 nm for all films (73.4 nm, 74.2 nm, and 86.7 nm for 26-SDC-CB, 26-SDC-CP, and 26-SDC-SG, respectively). Compared to other films, 26-SDC-CP exhibits additional peaks of crystallographic orientation (200), the intensity of which decreases with the increasing thickness and disappears at 800 nm. 26-SDC-SG 100 nm has an intense

peak of the (311) orientation, which could be a response from the Si substrate. Similarly to XRD results, 800 nm films have the highest peak intensity in the Raman spectra at 460–461 cm^{-1} (Fig. 4.10 (b, d, f)). Due to the symmetrical stretching of the Ce-O vibrational unit in 8-fold coordination, this peak is attributed to the F_{2g} peak of the symmetric breathing mode of the oxygen ion (O^{2-}) around cations [289]. When increasing the thickness, the intensity of the peak increases and it becomes sharper, which shows better crystallinity.

The actual thicknesses of the obtained films were estimated from the results of the scanning electron microscope and did not correspond to the desired values of the thickness (Table 4.2). It is extremely important to control the evaporation conditions. During the evaporation of 26-SDC films, we observed an uneven current flow and the fact that the quartz resonator showed an incorrect value of the thickness. 26-SDC-CB has the largest thickness deviation if compared to CP and SG. The reason for the deviation of the thickness from the expected one could be associated with the flow of the evaporation material which could consist of a single atom and of clusters. The evaporation of a solid solution is a complex process in which many factors can affect the thickness of the resulting film; moreover, this can change its chemical composition. The technical parameters of electron beam technology, such as the power of the electron gun, the substrate temperature, the deposition rate, and the evaporation time, affect the structure, the growth pattern, and the crystallinity of the films. Difficulty can arise when individual components go through the same processing conditions. High vacuum conditions result in a higher evaporation rate.

Table 4.2. SEM estimated SDC thin film thicknesses

Sample	Desired thickness (nm)				
	100	200	400	600	800
	Thickness from SEM analysis (nm)				
26-SDC-CB	95	548	1801	1020	1850
26-SDC-CP	105	333	475	2041	1548
26-SDC-SG	75	356	602	887	1676

Fig. 4.11 shows the SEM and AFM results of 26-SDC-CB, and it can be seen that the obtained SDC films are uniform, dense with no defects and have a rather rough surface. The highest surface roughness (the root mean square, R_q) value of 4.7 nm was calculated for 600 nm, and the lowest values were 2.8 nm for both 100 and 400 nm, respectively. The value of R_q depends on the deposition time at different powers of the electron beam gun [290]. In [290], it is reported that with an increase in the deposition time to 5 s at the initial evaporation stage and a lower e-beam gun power (< 0.66 kW), the surface roughness increases. After 5 s, it begins to decrease, and, after reaching 10 s, it increases again. At a higher gun power, the maximum value of R_q is observed at earlier times (< 5 s). At a later evaporation stage, the roughness of the films increases linearly, which is faster at medium e-beam gun powers [290]. An increase in the e-beam gun power results in an increase in the temperature of the substrate, and, subsequently, in an increase in the flux and kinetic energy of the evaporated particles [194,290].

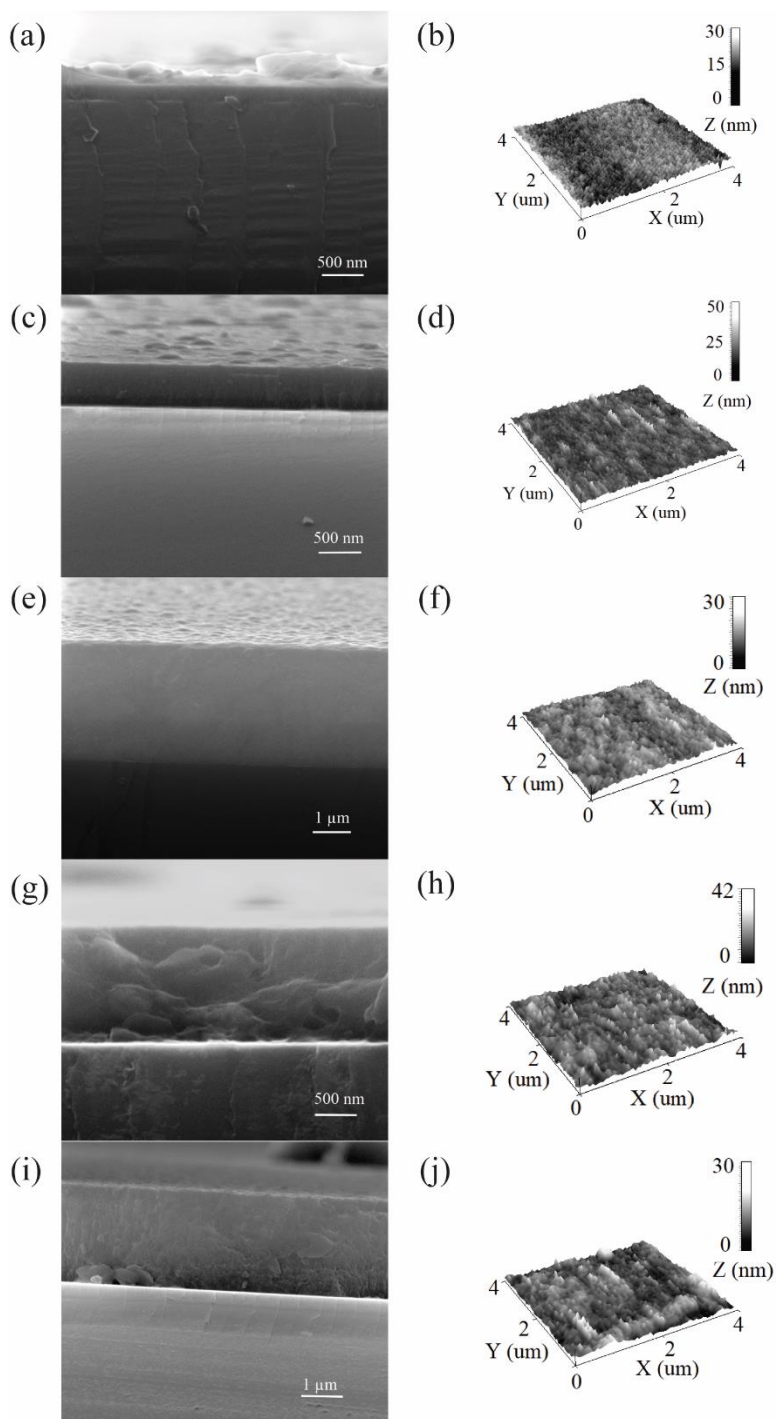


Fig. 4.11. SEM and 3D AFM images of 26-SDC-CB thin films on Si substrate with different thicknesses, where (a, b) 100 nm, (c, d) 200 nm, (e, f) 400 nm, (g, h) 600 nm, (i, j) 800 nm

4.1.4 Summary of the experimental results of SDC

The choice of the chemical synthesis method and its conditions, as well as the starting materials, affects the microstructural as well as electrical properties, and the thermal expansion of ceria-based ceramics. The presented results of the study of samarium-doped ceria ceramics can help to understand and choose a method for synthesising nanopowders with the best and most desired properties. The following conclusions were drawn from the investigation of SDC with various concentration synthesised by CB, CP, and SG:

1. According to thermal analysis, the decomposition of SDC does not differ in its concentration and corresponds to the decomposition behaviour of the precursor used for the synthesis. For each type of synthesis, the crystallisation mechanism and decomposition are different up to 896.85 °C, while the uneven growth of crystallites is possible. Moreover, SDC synthesised by CP and SG becomes thermally stable at about 700 °C, while SDC-CB is quite stable at lower temperatures, and further heat treatment has little effect on its mass change and decomposition.
2. Based on XRD results, compared to SDC-CB, a much higher temperature is necessary to obtain a single phase compound for SDC synthesised by co-precipitation and sol-gel. Moreover, the XRD analysis showed that different synthesis method has different growth of crystallites. For example, at 400 °C, the crystallite size for 20 SDC-CB is 40.80 nm, for 20 SDC-CP, it is 5.19 nm, and for 20 SDC-SG, it is 5.75 nm. At 800 °C, the crystallite size for 20 SDC-CB is 39.50 nm, for 20 SDC-CP, it is 42.46 nm, and for 20 SDC-SG, it is 32.57 nm.
3. According to the FT-IR spectra, with an increase in the calcination temperature, the purity of SDC nanopowders increases, since the peak of the metal-oxygen bond increases, and the peak of the residual bond decreases. However, after the final calcination, residues of organic compounds may still be observed in SDC-CB and SDC-SG.
4. SEM and TEM results have shown that the microstructure of SDC nanopowders consists of homogeneous particles of a small size (~36–90 nm). The SEM images of SDC ceramics showed no impurities or any other defects. The microstructure of 20 SDC-CB is denser with low porosity, and the average grain size is 2.1 µm. Meanwhile, 20 SDC-CP and 20 SDC-SG are denoted by a more porous nature with the average grain sizes being 0.5 µm and 2 µm, respectively.
5. According to the impedance spectroscopy measurement, the maximum value of the total ionic conductivity at all temperatures (the highest value is $3.04 \times 10^{-2} \text{ S} \times \text{cm}^{-1}$ at 800 °C) with the lowest activation energy in both temperature ranges (LT and HT) was obtained for 20 SDC-CB which also had better morphological properties compared to the other ceramics.
6. The synthesised SDCs were used as a target material to form thin films by using the electron beam evaporation technique. According to the SEM results, we observe deviation in the thicknesses. To obtain the desired thickness, the values

on the quartz crystal deposition controller should be about half as much, hence it will take less time to evaporate.

7. Summarising the obtained experimental results, ceramics synthesised by the combustion method showed the best properties. With regard to concentration, the conductivity increases with an increasing SDC concentration and reaches its maximum at 20 mol%. A further increase leads to a drop in the conductivity value. Thus, for the preparation of gadolinium-doped ceria, Gd concentrations were chosen up to 20 mol%, such as 10, 15, and 20 mol%. Combustion and coprecipitation were chosen as the synthesis methods since these methods are cheaper and easier to implement, and the materials offer superior properties if compared to sol-gel.

4.2 Gadolinium-doped ceria

4.2.1 Characterisation of GDC nanopowders

The thermal decomposition process reveals and characterises the individual characteristics of each sample prepared according to a specific synthesis method. The starting intermediate of the combustion synthesis (Fig. 4.12 (a)) shows that the decrease in the sample mass is more or less gradual, with the exception of the ranges between 30–150 °C and 250–350 °C. The first significant increase in the mass change of about 0.2–0.25% is related to the evaporation of moisture that was absorbed by the sample prior to the measurement. This process is confirmed by the DTA curve, which shows a clearly pronounced endothermic peak at the investigated stage. A further increase in the temperature leads to slow partial evaporation of the organic residue in the ceramic sample. The broad endothermic band on the DTA curve from 190 °C to 450 °C can be attributed to this process. This means that at this temperature stage, the release of a gaseous residue of hydrated carbon, which was formed during the combustion of the glycine nitrate precursor, is observed. The elongated endothermic behaviour of the DTA curve and the relatively wide temperature range confirm this conclusion. A small and broad exothermic peak in the temperature range from 360 °C to 500 °C suggests that this evaporation process competes with the partial oxidation of organic residue to carbon monoxide. The final mass change is approximately 0.25–0.5% of the total 0.45–0.75% and reflects the final purification of the ceramic phase from organic side phases. The broad endothermic band on the DTA curve from 450 °C to 800 °C corresponds to the onset of crystallisation of the final ceramic compound. It is also of interest to note that the increase in the sample mass, which begins at about 730–750 °C, is associated with the absorption of oxygen atoms from the air. This process is confirmed by a small endothermic peak in the DTA curve which is observed in the temperature range from 870 °C to 890 °C.

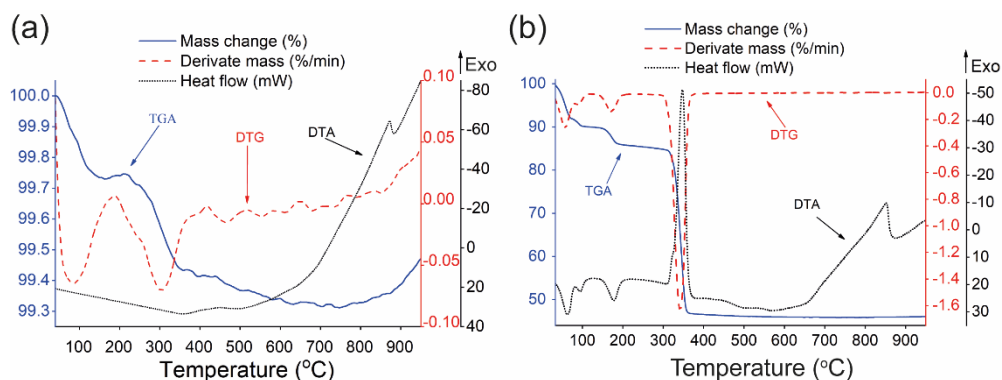


Fig. 4.12. Combined TGA–DTG–DTA curves of 10 GDC synthesised by (a) combustion (CB) and (b) co-precipitation (CP) syntheses. Figure (b) was published in [A3, 315]

In contrast to the CB synthesis, the mass change for sample precursors obtained during the co-precipitation (Fig. 4.12 (b)) method is significantly larger. The decomposition of the co-precipitation precursor is associated with the decomposition behaviour of hydrated oxalic acid. In the temperature range from 30 °C to 100 °C, the evaporation of water molecules with a mass change of about 12–13% was observed, which is confirmed by a strong endothermic peak on the DTA curve. A further increase in the temperature to 190 °C with a bright endothermic effect on the DTA curve is associated with the melting and partial decomposition of oxalic acid with the mass change in the sample of about 4–5%. The last mass change in the range from 310 °C to 370 °C is due to the final decomposition of the initial metal oxalate precursor. Approximately 38% of the mass change and the strong exothermic peak on the DTA curve can be attributed to the release of carbon dioxide whose formation is facilitated by the redox properties of ceria. In addition, as well as with CB, there is also a slight increase in the mass (0.16%) above 800 °C. This effect reflects an endothermic peak on the DTA curve within the temperature range from 850 °C to 950 °C. As we can see from the obtained results, the final tendency of the crystallisation of mixed oxide at elevated temperatures depends only on the sizes of crystallites, which were formed at approximately 400 °C. Moreover, the thermal decomposition of volatile organic impurities and the crystallisation of the double oxide are more dependent on the CP precursor than in the case of CB.

The X-ray diffraction patterns of GDC nanopowders calcined at various temperatures are presented in Fig. 4.13.

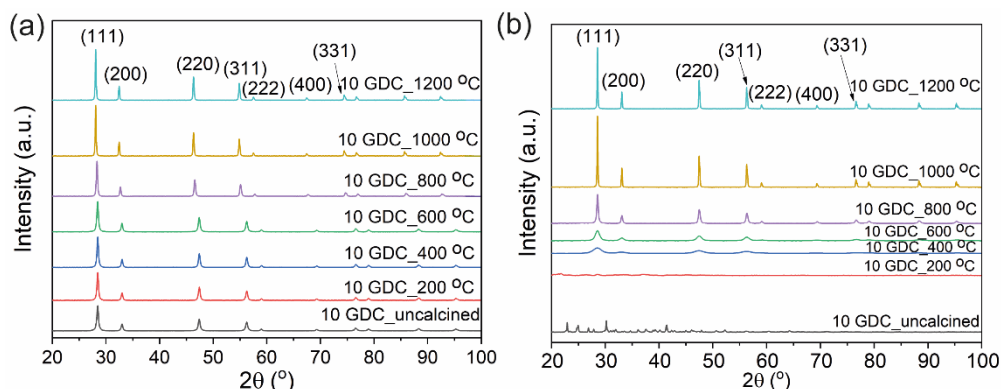


Fig. 4.13. XRD patterns of 10 GDC nanopowders synthesised by (a) combustion and (b) co-precipitation calcined at various temperatures

The obtained results show that GDC nanopowders feature a cubic fluorite crystalline lattice with an Fm-3m space group and the dominating (111) crystallographic plane. As in SDC-CP, we can observe additional peaks in GDC-CP corresponding to the remnants of oxalic acid. The cubic structure of 10 GDC-CB begins to form from uncalcined nanopowders, while for GDC-CP, it requires a higher calcination temperature (400 °C). Li *et al.* [246] found that the grain growth of CeO₂ ceramics is effectively suppressed by doping with both Sm³⁺ and Gd³⁺; however, the crystallite size increases with an increase in the calcination temperature. The calcination of ceramics depends on the diffusion processes combining individual powder grains into one cohesive material. Thus, with an increase in the calcination temperature, the intensity of the well-defined diffraction peaks increases, and the broadening decreases, which indicates an increase in crystallinity. The temperature dependence of the calculated crystallite sizes (see Eq. 3.24) and the lattice parameters (see Eq. 3.25) of the synthesised nanopowders are plotted in Fig. 4.1. As it can be seen, the tendency of the crystallite growth is similar to that in the case of SDC-CB and SDC-CP. However, the crystallite sizes and the lattice parameters of GDC nanopowders are smaller than those of SDC, since the ionic radius of Sm³⁺ (1.079 Å) is larger than the ionic radius of Gd³⁺ (1.053 Å) [291]. The lattice parameter of 10 GDC-CB decreases between the calcination temperatures from 600 °C to 1000 °C, and at higher temperatures, the lattice growth stabilises. Such results can be associated with an insufficient calcination temperature and incomplete formation of oxides. In the case of 10 GDC-CP, the lattice parameter gradually increases with an increase in the calcination temperature.

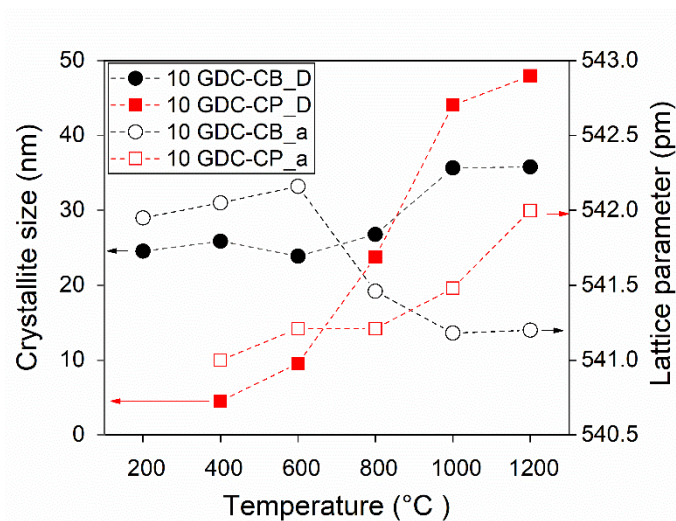
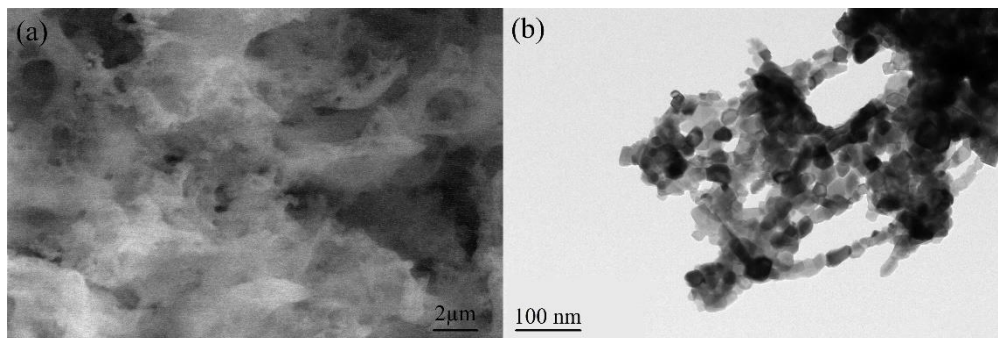


Fig. 4.14. Plot of the crystallite size (D) and lattice parameter (a) vs. calcination temperatures for 10 GDC nanopowders

The ICP–OES and SEM/EDS results of elemental analysis showed that the chemical composition of the obtained materials is controlled by the composition of the solution for synthesis. Moreover, the compaction of nanopowders during the calcination process can affect the properties of the ceramics.

Based on the morphological properties obtained by SEM, 10 GDC-CB (Fig. 4.15 (a)) shows a foamed structure similar to 20 SDC-CB (Fig. 4.4 (a)) which is typical of powders obtained by combustion synthesis. However, the TEM results show that the average size of nanoparticles is 24 nm, which is ~4 times smaller than 20 SDC-CB. In the case of 10 GDC-CP, the nanopowders are a coarse rod-ribbon microstructure typical of powders formed by CP, with an average size of nanoparticles of 23 nm (Fig. 4.15 (c)). Similar results for CP and CB were obtained by Zha *et al.* [292] who stated that, after further processing, the foamed structured powders can be used for the formation of an electrode. The TEM results of both ceramic nanopowders showed that they consist of small particles and are denoted by porous nature. Similar results were obtained for all GDC concentrations.



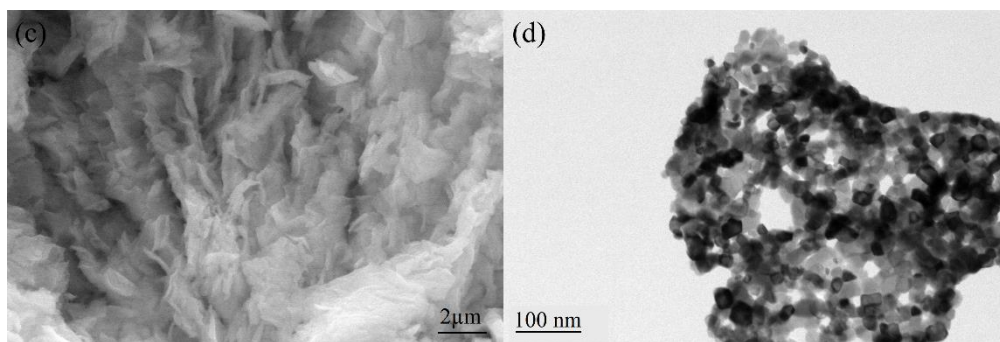


Fig. 4.15. SEM and TEM images of 10 GDC nanopowders synthesised by (a and b) combustion and (c and d) co-precipitation synthesis methods and calcined at 800 °C

The obtained FT-IR spectra of all GDC (CB and CP) show the same major peaks with the same tendency as SDC (Fig. 4.16). However, compared to SDC, the GDC peaks are less intense even at low temperatures, which indicates better purity of the powders. For example, the intensities of the peaks corresponding to traces of carbonate and bicarbonate (in the range between 1000–1600 cm^{-1}) and the O–H stretching mode (in the range between 2500–3800 cm^{-1}) are more intense for SDC nanopowders at all temperatures than for GDC.

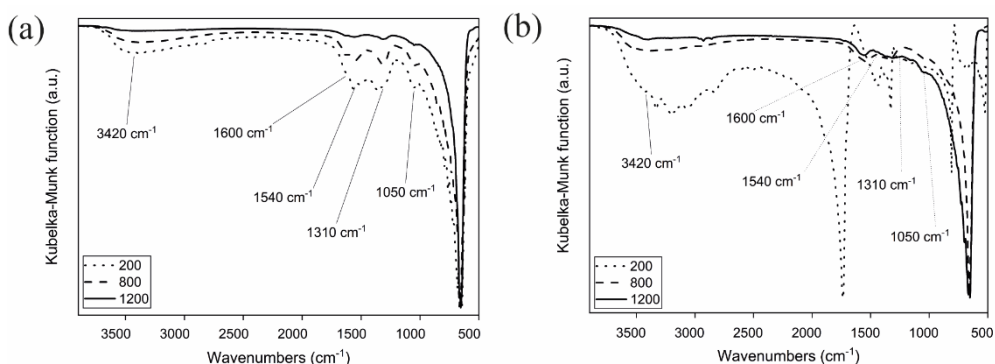


Fig. 4.16. FT-IR spectra of 10 GDC synthesised by (a) combustion and (b) co-precipitation

The peaks corresponding to the adsorption of CO_2 molecules on the surface of the powders (2300–2400 cm^{-1}), which are visible in several SDC spectra, are absent in GDC; moreover, after the final calcination, the intensity corresponding to organic residues is almost gone. The CeO_2 band increases with the increasing calcination temperature, and the absence of other peaks at higher temperatures confirms the purity of GDC nanopowders.

4.2.2 Characterisation of GDC ceramic pellets

The microstructure of the ceramic pellets and its sintering quality are important factors for the analysis of ionic conductivity. Burcu *et al.* [279] found that grain boundary resistances increase due to the low sintering capacity and increased

porosity in SDC electrolytes. The sintering capacity depends on the sintering time and temperature, the diffusion coefficient of atoms and the particle size. When powders are calcined, individual grains grow together, which helps to reduce the porosity of ceramics from 30–50% to merely a few percent. For the SEM measurement, pellets were broken in half, and, due to the roughness of the surface after the fracture, the sides were polished, cleaned with ethanol, and thermally etched at 1100 °C for 1 h. Fig. 4.17 presents a SEM image of the surface of GDC pellets annealed at 1200 °C for 5 h.

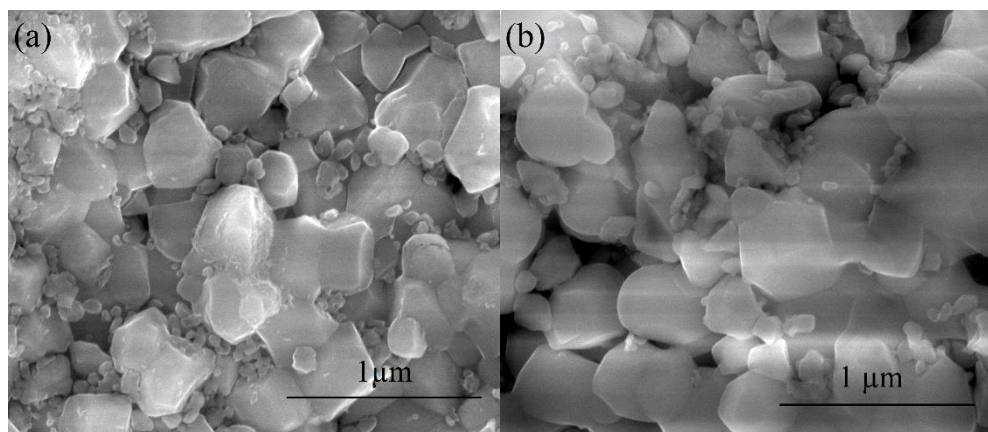


Fig. 4.17. Surface view of 10 GDC synthesised by (a) CP and (b) CB annealed at 1200 °C. Figure (a) was published in [A3, 315]

As it can be seen, GDC pellets consist of grains of various sizes with an average grain size of 0.32 μm (10 GDC-CP) and 0.307 μm (10 GDC-CB). The distribution of grains is uneven yet dense, without porosity, defects, and cracks.

The obtained complex impedance plots of GDC ceramics at various temperature and frequency ranges are presented in Fig. 4.18. It can be seen that with an increase in the concentration of Gd in GDC, the total resistance of the pellets also increases. Thus, 20 GDC have the highest value of the total resistance resulting in the lowest ionic conductivity at all temperature ranges, while the lowest resistance and the highest conductivity were obtained for 10 GDC. With an increasing temperature, we observe a decrease in resistance; therefore, conductivity increases. Koettgen *et al.* [41] compared the values of the bulk and the grain boundary conductivity GDC and SDC of various concentrations synthesised by the sol-gel method, and the highest bulk conductivity was found for $\text{Ce}_{0.93}\text{Sm}_{0.07}\text{O}_{1.965}$, which led to the maximum total conductivity. The authors reported the same tendency when the conductivity increased with an increase in the dopant to a certain value and subsequently decreased with a further increase in the dopant fraction [41]. As in SDC ceramics (see Subchapter 4.1.2), the highest σ_{total} was obtained for 20 SDC-CB, and the values of all the synthesised SDCs increased until $x = 0.2$ and decreased at 0.3.

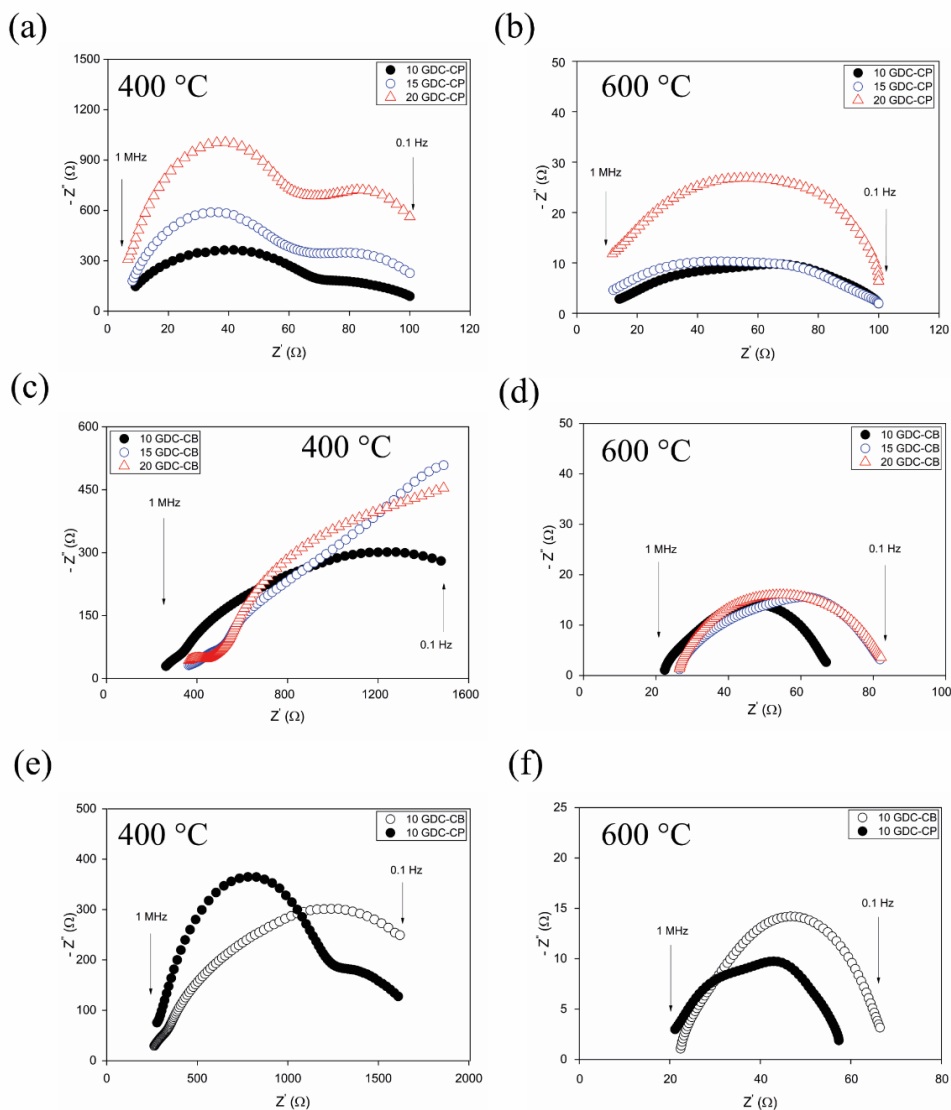


Fig. 4.18. Complex impedance plots of (a), (b) GDC-CP; (c), (d) GDC-CB; and (e), (f) 10 GDC synthesised by combustion and co-precipitation at 400 °C and 600 °C

The Arrhenius plot with the temperature dependences of the total ionic conductivities is shown in Fig. 4.19, where, due to redox reactions in the ceria lattice [287], a similar break in the slopes is observed as in the SDC ceramics.

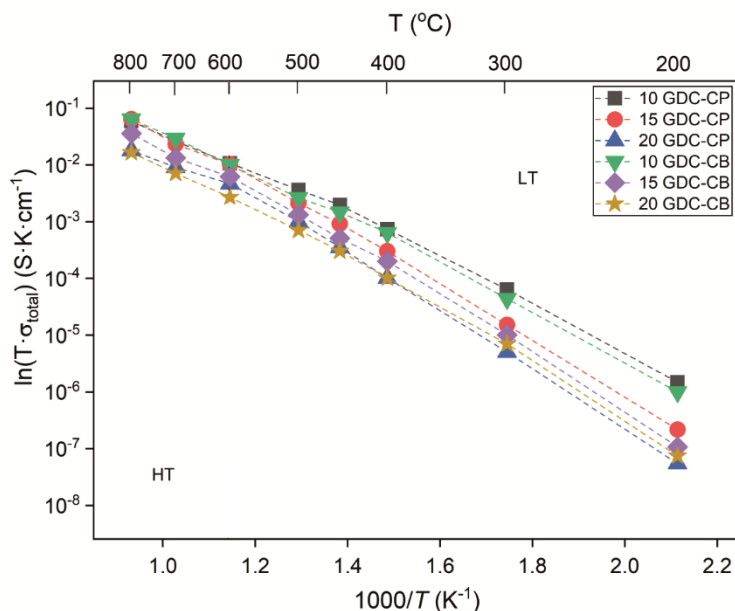


Fig. 4.19. Arrhenius plot of total conductivity for GDC synthesised by combustion and co-precipitation

The activation energies (ΔE_a) determined from the Arrhenius plots and the total ionic conductivity at 600 °C are shown in Table 4.3.

Table 4.3. Values of the activation energy at low (LT) and high (HT) temperature ranges and the total conductivity of GDC ceramic pellets. Results of the GDC-CP were published in [A3, 315]

Sample	ΔE_a (eV)		Total conductivity (10^{-2}) ($S \times cm^{-1}$)		
	LT	HT	400 °C	600 °C	800 °C
10 GDC-CP	0.85	0.67	0.07	1.1	5.9
15 GDC-CP	0.95	0.80	0.03	1	6.3
20 GDC-CP	0.99	0.85	0.01	0.5	1.8
10 GDC-CB	0.85	0.72	0.06	1	6
15 GDC-CB	0.92	0.84	0.02	0.8	5.5
20 GDC-CB	0.96	0.86	0.01	0.3	1.7

From the results shown in Fig. 4.19 and Table 4.3, we can observe a decrease in ΔE_a in the high-temperature range of all the concentrations of GDC. As in the case of SDC, this decrease is due to the absence of the association enthalpy at HT [272]. With an increase in the molar concentration of GDC, the activation energy increases and the total conductivity decreases, as well as the bulk and grain boundary conductivity. Thus, at 600 °C, 10 GDC-CP and 10 GDC-CB have the highest total ionic conductivity of $1.1 \times 10^{-2} S \times cm^{-1}$ and $1 \times 10^{-2} S \times cm^{-1}$, respectively. The activation energy at LT is 0.85 eV for both 10 GDC-CP and 10 GDC-CB; however, at HT, 10 GDC-CP has a lower value (0.65 eV) than 10 GDC-CB (0.72 eV). Fuentes

and Baker [293] obtained the same results for $\text{Gd}_{0.1}\text{Ce}_{0.9}\text{O}_{1.95}$ synthesised by a sol-gel ($\sigma_{\text{total}}=0.011 \text{ S}\times\text{cm}^{-1}$ at 600°C). Faruk Öksüzömer *et al.* [294] investigated $\text{Gd}_{0.1}\text{Ce}_{0.9}\text{O}_{1.95}$ and $\text{Gd}_{0.2}\text{Ce}_{0.8}\text{O}_{1.9}$ synthesised by the polyol process and obtained a higher conductivity of $0.0211 \text{ S}\times\text{cm}^{-1}$ at 800°C with low activation energies for 10 GDC.

4.2.3 Characterisation of GDC thin films

4.2.3.1 GDC thin films obtained by the electron beam evaporation technique

The synthesised $\text{Ce}_x\text{Gd}_{1-x}\text{O}_{2-x/2}$ pellets were evaporated on various substrates by using the e-beam technique. To investigate the effect of additional thermal treatment on the properties of thin GDC films, they were annealed at several temperatures ($600, 700, 800$, and 900°C) for 1 h. The results of the chemical composition of Gd_2O_3 in GDC thin films are summarised in Table 4.4.

Table 4.4. Chemical composition of evaporated GDC thin films obtained from XPS and ICP–OES measurements. Results of the GDC-CP were published in [A3, 315].

Notation	Gd content in thin film from ICP–OES (r.u)	Gd content in thin film from XPS (r.u)	Molar content of Gd_2O_3 in thin film (mol%)	Decrease of the molar content of Gd_2O_3 in thin film (%)
10-GDC-CP	0.13	0.13	6.90	31.0
15-GDC-CP	0.21	0.20	11.3	24.7
20-GDC-CP	0.27	0.26	14.4	28.0
10-GDC-CB	0.13	0.13	7.10	29.0
15-GDC-CB	0.21	0.20	11.4	24.0
20-GDC-CB	0.26	0.26	14	30.0

The results show that the chemical composition of GDC thin films is, on average, 28% lower than that of the target material used in the e-beam process (Table 4.4). As we can see, thin films evaporated from 15 GDC ceramics provide the formation of a 10-GDC thin film, the target of which (10 GDC ceramic pellet) has the highest ionic conductivity value [295]. The evaporation of at solid solution is a complex process and there are many factors which may influence the change in the chemical composition of thin films [296]. The difficulty arises when individual components denoted by different evaporation temperatures and evaporation rates, go through the same process conditions. The following equation can be used to determine the evaporation rate [295,296]:

$$F_{\text{max}} = 0.058p_v\sqrt{\frac{M}{T}} \quad (4.2)$$

where F_{max} is the evaporation rate in $(\text{g}/\text{cm}^2 - \text{s})$, p_v is the vapour pressure, M is the molecular mass, and T is the temperature. High vacuum conditions result in higher evaporation rates. Different elements evaporate at different evaporation rates during

the process; for example, metals evaporate as a function of the temperature and the vacuum level. Thus, the chemical composition of the resulting condensed material may differ from the target material used for the evaporation.

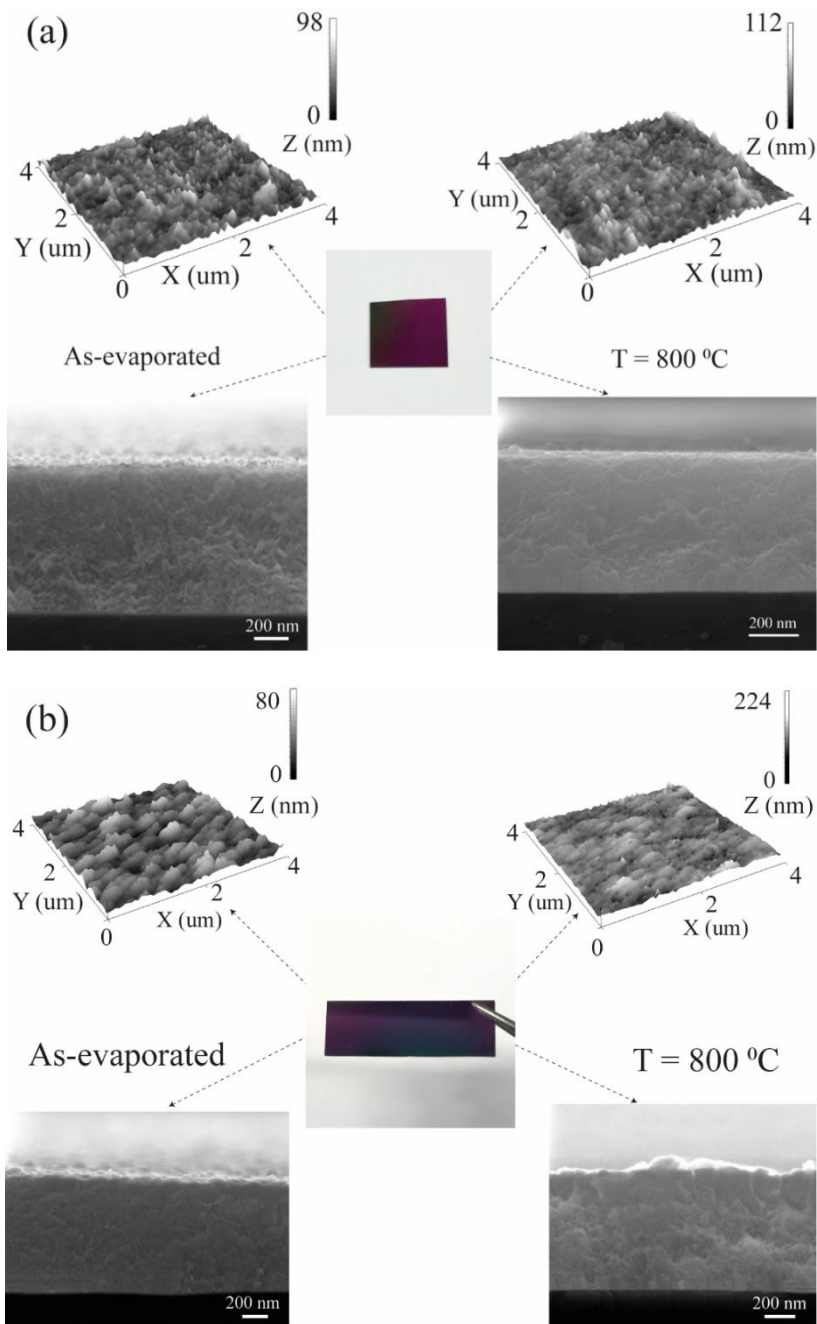


Fig. 4.20. Photo, SEM, and 3D AFM images of (a) 10-GDC and (b) 15-GDC thin films as-evaporated (left) and annealed at 800 °C (right). Published in [A3, 315]

The morphology and the surface roughness of GDC thin films are presented in Fig. 4.20. According to the SEM results, the annealing of the films insignificantly affected their morphology; the thickness varied slightly depending on the annealing temperature but was ~ 800 nm. As it can be seen, GDC-CP films are dense, and they contain nanoscale grains. However, the roughness changes with the increasing annealing temperature; the surfaces of the films are spiky (roughness kurtosis (R_{ku}) above 3 nm) and relatively rough. The results of the roughness parameters calculated from AFM images are shown in Figure 4.21 and summarised in Table 4.4.

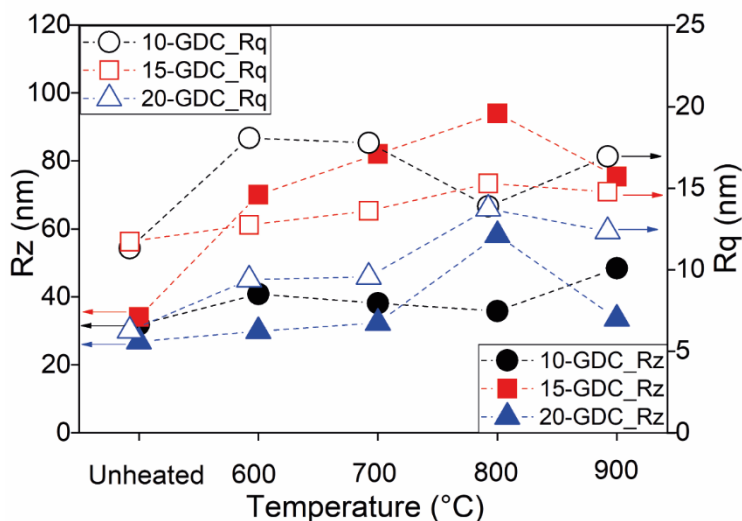


Fig. 4.21. Surface roughness parameters calculated from the AFM images of GDC-CP thin films as-evaporated and after additional thermal treatment at 600 °C, 700 °C, 800 °C, 900 °C for 1 h where R_q (the empty figures) is the root mean square and R_z (the filled figures) is the average height

The root mean square values (R_q) of 10-GDC-CP fluctuate with the annealing temperature and have their maximum value at 600 °C (18.08 nm), while the lowest value of 11.32 nm is delivered by the as-evaporated film. Overall, a different tendency of R_q was observed for 15-GDC-CP and 20-GDC-CP, values of which increase with the increasing annealing temperature, thus reaching a maximum point of 15.29 nm (15-GDC-CP) and 13.74 nm (20-GDC-CP) at 800 °C. The average roughness (R_a) values show the same trend as R_q for all the GDC-CP thin films (Fig. 4.19). When increasing the annealing temperature, the mobility of atoms increases, thus causing agglomeration of the particles and an increase in the particle size, which leads to an increase in roughness [297,298].

The obtained results of Raman spectroscopy (Fig. 4.22) showed a major peak at 463 cm^{-1} for all the GDC thin films. Films of pure CeO_2 , annealed at 600 °C, have a main peak at around 475 cm^{-1} which is ascribed to the symmetric breathing mode of oxygen atoms around CeO_2 (F_{2g} symmetric vibration), and films of pure Gd_2O_3 , annealed at 600 °C, show a peak at $\sim 360\text{--}370\text{ cm}^{-1}$, corresponding to the F_{2g}

symmetric vibration of Gd-O [299,300]. However, in the obtained GDC thin films (Fig. 4.22), the vibration mode of Gd-O is absent, which indicates the formation of a single phase. According to Prasada *et al.* [301], the formation of a single cubic phase of GDC occurs when Gd_2O_3 decomposes into the CeO_2 structure by partly substituting Ce^{4+} ions with Gd^{3+} , which leads to a shift of the F_{2g} symmetry. The resulting GDC peak at 463 cm^{-1} can be associated with the symmetric vibration of Ce-O with a shift of $\sim 12\text{ cm}^{-1}$ towards a lower wavenumber. Moreover, the peaks of as-evaporated 20-GDC and annealed at a lower temperature slightly shifted from 463 cm^{-1} to 461 cm^{-1} since these films are denoted by a higher concentration of Gd_2O_3 compared to 10-GDC and 15-GDC. The intensity of the peaks of all GDC increases with the increasing annealing temperature, which can be associated with the crystallinity improvement of the films and a decrease of the grain boundary phase volume [302–304]. Furthermore, the peaks become broader with the increasing doping concentration (17.8 cm^{-1} for 10-GDC, 20.2 cm^{-1} for 15-GDC, and 28.4 cm^{-1} for 20-GDC), which might be due to a decrease in the grain size [302]. Similar results were obtained by Zarkov *et al.* [302] who obtained a peak at 464.5 cm^{-1} of a layered CeO_2 film after annealing at 700°C . The authors investigated the properties of GDC thin films on Si and Si/YSZ substrates by chemical solution deposition.

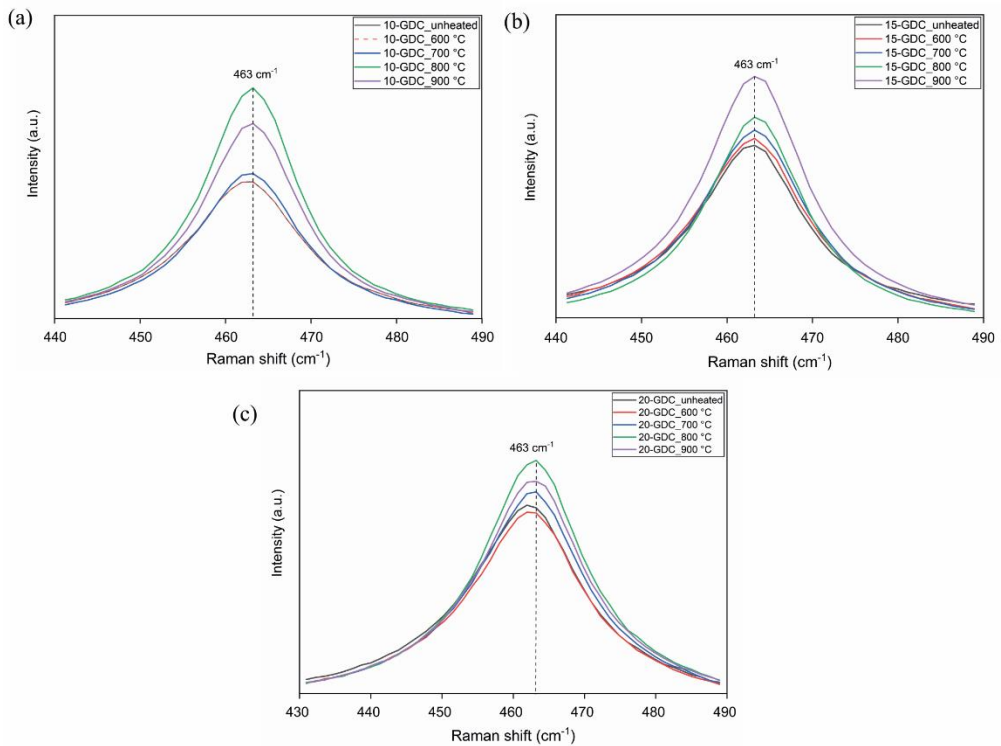


Fig. 4.22. Raman spectra of (a) 10-GDC-CP, (b) 15-GDC-CP, and (c) 20-GDC-CP thin films unheated and annealed at several temperatures. Published in [A3, 315]

The peak intensity of the 10-GDC-CP and 20-GDC-CP films increases with the increasing temperature, thus reaching a maximum at 800 °C, and the value further decreases upon annealing at 900 °C. While 15-GDC-CP has its maximum at 900 °C. Such results can be associated with a gradual growth of the crystal size, as well as simultaneous enhancement of the defects in the thin film and the growth of other crystalline phases [305]. At higher temperatures, these growths are more intense; therefore, the optimal annealing temperature for GDC thin films was found to be up to 800 °C, since at this temperature the overall crystallinity and roughness of the films are improved.

4.2.3.2 GDC thin films obtained by magnetron sputtering techniques

To compare the quality of thin films obtained by using different deposition methods, Gd_2O_3 and CeO_2 were deposited by layer-by-layer deposition using magnetron sputtering. During the magnetron sputtering, with increasing the number of the layers, the thickness of deposited single CeO_2 and Gd_2O_3 layers decreased, and the total thickness of each annealed GDC-4, GDC-6, GDC-12 multilayer system was in the range of 550-850 nm. The multilayer system of the thin films of CeO_2 and Gd_2O_3 and the process of their mixing are important for modifying the cerium dioxide lattice.

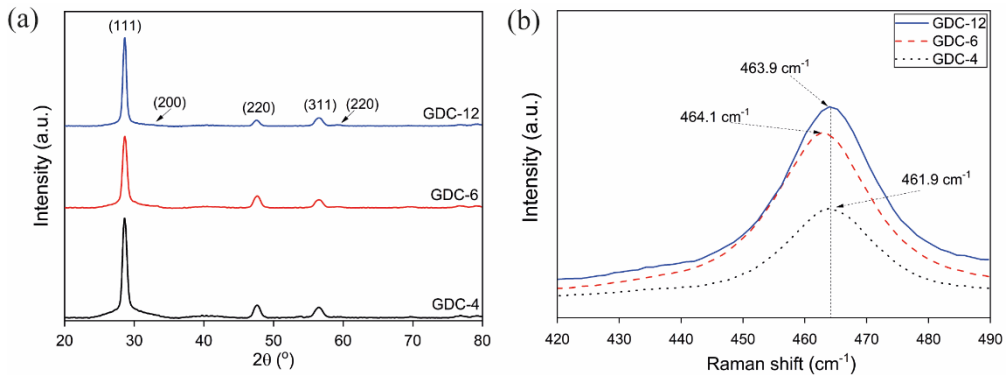


Fig.4.23. Results of (a) XRD patterns (b) and Raman spectra of gadolinia-ceria multilayered films. Published in [A2, 302]

From the XRD results (Fig. 4.23 (a)), we observe a cubic structure of the films, where the intensity of the peaks increases with the number of layers. Subsequently, GDC-12 has a higher crystallite size and lattice parameter (14.6 nm and 5.401 Å) than GDC-6 (11.4 nm and 5.394 Å) and GDC-4 (11.2 nm and 5.393 Å). This tendency is associated with the larger radius of the Gd^{3+} dopant (0.097 nm) compared to Ce^{4+} (0.090 nm) [306,307]. The Raman spectra of GDC-4 and GDC-6 thin films annealed at 700 °C showed a main peak at 464.1 cm^{-1} , while the GDC-12 peak shifted to 462.9 cm^{-1} (Fig. 4.23 (b)). Similarly, as in GDC-CP (Fig. 4.20), the results shows that the obtained peak corresponds to F_{2g} symmetry and confirms the formation of a single cubic fluorite phase which is indicated by the occupation of the

interstitial spaces in the ceria lattice by Gd^{+3} ions [299,301,308,309]. Moreover, we observe a slight broadening of the peaks (17.2 cm^{-1} to 18.8 cm^{-1}).

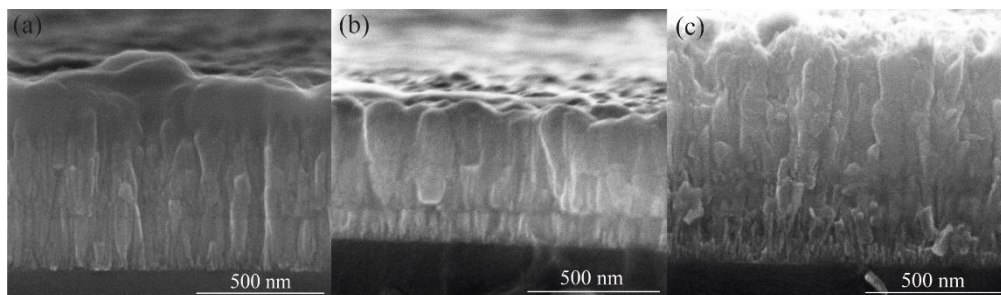


Fig.4.24. SEM images of the cross-section of (a) GDC-4, (b) GDC-6, and (c) GDC-12. Published in [A2, 302]

The cross-section view showed that GDC films have a dense columnar structure and a thickness of $\sim 700\text{ nm}$ (GDC-4), $\sim 550\text{ nm}$ (GDC-6), and $\sim 850\text{ nm}$ (GDC-12). In spite of the annealing, layer boundaries were still observed for GDC-4 and GDC-6, which indicates insufficient mixing between the layers.

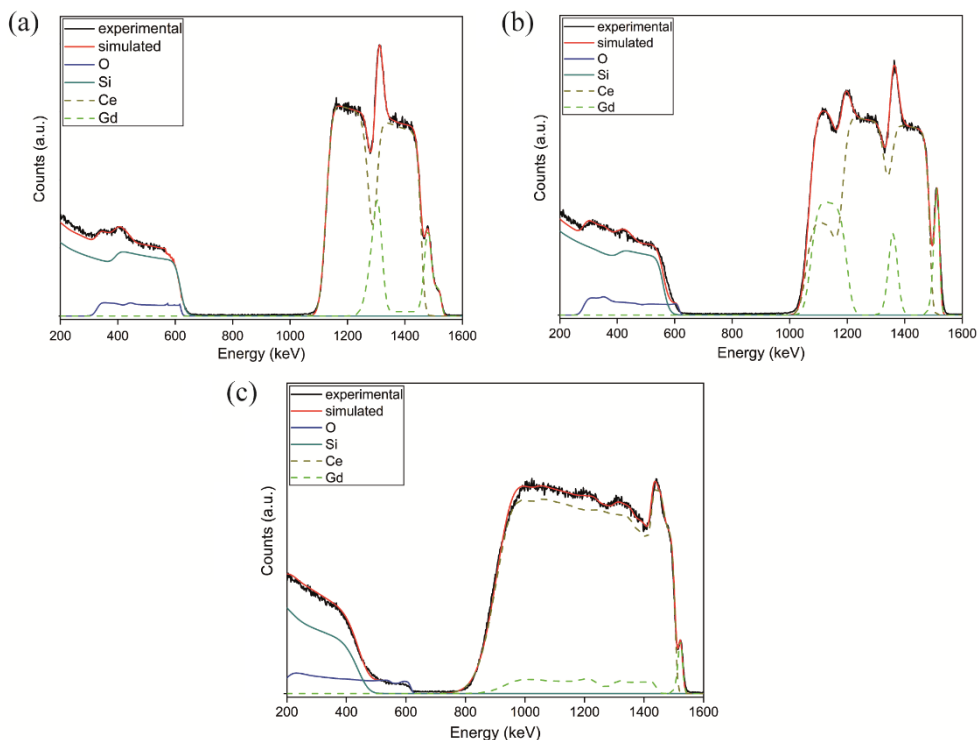


Fig.4.25. Experimental and simulated RBS spectra of (a) GDC-4, (b) GDC-6, and (c) GDC-12. Published in [A2, 302]

Rutherford Backscattering Spectroscopy (RBS) was applied for the element depth profiling of Gd and Ce so that to verify if the layer boundaries observed in SEM are present in annealed gadolinia-ceria films. Good agreement was obtained between the experimentally achieved data and the simulated data (by using *SIMNRA* v7.02 software) (Fig. 4. 25). Each deposited layer can be defined in 4 layers of Gd_2O_3 and CeO_2 . The high-energy edge of the gadolinium signal at 1.52 MeV corresponds to backscattering from the Gd_2O_3 layer on the surface, and the energy edge of cerium at 1.33 MeV corresponds to the CeO_2 layer and the second interface with the Gd_2O_3 layer. The 1.28 MeV energy edge refers to the boundary between the second Gd_2O_3 layer and the second CeO_2 layer, and 1.12 MeV refers to the scattering from the CeO_2 and Si interface. The RBS results of GDC-4 showed that diffusion between the individual layers of CeO_2 and Gd_2O_3 is at the initial stage, and diffusion happens only within a very narrow region of the interface. The RBS results of GDC-6 showed that its annealing caused partial formation of the gadolinia-doped ceria phase. A broad peak in the energy range from 1 MeV to 1.20 MeV corresponds to the diffusion between the CeO_2 and Gd_2O_3 layers at the Si interface, but only slight diffusion was manifested near the boundary region between the CeO_2 - Gd_2O_3 layers on the film surface. The RBS of GDC-12 showed a sharp peak in the energy range from 1.54 MeV to 1.50 MeV, related to the first layer of Gd_2O_3 , while the peak at 1.50–1.42 MeV is related to the first layer of CeO_2 . These separations are caused by incomplete mixing of the top layer; however, other layers are fully mixed as can be seen from the broad peak at the energy range from 1.42 MeV to 0.76 MeV. According to the obtained results, the main parameter affecting the formation of GDC thin films is the total thickness of the CeO_2 - Gd_2O_3 layers, and at least 12 layers are needed to form a single-phase gadolinia-doped ceria.

4.2.4 Summary of the experimental results of GDC

Since the formation method and the technological parameters affect the quality (the structural properties) and subsequently the application of the films, GDC thin films were deposited while using different approaches by two PVD methods. Gadolinium-doped ceria ceramics synthesised by CP were used as a target material for the formation of GDC thin films by the electron beam evaporation, and thin gadolinia and ceria multilayer systems were deposited layer-by-layer while using the reactive magnetron sputtering technique. The effect of additional heat treatment was investigated and the optimal annealing temperature for GDC thin films was determined. The following conclusions were made:

1. From the investigation of GDC nanopowders, we observed the same tendency of decomposition and crystallisation as in SDC, which corresponded to the synthesis methods. However, the XRD results showed that the lattice parameters and the crystallite sizes of GDC are smaller than SDC, since the ionic radius of Sm^{+3} (1.22 Å) is larger than the ionic radius of Gd^{+3} (1.19 Å). These results were further confirmed by TEM. Furthermore, based on the FT-IR results, GDC powders showed better purity

2. When increasing the molar concentration of the material, E_a increased, and the total ionic conductivity decreased. Thus, 10 GDC-CP and 10 GDC-CB ceramics have the highest σ_{total} at all temperatures (e.g., $1.1 \times 10^{-2} \text{ S} \times \text{cm}^{-1}$ at 600 °C (10 GDC-CP) and $1 \times 10^{-2} \text{ S} \times \text{cm}^{-1}$ at 600 °C (10 GDC-CB)) and the lowest E_a (0.85 eV (LT) and 0.67 eV (HT)). Moreover, we found that at lower temperatures (400 °C) SDC ceramics have higher values of the total ionic conductivity, at intermediate temperatures (600 °C) both SDC and GDC show nearly the same conductivity values, and at higher temperatures (800 °C) GDC has higher values.
3. The chemical analysis of the GDC thin films evaporated by using the electron beam technique showed a ~28% deviation of the resulting thin films from the concentration of the target material used for evaporation. The evaporation of a material containing various elements is a complex process since different elements require different evaporation conditions. Therefore, when the individual elements are subjected to the same conditions, deviation of the stoichiometry of the resulting thin films may occur. According to the experimental results, for the evaporation of thin films with the desired concentration, the target material must have a higher concentration (in our case, ~28% higher).
4. The additional heat treatment after the evaporation can improve the structure, crystallinity, density, morphology, and the general properties of the obtained films. However, it is important to determine the optimal heating temperature and time for the material undergoing the process. The annealing of GDC thin films at various temperatures for 1 h caused a fluctuation of the thickness (~800 nm) depending on the temperature, but insignificantly affected their morphology. According to the results of Raman spectroscopy and AFM, crystallinity and roughness improve with the increasing temperature, reaching the best values at 800 °C. Thus, for GDC thin films, thus the optimal annealing temperature is up to 800 °C.
5. GDC thin films deposited by reactive magnetron sputtering had a multilayer columnar structure with a thickness of ~550–850 nm. With fewer layers (GDC-4 and GDC-6), layer boundaries were observed despite annealing, which indicates insufficient mixing between the layers. However, with 12 layers of $\text{Gd}_2\text{O}_3\text{--CeO}_2$ (GDC-12), the layer boundaries tend to disappear, and the Raman band shifts to lower frequencies, thus indicating that after annealing, Gd^{3+} ions begin to dissolve in the ceria lattice and partially replace Ce^{4+} ions. In addition, the results of the diffusion of Ce and Gd in multilayered $\text{Gd}_2\text{O}_3\text{--CeO}_2$ systems showed that at least 12 layers are required to form single-phase gadolinia-doped ceria films.

4.3 Samarium-gadolinium-doped ceria

4.3.1 Characterisation of SGDC nanopowders

The thermal decomposition and crystallisation behaviour of samarium-gadolinium-doped-ceria (SGDC) nanopowders corresponds to the decomposition of the precursors used for the synthesis (Fig. 4.26) showing the same tendency as singly doped ceria nanopowders. As we can see, SGDC-CB is more in coincidence with GDC-CB compared to SDC-CB. However, the total mass change of SGDC-CB is about 0.21–0.44% (from 30 °C to 700 °C), which is less than the mass change of SDC-CB (3.5%, Fig.4.1 (a)) and GDC-CB (0.45–0.75%, Fig.4.12 (a)). No visible differences in the decomposition and crystallisation for SGDC-CP nanopowders in comparison with singly doped ceria were observed; the total mass change is ~55%, as in the case of SDC-CP and GDC-CP. These results show that co-doping during CB synthesis helps to obtain more thermally stable materials with a lower organic matter content compared to singly doped ceria.

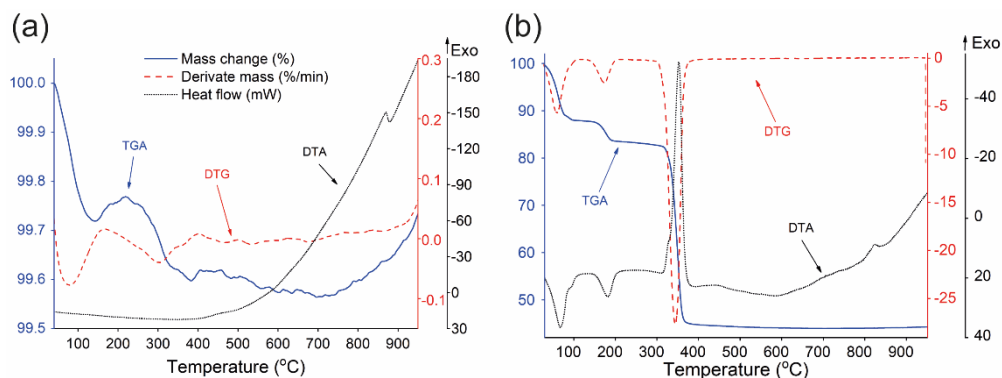


Fig. 4.26. Combined TGA–DTG–DTA curves of SGDC synthesised by (a) combustion (CB) and (b) co-precipitation (CP) syntheses.

The XRD results of co-doped ceria nanopowders confirmed a fluorite-type cubic structure (Fig. 4.27). The tendency of crystallite growth as a function of temperature is the same as for SDC and GDC, regardless of the synthesis method. Residual oxalic acid remains on SGDC-CP until it has reached 400 °C.

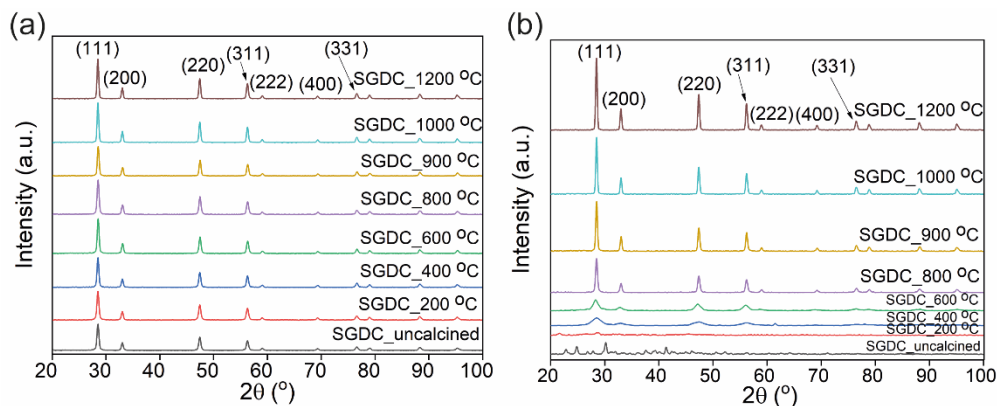


Fig. 4.27. XRD patterns of SGDC nanopowders synthesised by (a) combustion and (b) co-precipitation calcined at various temperatures

However, unlike SGDC, the diffraction peaks of singly doped ceria are more intense and sharper, which indicates higher crystallinity values (Table 4.5). The calculated crystallite sizes and lattice parameters of SGDC nanopowders as a function of temperature are plotted in Fig. 4.28. The average lattice parameters are 541.66 pm (10 GDC-CB), 541.38 pm (10 GDC-CP), 543.41 pm (10 SDC-CB), 543.33 pm (10 SDC-CP), 542.37 pm (SGDC-CB), and 548.7 pm (SGDC-CP).

Table 4.5. Calculated values of the crystallite size (nm) for synthesised ceria-based nanopowders at various temperatures

T (°C)	SGDC-CB	SGDC-CP	10 GDC-CB	10 GDC-CP	10 SDC-CB	10 SDC-CP
Raw	21.02	-	-	-	-	-
200	20.68	-	24.54	-	16.85	-
400	21.89	9.79	25.89	4.53	19.11	4.62
600	21.79	8.84	23.87	9.56	24.73	10.19
800	20.3	20.86	26.77	23.74	28.09	27.41
900	22.67	23.38	-	-	-	-
1000	24.65	25.13	35.66	44.06	36.81	45.74
1200	24.02	25.74	35.8	47.97	44.22	48.1

The differences in the lattice parameter and crystallite size are explained by the difference in the ionic radii of Sm^{3+} (1.079 Å), Gd^{3+} (1.053 Å), and Ce^{4+} (0.97 Å) [291]. For ceria doped with one dopant, we observe a gradual replacement of the Ce lattice by a larger ion of the dopant Sm or Gd, and when doped with Sm, the lattice parameter and the crystallite size are the greatest. In the case of co-doped ceria, Gd is replaced by a Sm dopant ion. However, the smaller value of the crystallite size in comparison with SDC and GDC can be explained by the lower concentration of Gd and Sm in SGDC [9]. At lower temperatures (Fig. 4.28), a sharp decrease in the lattice parameter is observed for both SGDC-CB and SGDC-CP, which can be associated with the incomplete formation of oxides.

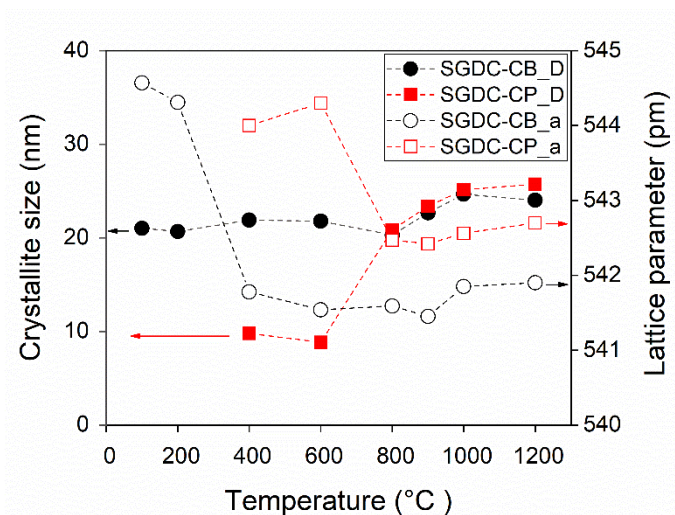


Fig. 4.28. Plot of the crystallite size (D) and lattice parameter (a) vs. calcination temperatures for SGDC nanopowders

From the SEM images, we observe compaction of the powders with an increase in the calcination temperature. The structure and morphology of nanopowders correspond to the synthesis method in use (Fig. 4.30). The purity of the synthesised SGDC nanopowders is confirmed by the obtained FT-IR spectra (Fig. 4.29). As it can be seen, at higher temperatures, organic residues are completely absent and only an intense CeO_2 band can be observed, especially for the samples synthesised by combustion. In addition, the peaks of SGDC-CB, as-synthesised and calcined at low temperatures, are less intense than SDC and GDC, which shows better purity.

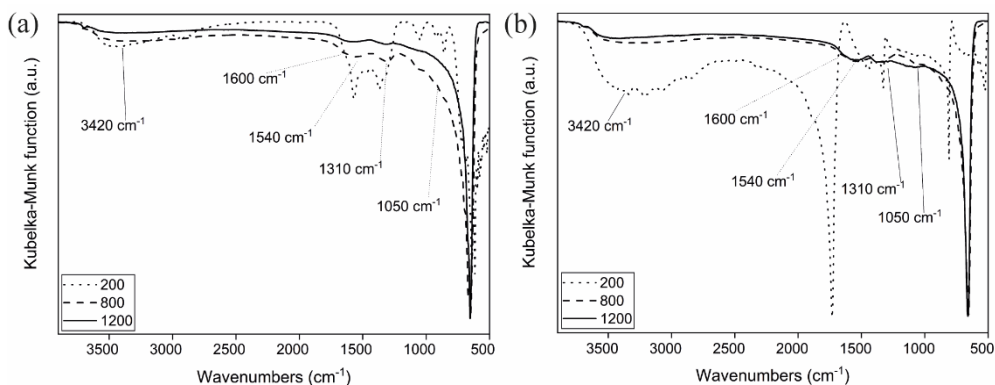


Fig. 4.29. FT-IR spectra of SGDC nanopowders synthesised by (a) combustion and (b) co-precipitation calcined at various temperatures

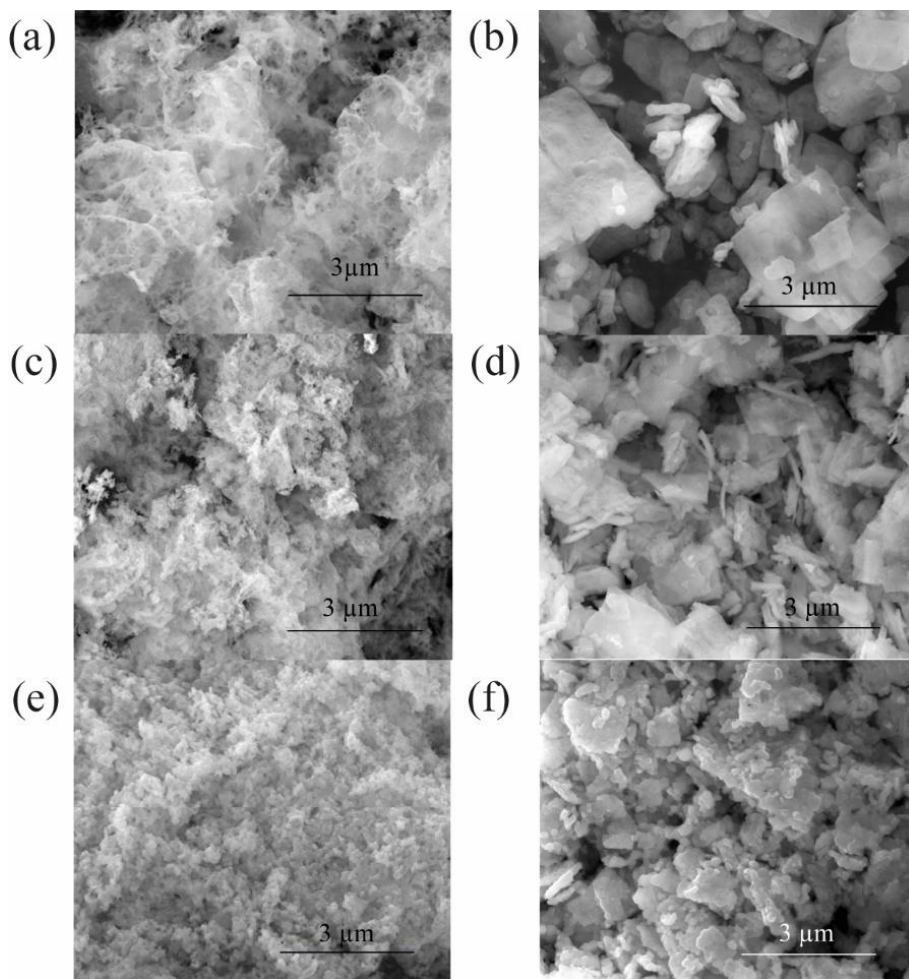


Fig. 4.30. SEM images of SGDC nanopowders synthesised by (a, c, e) combustion and (b, d, f) co-precipitation as-synthesised (a, b) and calcined at 900 °C (c, f) and 1100 °C (e, f)

4.3.2 Characterisation of SGDC ceramic pellets

SEM results of SGDC pellets show a microstructure similar to singly doped pellets: a dense structure with grains of an irregular size (1.21 μm and 0.832 μm), without defects and cracks (Fig. 4.31). The surface view of the pellets shows that the samples synthesised by CP are more uniformly formed, while CB is composed of small individual grains pressed together.

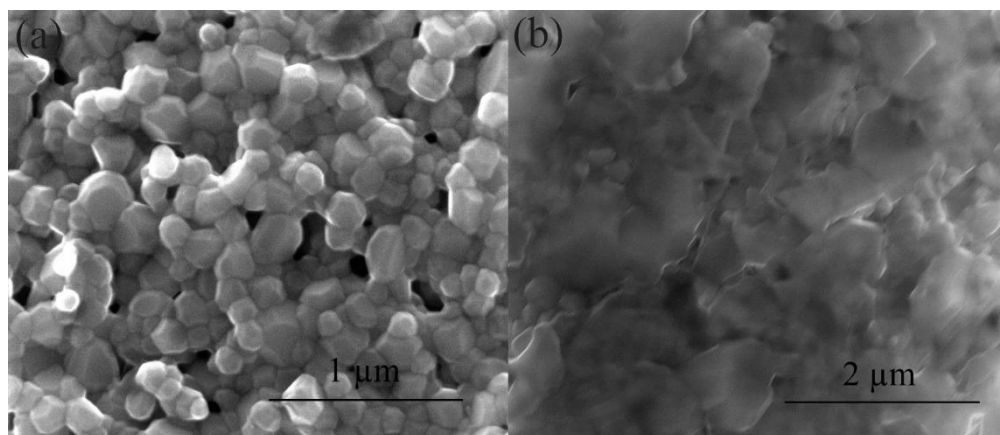


Fig. 4.31. SEM images of SGDC pellets synthesised by (a) combustion and (b) co-precipitation methods and annealed at 1200 °C

It can be seen from the impedance spectroscopy that the resistance of SGDC-CP pellets is several values of magnitude lower than that of ceramics synthesised by CB (Fig. 4.32 (a, b, and c)). For both SGDCs, the grain boundary conductivity was much higher compared to the bulk conductivity. However, pellets synthesised by co-precipitation showed higher values of the total conductivity at all temperatures, especially within the IT and LT ranges (Table 4.6).

Table 4.6. The activation energy at low (LT) and high (HT) temperature ranges and the total ionic conductivity of SGDC ceramics

Sample	ΔE_a (eV)		Total conductivity ($S \times cm^{-1}$)		
	LT	HT	400 °C	500 °C	600 °C
SGDC-CP	0.79	0.65	0.85×10^{-2}	8.5×10^{-2}	5.4×10^{-2}
SGDC-CB	0.81	0.76	0.39×10^{-2}	5.2×10^{-2}	2.2×10^{-2}

The Arrhenius plots of the total conductivity of the co-doped system versus the highest values of the singly doped ceria (20 SDC-CB and 10 GDC-CP) are presented in Fig. 4.32 (d). Co-doping of ceria helped to lower the activation energy in both temperature ranges and significantly increased the conductivity values, so σ_{total} are 5.4×10^{-2} and $2.2 \times 10^{-2} S \times cm^{-1}$ at 600 °C for SGDC-CP and SGDC-CB, respectively.

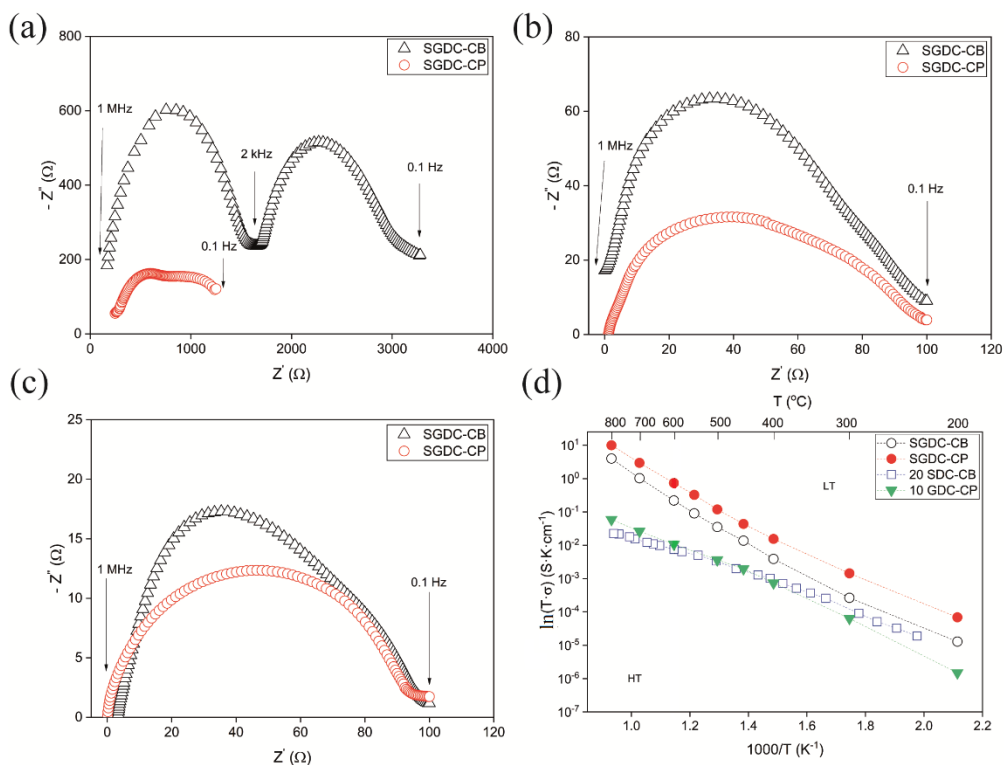


Fig. 4.32. Complex impedance plots of SGDC ceramics at (a) 400, (b) 500, and (c) 600 °C. Arrhenius plots (d) of total conductivity of ceria-based ceramics

Wang and co-authors [152] reported the σ_{total} of $0.046 \text{ S} \times \text{cm}^{-1}$ for $\text{Ce}_{0.85}\text{Gd}_{0.15-y}\text{Sm}_y\text{O}_{1.92}$ at 700 °C. Dikmen [154] reported σ_{total} of $6.5 \times 10^{-2} \text{ S} \times \text{cm}^{-1}$ at 700 °C with 0.59 eV E_a for $\text{Ce}_{0.8}\text{Gd}_{0.1}\text{Sm}_{0.1}\text{O}_{2-\delta}$. However, Coles-Aldridge and Baker [9] showed higher values of $2.23 \text{ S} \times \text{cm}^{-1}$ at 600 °C for $\text{Ce}_{0.825}\text{Sm}_{0.0875}\text{Gd}_{0.0875}\text{O}_{1.9125}$, such disagreement between the results is due to the different preparation methods and conditions, starting materials and sintering conditions. The obtained results are in good agreement with the literature and confirm that co-doping ceria with multiple dopants was beneficial compared to the singly-doped parent materials.

4.3.3 Summary of the experimental results of SGDC

Following a new approach of doping ceria with more than one dopant, which increases the conductivity values, samarium-gadolinium-doped ceria was synthesised by the combustion and co-precipitation methods. The following conclusions were made:

1. From the investigation of SGDC nanopowders, we observed the same tendency of crystallisation and decomposition as in singly doped ceria, which corresponded to the applied synthesis method. However, due to the lower concentration of Sm_2O_3 and Gd_2O_3 , smaller values of the crystallite sizes

compared to singly doped ceria were obtained for SGDC (i.e., 22.13 nm and 542.37 pm for SGDC-CB).

- Moreover, the results of TGA and FT-IR showed that SGDC is more thermally stable and pure even at a lower calcination temperature (400 °C).
- Co-doping of ceria with samarium and gadolinium significantly increased the total ionic conductivity of ceramics, which is indicated by the values of $5.4 \times 10^{-2} \text{ S} \times \text{cm}^{-1}$ (SGDC-CP) and $2.2 \times 10^{-2} \text{ S} \times \text{cm}^{-1}$ (SGDC-CB) at 600 °C.

4.4 Application of ceria-based ceramics as a diffusion barrier layer

With a decrease in the operating temperature of SOFC, the degradation rate can be reduced, and the lifetime of the cells can be increased. In the state-of-art cells the limitation occurs due to the overpotential of the cathode. The most popular cathode materials (for example, $\text{La}_{1-x}\text{Sr}_x\text{MnO}_{3-\delta}$ (LSM), $\text{La}_{0.6}\text{Sr}_{0.4}\text{FeO}_{3-\delta}$ (LSF), $\text{La}_{0.6}\text{Sr}_{0.4}\text{CoO}_{3-\delta}$ (LSC), $\text{La}_{0.6}\text{Sr}_{0.4}\text{Co}_{0.2}\text{Fe}_{0.8}\text{O}_{3-\delta}$ (LSCF)) contain strontium and, during annealing, they react chemically with the electrolyte (for example, with the YSZ electrolyte SrZrO_3 and $\text{La}_2\text{Zr}_2\text{O}_7$) which leads to a loss of power. Therefore, to improve the performance of the cell, an intermediate layer (a diffusion barrier-layer) is required between the cathode and the electrolyte. To prevent the diffusion of cations, the barrier-layer must be gastight, homogeneous, chemically stable, dense, and thin. An example of the interaction between the cathode, the barrier layer, and the electrolyte interfaces without and with a GDC barrier layer of a thickness of 400 and 800 nm is shown in Fig. 4.33.

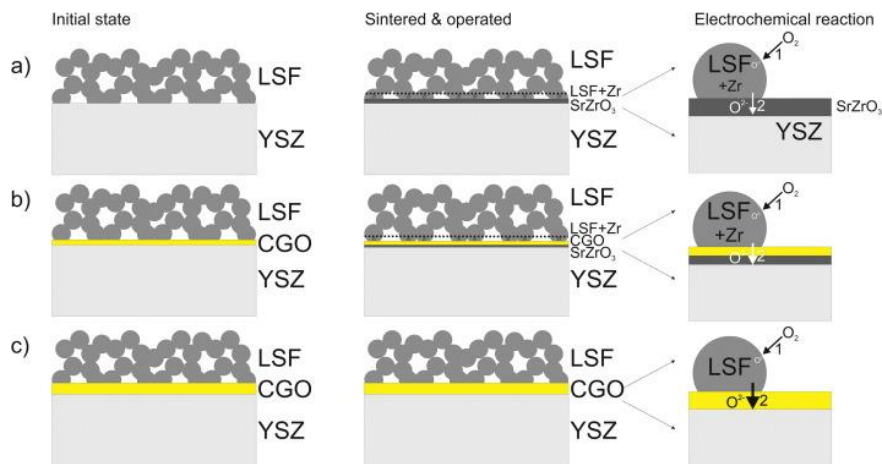


Fig. 4.33. Schematic model of the interaction between the cathode-barrier-electrolyte interfaces (a) without and with (b) 400 nm, (c) 800 nm thick GDC barrier layer. Reproduced from [196]

From the schematic model presented in [196], the diffusion of Sr from LSF and Zr from YSZ begins after the sintering process at high temperatures. To reduce the diffusion, the thickness of the barrier layer is suggested to be sufficient to cover the

surface and block the diffusion, but not to introduce any additional ohmic resistance (between 400 nm and 1 μm).

Since samarium-doped ceria and gadolinium-doped ceria do not react with most cathode materials, they can be used not only as an electrolyte material, but also as a barrier layer.

To investigate the possibility of using GDC as a diffusion barrier-layer between YSZ and the LSCF cathode, dense 26 GDC-CP (~ 700 nm) was successfully deposited on a porous anode supported cell with a YSZ electrolyte layer on the surface by using the e-beam technique. The diameter of the disk-shaped sample was ~ 25 mm.

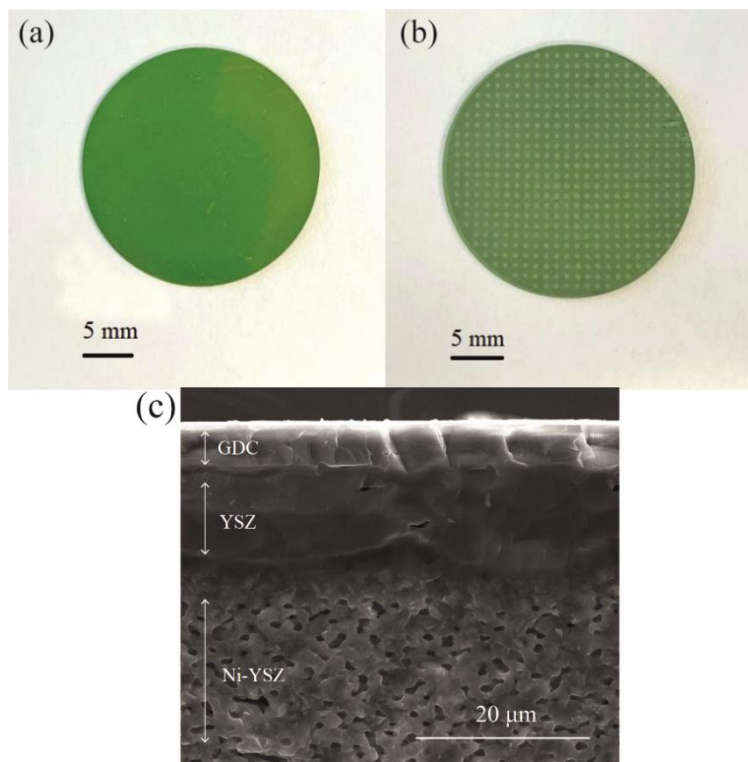


Fig. 4.34. Image of the (a) front side, (b) back side, and (c) SEM cross-sectional view of the YSZ-GDC on a porous metal substrate. The GDC barrier-layer is deposited on the smooth side (a)

The next step is to determine the electrochemical properties of the formed samples. After analysing the properties of the already formed layers, the cathode will be deposited on top of the GDC barrier layer. The suggested anode-supported cell is ideal for μ -SOFCs, which are designed to work at a low temperature. It will help to speed up the start-up time and open up new application opportunities.

5. CONCLUSIONS

1. From the investigation of ceria-based nanostructured ceramics, it was found that combustion synthesised $\text{Sm}_{0.2}\text{Ce}_{0.8}\text{O}_{2-\delta}$ (20 SDC-CB) nanopowders and annealed at 1200 °C exhibited the highest ionic conductivity of $1.1 \times 10^{-2} \text{ S} \times \text{cm}^{-1}$ at 600 °C, whereas 20 SDC synthesised by co-precipitation and sol-gel syntheses showed $0.92 \times 10^{-2} \text{ S} \times \text{cm}^{-1}$ and $0.95 \times 10^{-2} \text{ S} \times \text{cm}^{-1}$, respectively.
2. GDC nanopowders have smaller values of the lattice parameter and the crystallite size (i.e., 541.66 pm and 26.67 nm for 10 GDC-CB) than SDC (i.e., 543.41 pm and 27.27 nm for 10 SDC-CB) due to the differences in the ionic radii ($\text{Sm}^{+3} > \text{Gd}^{+3}$).
3. $\text{Gd}_{0.1}\text{Ce}_{0.9}\text{O}_{2-\delta}$ (10 GDC) ceramics showed higher total ionic conductivity of $1.1 \times 10^{-2} \text{ S} \times \text{cm}^{-1}$ at 600 °C for 10 GDC-CP and $1 \times 10^{-2} \text{ S} \times \text{cm}^{-1}$ at 600 °C for 10 GDC-CB.
4. The suggested technological parameters lead to the production of ceramics with desired properties. To obtain nanopowders, the coprecipitation method was chosen, since the synthesised ceramics have a high ionic conductivity and, in comparison with the combustion method, does not require high temperatures, which makes them safer. The best dopant concentration of Sm_2O_3 in SDC is 20 mol% and, for Gd_2O_3 in GDC, it is 10 mol%. The sintering temperatures for nanopowders should not be below 800 °C and the annealing temperature of ceramics should be 1200 °C.
5. SGDC showed smaller values of the crystallite sizes compared to singly doped ceria due to the lower concentration of Gd_2O_3 and Sm_2O_3 (i.e., 542.37 pm and 22.13 nm for SGDC-CB). The co-doping ceria, with mixed Sm_2O_3 and Gd_2O_3 (synthesised by combustion and co-precipitation) compared to the singly-doped parent materials, increase the total ionic conductivity of ceramics, while indicating the values of $5.4 \times 10^{-2} \text{ S} \times \text{cm}^{-1}$ and $2.2 \times 10^{-2} \text{ S} \times \text{cm}^{-1}$ at 600 °C for SGDC-CP and SGDC-CB, respectively. Moreover, SGDC is more pure and thermally stable even at a calcination temperature of 400 °C.
6. With regards to the deposited ceria-based ceramic thin films with the desired concentration obtained when using the electron beam evaporation technique, the target materials must have a higher concentration (~28% higher). The SEM results of the films obtained by electron beam evaporation, revealed a very dense and uniform structure, which is ideal for the electrolyte or the interlayer materials for SOFC.
7. In the case of layer-by-layer deposition while using the direct current magnetron sputtering technique, not less than 12 sandwich layers of gadolinia-ceria are required to form homogeneous single-phase ~850 nm thick GDC films. Furthermore, the additional annealing of GDC films improved the crystallinity and density of the films, ultimately reaching the best values at 800 °C. Whilst, at 900 °C we observe the dissolution of ceria on the surface with the formation of small clusters.

Recommendations

The electrical properties of ceria-based films must be tested to fully understand the dependence on the thin film formation methods, the annealing conditions, the choice of the dopant and its concentration. The developed technological route should be used to prepare the electrolyte and/or a diffusion-barrier layer in a full cell with porous electrodes for SOFC in order to check for any changes in the cell performance.

SANTRAUKA

IVADAS

Daugelį dešimtmečių į atsinaujinančiųjų ir mobiliųjų energijos šaltinių naujoves ir tyrimus buvo sutelktas pagrindinis mokslinių tyrimų dėmesys. Sparčiai įvairių mobiliųjų elektroninių prietaisų, modernių automobilių, išmaniųjų technologijų, įvairių jutiklių, net kosminių palydovų plėtrai būtina reikalauja didinti energijos gamybą, plėtoti baterijų ir kuro elementų tyrimus.

Dėl nepakankamos įkraunamų baterijų talpos žymiai išaugo įvairių tipų kuro elementų naudojimas, kuris sumažina aplinkos taršą, turi labai mažą emisiją ir didelį efektyvumą, gali veikti skirtingame darbinių temperatūrų intervale, atlaikyti cheminių ir mechaninių poveikius [1,3–5,3,10].

Vienas iš dažniausiai tiriamų ir naudojamų elektrocheminių energijos konvertavimo įrenginių yra kietojo oksido kuro elementai (KOKE). KOKE išskirtinis dėmesys buvo suteiktas dėl jų pranašumų prieš kitų tipų kuro elementus, dėl didelio efektyvumo (60–85 %), didelio cheminės energijos kiekio pavertimo elektros energija. KOKE gali veikti plačiame temperatūrų diapazone nuo 400 °C iki 1000 °C, esant skirtingiems elektrolitų tipams. Dažniausiai naudojami aukštoje temperatūroje (800–1000 °C) veikiantys KOKE. Tačiau aukšta darbinė temperatūra lemia ilgesnį kuro elemento darbinį paleidimo laiką, trumpesnį elementų komponentų eksploatacijos laiką, brangias medžiagas, taip pat išorinių komponentų formavimo sunkumus [5–7]. Todėl svarbu sumažinti kuro elementų darbinę temperatūrą. KOKE darbinės temperatūros sumažinimas (< 600 °C) arba jų nanostruktūrinių komponentų parinkimas leistų pasiekti pakankamą ilgalaikį kuro elementų stabilumą. Žematemperatūriniai KOKE (LT-KOKE), kurie veikia 400–650 °C temperatūroje, turi trumpesnį darbinį paleidimo laiką, jiems nebūtinos brangios medžiagos, jie gali būti naudojami nešiojamuosiuose įrenginiuose [32]. Vienas iš svarbių veiksnių sėkmingam LT-KOKE komercializavimui yra didelio joninio laidumo elektrolitas [9,10].

Plonų sluoksnių formavimo procesai ir jų technologiniai parametrai turi įtakos sluoksnių konstrukcinėms savybėms ir tolimesniam jų panaudojimui. Todėl labai svarbu parinkti ir ištirti įvairius technologinius procesus, kuriuos pasitelkus būtų suformuoti ploni sluoksniai ir pagerintos plonų sluoksnių fizikinės savybės. Labai sunku rasti medžiagą, kuri turėtų visas norimas savybes, įskaitant gerą elektrodų suderinamumą, didelį joninį laidumą ir stabilumą eksploatacijos metu arba redukuojančioje atmosferoje. Tačiau ištyrus plačiai naudojamų elektrolitų, tokių kaip gadolinio oksidu legiruoto cerio oksido ir samario oksidu legiruoto cerio oksido, savybes nuo pradinių nanomiltelių ir terminio apdirbimo sąlygų iki plonų sluoksnių formavimo ir jų mikrostruktūros poveikio joniniam laidumui, galima rasti tinkamiausią nanomiltelių gamybos būdą.

Cerio oksido pagrindu stabilizuota pagaminta keramika, pasižyminti dideliu joniniu laidumu, yra viena iš populiarių medžiagų, naudojamų LT-KOKE. Daugelis veiksnių gali turėti įtakos medžiagos joniniam laidumui, pavyzdžiui, keramikų priemaišinių metalo oksidų koncentracija, kristalitų dydis, morfologija, tankis,

grūdelių dydis, struktūra ir terminis plėtimasis. Šiuos parametrus galima valdyti, pritaikant cheminės sintezės metodą, legiruojančios medžiagos tipą ir koncentraciją, taip pat sintezės iškaitinimo ir atkaitinimo sąlygas. Išsamus šioje disertacijoje pateiktas mokslinis tyrimas siūlo tinkamiausias technologines sąlygas nanostruktūrinėms cerio oksido keramikoms, su atitinkamais LT-KOKE keliamais reikalavimais, gauti.

Tyrimo tikslas

Atsižvelgiant į cheminės sintezės metodus, pradinių metalo oksidų medžiagų koncentracijas, įvairių keramikų sintezės iškaitinimo ir plonų sluoksnių atkaitinimo temperatūras, plonų sluoksnių formavimo vakuuminius garinimo metodus, parinkti ir sistemingai bei išsamiai ištirti nanostruktūrinėmis metalo oksidų priemonėmis legiruoto cerio oksido keramikas, naudojamas žematemperatūriuose kietojo oksido kuro elementuose.

Tyrimo uždaviniai

1. Susintetinti cerio oksido stabilizuotas keramikas, įterpiančias skirtingos koncentracijos Gd ir Sm metalų oksidų priemaišas, taikant degimo, nusodinimo iš tirpalų cheminius sintezės metodus su tomis pačiomis pirminėmis sintezei reikalingomis medžiagomis ir zolių-gelių cheminį sintezės metodą.
2. Ištirti cheminių sintezės metodų, priemaišinių Gd ir Sm metalo oksidų, skirtingų sintezių iškaitinimo temperatūrų pasirinkimo įtaką susintetintų nanostruktūrinių cerio oksido pagrindu keramikų mikrostruktūros, paviršiaus morfologijos ir elektrinėms savybėms.
3. Pritaikyti vakuuminio garinimo elektronų spinduliu ir nuolatinės srovės reaktyvųjį magnetroninio dulkavimo procesus plonų sluoksnių ir daugiasluoksnių (4, 6 ir 12 sluoksnių) struktūrų ant Si pagrindo formavimui, parenkant technologinius procesų parametrus ir taikant papildomą terminį dangų atkaitinimą.
4. Ištirti plonų sluoksnių struktūrines, morfologines ir elektrines savybes.

Mokslinis naujumas

1. Pateiktas išsamus tyrimas, kaip nanomiltelių sintezių, taikant įvairius cheminių sintezių metodus, legiruojančių medžiagų ir jų koncentracijų, plonų sluoksnių formavimo skirtingų metodų, skirtingų nanomiltelių iškaitinimo ir plonų sluoksnių atkaitinimo temperatūrų pasirinkimas turi įtakos nanostruktūrinių metalo oksidų priemaišomis legiruoto cerio oksido pagrindo keramikų fizikinėms savybėms.
2. Pasiūlyti cheminių sintezių ir plonų sluoksnių formavimo metodai bei technologinės sąlygos keramikoms su atitinkamais LT-KOKE keliamais reikalavimais gauti.

Ginamieji teiginiai

1. Degimo ir nusodinimo iš tirpalų cheminių sintezių metodai yra tinkami sintetinti keraminius (samario oksidu legiruoto cerio oksido (SDC), gadolinio oksidu legiruoto cerio oksido (GDC) bei samario ir gadolinio oksidais legiruoto cerio oksido (SGDC) nanomiltelius, kurie pasižymi dideliu joniniu laidumu.
2. Metalų oksidų koncentracija lemia legiruoto cerio oksido pagrindu keramikų elektrines savybes–joninį laidumą: SDC nanomilteliams tinkama samario koncentracija 20 mol %, o GDC nanomilteliams–gadolinio koncentracija 10 mol %.
3. Garinimo elektronų spinduliu ir nuolatinės srovės reaktyviojo magnetroninio dulkinimo procesai yra tinkami formuoti iki 800 nm storio plonius sluoksnius. Tačiau, reikia atkreipti dėmesį į technologinius procesų parametrus ir pirminių medžiagų-taikinių koncentracijų parinkimą, nes suformuotuose plonuose sluoksniuose pakinta cheminė sudėtis. Darbe nustatytos tipinės nanomiltelių ir plonų sluoksnių cheminės sudėty.
4. Papildomas terminis plonų dangų atkaitinimas pagerina fizikines plonų sluoksnių savybes. Darbe pasiūlytos tipinės atkaitinimo temperatūros.

Disertacijos struktūra

Disertaciją sudaro 5 pagrindiniai skyriai: įvadas, literatūros apžvalga, darbo metodologija, rezultatai ir aptarimas bei išvados. Pirmas skyrius yra LT-SOFC literatūros apžvalga, apimanti jo struktūrą, medžiagas, formavimo būdus ir išskylančias problemas. 3 skyriuje pateikiamos medžiagos, eksperimentinė įranga ir analitiniai tyrimo metodai, taikomi šioje disertacijoje. 4 skyriuje pristatoma gautų rezultatų analizė ir diskusija. Rezultatai suskirstyti į 4 dalis, skirtas skirtingoms medžiagoms, jų charakteristikoms ir pritaikymui (SDC, GDC, SGDC ir pritaikymui). Išvados formuluojamos paskutiniame skyriuje, kuriame pabrėžiamas tyrimo tikslų įgyvendinimas. Disertacijos pabaigoje yra padėka, literatūros sąrašas, autorės gyvenimo aprašymas, publikacijų ir tarptautinių bei nacionalinių konferencijų sąrašas. Disertacijos apimtis – 166 puslapiai, iš jų 48 paveikslai, 16 lentelių, 56 sunumeruotos lygtys ir 315 literatūros šaltinių.

Autorės asmeninis indėlis

Dauguma rezultatų buvo gauti Kauno technologijos universiteto Medžiagų mokslo institute ir stažuojantis pagal *Erasmus+* programą Varšuvos technologijos universitete.

Autorė savarankiškai suplanavo eksperimentus, atliko cheminių sintezių eksperimentus, vykdė technologinius procesus ir daugelį analitinių matavimų (XRD, Ramano spektroskopijos, SEM, AFM, EIS).

Zolių-gelių sintezę ir termogravimetrinę analizę bei BET matavimus atliko Vilniaus universiteto mokslininkai Dr. Artūras Žalga ir Dr. Giedrė Gaidamavičienė. Dr. Mindaugas Andrulevičius atliko rentgeno spindulių fotoelektroninės spektroskopijos matavimus. Nusodinimo iš tirpalų cheminės sintezės ir impedanso

spektroskopijos matavimų metodikos patirtimi pasidalij Dr. Marzena Leszczyńska iš Varšuvos technologijos universiteto. Magnetroninio nusodinimo procesas ir Rezerfordo atbulinės sklaidos (RBS) tyrimai buvo atlikti Dr. Jurgitos Čyvienės ir Dr. Brigitos Abakevičienės, RBS rezultatų modeliavimas – doktoranto Luko Bastakio. Disertantė atliko SEM matavimus, prižiūrint Dr. Tomui Tamulevičiui. Doktorantė Algita Stankevičiūtė iš Varšuvos universiteto prisidėjo ruošiant antrąjį straipsnį bei impedanso spektroskopijos rezultatų analizę. Disertantė atliko plonasluoksnių dangų garinimą elektronų spinduliu prižiūrint Dr. Andriui Vasiliauskiui. Rezultatų interpretacija buvo atlikta konsultuojantis su disertacijos vadove Dr. Brigita Abakevičiene. Kiti publikacijų bendra autoriai prisidėjo idėjomis ir patarimais rengiant mokslines publikacijas.

Darbo aprobavimas

Disertacijoje pateikti rezultatai, publikuoti mokslo žurnaluose, įtrauktuose į „Clarivate Analytics Web of Science“ pagrindinį sąrašą (3 publikacijos), 1 publikacija konferencijų darbuose ir pristatyta tarptautinėse konferencijose (14 konferencijų), 9–iose konferencijose disertantė rezultatus pristatė pati.

LITERATŪROS APŽVALGA

Literatūros apžvalgoje aptariami įvairūs kuro elementai, jų medžiagos, privalumai ir trūkumai, kietojo oksido kuro elemento (KOKE) veikimo principas, pagrindinės medžiagos naudojamos KOKE elektroduose [16], išsamiai aprašomi elektrodų (anodo [14,45,46], elektrolito, katodo [68,69]) medžiagose vykstantys cheminiai procesai, darbinės temperatūros [105–107]. Taip pat pateikiamos elektrolito medžiagų joninio laidžio vertės [110,111,125,127,129–132,271,311,117–124], elektrolito medžiagų cheminės sintezės metodai [135,155–158,161,162,164], plonų sluoksnių formavimo ypatumai [166,167,176,179–183,312–314,168–175].

Joninis keramikų laidumas priklauso ne tik nuo priemaišinėmis metalų oksidų medžiagomis legiruoto cerio oksido keramikų, bet ir nuo priemaišų koncentracijos bei elektrinių savybių matavimo temperatūros [65]. Vienas iš būdų pagerinti keramikų joninį laidumą surasti legiruojančias medžiagas su tokiu metalų jonų spinduliu, kuris sukeltų mažiausius kristalinės gardelės iškraipymus [36–38]. Šiuo metu plačiausiai žinomos, pasižyminčios joniniu laidumu kietojo oksido medžiagos-cirkonio oksido ir cerio oksido pagrindu stabilizuotos keramikos, turinčios fluorito tipo gardelę. Esant didelei darbinei elektrodų temperatūrai (800–1000 °C) itrio oksidu stabilizuotas cirkonio oksidas (YSZ) yra dažniausiai naudojama keraminė medžiaga, kuri pasižymi dideliu joniniu laidumu ir geromis cheminėmis savybėmis [33,34]. O štai cerio oksido pagrindu stabilizuotos keramikos ($Ce_{1-x}M_xO_{2-\delta}$, čia M – Sm, Gd, Dy, Nb, Y, Ti ir Zn) yra vienos iš perspektyviausių medžiagų, naudojamų žematemperatūrinuose kietojo oksido kuro elementuose, kurių darbinė temperatūra siekia nuo 400 °C iki 700 °C [115,134,135]. Ypatingai gadolinio ir samario metalų oksidų priemaišomis legiruotas cerio oksidas pasižymi dideliu joniniu laidumu [9, 10, 44, 29, 35, 38–43].

Priemaišų koncentracija, įvairių cheminių sintezės metodų taikymas nanostruktūrinėms keramikoms gauti turi įtakos galutinės struktūros morfologinėms, struktūrinėms ir elektrinėms savybėms [36,48–51]. Pastaruoju metu taip pat siekiama parinkti tokios cheminės sudėties keramikas, kad būtų galima sumažinti darbinės kietojo oksido kuro elementų temperatūras. Sintezės produktų iškaitinimo temperatūra taip pat turi didelę įtaką elektrinėms savybėms. Parinkę, pavyzdžiui, 1100 °C sintezės produktų iškaitinimo temperatūrą gadolinio oksidu legiruoto cerio oksido keramikoms, galime tikėtis mažesnio joninio laidumo [47, 48, 60–62, 51–55, 57–59].

Taip pat sudėtinga surasti patį tinkamiausią plonų sluoksnių formavimo metodą, kuris leistų kontroliuoti plonų sluoksnių storius kelių dešimčių ar šimtų nanometrų lygmenyje. Vienas iš tinkamiausių fizikinio nusodinimo metodų – vakuuminis garinimas elektronų spinduliu, kurį pasitelkus galima suformuoti ypač plonus sluoksnius. Tačiau, reikia labai kruopščiai parinkti pirminių medžiagų-taikinių medžiagos cheminę sudėtį, kad suformuotas reikalingo storio plonas sluoksnis išlaikytų norimą metalų oksidų priemaišų koncentraciją. Todėl šiame darbe atliekamas sisteminis keraminių medžiagų tyrimas, taikant skirtingus cheminių sintezių metodus, parenkant sintezės iškaitinimo, keramikų atkaitinimo temperatūras.

MEDŽIAGOS, EKSPERIMENTINĖ ĮRANGA IR TYRIMŲ METODIKA

Cheminių sintezių metodai

Norint suprasti koks cheminės sintezės metodas yra tinkamiausias sintetinant cerio oksido stabilizuotas Gd ir Sm oksidų keramikas bei kurios metalų priemaišų koncentracijos komponentė yra tinkamiausia naudoti galutiniam produktui gauti, buvo susintetinti samario oksidu legiruoto cerio oksido (SDC) $Ce_{1-x}Sm_xO_{2-\delta}$ (čia $x = 0,1; 0,2; 0,26; 0,3$) nanomilteliai, taikant tris skirtingus cheminės sintezės metodus: degimo (CB), nusodinimo iš tirpalų (CP) ir zolių-gelių (SG). Gadolinio oksidu legiruoto cerio oksido (GDC) $Ce_{1-x}Gd_xO_{2-\delta}$, (čia $x = 0,1; 0,15; 0,2; 0,25$) nanomilteliai buvo susintetinti degimo (CB), nusodinimo iš tirpalų (CP) cheminės sintezės metodais ir jų fizikinės bei cheminės savybės buvo palygintos su SDC nanomiltelių susintetintų tais pačiais metodais, savybėmis. Norint nustatyti metalų priemaišų koncentracijos įtaką joniniam laidumui buvo susintetinti Sm ir Gd oksidais legiruoto cerio oksido (SGDC) $Ce_{1-2x}Sm_xGd_xO_{2-x}$, čia $x = 0,0875$) nanomilteliai. Sintezės iškaitinimo ir supresuotų tablečių atkaitinimo sąlygos (temperatūra, laikas, aplinka) buvo išlaikyti vienodi visoms keraminėms struktūroms, susintetintoms cheminių sintezių metodais. Parinkus tinkamas metalų priemaišų koncentracijas bei paruošus pradinius taikinius, vakuuminio garinimo elektronų spinduliu ir magnetroninio nusodinimo metodais buvo paruoštos plonos dangos.

Darbe naudojamų keraminių miltelių sąrašas, kuriame nurodyta miltelių cheminės sintezės metodų žymenys, priemaišų molinė koncentracija ir cheminė formulė, pateiktas 3.1 lentelėje.

3.1 lentelė. Darbe naudojamų keraminių miltelių sąrašas, (čia CB – degimo, CP – nusodinimo iš tirpalų, SG – zolių-gelių sintezių metodai)

Žymuo	Cheminė formulė	Priemaišų molinė koncentracija	Cheminės sintezės metodų žymenys
10 SDC	$\text{Sm}_{0,1}\text{Ce}_{0,9}\text{O}_{2-\delta}$	10 mol % Sm	CB, CP, SG
20 SDC	$\text{Sm}_{0,2}\text{Ce}_{0,8}\text{O}_{2-\delta}$	20 mol % Sm	CB, CP, SG
26 SDC	$\text{Sm}_{0,26}\text{Ce}_{0,74}\text{O}_{2-\delta}$	26 mol % Sm	CB, CP, SG
30 SDC	$\text{Sm}_{0,3}\text{Ce}_{0,7}\text{O}_{2-\delta}$	30 mol % Sm	CB, CP, SG
10 GDC	$\text{Gd}_{0,1}\text{Ce}_{0,9}\text{O}_{2-\delta}$	10 mol % Gd	CB, CP
15 GDC	$\text{Gd}_{0,15}\text{Ce}_{0,85}\text{O}_{2-\delta}$	15 mol % Gd	CB, CP
20 GDC	$\text{Gd}_{0,2}\text{Ce}_{0,8}\text{O}_{2-\delta}$	20 mol % Gd	CB, CP
25 GDC	$\text{Gd}_{0,25}\text{Ce}_{0,75}\text{O}_{2-\delta}$	25 mol % Gd	CB, CP
SGDC	$\text{Ce}_{0,825}\text{Sm}_{0,0875}\text{Gd}_{0,0875}\text{O}_{2-\delta}$	0,0875 mol % Sm ir Gd	CB, CP

Cheminiai reagentai ir tirpalai, naudoti cheminių sintezių metu:

- cerio (III) nitrato heksahidratas ($\text{Ce}(\text{NO}_3)_3 \times 6\text{H}_2\text{O}$, 99,0 %, *Fluka*);
- samario (III) nitrato heksahidratas ($\text{Sm}(\text{NO}_3)_3 \times 6\text{H}_2\text{O}$, 99,9 %, *Sigma Aldrich*);
- gadolinio (III) nitrato heksahidratas ($\text{Gd}(\text{NO}_3)_3 \times 6\text{H}_2\text{O}$, 99,9 %, *Sigma Aldrich*);
- glicinas ($\text{NH}_2\text{CH}_2\text{COOH}$, $\geq 99,0$ %, *Sigma Aldrich*);
- oksalo rūgštis ($\text{C}_2\text{H}_2\text{O}_4$, $\geq 99,0$ %, *Sigma Aldrich*);
- amonio hidroksidas 25% (NH_4OH , 25 %, *Sigma Aldrich*);
- L-(+)- vyno rūgštis ($\text{C}_4\text{H}_6\text{O}_6$) (TA) $\geq 99,5$ %, *Sigma Aldrich*);
- samario (III) oksidas (Sm_2O_3 , 99,99 %, *AlfaAesar*);
- amonio cerio (IV) nitratas ($(\text{NH}_4)_2\text{Ce}(\text{NO}_3)_4$, 99,99 %, *Sigma-Aldrich*);
- azoto rūgštis (HNO_3 , 66 %, *Reachem*);
- distiliuotas vanduo (H_2O).

Medžiagos panaudotos plonų dangų garinimui fizikiniais nusodinimo iš garų fazės metodais:

- acetonas 99,8 % ($\text{C}_3\text{H}_6\text{O}$) (*Reachem Slovakia s.r.o.*);
- N,N–dimetilformamidas ≥ 99 % (*Sigma-Aldrich*);
- azoto (N_2) dujos (*Aga Sia*, 96 %).

Disertacijos metu naudoti pagrindai: 500 μm storio komercinis silicis (Si) (dvipusio poliravimo 4 colių skersmens plokštelės, (100) ir (111) kristalografinių orientacijų, *p* tipo (*Sigma-Aldrich*)).

Cerio oksido stabilizuoti metalų oksidų nanomilteliai, susintetinti skirtingomis cheminėmis sintezėmis, buvo iškaitinti 200; 400; 600; 800; 900; 1000; 1100; 1200 °C temperatūrose 5 val. oro aplinkoje. Keraminės 10 mm skersmens tabletės iš susintetintų ir iškaitintų 800 °C temperatūroje buvo supresuotos 4 MPa slėgiu ir atkaitintos 1200 °C temperatūroje 2 val. oro aplinkoje.

Plonų dangų formavimo metodai

Vakuuminis garinimas elektronų spinduliu

SDC ir GDC supresuotos tabletės buvo naudojamos kaip taikiniai formuojant plonasluoksnes dangas ant skirtingų padėklų taikant vakuuminio garinimo elektronų spinduliu metodą. Sluoksnių storis kito nuo ~100 nm iki ~1 μm ir buvo kontroliuojamas kvarcinio jutiklio garinimo proceso metu. Garinimo proceso technologiniai parametrai pateikti 3.2 lentelėje.

3.2 lentelė. Vakuuminio garinimo elektronų spinduliu technologiniai parametrai

Vakuumo slėgis	10^{-5} Pa
Garinimo slėgis	0,7 Pa
Elektronų spindulio galia	10 kW
Maksimali srovė	500 mA
Elektronų spindulio atsilenkimo kampas	180°
Elektronų spindulio skersmuo	5 mm
Pagrindo temperatūra	200 $^\circ\text{C}$
Augimo greitis	~2 nm/s
Atstumas tarp elektronų spindulio ir pagrindo	250 mm
Dangų storio fiksavimas	Kvarcinis jutiklis

Nuolatinės srovės reaktyvusis magnetroninis dulkinimas

CeO_2 ir Gd_2O_3 plonos dangos buvo formuojamos nuolatinės srovės reaktyviuoju magnetroniniu dulkinimu reaktyvioje O_2/Ar dujų aplinkoje “*Leybold Heraeus-A-700-QE*” vakuuminėje sistemoje ant Si (111) pagrindo. Plonų sluoksnių nusodinimas buvo atliekamas naudojant grynus Ce (99,99 %) ir Gd (99,99 %) taikinius toje pačioje kameroje. Cerio oksido, stabilizuoto gadolinio oksidu (GDC), danga buvo nusodinama „sumuštinio“ principu, t. y. pirmiausia ant Si (111) padėklo nusodinamas $\text{Ce}_{x/1}\text{O}_{y/1}$ sluoksnis, po to $\text{Gd}_{x/2}\text{O}_{y/2}$, išlaikant 90 % $\text{Ce}_{x/1}\text{O}_{y/1}$ ir 10 % $\text{Gd}_{x/2}\text{O}_{y/2}$ santykį. Buvo suformuotos 4, 6 ir 12 Gd ir Ce oksidų sluoksniai (toliau tekste žymima GDC4, GDC6, GDC12). Visų suformuotų dangų galutinis storis buvo ~600–700 nm. Suformuoti ploni sluoksniai buvo atkaitinti 700 $^\circ\text{C}$ temperatūroje 1 val. Plonų dangų magnetroninio dulkinimo technologiniai parametrai pateikti 3.3 lentelėje.

3.3 lentelė. Magnetroninio dulkinimo parametrai

Vakuumo slėgis	2×10^{-4} Pa
Garinimo dujos	O_2/Ar dujų mišinys
Garinimo dujų slėgis	0,065 Pa
Takiniai	Ce (grynumas 99,99 %) ir Gd (grynumas 99,99 %)
Pagrindo temperatūra	150 $^\circ\text{C}$
Atstumas tarp taikinio ir pagrindo	16 cm
Įtampa	510 V
Srovė	0,4 A
Dangų storio fiksavimas	Kvarcinis jutiklis

Analitiniai tyrimo metodai

Toliau, 3.4 lentelėje, pateikiami darbe taikyti analitiniai tyrimo metodai ir naudota aparatūra.

3.4 lentelė. Analitinių tyrimo metodų ir tyrimų metu naudotos aparatūros santrauka

Metodai	Tyrimo metodai	Naudota aparatūra
Terminė analizė	Diferencinė skenuojamoji kalorimetrija (DSC)	6000 PerkinElmer kartu su DSC/DTA ir TGA
	Termogravimetrinė analizė (TGA)	
	Diferencinė terminė analizė (DTA)	
Struktūrinė analizė	Rentgeno spindulių difrakcija (XRD)	D8 Discover (Bruker AXS GmbH) difraktometras
	Rentgeno spindulių fotoelektroninė spektroskopija (XPS)	Thermo Scientific ESCALAB 250Xi
	Ramano spektroskopija	Renishaw inVia Raman spektrometras
Paviršiaus ploto tyrimai	Brunauer-Emmett-Teller tyrimas (BET)	KELVIN 1042 sorptometras
Elementinės sudėties analizė	Elektroninė dispersinė mikroskopija (EDX)	Quanta 200 FEG (FEI) kartu su rentgeno spindulių spektrometru Bruker XFlash 4030
	Induktyviai aktyvinta plazma optinės emisijos spektroskopija (ICP-OES)	ICP-OES, Vista-Pro, Varian
	Infraraudonųjų spindulių Furjė transformacijos spektroskopija (FT-IR)	Vertex 70 FT-IR spektrometras (Bruker Optik GmbH)
Topografijos ir morfologijos analizė	Skenuojamoji elektroninė mikroskopija (SEM)	Quanta 200 FEG (FEI) kartu su rentgeno spindulių spektrometru Bruker XFlash 4030
	Skvarbioji elektroninė mikroskopija (TEM)	Tecna G2 F20 X-TWIN (FEI, Nyderlandai, 2011)
	Atominių jėgų mikroskopija (AFM)	NT-206 (Microtestmachines Co.)
Elektrinių savybių analizė	Elektrocheminio impedanso spektroskopija (EIS)	Solartron 1255 automatinė sistema susrovės-įtampos maitinimo bloku LM7171; Alpha-AK analizatorius (Novocontrol Technologies) kartu su aukštatemperatūne (1200 °C) krosnimi

REZULTATAI IR JŲ APTARIMAS

Šiame skyriuje pateikti samario oksidu legiruoto cerio oksido, gadolinio oksidu legiruoto cerio oksido ir samario bei gadolinio oksidais legiruoto cerio oksido nanomiltelių, susintetintų skirtingais sintezių metodais, keramikų ir suformuotų

vakuuminio garinimo elektronų spinduliu bei magnetroniniu garinimu plonų dangų tyrimų eksperimentiniai rezultatai.

Samario oksidu legiruotas cerio oksidas

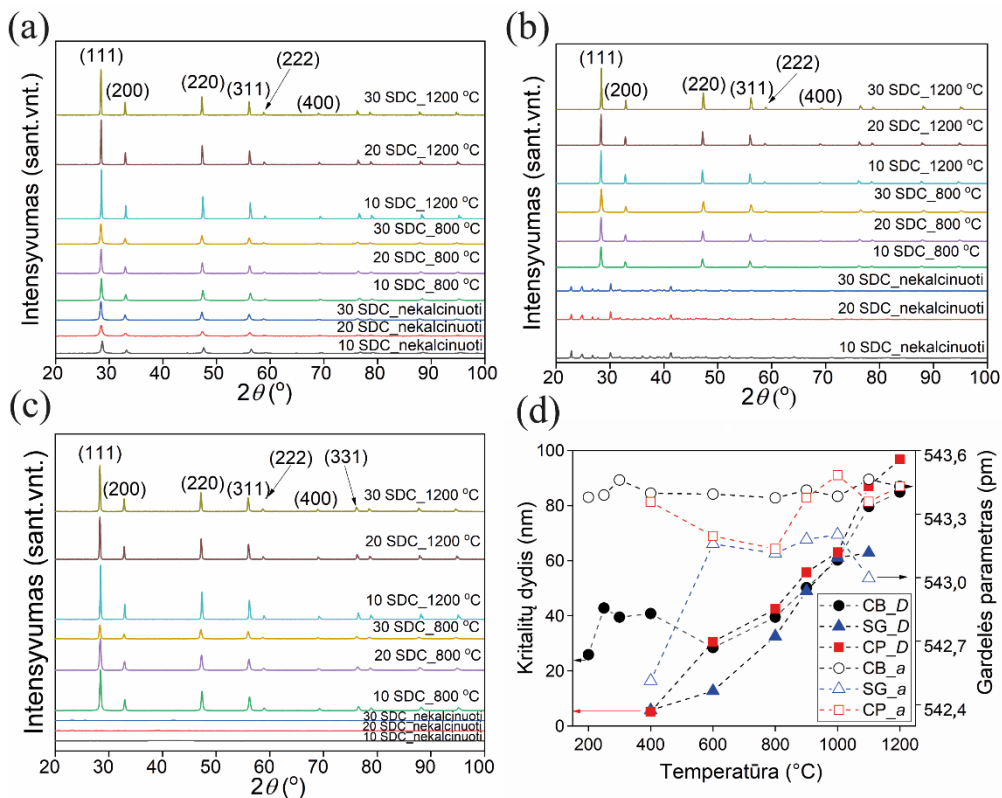
Samario oksidu legiruoto cerio oksido (SDC) nanomiltelių sintezė ir tyrimai

Samariu stabilizuoto cerio oksido taikytos skirtingos cheminės sintezės, leido pasirinkti atitinkamus sintezės procesų parametrus bei gauti susintetintus nanomiltelius su atitinkamomis fizikinėmis savybėmis.

Remiantis termogravimetrinės analizės rezultatais, degimo sintezės metodu (CB) susintetintų 20S DC miltelių terminis cheminių junginių išskaidymas susideda iš trijų sintezės produkto masės pokyčių. 20 SDC miltelių gautų nusodinimo būdu, cheminės reakcijos sutampa su oksalatų hidratų reakcijomis. 20 SDC miltelių gautų zolių-gelių metodu, cheminių junginių išskaidymas parodė, kad sintezės produktų masė sumažėja 34,79 %, o tai būdinga cheminėms reakcijoms su vyno rūgštimi esant 29,85 °C ir 311,73 °C temperatūrų intervalui [89]. Tolesnis temperatūros kėlimas sąlygoja vyno rūgšties junginių skilimą ir susidariusio gelio junginių procesą, kuris baigiasi ties ~391,94 °C temperatūra. Po to prasideda dvigubo oksido reakcija ir $\text{Ce}_{0,8}\text{Sm}_{0,2}\text{O}_{2-\delta}$ junginio kristalizacija. Kaip ir CP atveju, gelinio prekursoriaus išskaidymas ir temperatūros kėlimas nuo 391,94 °C iki 699,85 °C sąlygoja nedidelį sintezės produkto masės pokytį iki 0,87 %. Kiekvienos sintezės metu, kristalizacijos ir išskaidymo procesas, esant žemesnei nei 896,85 °C temperatūrai, yra skirtingas. Be to, SDC miltelių sintezė, taikant nusodinimo iš tirpalų (CP) ir zolių-gelių (SG) sintezių metodus, tampa stabili 700 °C temperatūroje, o taikant degimo sintezės metodą (CB) sintezė išlieka stabili ir žemose temperatūrose.

Susintetintų $\text{Ce}_{1-x}\text{Sm}_x\text{O}_{2-\delta}$ miltelių Sm kiekis junginyje, remiantis ICP–OES ir EDX tyrimais, sutampa su teoriniais skaičiavimais. Rezultatai apie elementinės sudėties tyrimus paskelbti [A1].

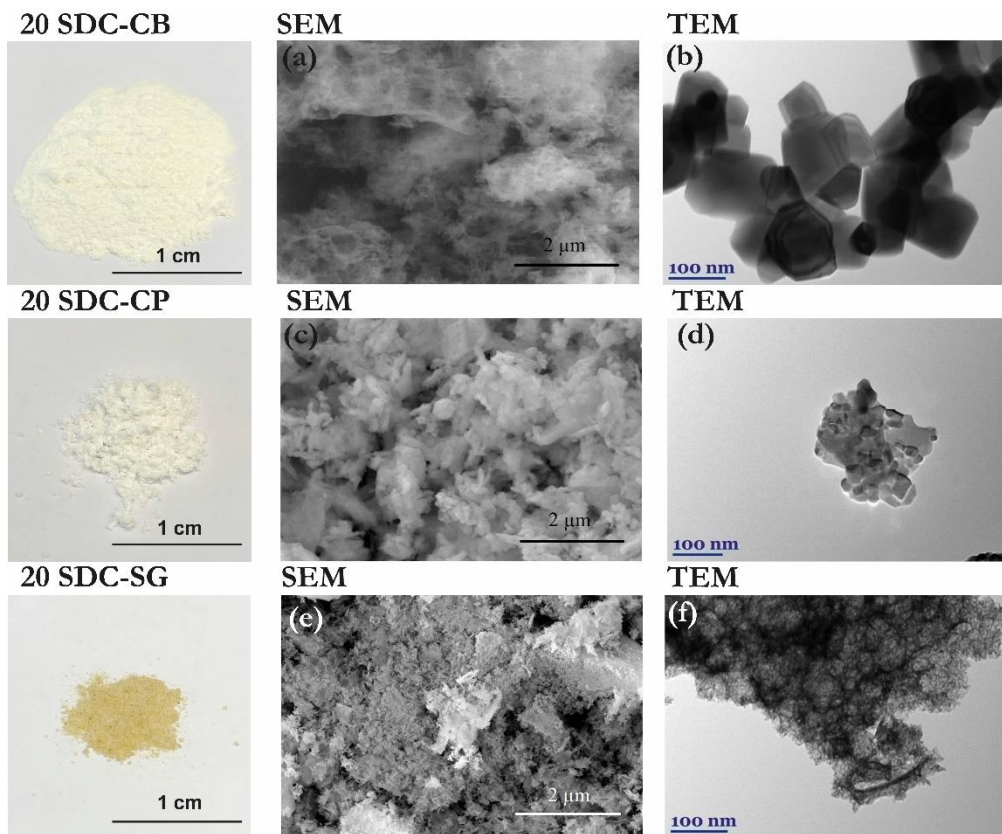
SDC susintetintų trimis skirtingais cheminių sintezių metodais nanomiltelių, iškaitintų 800 °C ir 1200 °C temperatūrose 5 val. rentgeno struktūrinės analizės tyrimo (XRD) rezultatai pateikiami 4.1 paveiksle. Nepriklausomai nuo pasirinkto sintezės metodo, visi SDC nanomilteliai pasižymi gryna kubine, Fm-3m tipo fluorito tipo struktūra (JCPDS Nr. 75-0158). SDC-CB bandinių matomos (111), (200), (220) ir (311) kristalografinių orientacijų smailės, esant visoms miltelių atkaitinimo temperatūroms. Rentgeno struktūrinės analizės tyrimų rezultatuose SDC-CP neatkaitintų miltelių buvo pastebėtos papildomos smailės, kurios galėjo atsirasti dėl prekursoriaus–oksalo rūgšties naudojimo [87,90].



4.1 pav. SDC nanomiltelių susintintų a) degimo, b) nusodinimo iš tirpalų, c) zolių-gelių sintezės metodais bei iškaitintų 800 °C ir 1200 °C temperatūrose, rentgenogramos; d) 20 SDC nanomiltelių, susintintų skirtingais cheminių sintezės metodais (CP – nusodinimo iš tirpalų, CB – degimo, SG – zolių-gelių) kristalitų dydžio, D , ir gardelės parametro, a , priklausomybė nuo nanomiltelių iškaitinimo temperatūrų

Nepriklausomai nuo pasirinkto sintezės metodo, didinant nanomiltelių iškaitinimo temperatūrą, smailių intensyvumas didėja, o pusplotis mažėja, tai reiškia, kad didėja medžiagos kristališkumas. Apskaičiuoti kristalitų dydžiai ir gardelės parametrai pateikiami 4.1 (d) paveiksle. Kaip galime matyti iš XRD rezultatų pritaikius SDC sintezei degimo sintezės metodą, kristalitų augimo greitis sparčiai didėja pagal atkaitinimo temperatūrą, bei aušinimo greitį ypač esant 126,85 °C–426,85 °C temperatūros intervalui. Po pirminio egzoterminio junginių skilimo, toliau didinant temperatūrą, nusistovi įprastas kristalitų augimo greitis. Toliau didinant nanomiltelių iškaitinimo temperatūrą kristalitų dydžiai sumažėja. Remdamiesi XRD tyrimais galime teigti, kad SDC-CB nanomiltelių sintezei reikia didesnės iškaitinimo temperatūros, kad gautume vienfazį junginį lyginant nanomiltelius gautus kitais SDC-CP ir SDC-SG sintezės būdais.

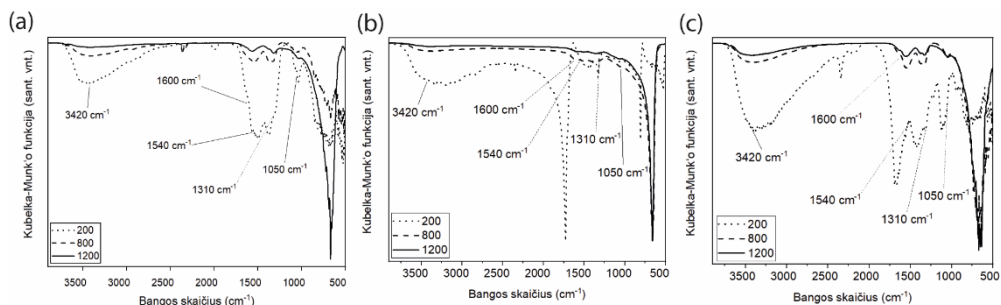
4.2 paveiksle pateikiami $\text{Ce}_{0,8}\text{Sm}_{0,2}\text{O}_{2-\delta}$ nanomiltelių SEM ir TEM vaizdai, kurie buvo gauti skirtingais sintezės metodais, iškaitinant nanomiltelius 800 °C temperatūroje 5 val. Iš gautų TEM vaizdų buvo nustatyta, kad SDC nanomiltelių mikrostruktūra sudaryta iš ~36–90 nm dydžio grūdelių.



4.2 pav. 20 SDC nanomiltelių, susintetintų CB – degimo, CP – nusodinimo iš tirpalų, SG – zolių-gelių sintezių metodais ir iškaitintų 800 °C temperatūroje, SEM ir TEM vaizdai

Iš SEM nuotraukų (4.2 pav.) galime teigti, kad susintetintų CB metodu nanomiltelių struktūra yra porėtos „kempinės“ pavidalo, taikant CP ir SG sintezių metodus, susidaro netaisiklingos formos aglomeratai, padengti mažesnio dyžio dalelėmis.

Remdamiesi skirtingų koncentracijų 10 SDC, 20 SDC ir 30 SDC nanomiltelių FT–IR spektrais, matome, kad esminių skirtumų spektruose nebuvo pastebėta taikant skirtingus cheminių sintezių metodus. Todėl darbe pateikiami tik 20 SDC koncentracijos nanomiltelių FT–IR spektrai, esant skirtingiems cheminių sintezių metodams (4.3 pav.). Visuose spektruose buvo pastebėta smailė ties 2500–3800 cm^{-1} , kurią sąlygoja O–H grupė, atsirandanti dėl vandens adsorbcijos iš aplinkos [93]. Taip pat stebima ir CO_2 molekulių adsorbcija ant paviršiaus, dėl šios priežasties keliuose spektruose matomos smailės 2300–2400 cm^{-1} intervale. Dėl organinių junginių susidarymo sintezės metu žemose temperatūrose, matomos anglies junginių smailės (1000–1600 cm^{-1} intervale) [94].

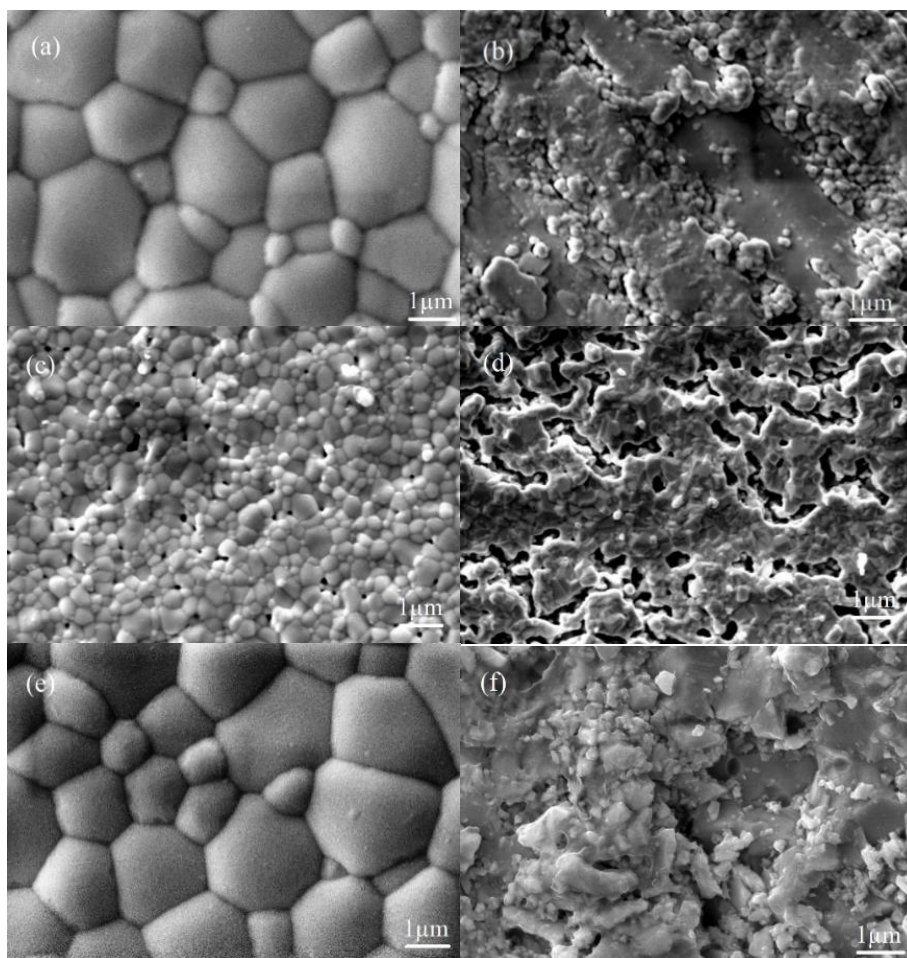


4.3 pav. FT–IR spektrai 20 SDC miltelių susintetintų a) degimo, b) nusodinimo iš tirpalų, c) zolių–gelių sintezės metodais

SDC-CP milteliai turi mažiausią anglies junginių kiekį. Tačiau milteliai išdžiovinę 200 °C temperatūroje CP ir SG būdu, turi smailę ties 1700 cm^{-1} , kuri yra būdinga karbonilo funkcinėms grupėms [96]. Buvo gauta, kad didinant iškaitinimo temperatūrą SDC nanomiltelių grynumas didėja (išgarinami organiniai junginiai, bei formuojasi stabilūs oksidai). Tačiau ir esant aukščiausiai atkaitinimo temperatūrai (1200 °C), SDC-CB ir SDC-SG susintetintuose milteliuose FT–IR spektruose stebima smailė yra žemiau 770 cm^{-1} , tai būdinga metalų oksidams [94, 97]. Šios smailės intensyvumas didėja, didinant nanomiltelių iškaitinimo temperatūrą. Kadangi CeO_2 junginių kreivės intensyvumas didėja, o kitų junginių smailių intensyvumai mažėja, galime teigti, kad didėja medžiagos grynumas (formuojasi SDC).

Samario oksidu legiruoto cerio oksido (SDC) keramikų tyrimai

SDC tablečių, kurios buvo atkaitintos 1200 °C temperatūroje 2 val., SEM nuotraukos pateikiamos 4.4 paveiksle. Kaip matome iš paviršiaus topografijos vaizdų, tablečių, suformuotų naudojant 20 SDC-CB miltelius, grūdelių dydis yra ~2,1 μm ir pasižymi tankesne struktūra nei tabletės, suformuotos iš 20 SDC-CP ir 20 SDC-SG miltelių, kurių grūdelių dydžiai atitinkamai yra ~0,5 μm ir ~2,0 μm .



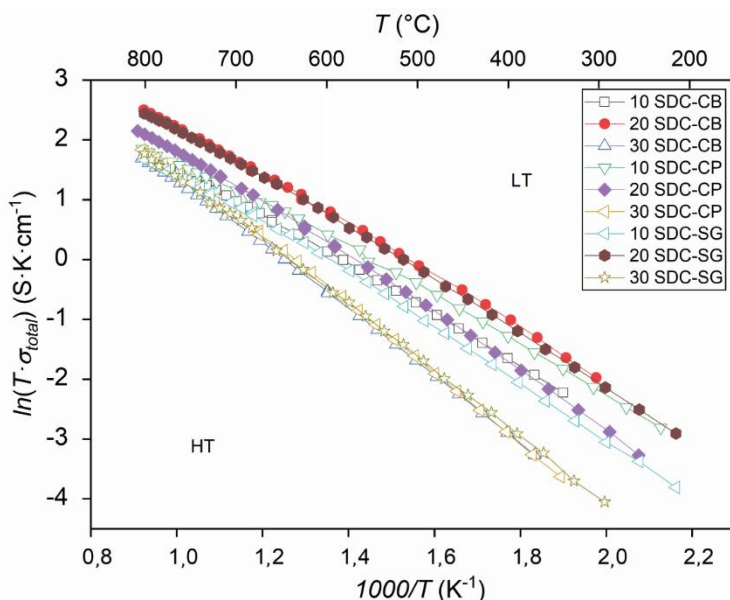
4.4 pav. 20 SDC supresuotų keramikų, susintetintų (a ir b) degimo, (c ir d) nusodinimo iš tirpalų, (e ir f) zolių-gelių sintezių metodais, SEM paviršiaus topografijos (a, c, e) ir skerspjuvio (b, d, f) vaizdai

Iš kompleksinės varžos spektroskopijos tyrimų matome, kad visų SDC tablečių, nepriklausomai nuo taikytų cheminių sintezės metodų ir Sm koncentracijos, turi skirtingas Nykvisto kreives. Iš gautų rezultatų matome, kad geriausias savitojo laidžio rezultatas, gautas 600 °C temperatūroje, yra: 20 SDC-CB keramikų $1,1 \times 10^{-2} \text{ S} \times \text{cm}^{-1}$, 20 SDC-CP keramikų $0,92 \times 10^{-2} \text{ S} \times \text{cm}^{-1}$ ir 20 SDC-SG $0,95 \times 10^{-2} \text{ S} \times \text{cm}^{-1}$, visų SDC skirtingų koncentracijų ir cheminių sintezių aktyvacijos energijos ir savitojo laidžio rezultatai pateikti 4.1 lentelėje.

4.1 lentelė. Skirtingų koncentracijų SDC keramikų, susintetintų CB – degimo, CP – nusodinimo iš tirpalų, SG – zolių-gelių sintezių metodais, aktyvacijos energijos, ΔE_a , ir joninio laidžio, σ , rezultatai

Bandinių žymuo	ΔE_a , eV		σ , $10^{-2} \text{ S} \times \text{cm}^{-1}$		
	LT	HT	400 °C	600 °C	800 °C
10 SDC-CB	0,81	0,61	0,67	0,71	2,06
20 SDC-CB	0,88	0,77	0,82	1,10	3,04
30 SDC-CB	1,11	0,97	0,03	0,59	1,47
10 SDC-CP	0,84	0,70	0,67	0,79	2,18
20 SDC-CP	0,95	0,80	0,78	0,92	2,35
30 SDC-CP	1,14	0,98	0,04	0,47	1,82
10 SDC-SG	0,92	0,71	0,34	0,70	2,16
20 SDC-SG	0,89	0,78	0,58	0,95	2,65
30 SDC-SG	1,10	0,99	0,08	0,54	1,67

Joninio laidžio priklausomybė nuo atvirkštinės temperatūros kinta pagal Arenijaus dėsnį, rezultatai pateikti 4.5 paveiksle. Iš grafiko matome, kad galime išskirti aukštų (HT) ir žemų (LT) temperatūrų sritis. Tai galima būtų paaiškinti, remiantis CeO_2 vykstančiomis reakcijomis gardelėje bei defektų sąveika [103, 104].

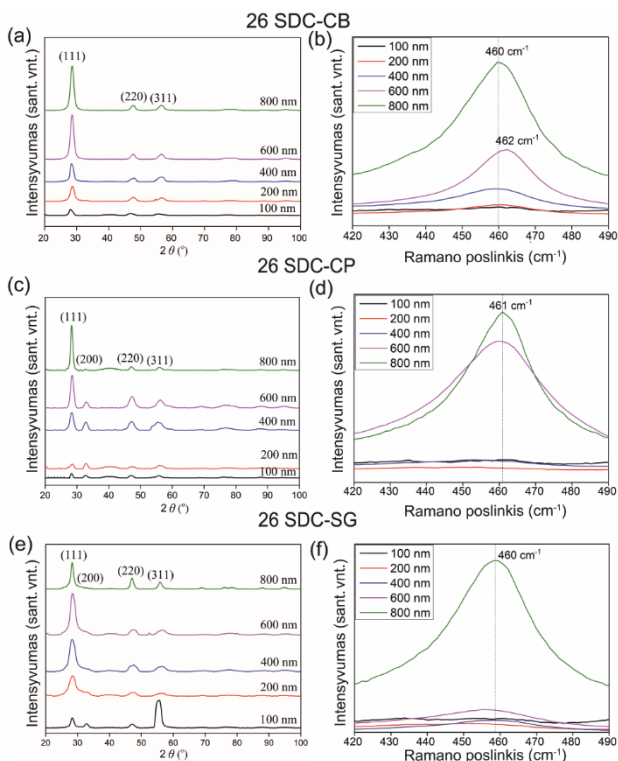


4.5 pav. SDC keramikų, susintetintų CB – degimo, CP – nusodinimo iš tirpalų, SG – zolių-gelių sintezių metodais, Arenijaus grafikai. Punktyrine linija atskirtos HT – aukštų temperatūrų, LT – žemų temperatūrų sritys

Žemiausios keramikų aktyvacijos energijos gautos tiek aukštų, tiek žemų temperatūrų intervaluose naudojant SDC-CB sintezės metodu susintetintus miltelius.

Samario oksidu legiruoto cerio oksido (SDC) plonų dangų formavimas ir tyrimai

Plonasluoksnių dangų formavimui buvo naudojamos 26 SDC koncentracijos supresuotos 10 mm skersmens tabletės–taikiniai. Plonasluoksnes dangos buvo formuojamos garinant nanomiltelius bei naudojant vakuuminę garinimo elektronų spindulio sistemą. Garinimo proceso metu buvo siekiama suformuoti plonasluoksnes dangas, kurių storis siektų 100 nm, 200 nm, 400 nm, 600 nm ir 800 nm. Suformuotų dangų ant Si pagrindo rentgeno struktūrinės analizės rezultatai pateikiami 4.6 pav. Visų gautų bandinių, nepriklausomai nuo sintezės metodo ar dangos storio, XRD analizės tyrimai parodė, kad gautos smailės atitinka fluorito tipo struktūrą. Kinta tik smailių intensyvumas, kuris priklauso nuo dangos storio. Kristalitų dydžiai esant 800 nm dangos storiui buvo gauti 73,4 nm, 74,2 nm ir 86,7 nm atitinkamai 26-SDC-CB, 26-SDC-CP ir 26-SDC-SG dangoms. Lygindami tarpusavyje plonasluoksnių keramikų rentgenogramas matome, kad keramikų, suformuotų naudojant 26-SDC-CP pradinius miltelius, rentgenograma turi papildomą (200) smailę ir smailės intensyvumas mažėja, didėjant dangos storiui, o visai išnyksta esant 800 nm dangos storiui. Iš 26-SDC-SG rentgenogramos matome, kad (311) orientacijos smailės intensyvumas yra didelis, esant 100 nm dangos storiui.



4.6 pav. 26-SDC plonų dangų, suformuotų iš pradinių miltelių, susintetintų (a, b) degimo, (c, d) nusodinimo iš tirpalų, (e, f) zolių–gelių sintezių metodais ant Si padėklo, rentgenogramos (a, c, e) ir Ramano spektrai (b, d, f)

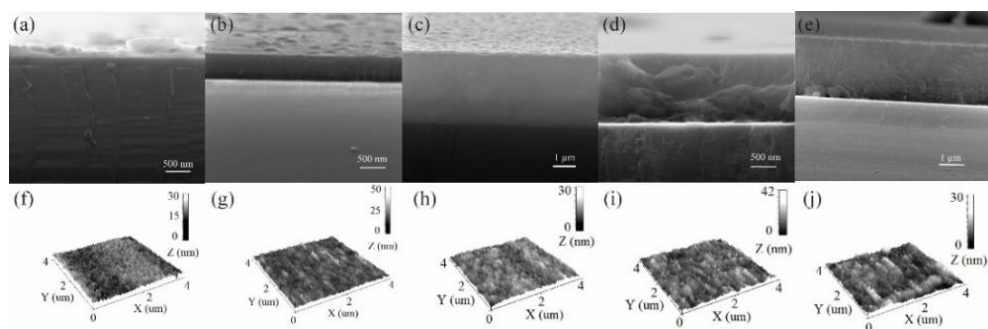
Remiantis Ramano spektroskopijos tyrimais, intensyviausios smailės (460–461 cm^{-1}) esant 800 nm dangos storiui 4.6(c), 4.6(d), 4.6(e) paveiksluose. Ramano spektroskopijos tyrimai, kaip ir rentgeno struktūrinės analizės tyrimai patvirtina, kad didėjant dangos storiui, smailių intensyvumas didėja, o tai parodo didėjantį dangos kristališkumą.

4.2 lentelė. SDC plonų dangų storio rezultatai

Bandinių žymuo	Planuotas garinimo proceso metu dangų storis, nm				
	100	200	400	600	800
	Dangų storis iš SEM tyrimų, nm				
26-SDC-CB	95	548	1801	1020	1850
26-SDC-CP	105	333	475	2041	1548
26-SDC-SG	75	356	602	887	1676

Atsirandantys storio nuokrypiai gali būti sąlygoti išgarintos medžiagos iš taikinio srauto, kadangi srautą gali sudaryti tiek atomai, tiek atomų klasteriai. Nevienalyčio junginio garinimas yra sudėtingas procesas, kadangi gautos dangos storis ir cheminė sudėtis priklauso nuo daugelio parametrų. Įtaką dangos storiui ir jos struktūrai gali daryti elektronų spindulio galia, padėklo temperatūra, nusodinimo greitis, garinimo laikas, taip pat garinamos sudėtinės medžiagos.

Iš SEM ir AFM rezultatų matome, kad suformuotos dangos pasižymi tankia struktūra, tačiau jų paviršius šiurkštus (4.7pav.).



4.7 pav. Skirtingų storių (a, b) 100 nm, (c, d) 200 nm, (e, f) 400 nm, (g, h) 600 nm, (i, j) 800 nm 26-SDC-CB plonų dangų ant Si pagrindo SEM ir 3D AFM vaizdai

Didžiausiu paviršiaus šiurkštumu (R_q) pasižymi keramikos suformuotos iš miltelių 26-SDC-CB, kurių sluoksnio storis buvo 600 nm. Didžiausias šiurkštumas buvo 4,7 nm, o mažiausias 2,8 nm bandinių, kurių storis 100 nm ir 400 nm. Paviršiaus šiurkštumas priklauso nuo nusodinimo laiko, esant skirtingoms elektronų spindulio galioms [107]. Didinant elektronų spindulio galią, didėja padėklo temperatūra, garinamo srauto energija ir dalelių kinetinė energija [81, 107].

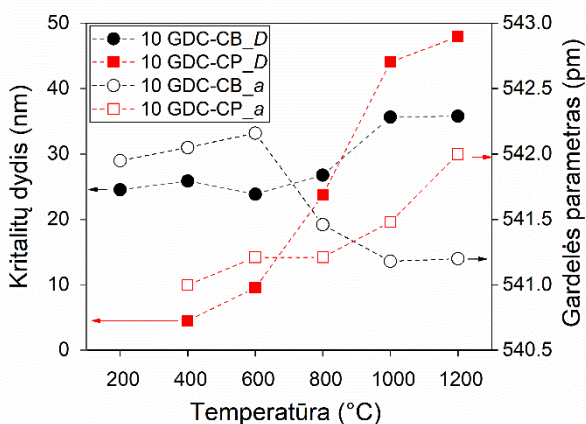
Apibendrinant gautus eksperimentinius rezultatus, geriausiomis savybėmis pasižymėjo dangos, suformuotos garinant SDC-CB miltelius. Deguonies jonų laidumas priklauso nuo Sm_2O_3 priemaišų koncentracijos ir pasiekia didžiausią vertę esant 20 mol %.

Taigi tolesniuose eksperimentuose sintetinant GDC miltelius buvo pasirinkti degimo ir nusodinimo iš tirpalų sintezės metodai, dėl savo pirminių medžiagų kainos ir paties paprastesnio sintezių proceso.

Gadolinio oksidu legiruotas cerio oksidas

Gadolinio oksidu legiruoto cerio oksido (GDC) nanomiltelių sintezė ir tyrimai

Tiriant GDC nanomiltelius, gautus skirtingų cheminių sintezių metodais, buvo pastebėtos tos pačios skilimo produktų ir kristalizacijos tendencijos, kaip ir sintetinant SDC nanomiltelius. Rentgeno struktūrinės analizės tyrimai parodė, kad GDC miltelių kristalinės gardelės konstantos ir kristalitų dydis yra mažesni lyginant su SDC milteliais. Tai galėjo sąlygoti skirtingas priemaišų jonų spindulys Sm^{+3} (1,079 Å), Gd^{+3} (1,053 Å) [108].

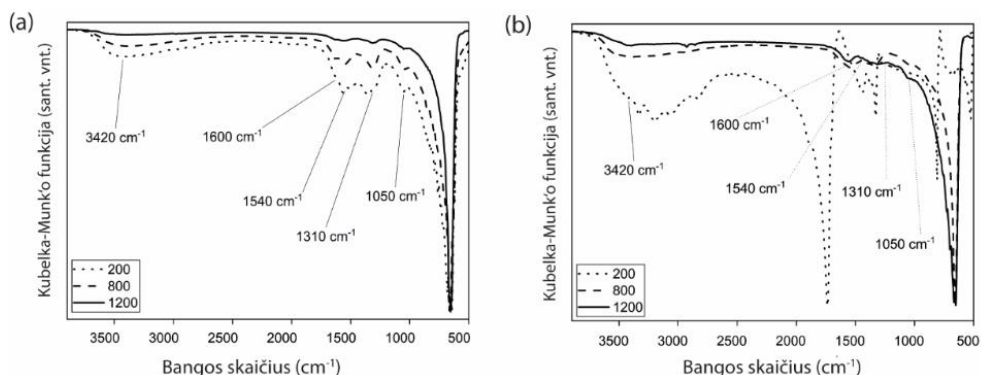


4.8 pav. Kristalitų dydžio (D) ir gardelės parametro (a) priklausomybė nuo iškaitinimo temperatūrų 10 GDC nanomilteliams, suformuotiems CP – nusodinimo iš tirpalų ir CB – degimo sintezių metodais

Cheminių sintezių (CP ir CB) metu iškaitinimo temperatūros įtaka gardelės konstantai ir kristalitų dydžiui pateikta 4.8 paveiksle. Kaip matome 10 GDC-CB miltelių kristalinės gardelės konstanta mažėja 600–1000 °C temperatūrų intervale ir didesnėse temperatūrose (daugiau nei 1000 °C) gardelės konstanta stabilizuojasi (nebekinta). Gardelės konstantos pokyčius galime sieti su nepakankama iškaitinimo temperatūra ir nepilnu oksidų susidarymu. Esant 10 GDC-CP milteliams, gardelės konstanta didėja, didinant iškaitinimo temperatūrą.

Visų susintetintų GDC nanomiltelių FT–IR tyrimai rodo tas pačias dominuojančias smailes, kaip ir SDC miltelių (4.9 pav.). Tačiau GDC smailių intensyvumas yra mažesnis lyginant su SDC smailėmis, net ir žemesnėse iškaitinimo temperatūrose, o tai leidžia spręsti apie didesnę miltelių grynumą. Po paskutinio iškaitinimo organinių liekanų kiekis žymiai sumažėjo, tą patvirtina ir FT–IR smailės. Matome, kad CeO_2 smailių intensyvumas didėja, didinant iškaitinimo temperatūrą, o

kitų smalių išnykimas/intensyvumo sumažėjimas patvirtina didesnę GDC miltelių grynumą.

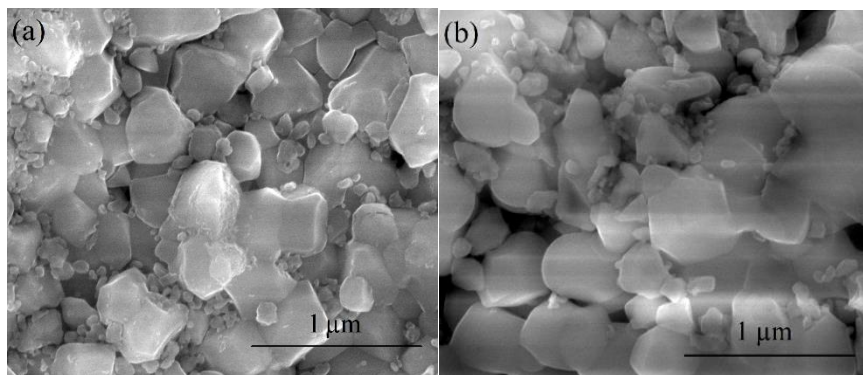


4.9 pav. FT–IR spektrai 10 GDC miltelių susintetintų a) degimo, b) nusodinimo iš tirpalų sintezės metodais

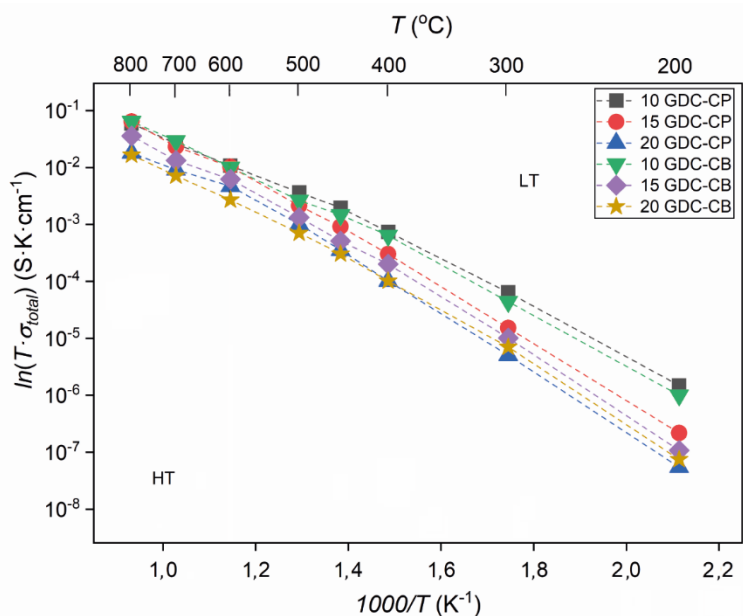
Gadolinio oksidu legiruoto cerio oksido (GDC) keramikų tyrimai

GDC tablečių, atkaitintų 1200 °C temperatūroje 5 val., SEM tyrimai parodė (4.10 pav.), kad vidutinis grūdelių dydis yra 0,32 μm (10 GDC-CP) ir 0,31 μm (10 GDC-CB). Kaip matome, grūdelių dydis yra panašus, tačiau grūdeliai yra netolygiai pasiskirstę tablečių presavimo metu.

Arenijaus grafikas, joninio laidžio priklausomybė nuo atvirkštinės temperatūros pateikiami 4.11 paveiksle. Kaip ir SDC atveju, galime išskirti aukštos (HT) ir žemos (LT) temperatūros intervalą. Aktyvacijos energijos vertės (ΔE_a) ir laidumo vertės, esant skirtingoms temperatūroms, gautos iš Arenijaus grafiko, pateikiamos 4.3 lentelėje.



4.10 pav. 10 GDC supresuotų keramikų, atkaitintų 1200 °C temperatūroje, susintetintų (a) nusodinimo iš tirpalų ir (b) degimo sintezių metodais, SEM paviršiaus topografijos vaizdai



4.11 pav. Skirtingos koncentracijos GDC keramikų, susintetintų CB –deginimo, CP – nusodinimo iš tirpalų sintezių metodais, Arenijaus grafikai

4.3 lentelė. Skirtingų koncentracijų DGC keramikų, susintetintų CB – degimo, CP – nusodinimo iš tirpalų sintezių metodais, aktyvacijos energijos, ΔE_a , ir joninio laidžio, σ , rezultatai

Bandinių žymuo	ΔE_a , eV		$\sigma \times 10^{-2}$, S \times cm $^{-1}$		
	LT	HT	400 °C	600 °C	800 °C
10 GDC-CP	0,85	0,67	0,07	1,10	5,9
15 GDC-CP	0,95	0,80	0,03	0,94	5,8
20 GDC-CP	0,99	0,85	0,01	0,68	1,6
10 GDC-CB	0,85	0,72	0,06	1,00	6,0
15 GDC-CB	0,92	0,84	0,02	0,80	5,5
20 GDC-CB	0,96	0,86	0,01	0,67	1,7

Iš gautų rezultatų galime teigti, kad didėjant Gd₂O₃ molinei koncentracijai aktyvacijos energija didėja, o bendras joninis laidumas mažėja. Taigi matome, kad geriausias joninis laidumas esant 600 °C temperatūrai buvo nustatytas tablečių, kurios pagamintos iš 10 GDC-CP ($1,1 \times 10^{-2}$ S \times cm $^{-1}$) ir 10 GDC-CB (1×10^{-2} S \times cm $^{-1}$) nanomiltelių. Atitinkamai aktyvacijos energijos žemųjų temperatūrų diapazone 0,85 eV abiejų medžiagų, o aukštųjų temperatūrų diapazone 0,65 eV 10 GDC-CP ir 0,72 eV 10 GDC-CB.

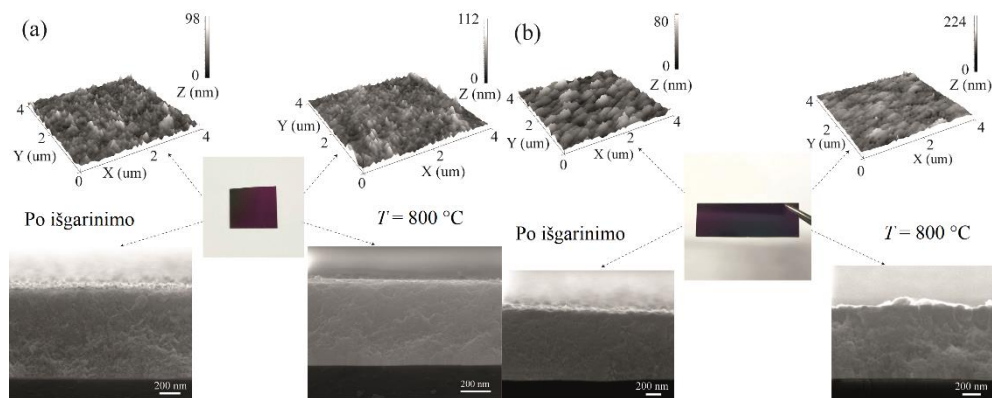
Gadolinio oksidu legiruoto cerio oksido (GDC) plonų dangų formavimas ir tyrimai

GDC plonų dangų formavimas vakuuminio garinimu elektronų spindulių metodu

Ploni sluoksniai buvo suformuoti garinant elektronu spinduliu tabletes pagamintas iš $\text{Ce}_x\text{Gd}_{1-x}\text{O}_{2-x/2}$ miltelių. Suformuoti GDC sluoksniai buvo papildomai atkaitinti 600 °C, 700 °C, 800 °C ir 900 °C temperatūrose 1 val. oro aplinkoje. Plonų sluoksnių cheminės sudėties rezultatai pateikiami 4.4 lentelėje.

4.4 lentelė. GDC plonų sluoksnių, suformuotų iš pradinių miltelių, susintetintų CP ir CB cheminėmis sintezėmis, sudėties tyrimai

Bandinių žymuo	Nustatytas Gd kiekis GDC keramikoje iš ICP-OES tyrimų	Nustatytas Gd kiekis GDC keramikoje iš XPS tyrimų	Gd ₂ O ₃ molinis kiekis dangose (mol %)	Gd ₂ O ₃ molinio kiekio sumažėjimas (%)
10-GDC-CP	0,133	0,131	6,9	31,0
15-GDC-CP	0,212	0,199	11,3	24,7
20-GDC-CP	0,265	0,261	14,4	28,0
10-GDC-CB	0,135	0,132	7,1	29,0
15-GDC-CB	0,213	0,201	11,4	24,0
20-GDC-CB	0,264	0,260	14,0	30,0

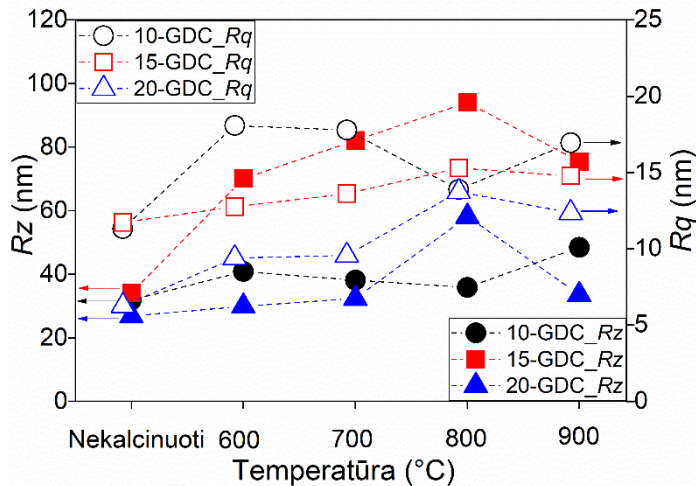


4.12 pav. SEM, 3D AFM vaizdai ir foto nuotraukos: (a) 10-GDC ir (b) 15-GDC plonų sluoksnių suformuotų garinimo elektronų spinduliu proceso metu (kairėje) ir atkaitintų 800 °C temperatūroje (dešinėje)

Iš gautų rezultatų matome, kad Gd₂O₃ koncentracija plonuose sluoksniuose apie 28 % mažesnė, lyginant su pradine tablečių medžiagos koncentracija. Garinant 15 GDC miltelių taikinį, formuojami 10 GDC ploni sluoksniai, o 10 GDC pasižymi geriausiu joniniu laidžiu (4.11 pav.) [109]. GDC plonų sluoksnių paviršiaus morfologijos ir šiurkštumo tyrimai, AFM tyrimai pateikiami 4.12 paveiksle.

Remdamiesi SEM tyrimais matome, kad plonų sluoksnių atkaitinimas daro įtaką paviršiaus morfologijai ir dangos storiui. Suformuoti GSC-CP sluoksniai pasižymi tankia nano struktūra. Be to, paviršiaus šiurkštumas kinta pagal atkaitinimo temperatūrą ir didėjant temperatūrai formuojasi struktūra su smailiomis iškilėmis paviršinėmis struktūromis (R_{ku}), kurių aukštis siekia apie 3 nm.

Plonasluoksnių keramikų paviršiaus morfologijos šiurkštumo vertės pateikiamos 4.13 pav. 10GDC-CP keramikų paviršiaus šiurkštumo (R_q) vertės yra didžiausios 18,08 nm, kai atkaitinimo temperatūra 600 °C, o mažiausios vertės 11,32 nm gaunamo tik suformuotų sluoksnių.



4.13 pav. GDC-CP plonų suoksnių, suformuotų garinant elektronų spindulio metodu ir papildomai atkaitinus prie 600 °C, 700 °C, 800 °C, 900 °C temperatūrose 1 val., paviršiaus morfologiniai šiurkštumo parametrai gauti AFM tyrimo metu. Čia R_q (tušios geometrinės figūros) – vidutinis kvadratinis šiurkštumas, R_z (pilnavidurės geometrinės figūros) – vidutinis aukštis

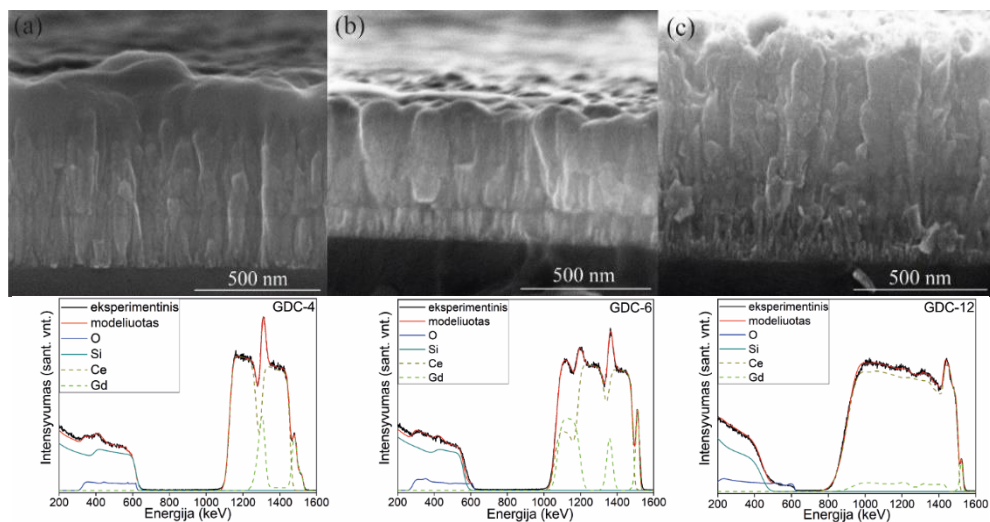
15 GDC-CP ir 20 GDC-CP keramikų paviršiaus vidutinio kvadratinio šiurkštumo (R_q) vertės didėja, didinant atkaitinimo temperatūrą. 15 GDC-CP ir 20 GDC-CP keramikų didžiausia paviršiaus šiurkštumo vertė yra 15,29 nm ir 13,74 nm atitinkamai, esant 800 °C atkaitinimo temperatūrai. Vidutinės šiurkštumo vertės (R_a) kinta taip pat kaip ir keramikų paviršiaus vidutinio kvadratinio šiurkštumo (R_q) vertės visoms GDC-CP plonasluoksniams keramikoms.

GDC plonų dangų formavimas nuolatinės srovės reaktyviojo magnetroninio dulkinimo metodu

Siekiant palyginti plonasluoksnes keramikas suformuotas skirtingais fizikiniais metodais, buvo suformuoti sluoksniai taikant nuolatinės srovės reaktyviojo magnetroninio dulkinimo metodą, garinant sluoksnį po sluoksnio Gd_2O_3 ir CeO_2 oksidus. Magnetroninio dulkinimo būdu, siekiant išlaikyti vienodą galutinį dangos

storį, didinant sluoksnių skaičių, buvo mažinami gadolinio ir samario oksidų sluoksnių storiai.

Iš rentgeno struktūrinės analizės tyrimų matome, kad visi sluoksniai pasižymi kubine struktūra ir smailių intensyvumas didėja, didinant Gd ir Ce oksidų sluoksnių skaičių. Be to didžiausius kristalitus (14,6 nm) ir didžiausią kristalinę gardelę (5,401 Å) turėjo GDC-12 bandinys (12 Gd ir Ce oksidų sluoksnių), lyginant su GDC-6 (11,4 nm bei 5,394 Å) ir GDC-4 (11,2 nm bei 5,393 Å). Ramano spektroskopijos tyrimai parodė, kad GDC-6 ir GDC-4 bandinių atkaitintų 700 °C temperatūroje, atveju dominuoja 464,1 cm⁻¹ smailė, o GDC-12 bandinio dominuojanti smailė pasislenka į 462,9 cm⁻¹ ir tai atitinka F_{2g} simetriją, bei patvirtina, kad gaunamas vienfazis kubinis fluorito tipo junginys. Be to, stebimas nedidelis smailių išplatėjimas nuo 17,2 cm⁻¹ iki 18,8 cm⁻¹.



4.14 pav. Skerspjūvio (a) GDC-4, (b) GDC-6 ir (c) GDC-12 plonų sluoksnių SEM vaizdai. Eksperimentiniai ir modeliuoti GDC-4, GDC-6 ir GDC-12 plonų sluoksnių RBS spektrų rezultatai publikuoti [A2]

SEM plonų sluoksnių skerspjūvio nuotraukos (4.14 pav.) parodė, kad GDC keramikos auga formuodamos tankias kolonijinės struktūros dangas ir dangų storiai buvo: GDC-4 (~700 nm), GDC-6 (~550 nm) ir GDC-12 (~850 nm). Net ir po atkaitinimo GDC-4 ir GDC-6 keramikose matomos sluoksnių ribos, tai parodo nepakankamą sluoksnių susimaišymą.

Modeliavimo (buvo naudojamas *SIMNRA* v7.02 programinis paketas) ir eksperimentiniai Rezerfordo atbulinės sklaidos (RBS) rezultatai (4.14 pav.) tarpusavyje koreliuoja. Kiekvienas nusodintas sluoksnis gali būti suskirstytas į keturis Gd₂O₃ ir CeO₂ sluoksnius. RBS rezultatai parodė, kad GDC-4 bandinio pradinis persimaišymas tarp Gd₂O₃ ir CeO₂ sluoksnių vyksta tik plonų sluoksnių paviršiuje. GDC-6 bandinio RBS tyrimai parodė, kad bandinių atkaitinimo metu formuojasi tik dalinė cerio oksido stabilizuota gadoliniumo fazė. Plati smailė 1–1,20

MeV energijų intervale rodo apie vykstančią difuziją CeO_2 ir Gd_2O_3 sluoksniuose, kurie yra Si (padėklo) paviršiuje ir tik nedidelė difuzija stebima tarp CeO_2 – Gd_2O_3 sluoksnių keramikos paviršiuje. GDC-12 bandinio RBS tyrimai GDC-12 bandinio parodė, kad smailės ties 1,50–1,42 MeV parodo Gd_2O_3 pirmą sluoksnį, o smailės ties 1,54–1,50 MeV parodo CeO_2 pirmąjį sluoksnį. Šios smailės atsiranda, dėl nevisiško viršutinių (paviršinių) sluoksnių susimaišymo, tačiau kiti (gilesni) sluoksniai visiškai susimaišę, tą parodo ir RBS tyrimai (atitinka 1,42–0,76 MeV energijas). Iš gautų rezultatų galime teigti, kad CeO_2 – Gd_2O_3 sluoksnių pradinis storis magnetroninio dulkinimo metu turi įtakos vienalyčio GDC junginio formavimuisi dulkinimo proceso metu. Taip pat, reikalinga formuoti nemažiau kaip 12 Gd ir Ce oksidų sluoksnių, kad galėtume gauti vienalytį (vienfazį) junginį.

Cerio oksido stabilizavimas

Anksčiau aprašyti SDC bei GDC tyrimai ir eksperimentų rezultatai, iškėlė klausimą, kaip pasikeistų fizikinės ir cheminės savybės galutinio produkto (SGDC), jeigu samario ir gadolinio oksidais legiruotumėme cerio oksidą. Taikant degimo (CB) ir nusodinimo iš tirpalų (CP) sintezių metodus, buvo susintetinti $\text{Ce}_{0,825}\text{Sm}_{0,0875}\text{Gd}_{0,0875}\text{O}_{2-\delta}$ nanomilteliai bei atlikti eksperimentiniai tyrimai.

Terminis išskaidymas ir kristalizacija daro įtaką cerio oksidui, stabilizuotam samario ir gadolinio oksidu (SGDC). Kristalizacijos procesas atitinka cerio oksido stabilizavimą atskirai samario oksidu ir gadolinio oksidu. Tačiau SGDC-CB reakcijos yra artimesnės GDC-CB reakcijomis nei su SDC-CB. Formuojant SGDC miltelius, bendras masės pokytis buvo 0,21–0,44 %, lyginant su SDC-CB (3,5 %) ir GDC-CB (0,45–0,75 %) susintetintas milteliais buvo žymiai mažesnis. Nebuvo pastebėta jokių sintezės pokyčių formuojant SGDC-CP miltelius, bendras masės pokytis buvo ~55 %, kaip ir taikant SDC-CP ir GDC-CP sintezių metodus. Šie rezultatai rodo, kad įterpiant priemaišas (stabilizuojant) CB sintezės metu gaunami termiškai stabilesni junginiai su mažesniu organinių priemaišų kiekiu.

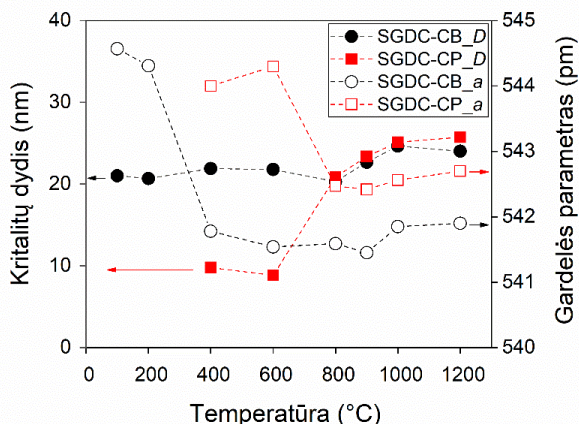
Apskaiciuota SGDC nanomiltelių kristalitų dydžio priklausomybė nuo CB ir CP sintezių iškaitinimo temperatūros pateikiama 4.5 lentelėje.

4.5 lentelė. Susintetintų CB–degimo ir CP–nusodinimo iš tirpalų sintezių metodais SGDC nanomiltelių kristalitų dydžio (nm) rezultatų priklausomybė nuo miltelių iškaitinimo temperatūros

T, °C	SGDC-CB	SGDC-CP	10 GDC-CB	10 GDC-CP	10 SDC-CB	10 SDC-CP
200	20,68	–	24,54	–	16,85	–
400	21,89	9,79	25,89	4,53	19,11	4,62
600	21,79	8,84	23,87	9,56	24,73	10,19
800	20,30	20,86	26,77	23,74	28,09	27,41
900	22,67	23,38	–	–	–	–
1000	24,65	25,13	35,66	44,06	36,81	45,74
1200	24,02	25,74	35,80	47,97	44,22	48,10

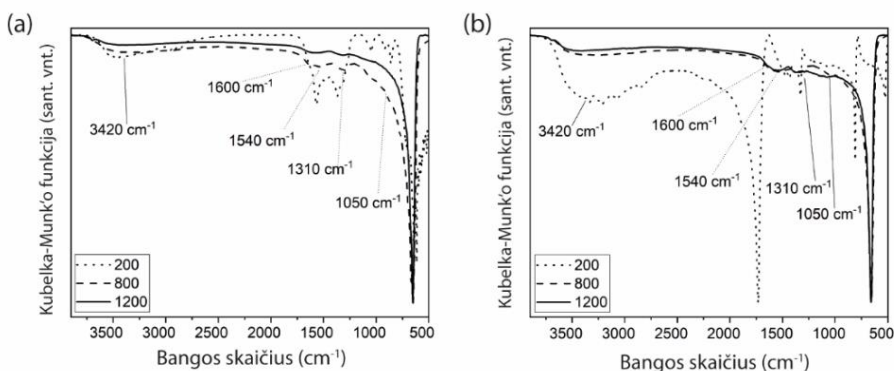
Skirtingi gardelės konstantų dydžiai gali būti paaiškinami, skirtingai jonų dydžiais Sm^{3+} (1,079 Å), Gd^{3+} (1,053 Å) ir Ce^{4+} (0,97 Å) [108]. Cerio oksidą

stabilizuojant Sm_2O_3 arba Gd_2O_3 oksidu (vienu iš jų), didžiausi kristalitai gaunami stabilizuojant cerio oksidą Sm_2O_3 . Stabilizuojant abiem oksidais (Sm_2O_3 ir Gd_2O_3) Gd jonas pakeičia Sm joną ir gaunamas mažesnis kristalitų dydis, lyginant su SDC ir GDC; tai gali būti paaiškinama susidarius mažesnei Gd ir Sm koncentracijai [9]. Esant mažesnei iškaitinimo temperatūrai, stebimas kristalinės gardelės sumažėjimas SGDC-CB ir SGDC-CP atvejais, tai gali būti susiję su nepilnu oksido susidarymu (4.15 pav.).



4.15 pav. Kristalitų dydžio (D) ir gardelės parametro (a) priklausomybė nuo SGDC nanomiltelių, susintetintų CB – degimo ir CP – nusodinimo iš tirpalų sintezių metodais, iškaitinimo temperatūros

Susintetintų SGDC miltelių grynumą patvirtina ir FT–IR tyrimai, pateikti 4.16 paveiksle. Esant aukštesnei nanomiltelių iškaitinimo temperatūrai, organinių junginių smailių visiškai nesimato ir stebima tik intensyvi CO_2 smailė ypač CB sintezės atveju. Be to, matome, kad susintetintų ir atkaitintų žemoje temperatūroje, SGDC-CB bandinių FT–IR smailių intensyvumas mažesnis; tai patvirtina, kad gauti milteliai yra grynesni.

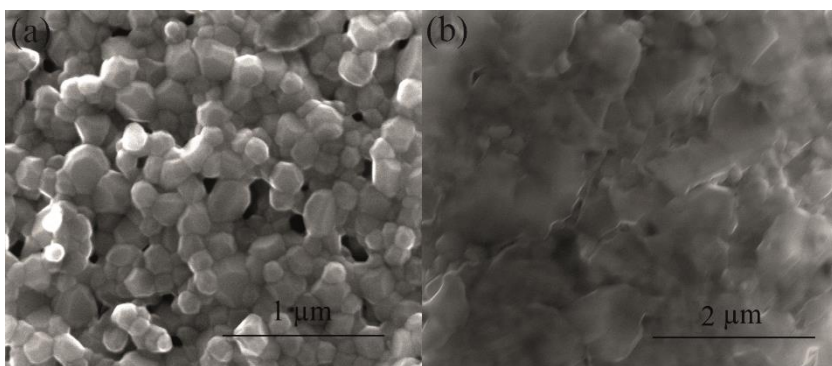


4.16 pav. SGDC nanomiltelių, susintetintų (a) degimo ir (b) nusodinimo iš tirpalų iškaitintų įvairiose (200 °C, 800 °C, 1200 °C) temperatūrose, FT–IR spektrai

Iš SEM tyrimų matome, kad didinant atkaitinimo temperatūrą, gaunami tankesni sluoksniai. Gautų nanomiltelių struktūra ir morfologija priklauso nuo pasirinkto sintezės metodo.

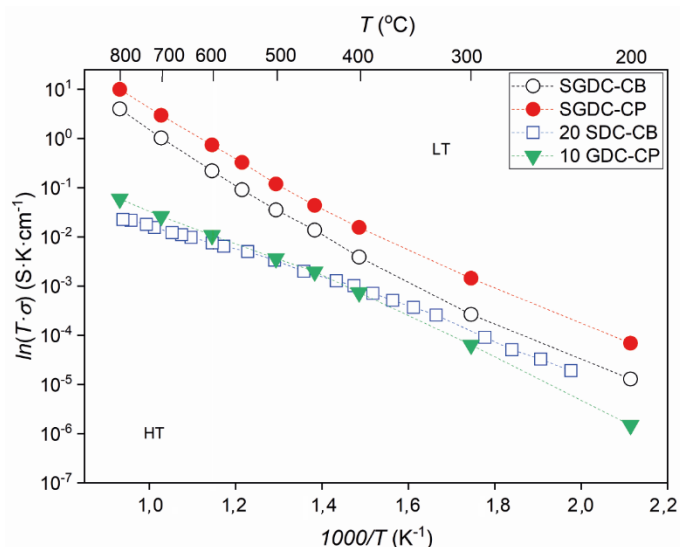
SGDC keramikų tyrimai

Tablečių, suformuotų iš susintetintų CB ir CP sintezių metodais SGDC miltelių, SEM tyrimai parodė, kad paviršiaus struktūra sutampa su CeO_2 stabilizuotu vienu iš oksidų (Gd ar Sm). Tablečių paviršiuje formuojasi tanki struktūra, sudaryta iš nevienodo dydžių grūdelių (0,832–1,21 μm). Paviršiuje nėra matomų defektų ar įtrūkimų (4.17 pav.). Kaip matome iš SEM paviršiaus tyrimų, CP sintezės metu gauti milteliai pasižymi grūdėtumu, o CB atveju stebimas grūdelių susispaudimas, susijungimas.



4.17 pav. SGDC tablečių, suformuotų iš susintetintų (a) CB ir (b) CP sintezių metodais ir iškaitintų 1200 °C temperatūroje SGDC nanomiltelių, SEM vaizdai

4.18 paveiksle pateikiamos SGDC tablečių bendro laidumo Areniaus kreivės, kurios lyginamos su geriausiu laidumu pasižyminčiomis 20 SDC-CB ir 10 GDC-CP tabletėmis. CeO_2 stabilizuojant Gd_2O_3 ir Sm_2O_3 leidžia sumažinti aktyvacijos energiją HT ir LT temperatūrų intervaluose, taip pat padidina joninį laidumą. Joninio laidžio gautos vertės yra 0,054 $\text{S}\times\text{cm}^{-1}$ (SGDC-CP) ir 0,022 $\text{S}\times\text{cm}^{-1}$ (SGDC-CB) 600 °C temperatūroje.



4.18 pav. SGDC, GDC, SDC keramikų Arenijaus grafikai

4.6 lentelė. Skirtingų koncentracijų SGDC keramikų, susintetintų CB – degimo, CP – nusodinimo iš tirpalų sintezių metodais, aktyvacijos energijos, ΔE_a , ir joninio laidžio, σ , rezultatai

Bandinių žymuo	ΔE_a , eV		σ , $S \times cm^{-1}$		
	LT	HT	400 °C	500 °C	600 °C
SGDC-CP	0,79	0,65	$0,85 \times 10^{-2}$	$8,5 \times 10^{-2}$	0,054
SGDC-CB	0,81	0,76	$0,39 \times 10^{-2}$	$5,2 \times 10^{-2}$	0,022

Wang ir kt. nustatė $Ce_{0,85}Gd_{0,15-y}Sm_yO_{1,92}$ keramikų $0,046 S \times cm^{-1}$ joninį laidį prie 700 °C temperatūroje [44]. Dikmen'as nustatė $Ce_{0,8}Gd_{0,1}Sm_{0,1}O_{2-\delta}$ keramikų $6,5 \times 10^{-2} S \times cm^{-1}$ joninį laidį ir 0,59 eV aktyvacijos energiją prie 700 °C temperatūroje [45]. Taip pat, Aldridge ir Baker gavo, kad $Ce_{0,825}Sm_{0,0875}Gd_{0,0875}O_{1,9125}$ keramikų joninis laidis $2,23 S \times cm^{-1}$ 600 °C temperatūroje [9]. Skirtingos joninio laidumo vertės gaunamos dėl skirtingų keramikos paruošimo bei atkaitinimo būdų. Mūsų darbe gautų joninio laidžio rezultatų vertės gerai sutampa su kitų autorių darbais, ir iš gautų rezultatų matome, kad CeO_2 stabilizavimas Gd_2O_3 ir Sm_2O_3 kartu pasižymi geresnėmis savybėmis nei stabilizuojant vienu iš jų.

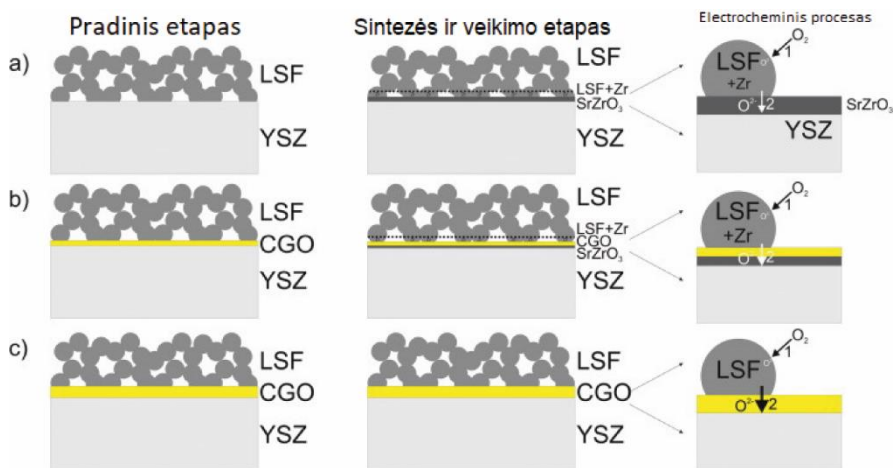
Legiruotų cerio oksidu keramikų kaip difuzinio (barjerinio) sluoksnio taikymas

Apžvelgus mokslinę literatūrą pastebėta, kad formuojant kietojo oksido kuro elementus didžiausia problema atsiranda dėl per didelio prieštampio katodo dalyje. Dažnai formuojant katodus yra naudojamas stroncis, kuris atkaitinimo metu (esant aukštai temperatūrai) chemiškai reaguoja su elektrolitu, tokių reakcijų metu susidaro parazitiniai junginiai, kurie mažina kuro elemento galią. Norint to išvengti tarp

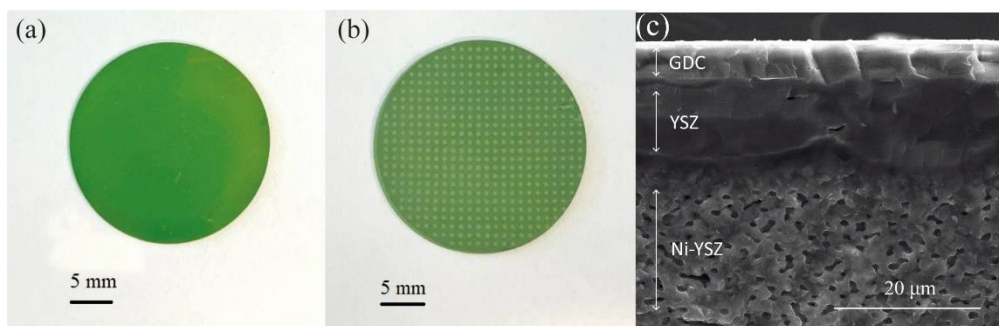
katodo ir elektrolito reikalingas difuzinis (barjerinis) sluoksnis. Difuzinis (barjerinis) sluoksnis turi būti vienalypis, chemiškai stabilus, tankus ir plonas, kad išvengtume katijonų difuzijos į elektrolitą. Elektrocheminės reakcijos tarp difuzinio sluoksnio ir katodo schematiškai pavaizduotos 4.19 paveiksle.

Siekiant išvengti katodo atomų difuzijos į elektrolitą difuzijos, (difuzinis) barjerinis sluoksnis turi padengti visą elektrolito paviršių (storis gali kisti nuo 400 nm iki 1 μm) ir neturėti papildomos varžos. Kadangi CeO_2 , stabilizuotas Gd_2O_3 ir Sm_2O_3 , nereaguoja su daugeliu katodinių medžiagų tai jį galima naudoti ne tik kaip elektrolitą, bet ir kaip difuzinį (barjerinį) sluoksnį. Kad difuzinis sluoksnis pasižymėtų norimomis savybėmis, labai svarbus sluoksnio formavimo būdas.

Norint ištirti, ar GDC tinka kaip difuzinis (barjerinis) sluoksnis tarp YSZ elektrolito ir LSCF katodo, buvo suformuotas 26GDC-CP (~ 700 nm) difuzinis sluoksnis ant Ni/YSZ sistemos, naudojant elektronų spindulio garinimo sistemą. Ni/YSZ sistema buvo disko formos, jos skersmuo ~ 25 mm (4.20 pav.).



4.19 pav. Difuzinio sluoksnio ir katodo modelio schema: (a) be GDC (CGO) difuzinio sluoksnio ir su (b) 400 nm, (c) 800 nm storio GDC (CGO) difuziniu sluoksniu [83]



4.20 pav. Porėto anodo-elektrolito-barjerinio sluoksnio kuro elemento fotonuotraukos (a) viršutinė dalis, (b) apatinė dalis. GDC ploni sluoksniai suformuoti ant viršutinės elemento dalies (a), (c) SEM skerspjūvio vaizdas

Tolimesni tyrimai bus skirti nustatyti difuzinio sluoksnio elektrocheminėms savybėms ir, išrinkus geriausius laidumo rezultatus, katodas bus suformuotas ant GDC difuzinio sluoksnio. Šitokia anodinė sistema puikiai tinka μ -SOFCs, kurios veikia žemose darbinėse temperatūrose.

IŠVADOS

1. Įvairių priemaišinių metalo oksidų koncentracijų (10–30 mol %) SDC, GDC ir SGDC nanostruktūrinės sudėties keramikos buvo susintetintos naudojant degimo, nusodinimo iš tirpalų ir zolių-gelių chemines sintezes. Nustatyta, kad supresuotus ir atkaitintus 1200 °C temperatūroje susintetintus nanomiltelius galima naudoti kaip taikinius, formuojant plonus sluoksnius vakuuminiu garinimu elektronų spinduliu.
2. Parinkus cheminės sintezės metodą, galima suformuoti cerio pagrindo keramikas, legiruotas priemaišomis, kurios pasižymi fluorito tipo nanostruktūra ir didesniu joniniu laidumu. Taikant degimo (CB) sintezę SDC keramikų (20 SDC) joninis laidumas 600 °C temperatūroje buvo $1,1 \times 10^{-2} \text{ S} \times \text{cm}^{-1}$, lyginant su nusodinimo iš tirpalų sinteze (CP) ir zolių-gelių (SG) sinteze gautomis joninio laidumo vertėmis $0,92 \times 10^{-2} \text{ S} \times \text{cm}^{-1}$, $0,95 \times 10^{-2} \text{ S} \times \text{cm}^{-1}$, atitinkamai.
3. GDC nanomilteliai pasižymi mažesne kristaline gardele ir kristalitų dydžiu (541,66 pm ir 26,67 nm 10 GDC-CB), lyginant su SDC nanomilteliais (543,41 pm ir 27,27 nm 10 SDC-CB), dėl mažesnio metalų priemaišų jono spindulio ($\text{Sm}^{+3} > \text{Gd}^{+3}$).
4. SGDC nanomilteliai, susintetinti degimo ir nusodinimo iš tirpalų sintezių metodais, turėjo mažesnę kristalinę gardele ir kristalitų dydžius (542,37 pm ir 22,13 nm SGDC-CB), lyginant su GDC ir SDC nanomilteliais, dėl mažesnės stabilizuojančių Sm ir Gd priemaišų koncentracijos ($\text{Ce}_{0,825}\text{Sm}_{0,0875}\text{Gd}_{0,0875}\text{O}_{2-\delta}$, čia $x = 0,0875$). GDC keramikos su 10 mol% Gd_2O_3 koncentracija, susintetintos nusodinimo iš tirpalų sinteze (CP), pasižymėjo 600 °C temperatūroje didesniu joniniu laidumu $1,1 \times 10^{-2} \text{ S} \times \text{cm}^{-1}$, lyginant su degimo sinteze (CB) gauta GDC keramika $1 \times 10^{-2} \text{ S} \times \text{cm}^{-1}$.
5. Atlikus sisteminius tyrimus nustatyta, kad tikslinga taikyti cheminės sintezės metodą, nusodinimo iš tirpalų sintezę (CP), su atitinkamais technologiniais parametrais (pH vertė, proceso temperatūra ir kt.), pradinėmis cheminėmis medžiagomis (metalų nitratas heksahidratas), pradinio produkto išdegimo temperatūra (800 °C), keramikų atkaitinimo temperatūra (1200 °C), kuri leidžia suformuoti stabilizuotas cerio oksido pagrindu nanostruktūrinės keramikas ($\text{Ce}_{1-x}\text{M}_x\text{O}_{2-\delta}$).
6. Nustatyta, kad mišriomis priemaišomis ir Sm_2O_3 , ir Gd_2O_3 legiruotas cerio oksidas (SGDC), taikant degimo (CB) ir nusodinimo iš tirpalų (CP) sintezes padidina 600 °C temperatūroje joninį laidumą $0,054 \text{ S} \times \text{cm}^{-1}$ (SGDC-CP) ir $0,022 \text{ S} \times \text{cm}^{-1}$ (SGDC-CB). Taip pat SGDC išlieka termiškai stabilus prie 400 °C išdegimo temperatūroje.
7. Norint suformuoti plonus sluoksnius, naudojant garinimą elektronų spinduliu, taikinių medžiagų cheminė sudėtis (koncentracija) turi būti apie 28 % didesnė.

Cheminių sintezių pritaikymas norimos koncentracijos pradinių medžiagų sintezei yra vienas iš būdų, leidžiančių kontroliuoti cheminę pirminių medžiagų sudėtį.

8. Formuojant plonus sluoksnius, sluoksnis po sluoksnio, naudojant magnetroninę dulkinimo sistemą, reikia ne mažiau kaip 12 (CeO_2 ir Gd_2O_3) sluoksnių ~850 nm storio GDC keramikai gauti. Papildomas plonų sluoksnių atkaitinimas 800 °C temperatūroje, pagerina struktūrų tankumą ir kristališkumą. Kaitinant plonus sluoksnius 900 °C ir aukštesnėse (t.y. viršijus Ce lydymosi temperatūrą) temperatūrose, sluoksnio paviršiuje pradeda kauptis Ce sankaupos–klasteriai.

Rekomendacijos

Norint visiškai suprasti, kokią įtaką cheminės sintezės metodas, atkaitinimo temperatūra, metalų oksidų priemaišų skirtingos koncentracijos turi plonų sluoksnių savybėms, būtina atlikti plonų sluoksnių elektrinių savybių matavimus. Elektrocheminio impedanso spektroskopijos (EIS) tyrimams reikia tam tikros geometrinės konstrukcijos plonų sluoksnių ir darbinių elektrodų paruošimo. Mokslinio tyrimo metu gautiems ploniems sluoksniams, kurių storis vyrauja nuo 100 nm iki 900 nm, reikalinga išskirtinė EIS įranga joniniam laidumui matuoti. Po atliktų sisteminių tyrimų su SDC, GDC, SGDC keramikomis bus tęsiami darbai su plonais sluoksniais, kurie bus naudojami kaip difuzinis (barjerinis) sluoksnis tarp anodo ir katodo kietojo oksido kuro elementuose.

6. ACKNOWLEDGEMENTS

The author used the facilities of the Institute of Materials Science of Kaunas University of Technology to carry out the research work presented in this dissertation.

I would like to express my sincere gratitude to my scientific supervisor Associate professor Dr. Brigita Abakevičienė, who has become not only a supervisor, but also a person, whose support and guidance helped to cope with the difficulties of my doctoral path. In moments of obstacles, Dr. Brigita Abakevičienė has always been by my side, supporting me, helping me to find answers, planning experiments, sharing valuable comments on scientific articles and this dissertation, and helping me with all the difficulties that came my way.

I would like to thank the co-authors of scientific articles and colleagues from Kaunas University of Technology and Warsaw University of Technology for their cooperation and assistance in completing this research.

I am also grateful to my family and friends who supported me during my doctoral studies and stood by me to the end, especially my parents who always believed in me and encouraged me to strive for the best.

Ең үлкен алғысымды Әке-Шешеме, сіңлім Ажар мен інім Жалғасқа және сүйікті Фатима мамаға айтқым келеді. Менің сіздерге алғысым шексіз. Өмірімнің ең үлкен бақыты мен байлығы – Әкем мен Анашым–Моя Вселенная.

7. REFERENCES

- [1] SAFI, R.; A. GHASEMI; R. SHOJA-RAZAVI, . Retraction notice to “Factors controlling magnetic properties of CoFe₂O₄ nanoparticles synthesized by chemical co-precipitation: Modeling and optimization using response surface methodology” [Ceram. Int. (2016) 15,818–15,825](S0272884216311129)(10.1016/j. Ceramics International. 2017. DOI 10.1016/j.ceramint.2017.05.112.
- [2] FUENTES, R.O.; R.T. BAKER, . Synthesis and properties of Gadolinium-doped ceria solid solutions for IT-SOFC electrolytes. *International Journal of Hydrogen Energy*. 2008. DOI 10.1016/j.ijhydene.2007.10.026.
- [3] LIOU, Y.C.; S.L. YANG, . A simple and effective process for Sr_{0.995}Ce_{0.95}Y_{0.05}O_{3-δ} and BaCe_{0.9}Nd_{0.1}O_{3-δ} solid electrolyte ceramics. *Journal of Power Sources*. 2008. DOI 10.1016/j.jpowsour.2008.01.012.
- [4] ZHENG, Y.; S. HE; L. GE; M. ZHOU; H. CHEN; ET AL., . Effect of Sr on Sm-doped ceria electrolyte. *International Journal of Hydrogen Energy*. 2011. DOI 10.1016/j.ijhydene.2011.01.042.
- [5] KUMAR, S.A.; P. KUPPUSAMI, *Enhancing the ionic conductivity in the ceria-based electrolytes for intermediate temperature solid oxide fuel cells*. , INC,2020. DOI 10.1016/b978-0-12-817445-6.00005-3.
- [6] SINGHAL, S.C., . Advances in solid oxide fuel cell technology. *Solid State Ionics*. 2000. DOI 10.1016/S0167-2738(00)00452-5.
- [7] FERGUS, J.W., . Materials challenges for solid-oxide fuel cells. *JOM*. 2007. DOI 10.1007/s11837-007-0153-x.
- [8] GAO, Z.; L. V. MOGNI; E.C. MILLER; J.G. RAILSBACK; S.A. BARNETT, . A perspective on low-temperature solid oxide fuel cells. *Energy and Environmental Science*. 2016. Vol. 9, p. 1602–1644. DOI 10.1039/c5ee03858h.
- [9] COLES-ALDRIDGE, A. V.; R.T. BAKER, . Oxygen ion conductivity in ceria-based electrolytes co-doped with samarium and gadolinium. *Solid State Ionics*. 2020. Vol. 347, p. 115255. DOI 10.1016/j.ssi.2020.115255.
- [10] KILNER, J.A., . Fast oxygen transport in acceptor doped oxides. *Solid State Ionics*. 2000. DOI 10.1016/S0167-2738(99)00313-6.
- [11] TRAVERSA, E., *Toward the miniaturization of solid oxide fuel cells*. *Electrochem. Soc. Interface*. 2009.
- [12] TIMURKUTLUK, B.; C. TIMURKUTLUK; M.D. MAT; Y. KAPLAN, . A review on cell/stack designs for high performance solid oxide fuel cells. *Renewable and Sustainable Energy Reviews*. 2016. Vol. 56, p. 1101–1121. DOI 10.1016/j.rser.2015.12.034.
- [13] BOUDGHENE STAMBOULI, A.; E. TRAVERSA, . Fuel cells, an alternative to standard sources of energy. *Renewable and Sustainable Energy Reviews*. 2002. DOI 10.1016/S1364-0321(01)00015-6.
- [14] MAHAPATRA, M.K.; P. SINGH, *Fuel Cells. Energy Conversion Technology*. , 2013. DOI 10.1016/B978-0-08-099424-6.00024-7.

- [15] LINDORFER, J.; D.C. ROSENFELD; H. BÖHM, *Fuel cells: Energy conversion technology*. , Elsevier Ltd,2020. DOI 10.1016/B978-0-08-102886-5.00023-2.
- [16] CORALLI, A.; B.J.M. SARRUF; P.E. V. DE MIRANDA; L. OSMIERI; S. SPECCHIA; ET AL., *Fuel cells*. , Elsevier Inc.,2018. DOI 10.1016/B978-0-12-814251-6.00002-2.
- [17] LENSER, C.; D. UDOMSILP; N.H. MENZLER; P. HOLTAPPELS; T. FUJISAKI; ET AL., *Solid oxide fuel and electrolysis cells*. , Elsevier Ltd.,2020. DOI 10.1016/b978-0-08-102726-4.00009-0.
- [18] RAVI CHANDRAN, P.; T. V. ARJUNAN, . A review of materials used for solid oxide fuel cell. *International Journal of ChemTech Research*. 2015.
- [19] ADAMS, T.A.; J. NEASE; D. TUCKER; P.I. BARTON, . Energy conversion with solid oxide fuel cell systems: A review of concepts and outlooks for the short- and long-term. *Industrial and Engineering Chemistry Research*. 2013. DOI 10.1021/ie300996r.
- [20] PAYNE, R.; J. LOVE; M. KAH, . Generating Electricity at 60% Electrical Efficiency from 1 - 2 kWe SOFC Products. *ECS Transactions*. 2019. DOI 10.1149/1.3205530.
- [21] SIMNER, S.P.; J.F. BONNETT; N.L. CANFIELD; K.D. MEINHARDT; J.P. SHELTON; ET AL., . Development of lanthanum ferrite SOFC cathodes. *Journal of Power Sources*. 2003. DOI 10.1016/S0378-7753(02)00455-X.
- [22] STAMBOULI, A.B.; E. TRAVERSA, . Solid oxide fuel cells (SOFCs): A review of an environmentally clean and efficient source of energy. *Renewable and Sustainable Energy Reviews*. 2002. DOI 10.1016/S1364-0321(02)00014-X.
- [23] DAMO, U.M.; M.L. FERRARI; A. TURAN; A.F. MASSARDO, . Solid oxide fuel cell hybrid system: A detailed review of an environmentally clean and efficient source of energy. *Energy*. 2019. DOI 10.1016/j.energy.2018.11.091.
- [24] STEELE, B.C.H., . Materials for IT-SOFC stacks - 35 years R&D: The inevitability of gradualness?. *Solid State Ionics*. 2000. DOI 10.1016/S0167-2738(00)00709-8.
- [25] HUIJSMANS, J.P.P.; F.P.F. VAN BERKEL; G.M. CHRISTIE, . Intermediate temperature SOFC - A promise for the 21st century. *Journal of Power Sources*. 1998. DOI 10.1016/S0378-7753(97)02789-4.
- [26] EG&G TECHNICAL SERVICES, I., *Fuel Cell Handbook (7th Edition)*. , 2004.
- [27] GE, L.; A. VERMA; R. GOETTLER; D. LOVETT; R.K.S. RAMAN; ET AL., . Oxide scale morphology and chromium evaporation characteristics of alloys for balance of plant applications in solid oxide fuel cells. *Metallurgical and Materials Transactions A: Physical Metallurgy and Materials Science*. 2013. DOI 10.1007/s11661-012-1492-y.
- [28] DOE; NREL, . 2011 NREL/DOE Hydrogen and Fuel Cell Manufacturing R&D Workshop Report. 2011.
- [29] SAADABADI, S.A.; A. THALLAM THATTAI; L. FAN; R.E.F. LINDEBOOM; H. SPANJERS; ET AL., . Solid Oxide Fuel Cells fuelled with biogas: Potential and constraints. *Renewable Energy*. 2019. DOI 10.1016/j.renene.2018.11.028.
- [30] SINGH, P.; N.Q. MINH, . Solid oxide fuel cells: Technology status. *International Journal of Applied Ceramic Technology*. 2004. DOI

- 10.1111/j.1744-7402.2004.tb00149.x.
- [31] DZIURDZIA, B.; Z. MAGONSKI; H. JANKOWSKI, *Commercialisation of Solid Oxide Fuel Cells - Opportunities and forecasts.IOP Conf. Ser. Mater. Sci. Eng.* 2016. DOI 10.1088/1757-899X/104/1/012020.
 - [32] GAO, Z.; L. V. MOGNI; E.C. MILLER; J.G. RAILSBACK; S.A. BARNETT, . A perspective on low-temperature solid oxide fuel cells. *Energy and Environmental Science*. 2016. DOI 10.1039/c5ee03858h.
 - [33] MOGENSEN, M.; N.M. SAMMES; G.A. TOMPSETT, . Physical, chemical and electrochemical properties of pure and doped ceria. *Solid State Ionics*. 2000. DOI 10.1016/S0167-2738(99)00318-5.
 - [34] KOETTGEN, J.; S. GRIESHAMMER; P. HEIN; B.O.H. GROPE; M. NAKAYAMA; ET AL., . Understanding the ionic conductivity maximum in doped ceria: Trapping and blocking. *Physical Chemistry Chemical Physics*. 2018. DOI 10.1039/c7cp08535d.
 - [35] KOETTGEN, J.; M. MARTIN, . Coordination Numbers in Sm-Doped Ceria Using X-ray Absorption Spectroscopy. *Journal of Physical Chemistry C*. 2019. DOI 10.1021/acs.jpcc.8b10494.
 - [36] MINERVINI, L.; M.O. ZACATE; R.W. GRIMES, . Defect cluster formation in M2O3-doped CeO2. *Solid State Ionics*. 1999. DOI 10.1016/s0167-2738(98)00359-2.
 - [37] MOGENSEN, M.; D. LYBYE; N. BONANOS; P. V. HENDRIKSEN; F.W. POULSEN, . Factors controlling the oxide ion conductivity of fluorite and perovskite structured oxides. *Solid State Ionics*. 2004. DOI 10.1016/j.ssi.2004.07.036.
 - [38] OMAR, S.; E.D. WACHSMAN; J.C. NINO, . A co-doping approach towards enhanced ionic conductivity in fluorite-based electrolytes. *Solid State Ionics*. 2006. DOI 10.1016/j.ssi.2006.08.014.
 - [39] SÁNCHEZ-BAUTISTA, C.; A.J. DOS SANTOS-GARCÍA; J. PEÑA-MARTÍNEZ; J. CANALES-VÁZQUEZ, . The grain boundary effect on dysprosium doped ceria. *Solid State Ionics*. 2010. DOI 10.1016/j.ssi.2010.09.025.
 - [40] PÉREZ-COLL, D.; D. MARRERO-LÓPEZ; P. NÚÑEZ; S. PIÑOL; J.R. FRADE, . Grain boundary conductivity of Ce0.8Ln0.2O2-δ ceramics (Ln = Y, La, Gd, Sm) with and without Co-doping. *Electrochimica Acta*. 2006. DOI 10.1016/j.electacta.2006.04.032.
 - [41] KOETTGEN, J.; M. MARTIN, . The ionic conductivity of Sm-doped ceria. *Journal of the American Ceramic Society*. 2020. Vol. 103, p. 3776–3787. DOI 10.1111/jace.17066.
 - [42] ZHANG, T.S.; J. MA; L.B. KONG; S.H. CHAN; J.A. KILNER, . Aging behavior and ionic conductivity of ceria-based ceramics: A comparative study. *Solid State Ionics*. 2004. DOI 10.1016/j.ssi.2004.03.003.
 - [43] STEPHENS, I.E.L.; J.A. KILNER, . Ionic conductivity of Ce1-xNd_xO2-x/ 2. *Solid State Ionics*. 2006. DOI 10.1016/j.ssi.2006.01.010.
 - [44] ZHU, J.X.; D.F. ZHOU; S.R. GUO; J.F. YE; X.F. HAO; ET AL., . Grain boundary conductivity of high purity neodymium-doped ceria nanosystem with and without the doping of molybdenum oxide. *Journal of Power Sources*. 2007.

- DOI 10.1016/j.jpowsour.2007.08.093.
- [45] SHRI PRAKASH, B.; S. SENTHIL KUMAR; S.T. ARUNA, . Properties and development of Ni/YSZ as an anode material in solid oxide fuel cell: A review. *Renewable and Sustainable Energy Reviews*. 2014. Vol. 36, p. 149–179. DOI 10.1016/j.rser.2014.04.043.
 - [46] LIN, Y.C.; W.C.J. WEI, . Porous Cu–Ni-YSZ cermets using CH₄ fuel for SOFC. *International Journal of Hydrogen Energy*. 2020. DOI 10.1016/j.ijhydene.2020.05.281.
 - [47] BESSLER, W.G.; M. VOGLER; H. STÖRMER; D. GERTHSEN; A. UTZ; ET AL., . Model anodes and anode models for understanding the mechanism of hydrogen oxidation in solid oxide fuel cells. *Physical Chemistry Chemical Physics*. 2010. Vol. 12, p. 13888–13903. DOI 10.1039/c0cp00541j.
 - [48] ZHU, H.; R.J. KEE; V.M. JANARDHANAN; O. DEUTSCHMANN; D.G. GOODWIN, . Modeling Elementary Heterogeneous Chemistry and Electrochemistry in Solid-Oxide Fuel Cells. *Journal of The Electrochemical Society*. 2005. DOI 10.1149/1.2116607.
 - [49] SUN, C.; U. STIMMING, . Recent anode advances in solid oxide fuel cells. *Journal of Power Sources*. 2007. DOI 10.1016/j.jpowsour.2007.06.086.
 - [50] KOIDE, H.; Y. SOMEYA; T. YOSHIDA; T. MARUYAMA, . Properties of Ni/YSZ cermet as anode for SOFC. *Solid State Ionics*. 2000. DOI 10.1016/s0167-2738(00)00652-4.
 - [51] JACOBSON, A.J., . Materials for solid oxide fuel cells. *Chemistry of Materials*. 2010. DOI 10.1021/cm902640j.
 - [52] FAES, A.; A. HESSLER-WYSER; A. ZRYD; J. VAN HERLE, . A review of RedOx cycling of solid oxide fuel cells anode. *Membranes*. 2012. DOI 10.3390/membranes2030585.
 - [53] FAES, A.; J.M. FUERBRINGER; D. MOHAMEDI; A. HESSLER-WYSER; G. CABOCHE; ET AL., *Design of experiment approach applied to reducing and oxidizing tolerance of anode supported solid oxide fuel cell. Part I: Microstructure optimization.J. Power Sources*. 2011. DOI 10.1016/j.jpowsour.2010.07.092.
 - [54] KOLODIAZHNYI, T.; A. PETRIC, . The applicability of Sr-deficient n-type SrTiO₃ for SOFC anodes. *Journal of Electroceramics*. 2005. DOI 10.1007/s10832-005-0375-7.
 - [55] ARMSTRONG, E.N.; J.W. PARK; N.Q. MINH, . High-performance direct ethanol solid oxide fuel cells. *Electrochemical and Solid-State Letters*. 2012. DOI 10.1149/2.010206esl.
 - [56] CHENG, Z.; J.H. WANG; Y. CHOI; L. YANG; M.C. LIN; ET AL., . From Ni-YSZ to sulfur-tolerant anode materials for SOFCs: Electrochemical behavior, in situ characterization, modeling, and future perspectives. *Energy and Environmental Science*. 2011. DOI 10.1039/c1ee01758f.
 - [57] ATKINSON, A.; S. BARNETT; R.J. GORTE; J.T.S. IRVINE; A.J. MCEVOY; ET AL., . Advanced anodes for high-temperature fuel cells. *Nature Materials*. 2004.
 - [58] CAILLOT, T.; G. GAUTHIER; P. DELICHÈRE; C. CAYRON; F.J. CADETE

- SANTOS AIRES, . Evidence of anti-coking behavior of La_{0.8}Sr_{0.2}Cr_{0.98}Ru_{0.02}O₃ as potential anode material for Solid Oxide Fuel Cells directly fed under methane. *Journal of Catalysis*. 2012. Vol. 290, p. 158–164. DOI 10.1016/j.jcat.2012.03.012.
- [59] AGUILAR, L.; S. ZHA; S. LI; J. WINNICK; M. LIU, . Sulfur-tolerant materials for the hydrogen sulfide SOFC. *Electrochemical and Solid-State Letters*. 2004. DOI 10.1149/1.1788613.
- [60] GONG, M.; X. LIU; J. TREMBLY; C. JOHNSON, . Sulfur-tolerant anode materials for solid oxide fuel cell application. *Journal of Power Sources*. 2007. DOI 10.1016/j.jpowsour.2007.03.026.
- [61] HUANG, Y.-H.; R.I. DASS; Z.-L. XING; J.B. GOODENOUGH, . Double Perovskites as Anode Materials for Solid-Oxide Fuel Cells. *ChemInform*. 2006. DOI 10.1002/chin.200628016.
- [62] LIU, Q.; X. DONG; G. XIAO; F. ZHAO; F. CHEN, . A novel electrode material for symmetrical SOFCs. *Advanced Materials*. 2010. DOI 10.1002/adma.201001044.
- [63] DELEEBEECK, L.; V. BIRSS, . Catalysis of the hydrogen oxidation reactions by Sr-doped LaMn_{1-δ}YCrO₃ ± δ oxides. *Solid State Ionics*. 2011. DOI 10.1016/j.ssi.2011.07.017.
- [64] DU, Z.; H. ZHAO; X. ZHOU; Z. XIE; C. ZHANG, . Electrical conductivity and cell performance of La_{0.3}Sr_{0.7}Ti_{1-x}Cr_xO_{3-δ} perovskite oxides used as anode and interconnect material for SOFCs. *International Journal of Hydrogen Energy*. 2013. DOI 10.1016/j.ijhydene.2012.10.099.
- [65] HOWELL, T.G.; C.P. KUHNELL; T.L. REITZ; A.M. SUKESHINI; R.N. SINGH, . A₂MgMoO₆ (A = Sr,Ba) for use as sulfur tolerant anodes. *Journal of Power Sources*. 2013. DOI 10.1016/j.jpowsour.2013.01.004.
- [66] ZHA, S.; P. TSANG; Z. CHENG; M. LIU, . Electrical properties and sulfur tolerance of La_{0.75}Sr_{0.25}Cr_{1-x}Mn_xO₃ under anodic conditions. *Journal of Solid State Chemistry*. 2005. DOI 10.1016/j.jssc.2005.03.027.
- [67] TAO, S.; J.T.S. IRVINE, . Phase transition in perovskite oxide La_{0.75}Sr_{0.25}Cr_{0.5}Mn_{0.5}O_{3-δ} observed by in situ high-temperature neutron powder diffraction. *Chemistry of Materials*. 2006. DOI 10.1021/cm061413n.
- [68] SHOLKLAPPER, T.Z.; C.P. JACOBSON; S.J. VISCO; L.C. DEJONGHE, . Synthesis of dispersed and contiguous nanoparticles in solid oxide fuel cell electrodes. *Fuel Cells*. 2008. DOI 10.1002/fuce.200800030.
- [69] VOHS, J.M.; R.J. GORTE, . High-performance SOFC cathodes prepared by infiltration. *Advanced Materials*. 2009. DOI 10.1002/adma.200802428.
- [70] JIANG, S.P., . Development of lanthanum strontium manganite perovskite cathode materials of solid oxide fuel cells: A review. *Journal of Materials Science*. 2008. DOI 10.1007/s10853-008-2966-6.
- [71] FLEIG, J., . Solid Oxide Fuel Cell Cathodes: Polarization Mechanisms and Modeling of the Electrochemical Performance. *Annual Review of Materials Research*. 2003. DOI 10.1146/annurev.matsci.33.022802.093258.
- [72] HORITA, T.; K. YAMAJI; N. SAKAI; H. YOKOKAWA; T. KAWADA; ET AL., . Oxygen reduction sites and diffusion paths at La_{0.9}Sr_{0.1}MnO_{3-x}/yttria-

- stabilized zirconia interface for different cathodic overvoltages by secondary-ion mass spectrometry. *Solid State Ionics*. 2000. DOI 10.1016/S0167-2738(99)00276-3.
- [73] KIM, J.D.; G.D. KIM; J.W. MOON; H.W. LEE; K.T. LEE; ET AL., . Effect of percolation on electrochemical performance. *Solid State Ionics*. 2000. DOI 10.1016/S0167-2738(00)00681-0.
- [74] WILSON, J.R.; J.S. CRONIN; A.T. DUONG; S. RUKES; H.Y. CHEN; ET AL., . Effect of composition of La_{0.8}Sr_{0.2}MnO₃-Y₂O₃-stabilized ZrO₂ cathodes. Correlating three-dimensional microstructure and polarization resistance. *Journal of Power Sources*. 2010. DOI 10.1016/j.jpowsour.2009.09.074.
- [75] YOKOKAWA, H.; N. SAKAI; T. KAWADA; M. DOKIYA, . Thermodynamic stabilities of perovskite oxides for electrodes and other electrochemical materials. *Solid State Ionics*. 1992. DOI 10.1016/0167-2738(92)90090-C.
- [76] YOKOKAWA, H.; N. SAKAI; T. KAWADA; M. DOKIYA, . Thermodynamic Analysis of Reaction Profiles Between LaMO₃ (M = Ni , Co , Mn) and ZrO₂. *Journal of The Electrochemical Society*. 1991. DOI 10.1149/1.2086043.
- [77] LIU, Y.; H. LIU; L. CUI; K. ZHANG, . The ratio of food-to-microorganism (F/M) on membrane fouling of anaerobic membrane bioreactors treating low-strength wastewater. *Desalination*. 2012. DOI 10.1016/j.desal.2012.04.026.
- [78] LIU, Y.L.; A. HAGEN; R. BARFOD; M. CHEN; H.J. WANG; ET AL., . Microstructural studies on degradation of interface between LSM-YSZ cathode and YSZ electrolyte in SOFCs. *Solid State Ionics*. 2009. DOI 10.1016/j.ssi.2009.07.011.
- [79] MITTERDORFER, A.; L.J. GAUCKLER, . La₂Zr₂O₇ formation and oxygen reduction kinetics of the La_{0.85}Sr_{0.15}Mn_yO₃, O₂(g)|YSZ system. *Solid State Ionics*. 1998. DOI 10.1016/s0167-2738(98)00195-7.
- [80] CHEN, M.; A. NICHOLAS GRUNDY; B. HALLSTEDT; L.J. GAUCKLER, . Thermodynamic modeling of the La-Mn-Y-Zr-O system. *Calphad: Computer Coupling of Phase Diagrams and Thermochemistry*. 2006. DOI 10.1016/j.calphad.2006.04.003.
- [81] CHRONEOS, A.; B. YILDIZ; A. TARANCÓN; D. PARFITT; J.A. KILNER, . Oxygen diffusion in solid oxide fuel cell cathode and electrolyte materials: Mechanistic insights from atomistic simulations. *Energy and Environmental Science*. 2011. DOI 10.1039/c0ee00717j.
- [82] CHRONEOS, A.; D. PARFITT; J.A. KILNER; R.W. GRIMES, . Anisotropic oxygen diffusion in tetragonal La₂NiO_{4+δ}: Molecular dynamics calculations. *Journal of Materials Chemistry*. 2010. DOI 10.1039/b917118e.
- [83] NAUMOVICH, E.N.; V. V. KHARTON, . Atomic-scale insight into the oxygen ionic transport mechanisms in La₂NiO₄-based materials. *Journal of Molecular Structure: THEOCHEM*. 2010. DOI 10.1016/j.theochem.2009.12.003.
- [84] HOU, B.; C.C. WANG; X. CUI; Y. CHEN, . Chromium deposition and poisoning of La₂NiO₄ cathode of solid oxide fuel cell. *Royal Society Open Science*. 2018. DOI 10.1098/rsos.180634.

- [85] PÉREZ-COLL, D.; A. AGUADERO; M.J. ESCUDERO; P. NÚÑEZ; L. DAZA, . Optimization of the interface polarization of the La₂NiO₄-based cathode working with the Ce_{1-x}Sm_xO_{2-δ} electrolyte system. *Journal of Power Sources*. 2008. DOI 10.1016/j.jpowsour.2007.12.030.
- [86] KOVROVA, A.I.; V.P. GORELOV; A. V. KUZMIN; E.S. TROPIN; D.A. OSINKIN, . Influence of Ce_{0.8}R_{0.2}O_{2-a} (R = Y, Sm, Tb) submicron barrier layers at the La₂NiO_{4+δ}/YSZ boundary on the electrochemical performance of a cathode. *Journal of Solid State Electrochemistry*. 2021. DOI 10.1007/s10008-021-04942-w.
- [87] KHARTON, V. V.; A.A. YAREMCHENKO; A.L. SHAULA; M. V. PATRAKEEV; E.N. NAUMOVICH; ET AL., . Transport properties and stability of Ni-containing mixed conductors with perovskite- and K₂NiF₄-type structure. *Journal of Solid State Chemistry*. 2004. DOI 10.1016/S0022-4596(03)00261-5.
- [88] SAYERS, R.; J.E. PARKER; C.C. TANG; S.J. SKINNER, . In situ compatibility studies of lanthanum nickelate with a ceria-based electrolyte for SOFC composite cathodes. *Journal of Materials Chemistry*. 2012. DOI 10.1039/c2jm14384d.
- [89] SAYERS, R.; M. RIEU; P. LENORMAND; F. ANSART; J.A. KILNER; ET AL., *Development of lanthanum nickelate as a cathode for use in intermediate temperature solid oxide fuel cells*. *Solid State Ionics*. 2011. DOI 10.1016/j.ssi.2010.02.014.
- [90] TARANCÓN, A.; M. BURRIEL; J. SANTISO; S.J. SKINNER; J.A. KILNER, . Advances in layered oxide cathodes for intermediate temperature solid oxide fuel cells. *Journal of Materials Chemistry*. 2010. DOI 10.1039/b922430k.
- [91] DA SILVA, F.S.; T.M. DE SOUZA, . Novel materials for solid oxide fuel cell technologies: A literature review. *International Journal of Hydrogen Energy*. 2017. DOI 10.1016/j.ijhydene.2017.08.105.
- [92] KAUR, P.; K. SINGH, . Review of perovskite-structure related cathode materials for solid oxide fuel cells. *Ceramics International*. 2020. DOI 10.1016/j.ceramint.2019.11.066.
- [93] SIMNER, S.P.; M.D. ANDERSON; M.H. ENGELHARD; J.W. STEVENSON, . Degradation mechanisms of La-Sr-Co-Fe-O₃ SOFC cathodes. *Electrochemical and Solid-State Letters*. 2006. DOI 10.1149/1.2266160.
- [94] SHAH, M.; G. HUGHES; P.W. VOORHEES; S.A. BARNETT, . Stability and Performance of LSCF-Infiltrated SOFC Cathodes: Effect of Nano-Particle Coarsening. *ECS Transactions*. 2019. DOI 10.1149/1.3570195.
- [95] USHKALOV, L.; O.D. VASYLYEV; Y. PRYSCHPEA; A. SAMELYUK; V. MELAKH, . Synthesis and Study of LSCF Perovskites for IT SOFC Cathode Application. *ECS Transactions*. 2019. DOI 10.1149/1.3205796.
- [96] AHUJA, A.; M. GAUTAM; A. SINHA; J. SHARMA; P.K. PATRO; ET AL., . Effect of processing route on the properties of LSCF-based composite cathode for IT-SOFC. *Bulletin of Materials Science*. 2020. DOI 10.1007/s12034-020-2075-y.
- [97] MAZO, G.N.; S.N. SAVVIN; A.M. ABAKUMOV; J. HADERMANN; Y.A.

- DOBROVOL'SKII; ET AL., . Lanthanum-strontium cuprate: A promising cathodic material for solid oxide fuel cells. *Russian Journal of Electrochemistry*. 2007. DOI 10.1134/S1023193507040106.
- [98] BEBELIS, S.; N. KOTSIANOPOULOS; A. MAI; F. TIETZ, . Electrochemical characterization of perovskite-based SOFC cathodes. *Journal of Applied Electrochemistry*. 2006. DOI 10.1007/s10800-006-9215-y.
- [99] DIGIUSEPPE, G.; V. BODDAPATI, . Characterization of Solid Oxide Fuel Cells with LSCF-SDC Composite Cathodes. *Journal of Energy*. 2018. DOI 10.1155/2018/4041960.
- [100] KIEBACH, R.; W. ZHANG; M. CHEN; K. NORRMAN; H.J. WANG; ET AL., . Stability of $\text{La}_{0.6}\text{Sr}_{0.4}\text{Co}_{0.2}\text{Fe}_{0.8}\text{O}_3/\text{Ce}_{0.9}\text{Gd}_{0.1}\text{O}_2$ cathodes during sintering and solid oxide fuel cell operation. *Journal of Power Sources*. 2015. DOI 10.1016/j.jpowsour.2015.02.064.
- [101] OH, D.; D. GOSTOVIC; E.D. WACHSMAN, . Mechanism of $\text{La}_{0.6}\text{Sr}_{0.4}\text{Co}_{0.2}\text{Fe}_{0.8}\text{O}_3$ cathode degradation. *Journal of Materials Research*. 2012. DOI 10.1557/jmr.2012.222.
- [102] PELLEGRINELLI, C.; Y.-L. HUANG; E.D. WACHSMAN, . Effect of H_2O and CO_2 on LSCF-GDC Composite Cathodes . *ECS Transactions*. 2019. DOI 10.1149/09101.0665ecst.
- [103] XI, X.; A. KONDO; T. KOZAWA; M. NAITO, . LSCF-GDC composite particles for solid oxide fuel cells cathodes prepared by facile mechanical method. *Advanced Powder Technology*. 2016. DOI 10.1016/j.appt.2016.02.022.
- [104] REMBELSKI, D.; J.P. VIRICELLE; L. COMBEMALE; M. RIEU, *Characterization and comparison of different cathode materials for SC-SOFC: LSM, BSCF, SSC, and LSCF.Fuel Cells*. 2012. DOI 10.1002/fuce.201100064.
- [105] WACHSMAN, E.D.; K.T. LEE, . Lowering the temperature of solid oxide fuel cells. *Science*. 2011. DOI 10.1126/science.1204090.
- [106] ZAKARIA, Z.; S.H. ABU HASSAN; N. SHAARI; A.Z. YAHAYA; Y. BOON KAR, . A review on recent status and challenges of yttria stabilized zirconia modification to lowering the temperature of solid oxide fuel cells operation. *International Journal of Energy Research*. 2020. DOI 10.1002/er.4944.
- [107] ZAKARIA, Z.; Z. AWANG MAT; S.H. ABU HASSAN; Y. BOON KAR, . A review of solid oxide fuel cell component fabrication methods toward lowering temperature. *International Journal of Energy Research*. 2020. DOI 10.1002/er.4907.
- [108] GOODENOUGH, J.B., . Oxide-ion electrolytes. *Annual Review of Materials Research*. 2003. DOI 10.1146/annurev.matsci.33.022802.091651.
- [109] WEI, C.C.; K. LI, . Yttria-stabilized zirconia (YSZ)-based hollow fiber solid oxide fuel cells. *Industrial and Engineering Chemistry Research*. 2008. DOI 10.1021/ie070960v.
- [110] PRABHAKARAN, K.; M.O. BEIGH; J. LAKRA; N.M. GOKHALE; S.C. SHARMA, . Characteristics of 8 mol% yttria stabilized zirconia powder prepared by spray drying process. *Journal of Materials Processing Technology*. 2007. DOI 10.1016/j.jmatprotec.2007.01.019.
- [111] BADWAL, S.P.S.; F.T. CIACCHI; D. MILOSEVIC, . Scandia-zirconia

- electrolytes for intermediate temperature solid oxide fuel cell operation. *Solid State Ionics*. 2000. DOI 10.1016/S0167-2738(00)00356-8.
- [112] SINGH, R.; S.B. CHAVAN, . Processing and Properties of Scandia-doped Zirconia Electrolyte for Intermediate Temperature SOFC. *ECS Transactions*. 2019. DOI 10.1149/1.2729336.
- [113] DU, Y.; N.M. SOMMES, *Interactions and compatibilities of LSGM electrolyte and LSCM anode*. *Proc. - Electrochem. Soc.* 2005. DOI 10.1149/200507.1127pv.
- [114] YAMAJI, K.; T. HORITA; M. ISHIKAWA; N. SAKAI; H. YOKOKAWA, . Chemical stability of the $\text{La}_{0.9}\text{Sr}_{0.1}\text{Ga}_{0.8}\text{Mg}_{0.2}\text{O}_{2.85}$ electrolyte in a reducing atmosphere. *Solid State Ionics*. 1999. DOI 10.1016/S0167-2738(99)00039-9.
- [115] JAISWAL, N.; K. TANWAR; R. SUMAN; D. KUMAR; S. UPPADHYA; ET AL., . A brief review on ceria based solid electrolytes for solid oxide fuel cells. *Journal of Alloys and Compounds*. 2019. DOI 10.1016/j.jallcom.2018.12.015.
- [116] OZLU TORUN, H.; S. CAKAR; E. ERSOY; O. TURKOGLU, . The bulk electrical conductivity properties of $\delta\text{-Bi}_2\text{O}_3$ solid electrolyte system doped with Yb_2O_3 . *Journal of Thermal Analysis and Calorimetry*. 2015. DOI 10.1007/s10973-015-4785-8.
- [117] JIANG, Y.; J. GAO; M. LIU; Y. WANG; G. MENG, . Fabrication and characterization of Y_2O_3 stabilized ZrO_2 films deposited with aerosol-assisted MOCVD. *Solid State Ionics*. 2007. DOI 10.1016/j.ssi.2006.10.009.
- [118] IVANOV, V. V.; A.S. LIPILIN; Y.A. KOTOV; V.R. KHRUSTOV; S.N. SHKERIN; ET AL., . Formation of a thin-layer electrolyte for SOFC by magnetic pulse compaction of tapes cast of nanopowders. *Journal of Power Sources*. 2006. DOI 10.1016/j.jpowsour.2005.11.039.
- [119] BRAHIM, C.; A. RINGUEDÉ; M. CASSIR; M. PUTKONEN; L. NIINISTÖ, . Electrical properties of thin yttria-stabilized zirconia overlayers produced by atomic layer deposition for solid oxide fuel cell applications. *Applied Surface Science*. 2007. DOI 10.1016/j.apsusc.2006.08.043.
- [120] ZHANG, T.S.; J. MA; H. CHENG; S.H. CHAN, . Ionic conductivity of high-purity Gd-doped ceria solid solutions. *Materials Research Bulletin*. 2006. DOI 10.1016/j.materresbull.2005.09.008.
- [121] HUANG, W.; P. SHUK; M. GREENBLATT, . Hydrothermal Synthesis and Properties of $\text{Ce}_{1-x}\text{Sm}_x\text{O}_{2-x/2}$ and $\text{Ce}_{1-x}\text{Ca}_x\text{O}_{2-x}$ Solid Solutions. *Chemistry of Materials*. 1997. DOI 10.1021/cm970425t.
- [122] VAN HERLE, J.; T. HORITA; T. KAWADA; N. SAKAI; H. YOKOKAWA; ET AL., . Low temperature fabrication of (Y,Gd,Sm)-doped ceria electrolyte. *Solid State Ionics*. 1996. DOI 10.1016/0167-2738(96)00297-4.
- [123] XU, H.; H. YAN; Z. CHEN, . Sintering and electrical properties of $\text{Ce}_{0.8}\text{Y}_{0.2}\text{O}_{1.9}$ powders prepared by citric acid-nitrate low-temperature combustion process. *Journal of Power Sources*. 2006. DOI 10.1016/j.jpowsour.2006.09.021.
- [124] SINGH, N.; N.K. SINGH; D. KUMAR; O. PARKASH, . Effect of co-doping of

- Mg and La on conductivity of ceria. *Journal of Alloys and Compounds*. 2012. DOI 10.1016/j.jallcom.2011.12.137.
- [125] HIRANO, M.; M. INAGAKI; Y. MIZUTANI; K. NOMURA; M. KAWAI; ET AL., . Mechanical and electrical properties of Sc₂O₃-doped zirconia ceramics improved by postsintering with HIP. *Solid State Ionics*. 2000. DOI 10.1016/S0167-2738(00)00706-2.
- [126] KIM, G.; N. LEE; K.B. KIM; B.K. KIM; H. CHANG; ET AL., . Various synthesis methods of aliovalent-doped ceria and their electrical properties for intermediate temperature solid oxide electrolytes. *International Journal of Hydrogen Energy*. 2013. Vol. 38, p. 1571–1587. DOI 10.1016/j.ijhydene.2012.11.044.
- [127] ZHANG, J.; C. LENSER; N.H. MENZLER; O. GUILLON, . Comparison of solid oxide fuel cell (SOFC) electrolyte materials for operation at 500 °C. *Solid State Ionics*. 2020. Vol. 344, p. 115138. DOI 10.1016/j.ssi.2019.115138.
- [128] TIAN, R.; F. ZHAO; F. CHEN; C. XIA, *Sintering of Samarium-doped ceria powders prepared by a glycine-nitrate process*. *Solid State Ionics*. 2011. DOI 10.1016/j.ssi.2010.08.003.
- [129] SINGH, N.K.; P. SINGH; D. KUMAR; O. PARKASH, . Electrical conductivity of undoped, singly doped, and co-doped ceria. *Ionics*. 2012. DOI 10.1007/s11581-011-0604-9.
- [130] SINGH, N.; O. PARKASH; D. KUMAR, . Preparation and characterization of Al and La co-doped (Ce_{1-x-y}Al_xLa_yO_{2-(x+y)/2}) ceria. *Ionics*. 2013. DOI 10.1007/s11581-012-0698-8.
- [131] SANTOS, T.H.; J.P.F. GRILO; F.J.A. LOUREIRO; D.P. FAGG; F.C. FONSECA; ET AL., . Structure, densification and electrical properties of Gd³⁺ and Cu²⁺ co-doped ceria solid electrolytes for SOFC applications: Effects of Gd₂O₃ content. *Ceramics International*. 2018. DOI 10.1016/j.ceramint.2017.11.009.
- [132] MADHURI, C.; K. VENKATARAMANA; J. SHANKER; C.V. REDDY, . Effect of La³⁺, Pr³⁺, and Sm³⁺ triple-doping on structural, electrical, and thermal properties of ceria solid electrolytes for intermediate temperature solid oxide fuel cells. *Journal of Alloys and Compounds*. 2020. Vol. 849, p. 156636. DOI 10.1016/j.jallcom.2020.156636.
- [133] VENKATARAMANA, K.; C. MADHURI; Y. SURESH REDDY; G. BHIKSHAMIAH; C. VISHNUVARDHAN REDDY, . Structural, electrical and thermal expansion studies of tri-doped ceria electrolyte materials for IT-SOFCs. *Journal of Alloys and Compounds*. 2017. Vol. 719, p. 97–107. DOI 10.1016/j.jallcom.2017.05.022.
- [134] KHAKPOUR, Z.; A.A. YOUZBASHI; A. MAGHSOUDIPOUR, . Influence of Gd³⁺ and Dy³⁺ co-doping and sintering regime on enhancement of electrical conductivity of ceria-based solid electrolyte. *Ionics*. 2014. DOI 10.1007/s11581-014-1090-7.
- [135] WANG, S.F.; C.T. YEH; Y.R. WANG; Y.C. WU, . Characterization of samarium-doped ceria powders prepared by hydrothermal synthesis for use in solid state oxide fuel cells. *Journal of Materials Research and Technology*. 2013. DOI 10.1016/j.jmrt.2013.01.004.

- [136] INABA, H.; H. TAGAWA, . Ceria-based solid electrolytes. *Solid State Ionics*. 1996. DOI 10.1016/0167-2738(95)00229-4.
- [137] CHEN, W.; A. NAVROTSKY, . Thermochemical study of trivalent-doped ceria systems: $\text{CeO}_2\text{-M O}_{1.5}$ ($\text{M} = \text{La}, \text{Gd}, \text{and Y}$). *Journal of Materials Research*. 2006. DOI 10.1557/jmr.2006.0400.
- [138] OMAR, S.; J.C. NINO, . Consistency in the chemical expansion of fluorites: A thermal revision of the doped ceria. *Acta Materialia*. 2013. DOI 10.1016/j.actamat.2013.05.029.
- [139] ARUNKUMAR, P.; M. MEENA; K.S. BABU, . A review on cerium oxide-based electrolytes for ITSOFC. *Nanomaterials and Energy*. 2012. DOI 10.1680/nme.12.00015.
- [140] STEELE, B.C.H., . Appraisal of $\text{Ce}_{1-y}\text{Gd}_y\text{O}_{2-y/2}$ electrolytes for IT-SOFC operation at 500 °C. *Solid State Ionics*. 2000. DOI 10.1016/S0167-2738(99)00319-7.
- [141] OU, D.R.; T. MORI; F. YE; T. KOBAYASHI; J. ZOU; ET AL., . Oxygen vacancy ordering in heavily rare-earth-doped ceria. *Applied Physics Letters*. 2006. DOI 10.1063/1.2369881.
- [142] KIM, D. -J, . Lattice Parameters, Ionic Conductivities, and Solubility Limits in Fluorite-Structure MO_2 Oxide [$\text{M} = \text{Hf}^{4+}, \text{Zr}^{4+}, \text{Ce}^{4+}, \text{Th}^{4+}, \text{U}^{4+}$] Solid Solutions. *Journal of the American Ceramic Society*. 1989. DOI 10.1111/j.1151-2916.1989.tb07663.x.
- [143] HONG, S.J.; A. V. VIRKAR, . Lattice Parameters and Densities of Rare-Earth Oxide Doped Ceria Electrolytes. *Journal of the American Ceramic Society*. 1995. Vol. 78, p. 433–439. DOI 10.1111/j.1151-2916.1995.tb08820.x.
- [144] KILNER, J.A.; R.J. BROOK, . A study of oxygen ion conductivity in doped non-stoichiometric oxides. *Solid State Ionics*. 1982. DOI 10.1016/0167-2738(82)90045-5.
- [145] YAHIRO, H.; Y. EGUCHI; K. EGUCHI; H. ARAI, . Oxygen ion conductivity of the ceria-samarium oxide system with fluorite structure. *Journal of Applied Electrochemistry*. 1988. DOI 10.1007/BF01022246.
- [146] EGUCHI, K.; T. SETOGUCHI; T. INOUE; H. ARAI, . Electrical properties of ceria-based oxides and their application to solid oxide fuel cells. *Solid State Ionics*. 1992. DOI 10.1016/0167-2738(92)90102-U.
- [147] OMAR, S.; E.D. WACHSMAN; J.L. JONES; J.C. NINO, . Crystal structure-ionic conductivity relationships in doped ceria systems. *Journal of the American Ceramic Society*. 2009. DOI 10.1111/j.1551-2916.2009.03273.x.
- [148] FANG, P.; S.P. LI; J.Q. LU; Z.Y. PU; S.Q. CEN; ET AL., . Effect of phase structure on electrical conductivity of $\text{Ce}_x\text{Gd}_{1-x}\text{O}_{2-\delta}$ solid electrolytes. *Materials Science and Engineering B: Solid-State Materials for Advanced Technology*. 2009. DOI 10.1016/j.mseb.2009.08.006.
- [149] MORI, T.; Y. WANG; J. DRENNAN; G. AUCHTERLONIE; J.G. LI; ET AL., . Influence of particle morphology on nanostructural feature and conducting property in Sm-doped CeO_2 sintered body. *Solid State Ionics*. 2004. DOI 10.1016/j.ssi.2004.09.046.
- [150] CHEN, X.J.; K.A. KHOR; S.H. CHAN; L.G. YU, . Influence of microstructure

- on the ionic conductivity of yttria-stabilized zirconia electrolyte. *Materials Science and Engineering A*. 2002. DOI 10.1016/S0921-5093(01)01935-9.
- [151] RUIZ-MORALES, J.C.; D. MARRERO-LÓPEZ; M. GÁLVEZ-SÁNCHEZ; J. CANALES-VÁZQUEZ; C. SAVANIU; ET AL., . Engineering of materials for solid oxide fuel cells and other energy and environmental applications. *Energy and Environmental Science*. 2010. DOI 10.1039/c0ee00166j.
- [152] WANG, F.Y.; B.Z. WAN; S. CHENG, . Study on Gd³⁺ and Sm³⁺ co-doped ceria-based electrolytes. *Journal of Solid State Electrochemistry*. 2005. DOI 10.1007/s10008-004-0575-0.
- [153] WANG, F.Y.; B.Z. WAN; S. CHENG, . Study on Gd³⁺ and Sm³⁺ co-doped ceria-based electrolytes. *Journal of Solid State Electrochemistry*. 2005. Vol. 9, p. 168–173. DOI 10.1007/s10008-004-0575-0.
- [154] DIKMEN, S., . Effect of co-doping with Sm³⁺, Bi³⁺, La³⁺, and Nd³⁺ on the electrochemical properties of hydrothermally prepared gadolinium-doped ceria ceramics. *Journal of Alloys and Compounds*. 2010. Vol. 491, p. 106–112. DOI 10.1016/j.jallcom.2009.11.006.
- [155] KARACA, T.; T.G. ALTINÇEKİÇ; M. FARUK ÖKSÜZÖMER, . Synthesis of nanocrystalline samarium-doped CeO₂ (SDC) powders as a solid electrolyte by using a simple solvothermal route. *Ceramics International*. 2010. DOI 10.1016/j.ceramint.2009.12.005.
- [156] LIU, J.; J. YE; P. LIU; L. CHEN; M. ZHANG, . Synthesis of monodisperse samarium-doped ceria nanocrystals via a microemulsion-mediated hydrothermal method with secondary light irradiation treatment. *Materials Letters*. 2011. DOI 10.1016/j.matlet.2010.10.013.
- [157] PATIL, B.B.; S.H. PAWAR, . Spray pyrolytic synthesis of samarium doped ceria (Ce 0.8 Sm 0.2 O 1.9) films for solid oxide fuel cell applications. *Applied Surface Science*. 2007. DOI 10.1016/j.apsusc.2006.11.007.
- [158] SHAO, Z.; S.M. HALLE, . A high-performance cathode for the next generation of solid-oxide fuel cells. *Nature*. 2004. DOI 10.1038/nature02863.
- [159] ARABACI, A., . Synthesis and characterization of Pr/Gd co-doped ceria by using the citric acid–nitrate combustion method. *Solid State Ionics*. 2018. DOI 10.1016/j.ssi.2018.09.012.
- [160] ARABACI, A.; M.F. ÖKSÜZÖMER, . Ionic conductivity of Ce_{0.9-x}Gd_{0.1}Sm_xO_{2-δ} co-doped ceria electrolytes. *Acta Physica Polonica A*. 2018. Vol. 134, p. 122–124. DOI 10.12693/APhysPolA.134.122.
- [161] FU, L.; J. YANG; W. LIU, . Combustion synthesis of bulk nanocrystalline iron alloys. *Progress in Natural Science: Materials International*. 2016. DOI 10.1016/j.pnsc.2016.01.011.
- [162] CHICK, L.A.; L.R. PEDERSON; G.D. MAUPIN; J.L. BATES; L.E. THOMAS; ET AL., . Glycine-nitrate combustion synthesis of oxide ceramic powders. *Materials Letters*. 1990. DOI 10.1016/0167-577X(90)90003-5.
- [163] HUANG, D.-P.; Q. XU; H.-X. LIU; W. CHEN; K. ZHAO; ET AL., . MICROSTRUCTURE DEPENDENCE OF OXYGEN-ION CONDUCTIVITY OF SAMARIUM-DOPED CERIA CERAMICS. *Solid State Ionics*. 2012.
- [164] DENG, T.; C. ZHANG; Y. XIAO; A. XIE; Y. PANG; ET AL., . One-step synthesis

- of samarium-doped ceria and its CO catalysis. *Bulletin of Materials Science*. 2015. DOI 10.1007/s12034-015-0994-9.
- [165] MACEDO, D.A.; R.P.S. DUTRA; R.M. NASCIMENTO; J.M. SASAKI; M.R. CESÁRIO; ET AL., . Synthesis of Ce_{0.8}Sm_{0.2}O_{1.9} solid electrolyte by a proteic sol-gel green method. *Crystal Research and Technology*. 2016. DOI 10.1002/crat.201600052.
- [166] CHANG, H.; J. YAN; H. CHEN; G. YANG; J. SHI; ET AL., . Preparation of thin electrolyte film via dry pressing/heating /quenching/calcining for electrolyte-supported SOFCs. *Ceramics International*. 2019. DOI 10.1016/j.ceramint.2019.02.026.
- [167] EL HABRA, N.; M. BOLZAN; C. DE ZORZI; M. FAVARO; M. CASARIN; ET AL., . Stabilized Zirconia-Based Materials for Solid Oxide Fuel Cells (SOFC) obtained by MOCVD and Aerosol-CVD. *ECS Transactions*. 2019. DOI 10.1149/1.3207670.
- [168] SAWKA, A.; A. KWATERA, . Synthesis of non-porous and nanocrystalline lanthana-doped zirconia layers by MOCVD method at low temperatures and pressure. *Ceramics International*. 2019. DOI 10.1016/j.ceramint.2019.03.199.
- [169] UHLENBRUCK, S.; N. JORDAN; D. SEBOLD; H.P. BUCHKREMER; V.A.C. HAANAPPEL; ET AL., . Thin film coating technologies of (Ce,Gd)O₂- δ interlayers for application in ceramic high-temperature fuel cells. *Thin Solid Films*. 2007. DOI 10.1016/j.tsf.2006.10.127.
- [170] LAUKAITIS, G.; D. VIRBUKAS, . The structural and electrical properties of GDC10 thin films formed by e-beam technique. *Solid State Ionics*. 2013. DOI 10.1016/j.ssi.2013.05.024.
- [171] LAUKAITIS, G.; J. DUDONIS; D. MILCIUS, . Gadolinium doped ceria thin films deposited by e-beam technique. *Solid State Ionics*. 2008. DOI 10.1016/j.ssi.2007.12.029.
- [172] JO, S.; B. SHARMA; D.H. PARK; J. HA MYUNG, . Materials and nano-structural processes for use in solid oxide fuel cells: a review. *Journal of the Korean Ceramic Society*. 2020. DOI 10.1007/s43207-020-00022-3.
- [173] XU, W.; X. ZHANG; K. ZHOU; S. NIU; F. CHANG; ET AL., . Nano-Structured 7YSZ Electrolyte Layer for Solid Oxide Fuel Cell Prepared by Plasma Spray-Physical Vapor Deposition. *Xiyou Jinshu Cailiao Yu Gongcheng/Rare Metal Materials and Engineering*. 2019.
- [174] NURK, G.; M. VESTLI; P. MÖLLER; R. JAANISO; M. KODU; ET AL., . Mobility of Sr in Gadolinia Doped Ceria Barrier Layers Prepared Using Spray Pyrolysis, Pulsed Laser Deposition and Magnetron Sputtering Methods. *Journal of The Electrochemical Society*. 2016. DOI 10.1149/2.0531602jes.
- [175] FONSECA, F.C.; S. UHLENBRUCK; R. NEDÉLÉC; H.P. BUCHKREMER, . Properties of bias-assisted sputtered gadolinia-doped ceria interlayers for solid oxide fuel cells. *Journal of Power Sources*. 2010. DOI 10.1016/j.jpowsour.2009.09.050.
- [176] MAI, A.; V.A.C. HAANAPPEL; F. TIETZ; D. STÖVER, . Ferrite-based perovskites as cathode materials for anode-supported solid oxide fuel cells.

- Part II. Influence of the CGO interlayer. *Solid State Ionics*. 2006. DOI 10.1016/j.ssi.2005.12.010.
- [177] NOH, H.-S.; H. LEE; J.-H. LEE; H.-W. LEE; J.-W. SON, . Thin Film Electrolyte Micro-SOFC: Fabrication and Performance Improvement through Thin Film Electrolyte and Nano-Structure Electrodes. *ECS Transactions*. 2019. DOI 10.1149/1.3205607.
- [178] ZHAO, L.; K. SASAKI; S.R. BISHOP, . Fabrication and Characterization of Intermediate Temperature Solid Oxide Fuel Cells by Pulsed Laser Deposition. *ECS Transactions*. 2013. DOI 10.1149/05701.0843ecst.
- [179] HIERSO, J.; P. BOY; K. VALLÉ; J. VULLIET; F. BLEIN; ET AL., . Nanostructured ceria based thin films ($\leq 1 \mu\text{m}$) As cathode/electrolyte interfaces. *Journal of Solid State Chemistry*. 2013. DOI 10.1016/j.jssc.2012.08.021.
- [180] PLONCZAK, P.; M. JOOST; J. HJELM; M. SØGAARD; M. LUNDBERG; ET AL., . A high performance ceria based interdiffusion barrier layer prepared by spin-coating. *Journal of Power Sources*. 2011. DOI 10.1016/j.jpowsour.2010.08.108.
- [181] SCHERRER, B.; J. MARTYNCZUK; H. GALINSKI; J.G. GROLIG; S. BINDER; ET AL., . Microstructures of YSZ and CGO thin films deposited by spray pyrolysis: Influence of processing parameters on the porosity. *Advanced Functional Materials*. 2012. DOI 10.1002/adfm.201200454.
- [182] CONSTANTIN, G.; C. ROSSIGNOL; J.P. BARNES; E. DJURADO, . Interface stability of thin, dense CGO film coating on YSZ for solid oxide fuel cells. *Solid State Ionics*. 2013. DOI 10.1016/j.ssi.2013.01.015.
- [183] CHOI, H.J.; Y.H. NA; D.W. SEO; S.K. WOO; S.D. KIM, . Densification of gadolinia-doped ceria diffusion barriers for SOECs and IT-SOFCs by a sol-gel process. *Ceramics International*. 2016. DOI 10.1016/j.ceramint.2015.08.143.
- [184] DAVID A, G.; S. ISMAT SHAH, *Handbook of Thin Film Process Technology*. , 2018.
- [185] WILL, J.; A. MITTERDORFER; C. KLEINLOGEL; D. PEREDNIS; L.J. GAUCKLER, . Fabrication of thin electrolytes for second-generation solid oxide fuel cells. *Solid State Ionics*. 2000. DOI 10.1016/S0167-2738(00)00624-X.
- [186] LEE, S.; W. YU; G.Y. CHO; S.W. CHA, . Effect of Microstructure Control of Thin Film Yttria Stabilized Zirconia Electrolyte for Solid Oxide Fuel Cells by Adjusting Oblique Angle and Target Substrate Distance of Sputtering Process. *ECS Transactions*. 2019. DOI 10.1149/09101.1097ecst.
- [187] LAFFEZ, P.; Q. SIMON; Y. KIKUCHI; R. RETOUX; F. GIOVANNELLI; ET AL., . Growth of polycrystalline $\text{Pr}_4\text{Ni}_3\text{O}_{10}$ thin films for intermediate temperature solid oxide fuel cell cathode by radio frequency magnetron co-sputtering. *Thin Solid Films*. 2020. DOI 10.1016/j.tsf.2019.137705.
- [188] REZUGINA, E.; A.L. THOMANN; H. HIDALGO; P. BRAULT; V. DOLIQUE; ET AL., . Ni-YSZ films deposited by reactive magnetron sputtering for SOFC applications. *Surface and Coatings Technology*. 2010. DOI 10.1016/j.surfcoat.2010.01.006.

- [189] NÉDÉLEC, R.; S. UHLENBRUCK; D. SEBOLD; V.A.C. HAANAPPEL; H.P. BUCHKREMER; ET AL., . Dense yttria-stabilised zirconia electrolyte layers for SOFC by reactive magnetron sputtering. *Journal of Power Sources*. 2012. DOI 10.1016/j.jpowsour.2012.01.054.
- [190] BOULEAU, L.; N. COTON; P. COQUOZ; R. IHRINGER; A. BILLARD; ET AL., . GDC buffer layer synthesized by reactive magnetron sputtering: Effect of total pressure and thickness on SOFC performances. *Crystals*. 2020. DOI 10.3390/cryst10090759.
- [191] SOLOVYEV, A.A.; S. V. RABOTKIN; K.A. KUTERBEKOV; T.A. KOKETAY; S.A. NURKENOV; ET AL., . Comparison of sputter-deposited Single and multilayer electrolytes based on gadolinia-doped ceria and yttria-stabilized zirconia for solid oxide fuel cells. *International Journal of Electrochemical Science*. 2020. DOI 10.20964/2020.01.43.
- [192] CODDET, P.; M.L. AMANY; J. VULLIET; A. CAILLARD; A.L. THOMANN, . YSZ/GDC bilayer and gradient barrier layers deposited by reactive magnetron sputtering for solid oxide cells. *Surface and Coatings Technology*. 2019. DOI 10.1016/j.surfcoat.2018.09.085.
- [193] HONG, Y.S.; S.H. KIM; W.J. KIM; H.H. YOON, *Fabrication and characterization GDC electrolyte thin films by e-beam technique for IT-SOFC*. *Curr. Appl. Phys.* 2011. DOI 10.1016/j.cap.2011.03.071.
- [194] LAUKAITIS, G.; J. DUDONIS, . Microstructure of gadolinium doped ceria oxide thin films formed by electron beam deposition. *Journal of Alloys and Compounds*. 2008. DOI 10.1016/j.jallcom.2007.04.223.
- [195] LAUKAITIS, G.; J. DUDONIS; D. MILČIUS, . Formation of Gadolinium Doped Ceria Oxide Thin Films by Electron Beam Deposition. *Materials Science*. 2007.
- [196] SZYMCZEWSKA, D.; A. CHRZAN; J. KARCZEWSKI; S. MOLIN; P. JASINSKI, . Spray pyrolysis of doped-ceria barrier layers for solid oxide fuel cells. *Surface and Coatings Technology*. 2017. DOI 10.1016/j.surfcoat.2017.01.066.
- [197] MARTÍNEZ-AMESTI, A.; A. LARRAÑAGA; L.M. RODRÍGUEZ-MARTÍNEZ; A.T. AGUAYO; J.L. PIZARRO; ET AL., . Reactivity between La(Sr)FeO₃ cathode, doped CeO₂ interlayer and yttria-stabilized zirconia electrolyte for solid oxide fuel cell applications. *Journal of Power Sources*. 2008. DOI 10.1016/j.jpowsour.2008.06.049.
- [198] SZYMCZEWSKA, D.; J. KARCZEWSKI; A. CHRZAN; P. JASINSKI, . CGO as a barrier layer between LSCF electrodes and YSZ electrolyte fabricated by spray pyrolysis for solid oxide fuel cells. *Solid State Ionics*. 2017. DOI 10.1016/j.ssi.2016.11.008.
- [199] STOJANOVIC, B.D.; A.S. DZUNUZOVIC; N.I. ILIC, *Review of methods for the preparation of magnetic metal oxides*. *Magn. Ferroelectr. Multiferroic Met. Oxides*. 2018. DOI 10.1016/B978-0-12-811180-2.00017-7.
- [200] VARMA, A.; A.S. MUKASYAN; A.S. ROGACHEV; K. V. MANUKYAN, . Solution Combustion Synthesis of Nanoscale Materials. *Chemical Reviews*. 2016. Vol. 116, p. 14493–14586. DOI 10.1021/acs.chemrev.6b00279.

- [201] MUKASYAN, A.S.; K. V. MANUKYAN, *One- and two-dimensional nanostructures prepared by combustion synthesis.* , Elsevier Inc.,2019. DOI 10.1016/B978-0-12-815751-0.00004-3.
- [202] SHAO, Z.; W. ZHOU; Z. ZHU, . Advanced synthesis of materials for intermediate-temperature solid oxide fuel cells. *Progress in Materials Science.* 2012. DOI 10.1016/j.pmatsci.2011.08.002.
- [203] HWANG, C.C.; T.H. HUANG; J.S. TSAI; C.S. LIN; C.H. PENG, . Combustion synthesis of nanocrystalline ceria (CeO₂) powders by a dry route. *Materials Science and Engineering B: Solid-State Materials for Advanced Technology.* 2006. DOI 10.1016/j.mseb.2006.01.021.
- [204] KALYK, F.; A. STANKEVIČIŪTĖ; G. BUDRYTĖ; G. GAIDAMAVIČIENĖ; A. ŽALGA; ET AL., . Comparative study of samarium-doped ceria nanopowders synthesized by various chemical synthesis routes. *Ceramics International.* 2020. Vol. 46, p. 24385–24394. DOI 10.1016/j.ceramint.2020.06.221.
- [205] JADHAV, L.D.; S.P. PATIL; A.P. JAMALE; A.U. CHAVAN, . Solution combustion synthesis: Role of oxidant to fuel ratio on powder properties. *Materials Science Forum.* 2013. Vol. 757, p. 85–98. DOI 10.4028/www.scientific.net/MSF.757.85.
- [206] WELLER, J.M.; J.A. WHETTEN; C.K. CHAN, . Nonaqueous Polymer Combustion Synthesis of Cubic Li₇La₃Zr₂O₁₂ Nanopowders. *ACS Applied Materials and Interfaces.* 2020. DOI 10.1021/acsami.9b19981.
- [207] CHENG, L.; L. LUO; X. XU; J. SHI; Y. WU, . Preparation of GDC Nanopowder with Different Gadolinium Contents by Combustion Method and Its Electrical Conductivity. *Kuei Suan Jen Hsueh Pao/Journal of the Chinese Ceramic Society.* 2018. DOI 10.14062/j.issn.0454-5648.2018.03.07.
- [208] KOBAYASHI, H.; A. HAYAKAWA; K.D.K.A. SOMARATHNE; E.C. OKAFOR, . Science and technology of ammonia combustion. *Proceedings of the Combustion Institute.* 2019. DOI 10.1016/j.proci.2018.09.029.
- [209] THODA, O.; G. XANTHOPOULOU; G. VEKINIS; A. CHRONEOS, . Review of Recent Studies on Solution Combustion Synthesis of Nanostructured Catalysts. *Advanced Engineering Materials.* 2018. DOI 10.1002/adem.201800047.
- [210] MORSI, K., . Combustion synthesis and the electric field: A review. *International Journal of Self-Propagating High-Temperature Synthesis.* 2017. DOI 10.3103/S1061386217030037.
- [211] WAGMAN, D.D.; W.H. EVANS; V.B. PARKER; R.H. SCHUMM; I. HALOW; ET AL., . The NBS Tables of Chemical Thermodynamic Properties. *Journal of Physical and Chemical Reference Data.* 1982.
- [212] EMENOV, N.N.; M. BOUDART, . Some Problems in Chemical Kinetics and Reactivity, Vol. 2. *Physics Today.* 1960.
- [213] SHTEINBERG, A.S.; V.A. SHCHERBAKOV; Z.A. MUNIR, . Kinetics of combustion in the layered Ni-Al system. *Combustion Science and Technology.* 2001. DOI 10.1080/00102200108907837.
- [214] AZATYAN, V. V., . Chain reactions of gas combustion, explosion, and detonation: Chemical methods for process management. *Review Journal of*

Chemistry. 2017.

- [215] ROGACHEV, A.S., *Combustion for Material Synthesis*. , 2014. DOI 10.1201/b17842.
- [216] SINGH, K.; S.A. ACHARYA; S.S. BHOGA, . Low temperature processing of dense samarium-doped CeO₂ ceramics: Sintering and intermediate temperature ionic conductivity. *Ionics*. 2007. Vol. 13, p. 429–434. DOI 10.1007/s11581-007-0123-x.
- [217] RANE, A.V.; K. KANNY; V.K. ABITHA; S. THOMAS, *Methods for Synthesis of Nanoparticles and Fabrication of Nanocomposites*. , Elsevier Ltd., 2018. DOI 10.1016/b978-0-08-101975-7.00005-1.
- [218] FEITKNECHT, W.; P. SCHINDLER, . Solubility constants of metal oxides, metal hydroxides and metal hydroxide salts in aqueous solution. *Pure and Applied Chemistry*. 1963.
- [219] SHAO, Z.; W. ZHOU; Z. ZHU, . Advanced synthesis of materials for intermediate-temperature solid oxide fuel cells. *Progress in Materials Science*. 2012. Vol. 57, p. 804–874. DOI 10.1016/j.pmatsci.2011.08.002.
- [220] KALISZEWSKI, M.S.; A.H. HEUER, . Alcohol Interaction with Zirconia Powders. *Journal of the American Ceramic Society*. 1990. DOI 10.1111/j.1151-2916.1990.tb09787.x.
- [221] LI, J.G.; T. IKEGAMI; J.H. LEE; T. MORI, . Characterization and sintering of nanocrystalline CeO₂ powders synthesized by a mimic alkoxide method. *Acta Materialia*. 2001. DOI 10.1016/S1359-6454(00)00327-X.
- [222] MURALIDHARAN, P.; S.H. JO; D.K. KIM, . Electrical conductivity of submicrometer gadolinia-doped ceria sintered at 1000°C using precipitation-synthesized nanocrystalline powders. *Journal of the American Ceramic Society*. 2008. DOI 10.1111/j.1551-2916.2008.02644.x.
- [223] LI, S.; R. GUO; J. LI; Y. CHEN; W. LIU, . Synthesis of NiO-ZrO₂ powders for solid oxide fuel cells. *Ceramics International*. 2003. DOI 10.1016/S0272-8842(03)00031-2.
- [224] WANG, Y.; T. MORI; J.G. LI; Y. YAJIMA; J. DRENNAN, . Synthesis, characterization and sinterability of 10 mol% Sm₂ O₃-doped CeO₂ nanopowders via carbonate precipitation. *Journal of the European Ceramic Society*. 2006. DOI 10.1016/j.jeurceramsoc.2005.07.028.
- [225] PRASAD, S.; V. KUMAR; S. KIRUBANANDAM; A. BARHOUM, *Engineered nanomaterials: Nanofabrication and surface functionalization*. , Elsevier Inc., 2018. DOI 10.1016/B978-0-323-51254-1.00011-7.
- [226] BRANDA, F., *The Sol-Gel Route to Nanocomposites*. *Adv. Nanocomposites - Synth. Charact. Ind. Appl.* 2011. DOI 10.5772/15454.
- [227] LAKSHMI, B.B.; C.J. PATRISSI; C.R. MARTIN, . Sol-Gel Template Synthesis of Semiconductor Oxide Micro- and Nanostructures. *Chemistry of Materials*. 1997. DOI 10.1021/cm970268y.
- [228] DARAIO, C.; S. JIN, *Synthesis and Patterning Methods for Nanostructures Useful for Biological Applications*. 2012. DOI 10.1007/978-0-387-31296-5_2.
- [229] CÉLÉRIER, S.; C. LABERTY; F. ANSART; P. LENORMAND; P. STEVENS, . New

- chemical route based on sol-gel process for the synthesis of oxyapatite La₉33Si₆O₂₆. *Ceramics International*. 2006. DOI 10.1016/j.ceramint.2005.03.001.
- [230] VIAZZI, C.; A. DEBONI; J. ZOPPAS FERREIRA; J.P. BONINO; F. ANSART, . Synthesis of Yttria Stabilized Zirconia by sol-gel route: Influence of experimental parameters and large scale production. *Solid State Sciences*. 2006. DOI 10.1016/j.solidstatesciences.2006.02.053.
- [231] KESSLER, V.G.; G.A. SEISENBAEVA; P. WERNDRUP; S. PAROLA; G.I. SPIJKSMA, *Design of molecular structure and synthetic approaches to single-source precursors in the sol-gel technology*. *Mater. Sci. Pol.* 2005.
- [232] LIVAGE, J.; F. BABONNEAU; M. CHATRY; L. COURY, . Sol-gel synthesis and NMR characterization of ceramics. *Ceramics International*. 1997. DOI 10.1016/0272-8842(95)00133-6.
- [233] CHANGRONG, X.; C. HUAQIANG; W. HONG; Y. PINGHUA; M. GUANGYAO; ET AL., . Sol-gel synthesis of yttria stabilized zirconia membranes through controlled hydrolysis of zirconium alkoxide. *Journal of Membrane Science*. 1999. DOI 10.1016/S0376-7388(99)00137-4.
- [234] PECHINI, M., . Patent No. 3,330,697. *United States Patent Office*. 1967.
- [235] LOGANATHAN, S.; R.B. VALAPA; R.K. MISHRA; G. PUGAZHENTHI; S. THOMAS, *Thermogravimetric Analysis for Characterization of Nanomaterials*. , Elsevier Inc., 2017. DOI 10.1016/B978-0-323-46139-9.00004-9.
- [236] EBNESAJJAD, S., *Surface and Material Characterization Techniques*. *Surf. Treat. Mater. Adhes. Bond.* 2014. DOI 10.1016/b978-0-323-26435-8.00004-6.
- [237] *Methods for Assessing Surface Cleanliness*. *Dev. Surf. Contam. Cleaning*, Vol. 12. 2019. DOI 10.1016/b978-0-12-816081-7.00003-6.
- [238] RUFFELL, A.; P. WILTSHIRE, . Conjunctive use of quantitative and qualitative X-ray diffraction analysis of soils and rocks for forensic analysis. *Forensic Science International*. 2004. DOI 10.1016/j.forsciint.2004.03.017.
- [239] LUTTEROTTI, L.; D. CHATEIGNER; S. FERRARI; J. RICOTE, *Texture, residual stress and structural analysis of thin films using a combined X-ray analysis*. *Thin Solid Films*. 2004. DOI 10.1016/j.tsf.2003.10.150.
- [240] LEONI, M.; R. DI MAGGIO; S. POLIZZI; P. SCARDI, . X-ray diffraction methodology for the microstructural analysis of nanocrystalline powders: Application to cerium oxide. *Journal of the American Ceramic Society*. 2004. DOI 10.1111/j.1551-2916.2004.01133.x.
- [241] SCHERRER, P., . Determination of the internal structure and size of colloid particles by X-rays. *Göttinger Nachrichten Gesell.* 1918.
- [242] PATTERSON, A.L., . The scherrer formula for X-ray particle size determination. *Physical Review*. 1939. DOI 10.1103/PhysRev.56.978.
- [243] NASROLLAHZADEH, M.; M. ATAROD; M. SAJJADI; S.M. SAJJADI; Z. ISSAABADI, *Plant-Mediated Green Synthesis of Nanostructures: Mechanisms, Characterization, and Applications*. , 1st ed., Elsevier Ltd., 2019. DOI 10.1016/B978-0-12-813586-0.00006-7.

- [244] HANAOR, D.A.H.; M. GHADIRI; W. CHRZANOWSKI; Y. GAN, . Scalable surface area characterization by electrokinetic analysis of complex anion adsorption. *Langmuir*. 2014. DOI 10.1021/la503581e.
- [245] MOURDIKOU DIS, S.; R.M. PALLARES; N.T.K. THANH, . Characterization techniques for nanoparticles: Comparison and complementarity upon studying nanoparticle properties. *Nanoscale*. 2018. DOI 10.1039/c8nr02278j.
- [246] LI, J.G.; Y. WANG; T. Ikegami; T. MORI; T. Ishigaki, . Reactive 10 mol% RE₂O₃ (RE = Gd and Sm) doped CeO₂ nanopowders: Synthesis, characterization, and low-temperature sintering into dense ceramics. *Materials Science and Engineering B: Solid-State Materials for Advanced Technology*. 2005. Vol. 121, p. 54–59. DOI 10.1016/j.mseb.2005.03.001.
- [247] STOKES, D.J., *Principles and Practice of Variable Pressure/Environmental Scanning Electron Microscopy (VP-ESEM)*. , 2008. DOI 10.1002/9780470758731.
- [248] INKSON, B.J., *Scanning Electron Microscopy (SEM) and Transmission Electron Microscopy (TEM) for Materials Characterization. Mater. Charact. Using Nondestruct. Eval. Methods*. 2016. DOI 10.1016/B978-0-08-100040-3.00002-X.
- [249] KRYSZTOF, M.; W. SŁÓWKO, . Optimisation of secondary electron detector for variable pressure SEM with Monte Carlo method. *Vacuum*. 2008. DOI 10.1016/j.vacuum.2008.01.017.
- [250] JIRUŠE, J.; M. HAVELKA; F. LOPOUR, . Novel field emission SEM column with beam deceleration technology. *Ultramicroscopy*. 2014. DOI 10.1016/j.ultramic.2014.05.006.
- [251] SUTTON, M.A.; N. LI; D.C. JOY; A.P. REYNOLDS; X. LI, . Scanning electron microscopy for quantitative small and large deformation measurements Part I: SEM imaging at magnifications from 200 to 10,000. *Experimental Mechanics*. 2007. DOI 10.1007/s11340-007-9042-z.
- [252] POLINI, A.; F. YANG, *Physicochemical characterization of nanofiber composites. Nanofiber Compos. Biomed. Appl.* 2017. DOI 10.1016/B978-0-08-100173-8.00005-3.
- [253] WANG, G.C., *Slag processing. Util. Slag Civ. Infrastruct. Constr.* 2016. DOI 10.1016/b978-0-08-100381-7.00005-7.
- [254] GOMADAM, P.M.; J.W. WEIDNER, . Analysis of electrochemical impedance spectroscopy in proton exchange membrane fuel cells. *International Journal of Energy Research*. 2005. DOI 10.1002/er.1144.
- [255] ZHANG, X.; T. ZHANG; H. CHEN; Y. CAO, . A review of online electrochemical diagnostic methods of on-board proton exchange membrane fuel cells. *Applied Energy*. 2021. DOI 10.1016/j.apenergy.2021.116481.
- [256] CESIULIS, H.; N. TSYNTSARU; A. RAMANAVICIUS; G. RAGOISHA, *The Study of Thin Films by Electrochemical Impedance Spectroscopy*. 2016. DOI 10.1007/978-3-319-30198-3_1.
- [257] HOLDYNSKI, M.; M. SINTYUREVA; X. LIU; M. LESZCZYNSKA; F. KROK; ET AL., . Structure and conductivity in the Bi₄Nb_{1-x}Y_xO_{8.5-x} oxide-ion conducting system. *Solid State Ionics*. 2018. Vol. 328, p. 8–16. DOI

- 10.1016/j.ssi.2018.11.003.
- [258] MATHER, R.R., *Surface modification of textiles by plasma treatments.* , Woodhead Publishing Limited, 2009. DOI 10.1533/9781845696689.296.
 - [259] ARONNIEMI, M.; J. SAINIO; J. LAHTINEN, . Aspects of using the factor analysis for XPS data interpretation. *Surface Science.* 2007. DOI 10.1016/j.susc.2006.10.010.
 - [260] MAURICE, P.A., *Applications of atomic-force microscopy in environmental colloid and surface chemistry.* *Colloids Surfaces A Physicochem. Eng. Asp.* 1996. DOI 10.1016/0927-7757(95)03372-6.
 - [261] RAJA, P.M. V; A.R. BARRON, . Physical methods in chemistry and nano science. *Nature.* 1934.
 - [262] ZHANG, T.; W. PENG; K. SHEN; S. YU, . AFM measurements of adhesive forces between carbonaceous particles and the substrates. *Nuclear Engineering and Design.* 2015. DOI 10.1016/j.nucengdes.2015.06.022.
 - [263] HAUGSTAD, G., *Atomic Force Microscopy: Understanding Basic Modes and Advanced Applications.* , 2012. DOI 10.1002/9781118360668.
 - [264] ÁLVAREZ-GARCÍA, J.; V. IZQUIERDO-ROCA; A. PÉREZ-RODRÍGUEZ, . Raman Spectroscopy on Thin Films for Solar Cells. *Advanced Characterization Techniques for Thin Film Solar Cells.* 2011. p. 365–386.
 - [265] RAMAN, C. V.; K.S. KRISHNAN, . A new type of secondary radiation [11]. *Nature.* 1928.
 - [266] SMITH, E.; G. DENT, *Introduction, Basic Theory and Principles.* *Mod. Raman Spectrosc. - A Pract. Approach.* 2005. DOI 10.1002/0470011831.ch1.
 - [267] GAIDAMAVIČIENĖ, G.; B. ABAKEVIČIENĖ; A. ŽALGA, . Oxalic acid assisted synthesis of the gadolinium-doped ceria oxide-ion conductor as electrolyte for the solid oxide fuel cells. *Chemical Papers.* 2019. Vol. 73, p. 891–899. DOI 10.1007/s11696-018-0648-7.
 - [268] BRAZIULIS, G.; G. JANULEVICIUS; R. STANKEVICIUTE; A. ZALGA, . Aqueous sol-gel synthesis and thermoanalytical study of the alkaline earth molybdate precursors. *Journal of Thermal Analysis and Calorimetry.* 2013. DOI 10.1007/s10973-013-3579-0.
 - [269] HAN, X.; L. TIAN; H. JIANG; L. KONG; J. LV; ET AL., . Facile transformation of low cost melamine-oxalic acid into porous graphitic carbon nitride nanosheets with high visible-light photocatalytic performance. *RSC Advances.* 2017. DOI 10.1039/c7ra01205e.
 - [270] ARABAC, A.; M.F. ÖKSÜZÖMER, . Preparation and characterization of 10 mol% Gd doped CeO₂ (GDC) electrolyte for SOFC applications. *Ceramics International.* 2012. DOI 10.1016/j.ceramint.2012.05.030.
 - [271] KIM, G.; N. LEE; K.B. KIM; B.K. KIM; H. CHANG; ET AL., . Various synthesis methods of aliovalent-doped ceria and their electrical properties for intermediate temperature solid oxide electrolytes. *International Journal of Hydrogen Energy.* 2013. DOI 10.1016/j.ijhydene.2012.11.044.
 - [272] MOKKELBOST, T.; I. KAUS; T. GRANDE; M.A. EINARSRUD, . Combustion synthesis and characterization of nanocrystalline CeO₂-based powders. *Chemistry of Materials.* 2004. DOI 10.1021/cm048583p.

- [273] ACCARDO, G.; C. FERONE; R. CIOFFI; D. FRATTINI; L. SPIRIDIGLIOZZI; ET AL., . Electrical and microstructural characterization of ceramic gadolinium-doped ceria electrolytes for ITSOFCs by sol-gel route. *Journal of Applied Biomaterials and Functional Materials*. 2016. DOI 10.5301/jabfm.5000265.
- [274] PALNEEDI, H.; V. MANGAM; S. DAS; K. DAS, . Effect of fuel-to-nitrate ratio on the powder characteristics of nanosized CeO₂ synthesized by mixed fuel combustion method. *Journal of Alloys and Compounds*. 2011. DOI 10.1016/j.jallcom.2011.07.087.
- [275] BOLIS, V.; G. CERRATO; G. MAGNACCA; C. MORTERRA, . Surface acidity of metal oxides. Combined microcalorimetric and IR-spectroscopic studies of variously dehydrated systems. *Thermochimica Acta*. 1998. DOI 10.1016/s0040-6031(97)00440-1.
- [276] AMARSINGH BHABU, K.; J. THEERTHAGIRI; J. MADHAVAN; T. BALU; G. MURALIDHARAN; ET AL., . Cubic fluorite phase of samarium doped cerium oxide (CeO₂)_{0.96}Sm_{0.04} for solid oxide fuel cell electrolyte. *Journal of Materials Science: Materials in Electronics*. 2016. DOI 10.1007/s10854-015-3925-z.
- [277] CHEN, W.; F. LI; J. YU, . Combustion synthesis and characterization of nanocrystalline CeO₂-based powders via ethylene glycol-nitrate process. *Materials Letters*. 2006. DOI 10.1016/j.matlet.2005.07.088.
- [278] SWANSON, M.; N. TANGTRAKARN; M. SUNDER; P.D. MORAN, . Impact of the presence of grain boundaries on the in-plane ionic conductivity of thin film Gd-doped CeO₂. *Solid State Ionics*. 2010. DOI 10.1016/j.ssi.2010.01.020.
- [279] AYGÜN, B.; H. ÖZDEMİR; M.A.F. ÖKSÜZÖMER, . Structural, morphological and conductivity properties of samaria doped ceria (Sm_xCe_{1-x}O_{2-x/2}) electrolytes synthesized by electrospinning method. *Materials Chemistry and Physics*. 2019. Vol. 232, p. 82–87. DOI 10.1016/j.matchemphys.2019.04.067.
- [280] ZHAN, Z.; T.-L. WEN; H. TU; Z.-Y. LU, . AC Impedance Investigation of Samarium-Doped Ceria. *Journal of The Electrochemical Society*. 2001. DOI 10.1149/1.1359198.
- [281] TOOR, S.Y.; E. CROISSET, . Reducing sintering temperature while maintaining high conductivity for SOFC electrolyte: Copper as sintering aid for Samarium Doped Ceria. *Ceramics International*. 2020. Vol. 46, p. 1148–1157. DOI 10.1016/j.ceramint.2019.09.083.
- [282] CHOURASHIYA, M.G.; J.Y. PATIL; S.H. PAWAR; L.D. JADHAV, . Studies on structural, morphological and electrical properties of Ce_{1-x}Gd_xO_{2-(x/2)}. *Materials Chemistry and Physics*. 2008. DOI 10.1016/j.matchemphys.2007.10.028.
- [283] HUANG, Q.A.; M. LIU; M. LIU, . Impedance Spectroscopy Study of an SDC-based SOFC with High Open Circuit Voltage. *Electrochimica Acta*. 2015. DOI 10.1016/j.electacta.2014.11.065.
- [284] WATTANATHANA, W.; C. VERANITISAGUL; S. WANNAPAIBOON; W. KLYSUBUN; N. KOONSAENG; ET AL., . Samarium doped ceria (SDC) synthesized by a metal triethanolamine complex decomposition method:

- Characterization and an ionic conductivity study. *Ceramics International*. 2017. Vol. 43, p. 9823–9830. DOI 10.1016/j.ceramint.2017.04.162.
- [285] PENG, R.; C. XIA; Q. FU; G. MENG; D. PENG, . Sintering and electrical properties of $(\text{CeO}_2)_{0.8}(\text{Sm}_2\text{O}_3)_{0.1}$ powders prepared by glycine-nitrate process. *Materials Letters*. 2002. Vol. 56, p. 1043–1047. DOI 10.1016/S0167-577X(02)00673-0.
- [286] FU, Y.P.; S.B. WEN; C.H. LU, . Preparation and characterization of samaria-doped ceria electrolyte materials for solid oxide fuel cells. *Journal of the American Ceramic Society*. 2008. DOI 10.1111/j.1551-2916.2007.01923.x.
- [287] ANANTHARAMAN, S.B.; R. BAURI, . Effect of sintering atmosphere on densification, redox chemistry and conduction behavior of nanocrystalline Gd-doped CeO_2 electrolytes. *Ceramics International*. 2013. DOI 10.1016/j.ceramint.2013.05.059.
- [288] HUANG, K.; M. FENG; J.B. GOODENOUGH, . Synthesis and electrical properties of dense $\text{Ce}_{0.9}\text{Gd}_{0.1}\text{O}_{1.95}$ ceramics. *Journal of the American Ceramic Society*. 1998. DOI 10.1111/j.1151-2916.1998.tb02341.x.
- [289] MANDAL, B.P.; V. GROVER; M.R. PAI; A.K. TYAGI, . Improvement of physico-chemical properties by addition of H_2O_2 : An extensive case study on the RE-doped ceria system (RE = Gd, Sm). *Journal of Materials Research*. 2009. DOI 10.1557/jmr.2009.0352.
- [290] GALDIKAS, A.; R. ČERAPAITĖ-TRUŠINSKIENE; G. LAUKAITIS; J. DUDONIS, . Real-time kinetic modeling of YSZ thin film roughness deposited by e-beam evaporation technique. *Applied Surface Science*. 2008. DOI 10.1016/j.apsusc.2008.06.191.
- [291] SHANNON, R.D., . Revised effective ionic radii and systematic studies of interatomic distances in halides and chalcogenides. *Acta Crystallographica Section A*. 1976.
- [292] ZHA, S.; A. MOORE; H. ABERNATHY; M. LIU, . GDC-Based Low-Temperature SOFCs Powered by Hydrocarbon Fuels. *Journal of The Electrochemical Society*. 2004. DOI 10.1149/1.1764566.
- [293] FUENTES, R.O.; R.T. BAKER, . Structural, morphological and electrical properties of $\text{Gd}_{0.1}\text{Ce}_{0.9}\text{O}_{1.95}$ prepared by a citrate complexation method. *Journal of Power Sources*. 2009. Vol. 186, p. 268–277. DOI 10.1016/j.jpowsour.2008.09.119.
- [294] ÖKSÜZÖMER, M.A.F.; G. DÖNMEZ; V. SARIBOĞA; T.G. ALTINÇEKİÇ, . Microstructure and ionic conductivity properties of gadolinia doped ceria ($\text{Gd}_x\text{Ce}_{1-x}\text{O}_{2-x/2}$) electrolytes for intermediate temperature SOFCs prepared by the polyol method. *Ceramics International*. 2013. Vol. 39, p. 7305–7315. DOI 10.1016/j.ceramint.2013.02.069.
- [295] CHOURASHIYA, M.G.; L.D. JADHAV, . Synthesis and characterization of 10%Gd doped ceria (GDC) deposited on NiO -GDC anode-grade-ceramic substrate as half cell for IT-SOFC. *International Journal of Hydrogen Energy*. 2011. DOI 10.1016/j.ijhydene.2010.12.083.
- [296] MACKAY, D.; I. VAN WESENBEECK, . Correlation of chemical evaporation rate with vapor pressure. *Environmental Science and Technology*. 2014. DOI

- 10.1021/es5029074.
- [297] OTIENO, F.; M. AIRO; R.M. ERASMUS; A. QUANDT; D.G. BILLING; ET AL., . Annealing effect on the structural and optical behavior of ZnO:Eu³⁺ thin film grown using RF magnetron sputtering technique and application to dye sensitized solar cells. *Scientific Reports*. 2020. Vol. 10, p. 1–10. DOI 10.1038/s41598-020-65231-6.
 - [298] HAJAKBARI, F.; M. ENSANDOUST, . Study of thermal annealing effect on the properties of silver thin films prepared by DC magnetron sputtering. *Acta Physica Polonica A*. 2016. Vol. 129, p. 680–682. DOI 10.12693/APhysPolA.129.680.
 - [299] KHALIPOVA, O.S.; V. LAIR; A. RINGUEDÉ, . Electrochemical synthesis and characterization of Gadolinia-Doped Ceria thin films. *Electrochimica Acta*. 2014. DOI 10.1016/j.electacta.2013.11.022.
 - [300] MEDISETTI, S.; J. AHN; S. PATIL; A. GOEL; Y. BANGARU; ET AL., . Synthesis of GDC electrolyte material for IT-SOFCs using glucose & fructose and its characterization. *Nano-Structures and Nano-Objects*. 2017. Vol. 11, p. 7–12. DOI 10.1016/j.nanoso.2017.05.009.
 - [301] HARI PRASAD, D.; H.R. KIM; J.S. PARK; J.W. SON; B.K. KIM; ET AL., . Superior sinterability of nano-crystalline gadolinium doped ceria powders synthesized by co-precipitation method. *Journal of Alloys and Compounds*. 2010. Vol. 495, p. 238–241. DOI 10.1016/j.jallcom.2010.01.137.
 - [302] ZARKOV, A.; A. STANULIS; L. MIKOLIUNAITE; A. KATELNIKOVAS; V. JASULAITIENE; ET AL., . Chemical solution deposition of pure and Gd-doped ceria thin films: Structural, morphological and optical properties. *Ceramics International*. 2017. DOI 10.1016/j.ceramint.2016.12.070.
 - [303] SAITZEK, S.; J.F. BLACH; S. VILLAIN; J.R. GAVARRI, . Nanostructured ceria: A comparative study from X-ray diffraction, Raman spectroscopy and BET specific surface measurements. *Physica Status Solidi (A) Applications and Materials Science*. 2008. DOI 10.1002/pssa.200723419.
 - [304] TANIGUCHI, T.; T. WATANABE; N. SUGIYAMA; A.K. SUBRAMANI; H. WAGATA; ET AL., . Identifying defects in ceria-based nanocrystals by UV resonance Raman spectroscopy. *Journal of Physical Chemistry C*. 2009. DOI 10.1021/jp9049457.
 - [305] CHIN, H.S.; L.S. CHAO, . The effect of thermal annealing processes on structural and photoluminescence of zinc oxide thin film. *Journal of Nanomaterials*. 2013. Vol. 2013, DOI 10.1155/2013/424953.
 - [306] BASTAKYS, L.; F. KALYK; L. MARCINAUSKAS; J. ČYVIENĖ; B. ABAKEVIČIENĖ, . Structural investigation of gadolinia-ceria multilayered thin films deposited by reactive magnetron sputtering. *Materials Letters*. 2020. Vol. 271, DOI 10.1016/j.matlet.2020.127762.
 - [307] MUTHUKKUMARAN, K.; P. KUPPUSAMI; R. KESAVAMOORTHY; T. MATHEWS; E. MOHANDAS; ET AL., . Microstructural studies of bulk and thin film GDC. *Ionics*. 2008. Vol. 14, p. 165–171. DOI 10.1007/s11581-007-0152-5.
 - [308] MCBRIDE, J.R.; K.C. HASS; B.D. POINDEXTER; W.H. WEBER, . Raman and x-ray studies of Ce_{1-x}RE_xO_{2-y}, where RE=La, Pr, Nd, Eu, Gd, and Tb.

- Journal of Applied Physics*. 1994. DOI 10.1063/1.357593.
- [309] ZHANG, S.; J. LI; X. GUO; L. LIU; H. WEI; ET AL., . Nanostructured composite films of ceria nanoparticles with anti-UV and scratch protection properties constructed using a layer-by-layer strategy. *Applied Surface Science*. 2016. DOI 10.1016/j.apsusc.2016.04.151.
 - [310] GONDOLINI, A.; E. MERCADELLI; A. SANSON; S. ALBONETTI; L. DOUBOVA; ET AL., . Microwave-assisted synthesis of gadolinia-doped ceria powders for solid oxide fuel cells. *Ceramics International*. 2011. DOI 10.1016/j.ceramint.2011.01.010.
 - [311] PATIL, B.B.; S. BASU, *Synthesis and characterization of PdO-NiO-SDC nano-powder by glycine-nitrate combustion synthesis for anode of IT-SOFC*. *Energy Procedia*. 2014. DOI 10.1016/j.egypro.2014.07.308.
 - [312] NOH, H.-S.; H. LEE; J.-H. LEE; H.-W. LEE; J.-W. SON, . Thin Film Electrolyte Micro-SOFC: Fabrication and Performance Improvement through Thin Film Electrolyte and Nano-Structure Electrodes. *ECS Transactions*. 2009. DOI 10.1149/1.3205607.
 - [313] ZHAO, L.; K. SASAKI; S.R. BISHOP, . Fabrication and Characterization of Intermediate Temperature Solid Oxide Fuel Cells by Pulsed Laser Deposition. *ECS Transactions*. 2013. DOI 10.1149/05701.0843ecst.
 - [314] GLOCKER, D.A.; S. ISMAT SHAH, *Handbook of thin film process technology: 98/1 reactive sputtering*. , 2018. DOI 10.1201/9781351072786.
 - [315] Kalyk, F.; Žalga, A.; Vasiliauskas, A.; Tamulevičius, T.; Tamulevičius, S.; Abakevičienė, B, Synthesis and electron-beam evaporation of gadolinium-doped ceria thin films. *Coatings. Basel: MDPI*. 2022. DOI:10.3390/coatings12060747.

8. CURRICULUM VITAE

Name, Surname: Fariza Kalyk

Date of birth: 01.09.1993

Email: fariza.kalyk@ktu.lt

Phone: +37062903862

ORCID: <https://orcid.org/0000-0002-0926-3259>

LinkedIn: <https://www.linkedin.com/in/fariza-kalyk-b45b941b1/>

ResearchGate: <https://www.researchgate.net/profile/Fariza-Kalyk-2>

EMPLOYMENT HISTORY

Research Laboratory of Surfaces and Thin Films, Kaunas University of Technology

Project Junior Researcher, *September 2021 (Kaunas, Lithuania)*

Research Laboratory of Surfaces and Thin Films, Kaunas University of Technology

Project Engineer, *April 2021 – May 2021 (Kaunas, Lithuania)*

Research Laboratory of Vacuum and Plasma Processes, Kaunas University of Technology

Project Junior Researcher, *November 2018 – December 2018 (Kaunas, Lithuania)*

Multidisciplinary college

Teacher of Physics, *July 2015 – July 2016 (Almaty, Kazakhstan)*

EDUCATION

Kaunas University of Technology

PhD in Materials Science, *September 2017 – September 2021*

Awards:

- Research Council of Lithuania, PhD student scholarship for academic achievements, *2021*
- KTU (Kaunas University of Technology) contest of the most active PhD students, *2020*
- Best poster presentation at 13th International Symposium on Systems with Fast Ionic Transport (ISSFIT-13) conference(Minsk, Belarus), *2018*

Abai Kazakh National Pedagogical University

Master of Natural Sciences, *2015–2017*

Abai Kazakh National Pedagogical University

Bachelor of Science in Education with a degree in Physics, *2011–2015*

PROFESSIONAL SKILLS AND LANGUAGES

- Combustion chemical synthesis, Co-precipitation chemical synthesis, Electron-beam evaporation, X-ray diffraction spectroscopy, Impedance spectroscopy, Atomic force microscopy, Fourier-transform infrared spectroscopy, Raman spectroscopy, Scanning electron microscopy, Spray pyrolysis.

INTERNSHIPS

Erasmus internship, October 2021 – May 2022 (Gdansk, Poland)

Faculty of Electronics, Telecommunications and Informatics, Gdańsk University of Technology

Erasmus internship, February 2018 – June 2018 (Warsaw, Poland)

Institute of Solid-State Ionics, Warsaw University of Technology

Academic mobility exchange, September 2016 – February 2017 (Kaunas, Lithuania)

Kaunas University of Technology

Academic mobility exchange, September 2012 – February 2013 (Linz, Austria)

Private University of Education Diocese of Linz

9. LIST OF PUBLICATIONS AND CONFERENCES RELATED TO THE DISSERTATION

List of publications related to the dissertation

A1. KALYK, Fariza; STANKEVIČIŪTĖ, Algita; BUDRYTĖ, Gintarė; GAIDAMAVIČIENĖ, Giedrė; ŽALGA, Artūras; KRIŪKIENĖ, Rita; KAVALIAUSKAS, Žydrūnas; LESZCZYŃSKA, Marzena; ABAKEVIČIENĖ, Brigita. Comparative study of samarium-doped ceria nanopowders synthesized by various chemical synthesis routes. *Ceramics International*. 2020, Vol. 46, iss. 15, p. 24385-24394. DOI: 10.1016/j.ceramint.2020.06.221. [IF: 3.830; AIF: 3.004; IF/AIF: 1.274; Q1 (2019, InCites JCR SCIE)].

A2. BASTAKYS, Lukas; KALYK, Fariza; MARCINAUSKAS, Liutauras; ČYVIENĖ, Jurgita; ABAKEVIČIENĖ, Brigita. Structural investigation of gadolinia-ceria multilayered thin films deposited by reactive magnetron sputtering. *Materials Letters*. 2020, Vol. 271, art. no. 127762, p. 1-4. DOI: 10.1016/j.matlet.2020.127762. [IF: 3.204; AIF: 4.950; IF/AIF: 0.647; Q2 (2019, InCites JCR SCIE)].

A3. KALYK, Fariza; ŽALGA, Artūras; VASILIAUSKAS, Andrius; TAMULEVIČIUS, Tomas; TAMULEVIČIUS, Sigita; ABAKEVIČIENĖ, Brigita. Synthesis and electron-beam evaporation of gadolinium-doped ceria thin films. *Coatings. Basel: MDPI*. 2022, vol. 12, iss. 6, art. no. 747, p. 1-16, ISSN 2079-6412. DOI:10.3390/coatings12060747. [IF: 2.881; AIF: 5.285; IF/AIF: 0.545; Q2 (2020, InCites JCR SCIE)]

Publications in conference proceedings

A4. STANKEVIČIŪTĖ, Algita; KALYK, Fariza; BUDRYTĖ, Gintarė; ABAKEVIČIENĖ, Brigita. Study of glycine nitrate precursor method for the combustion synthesis of Samarium-doped ceria. *CYSENI 2018: 15th international conference of young scientists on energy issues*, 23-25 May 2018, Kaunas, Lithuania. Kaunas: Lithuanian Energy Institute. eISSN 1822-7554. 2018, p. 244-250.

List of conference contributions related to the dissertation

1. Kalyk, Fariza; Tamulevičius, Tomas; Tamulevičius, Sigita; Abakevičienė, Brigita. Synthesis And Electron-Beam Evaporation of Gadolinium-Doped Ceria Thin Films. *23rd International Conference of Solid State Ionics (SSI-23)*, 17–22 July 2022, Boston Park Plaza in Boston, Massachusetts, USA.
2. Kalyk, Fariza; Abakevičienė, Brigita. Synthesis and evaporation of gadolinium-doped ceria electrolyte for IT-SOFC applications. *NBCM 2020: international conference on nanostructured bioceramic materials*, 1–3 December 2020, Vilnius, Vilnius University: conference book.
3. Kalyk, Fariza; Abakevičienė, Brigita. The evaluation of gadolinia-doped ceria electrolyte for IT-SOFC deposited by E-beam evaporation technique. *Advanced*

- materials and technologies: book of abstracts of 22nd international conference-school*, 24–28 August 2020, Palanga, Lithuania. Kaunas : Kaunas University of Technology. ISSN 1822-7759. 2020, A-P151, p. 181.
4. Kalyk, Fariza; Abakevičienė, Brigita. Characterisation of ceria based electrolytes prepared by glycine-nitrate combustion and co-precipitation synthesis routes: poster. *Advanced materials and technologies: book of abstracts of 21st international conference-school*, 19–23 August 2019, Palanga, Lithuania. Kaunas: Kaunas University of Technology. ISSN 1822-7759. 2019, P76, p. 110.
 5. Bastakys, Lukas; Kalyk, Fariza; Marcinauskas, Liutauras; Cyvienė, Jurgita; Abakeviciene, Brigita. Compositional and structural analysis of gadolinia-doped ceria thin films deposited by reactive magnetron sputtering. *E-MRS 2019 fall meeting*, 16–19 September, Warsaw, Poland. Warsaw: Warsaw University of Technology. 2019, art. no. M.PII.22, p. 1.
 6. Shalkhar, O.; Kalyk, F.; Abakevičienė, B. Structural characterization of samarium-doped ceria prepared by combustion and co-precipitation syntheses. *Matematika ir gamtos mokslai: teorija ir taikymai: XVII studentų konferencijos pranešimų medžiaga = Mathematics and natural sciences: theory and applications: material of the 17th students' presentation conference*/Bronė Narkevičienė (ats. redaktorė). Kaunas: KTU. eISSN 2669-056X. 2019, p. 35-36.
 7. Kalyk, Fariza; Stankevičiūtė, Algita; Leszczyńska-Redek, Marzena; Abakevičienė, Brigita. Comparative study of samarium doped ceria nanopowders synthesized by various chemical synthesis routes. *ANM2019: 14th international conference on advanced nanomaterials. 7th international conference on advanced graphene materials. 7th international conference on hydrogen energy. 5th international conference on advanced magnetic and spintronics materials. 3rd international conference on advanced polymer materials and nanocomposites. 2nd international conference on advanced nanoelectronics and organic light emitting diodes*: 17–19 July 2019, University of Aveiro, Portugal. [Aveiro]: ANM2019. 2019, 34, p. [1].
 8. Kalyk, Fariza; Stankevičiūtė, Algita; Leszczyńska-Redek, Marzena; Abakevičienė, Brigita. Investigation of ceria based electrolytes for solid oxide fuel cells obtained by different chemical synthesis techniques. *22nd international conference on solid state ionics (SSI-22)*, PyeongChang, Korea, June 16–21, 2019. Seoul: SSI-22. 2019, P-TUE-208, p. [1].
 9. Shalkhar, Olzhas; Kalyk, Fariza; Abakevičienė, Brigita. Structural characterization of Samarium-doped ceria prepared by combustion and co-precipitation syntheses: poster. *Open readings 2019: 62nd international conference for students of physics and natural sciences*, March 19–22, Vilnius, Lithuania: abstract book. Vilnius: Vilnius University, 2019, P3-98. ISBN 9786090701379. p. 374.
 10. Kalyk, Fariza; Leszczyńska-Redek, Marzena; Malys, Marcin; Krok, Franciszek; Kriūkienė, Rita; Abakevičienė, Brigita. Characterization of samarium-doped ceria ceramics prepared by co-precipitation synthesis. *Advanced materials and*

technologies: book of abstracts of 20th international conference-school, 27–31 August 2018, Palanga, Lithuania. Kaunas: Kaunas University of Technology. ISSN 1822-7759. 2018, P132, p. 167.

11. Venslauskaitė, Eglė; Gaidamavičienė, Giedrė; Žalga, Artūras; Kalyk, Fariza; Abakevičienė, Brigita. Sol-gel synthesis and characterization of samarium-doped ceria ceramics. *13th international symposium on systems with fast ionic transport (ISSFIT-13)*, July 3–7, 2018, Minsk, Belarus: program and abstracts. Minsk: Belarusian State Technological University. 2018, p. 71.
12. Kalyk, Fariza; Stankevičiūtė, Algita; Leszczynska-Redek, Marzena; Budrytė, Gintarė; Abakevičienė, Brigita. Structural, morphological, and electrical properties of samarium-doped ceria ceramics prepared by glycine-nitrate combustion synthesis. *13th international symposium on systems with fast ionic transport (ISSFIT-13)*, July 3–7, 2018, Minsk, Belarus: program and abstracts. Minsk: Belarusian State Technological University. 2018, p. 70.
13. Stankevičiūtė, Algita; Kalyk, Fariza; Budrytė, Gintarė; Abakevičienė, Brigita. Synthesis and properties of samaria-doped ceria nanopowders prepared by glycine nitrate combustion method = Samario oksidu modifikuotų cerio oksido nanomiltelių, gautų išdeginimo sintezės metu, fizikinių savybių tyrimai. *42-oji Lietuvos nacionalinė fizikos konferencija*, 2017 m. spalio 4–6 d., Vilnius: programa ir pranešimų tezės. Vilnius: Vilniaus universitetas, 2017. ISBN 9786094598807. p. 226. DOI: 10.15388/proceedings/LNFK.42.
14. Stankevičiūtė, Algita; Kalyk, Fariza; Budrytė, Gintarė; Abakevičienė, Brigita. Combustion synthesis and characterization of samaria-doped ceria electrolyte for IT-SOFCs. *E-MRS Fall Meeting 2017*, 18–21 September, Warsaw University of Technology, Warsaw, Poland. Warsaw: Warsaw University of Technology. 2017, A.P1.7, p. 1.

UDK 539.216+620.3+621.352.6](043.3)

SL344. 2022-*-* , * leidyb. apsk. l. Tiražas 14 egz. Užsakymas * .

Išleido Kauno technologijos universitetas, K. Donelaičio g. 73, 44249 Kaunas
Spausdino leidyklos „Technologija“ spaustuvė, Studentų g. 54, 51424 Kaunas